

# Ion electrosorption in nanoporous carbons

Dissertation

at the Institute of Physics  
Montanuniversität Leoben, Austria

Christian Prehal



submitted in fulfillment of the requirements for the degree of  
Doktor der montanistischen Wissenschaften

Leoben, August 2017



«Unsere Einstellung gegenüber der Zukunft muss sein: Wir sind  
jetzt verantwortlich für das, was in der Zukunft geschieht.»

Karl Popper

*dedicated to my family*



## Eidesstattliche Erklärung

Ich erkläre an Eides statt, dass ich diese Arbeit selbstständig verfasst, andere als die angegebenen Quellen und Hilfsmittel nicht benützt und mich auch sonst keiner unerlaubten Hilfsmittel bedient habe.

## Affidavit

I declare in lieu of oath, that I wrote this thesis and performed the associated research myself, using only literature cited in this volume.

15.08.2017

Datum

A handwritten signature in blue ink, consisting of several loops and a long horizontal stroke at the end.

Unterschrift



# Acknowledgements

I warmly thank my supervisor Univ.-Prof. Dr. Oskar Paris for his support, both in scientific and personal concerns. His (office-) door was literally most of the times open in particular for extensive science-related discussions. His enthusiasm, curiosity in scientific problems and attitude regarding good scientific practice had a big impact on my own way of working and will certainly guide me in future.

Moreover I would like to thank all my colleagues and friends at the Institute of Physics for the good time, the many off-topic discussions and the support in any respect, but especially for sharing uncountable hours of CPU power. Particular thanks go to Christian Koczwar, who joined the “supercap-collective” in September 2015 and contributed with his programming and informatics skills significantly to the success of the present work.

Furthermore I would like to thank Prof. Dr. Volker Presser from INM Saarbrücken for the strong support, good advices and extensive discussions about supercapacitors and ion electrosorption in generell. I thank Anna Schreiber, Benjamin Krüner, Dr. Daniel Weingarth and Nicolas Jäckel from INM Saarbrücken for providing more than enough carbon samples, a number of measurements and great support in electrochemical measurements.

Special thanks go to all people working at the Austrian SAXS Beamline at the Synchrotron ELETTRA. In particular I thank Max Burian and Heinz Amenitsch for their professional scientific support and for making every single beamtime an enjoyable (culinary) experience.

Moreover I would like to show my gratitude to Frau Heide Kirchberger from the secretary’s office for managing so much of my organizational work and Heinz Pirker and Peter Moharitsch for their support in technical issues.

Especially I thank all my friends for taking care of a healthy amount of distraction during my dissertation.

A very important factor in my life is my family. Thank you for guiding me into the right direction, supporting me in all my decisions and coping so thoughtful with my everyday moods during stressful periods.





# Abstract

A fundamental understanding of the mechanisms controlling ion charge storage and transport in confinement of carbon nanopores is essential to improve the performance of supercapacitors or devices for capacitive desalination. A key to verify detailed predictions of atomistic simulations is information obtained from experimental data about the spatial distribution of ions and solvent molecules within the nanopores.

In the framework of the present thesis *in situ* small angle X-ray scattering (*in situ* SAXS) was established as an experimental method to study ion rearrangements during charging and discharging of an *in situ* supercapacitor cell, using aqueous electrolytes and nanoporous carbons as electrodes. The high X-ray flux of the Austrian SAXS beamline at the Synchrotron radiation source ELETTRA (Trieste, Italy) enables time resolutions in the sub-second regime.

A detailed analysis of the X-ray transmission (XRT) signal allowed a quantification of the *global* cation and anion concentration change as a function of the applied cell voltage. During charging, only the balance between counter-ion and co-ion concentration is disturbed, where the total ion concentration remains constant. A first attempt to analyze the SAXS data revealed also *local* ion rearrangements within the nanopore structure, by interpreting correlation length parameters as a function of electrode charge and considering a so-called two-phase model. However, the complexity induced by the multiphase character of the system makes a detailed interpretation of the *in situ* SAXS data and understanding of the ongoing physical processes a challenging task.

For that reason a novel data analysis strategy was developed, involving atomistic Monte Carlo simulations to obtain equilibrium ion positions for each electrode charge within structural models of the nanoporous carbons. Carbon models and ion concentration are determined by experimental SAXS and XRT data. Subsequent Fourier transformation of the simulation box yields simulated SAXS curves which can in turn be compared with the experimental *in situ* SAXS measurements as a function of the electrode charge. This approach allowed the precise prediction of location (quantified by a degree of confinement) and desolvation of ions within the carbon nanopore confinement.

As a main result, charge was found to be stored most effectively in sites of the carbon structure with highest possible geometrical confinement, accompanied with partial

desolvation of ions. Moreover length-scale dependent ion kinetics was found by investigating *in situ* SAXS data applying cyclic voltammetry with different scan rates.

# Kurzfassung

Ein grundlegendes Verständnis über Mechanismen der ionischen Ladungsspeicherung und des Ionen-transportes in Kohlenstoff-Nanoporen ist essentiell, um das Leistungsvermögen von Superkondensatoren oder der kapazitiven Meerwasserentsalzung zu verbessern. Um detaillierte Vorhersagen von atomistischen Simulationen zu verifizieren, sind experimentelle Daten mit Information über die strukturelle Anordnung von Ionen und Lösungsmittelmolekülen innerhalb der Nanoporen von Nöten.

Im Rahmen der vorliegenden Arbeit wurde *in situ* Röntgenkleinwinkelstreuung (*in situ* SAXS) als experimentelle Methode zur Untersuchung der Ionen-Elektrosorption während des Ladens und Entladens einer *in situ* Superkondensatorzelle etabliert. Für die *in situ* Zellen wurden dabei Elektroden aus nanoporösem Kohlenstoff und Elektrolyten aus hochmolaren wässrigen Lösungen verwendet. Der hohe Röntgenfluss der österreichischen SAXS-Beamline an der Synchrotronstrahlungsquelle ELETTRA (Triest, Italien) ermöglicht Zeitauflösungen von weniger als einer Sekunde.

Mit Hilfe einer detaillierten Analyse des Transmissionssignals (XRT) konnte die *globale* Kationen- und Anionen-Konzentrationsänderung in der Arbeitselektrode als Funktion der angelegten Zellspannung berechnet werden. Während des Ladens steigt die Gegenionenkonzentration, während die Koionenkonzentration absinkt; die Gesamtionenkonzentration bleibt dabei konstant. Außerdem konnte mit Hilfe eines Zweiphasenmodells und Korrelationslängenparametern gezeigt werden, dass die Streudaten Informationen über die *lokale* strukturelle Umordnung der Ionen innerhalb der Nanoporen enthalten. Ein detailliertes Verständnis der *in situ* SAXS Daten und der ablaufenden physikalischen Prozesse gestaltet sich auf Grund des Multiphasencharakters des streuenden Systems jedoch als äußerst schwierig.

Aus diesem Grund wurde eine neue Methode zur Datenanalyse entwickelt, innerhalb derer die Ionenpositionen in Strukturmodellen der nanoporösen Kohlenstoffe als Funktion der Elektrodenladung mit Hilfe von atomistischen Monte Carlo Simulationen bestimmt werden. Dabei werden sowohl Kohlenstoffmodelle als auch Ionenkonzentrationen aus SAXS bzw. XRT Daten bestimmt. Eine Fourier Transformation der Simulationsbox liefert simulierte SAXS Kurven, welche wiederum mit gemessenen *in situ* SAXS Kurven bei jeder angelegten Zellspannung verglichen werden können. Dieser Ansatz erlaubt eine präzise Vorhersage des Ortes (quantifiziert

mit dem „Degree of Confinement“, DoC) und des Grades der Dehydratisierung der Ionen innerhalb der Nanoporenstruktur.

Ein wichtiges Resultat dieser Analyse hat gezeigt, dass Gegenionen bei Anlegen einer Spannung sich in Poren mit besonders hohem DoC begeben und dabei unter energetischem Aufwand partiell ihre Wasserhülle abgeben. Auf Grund der generell stärkeren Lokalisierung der Elektrodenladung in derartig engen Poren funktioniert die Ladungsspeicherung gerade dort am effektivsten. Außerdem konnten Unterschiede in der Ionenkinetik während des Ladens und Entladens auf unterschiedlichen Längenskalen des Porensystems festgestellt werden.

# Contents

<b>1</b>	<b>Introduction</b> .....	<b>1</b>
<b>2</b>	<b>Fundamentals</b> .....	<b>7</b>
2.1	Interaction of matter with X-rays .....	7
2.2	Kinematic scattering theory .....	8
2.3	Small angle X-ray scattering .....	11
2.3.1	Non particulate systems .....	12
2.4	Supercapacitors .....	17
2.4.1	Physical electrochemistry .....	18
2.4.2	Electrical double-layer capacitance .....	21
2.4.3	Supercapacitors with nanoporous electrodes .....	23
2.4.4	Faradaic contributions .....	26
2.5	Materials .....	28
2.5.1	Carbon electrode materials .....	28
2.5.2	Aqueous electrolytes and ion hydration .....	31
2.6	Monte Carlo Simulation .....	34
2.6.1	Long-range interactions (Ewald summation) .....	36
<b>3</b>	<b>Experimental</b> .....	<b>41</b>
3.1	Electrodes and electrolytes .....	41
3.2	The in-situ experiment .....	43
3.2.1	<i>In situ</i> cell design .....	45
3.2.2	Primary SAXS data treatment .....	47
<b>4</b>	<b>Simulating equilibrium ion positions in nanoporous carbons</b> .....	<b>51</b>
4.1	General structure .....	51
4.2	Induced electrode charges .....	56
4.3	Structure of C++ Code .....	60
4.4	Control parameters .....	62

4.5	Long range interactions .....	65
<b>5</b>	<b>Results and Discussion .....</b>	<b>69</b>
5.1	<i>Ex situ</i> characterization of disordered nanoporous carbons .....	69
5.1.1	SAXS on empty disordered nanoporous carbons .....	70
5.1.2	SAXS on disordered nanoporous carbons filled with liquid .....	71
5.1.3	Absolute SAXS measurements on disordered nanoporous carbons .....	74
5.1.4	X-ray diffraction .....	78
5.1.5	Generating a 3D model of the pore structure .....	79
5.2	<i>In situ</i> X-ray transmission to quantify global ion concentration .....	87
5.3	A two-phase model approach to interpret the <i>in situ</i> SAXS data .....	90
5.4	A new data analysis approach .....	103
5.4.1	Quantifying the local rearrangement and the degree of confinement ..	109
5.4.2	Quantifying desolvation and the local electrode charge .....	113
5.4.3	Arrangement and kinetics of ions .....	116
5.4.4	Empirical ion rearrangement algorithm .....	119
5.4.5	The data analysis strategy – summary .....	121
<b>6</b>	<b>Conclusions and Outlook .....</b>	<b>125</b>
<b>7</b>	<b>Bibliography .....</b>	<b>131</b>
	<b>Abbreviations .....</b>	<b>141</b>
	<b>List of publications .....</b>	<b>143</b>
	<b>Appendix A .....</b>	<b>145</b>
	<b>Appendix B .....</b>	<b>155</b>

# 1 Introduction

Energy storage is one of the biggest technological challenges for humanity in times of climate change. In order to keep the global warming to a maximum of 2 °C compared to pre-industrial times, global CO<sub>2</sub> gas emissions need to be halved by the year 2050.<sup>1</sup> Despite political efforts a more recent study<sup>2</sup> predicts that the most likely event is an energy rise between 2 and 4.9 °C by the end of the 21<sup>st</sup> century. The future emission level (red curve in Fig. 1.1a-b) is calculated from a model based on population, the gross domestic product (GDP) per capita and the CO<sub>2</sub> emission per unit of GDP.<sup>3</sup> It lies in-between alternative predictions based on models considering different socioeconomic scenarios, so-called representative concentration scenarios (RCPs).<sup>3</sup> The likelihood of fulfilling the Paris climate agreement of 1.5 °C global temperature rise is estimated with less than 1% and the most likely event is an energy rise of 3.2 °C by the year 2100 (Fig. 1.1c). Apparently the situation appears to be rather dramatic.

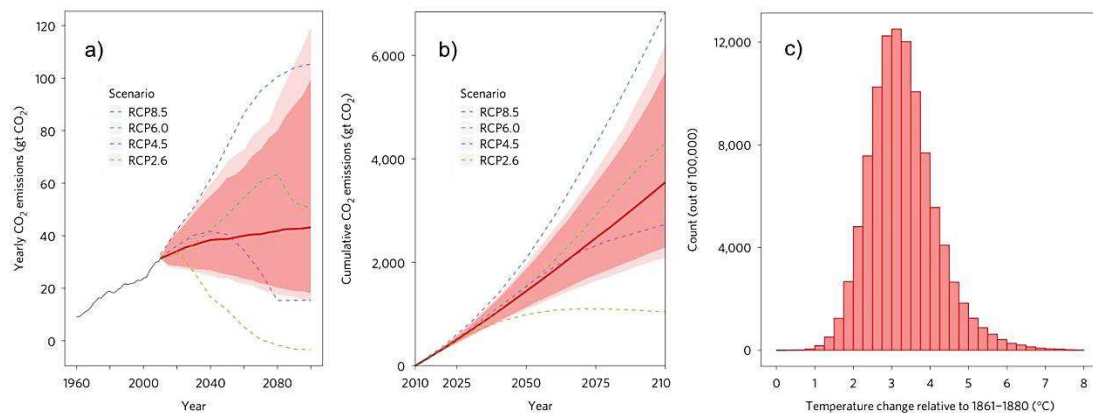


**Fig. 1.1:** Yearly (a) and cumulative (b) CO<sub>2</sub> emissions predicted by model calculations from Ref.<sup>2</sup> (red curve) and for different representative concentration pathways (RCPs, dashed lines). The probability distribution reaching a certain temperature rise by the year 2100 is given in (c). Reproduced with permission from Ref.<sup>2</sup>. © Nature Publishing Group.

One essential measure to reduce CO<sub>2</sub> emissions is the conversion of the current fossil fuel based transportation system to an electric mobility based system and (probably in further consequence) to a fuel cell based system. To reach practical maximum ranges and charging times of electric vehicles, electric energy storage devices with high energy and power densities are required. Along with the transition towards electric mobility

in transportation, the production of electricity needs to be converted to a system containing 100% clean (renewable) sources of energy. Large scale storage of grid electricity is required, since the power output of renewable sources of energy, like wind or solar energy, strongly fluctuates, depending on weather conditions and the season of the year. Among other storage technologies, like hydropower or chemical (gas) storage electric energy storage in the form of batteries or supercapacitors is considered as a key player for future grid storage.<sup>4</sup> Also private households use more and more photovoltaic panels to produce their own electricity, stored in electric energy storage devices like batteries.<sup>5</sup>

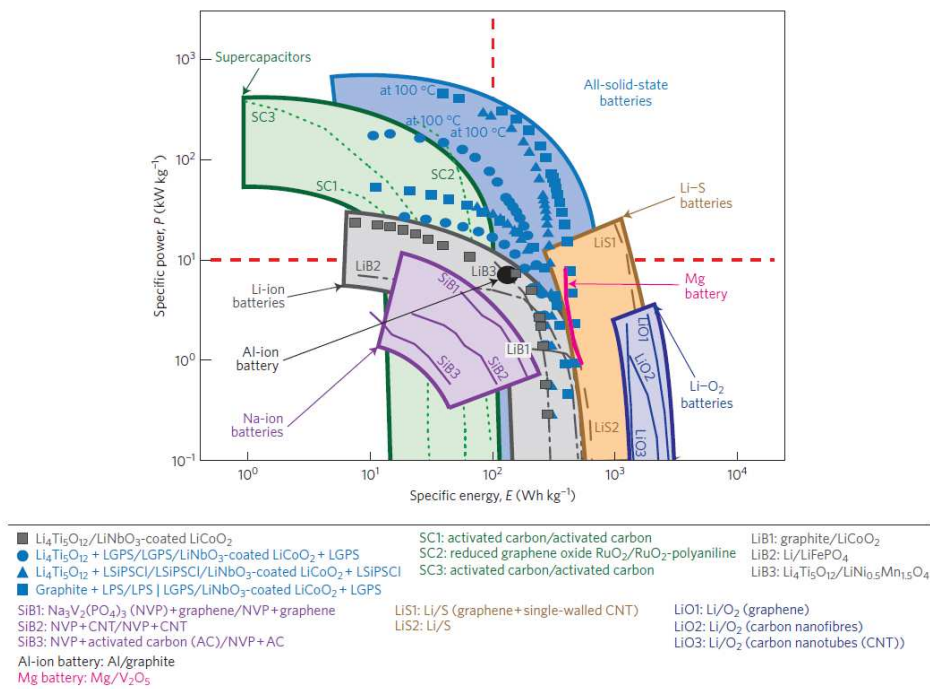


**Fig. 1.2:** Ragone-plot of different electric energy storage technologies (some of them currently only implemented on a lab scale). To estimate the ability for implementation to a commercial product additional factors have to be considered (such as long term stability). High power densities of all-solid-state batteries are only achieved at elevated temperatures (100 °C). Reproduced with permission from Ref.<sup>6</sup>. © Nature Publishing Group.

Supercapacitors are efficient electric energy storage devices with high power densities, extremely long cycle lifetimes, and relatively low energy densities. Compared to batteries supercapacitors are, despite of their low energy densities, beneficial for applications where high power densities (up to 100 kW/kg) and long cycle lifetimes ( $> 10^6$  cycles) are demanded. The power densities of supercapacitors exceed those of most novel battery technologies (see Fig. 1.2; high power densities of all-solid-state



batteries are only achieved at elevated temperatures).<sup>6</sup> Sustainable energy management of renewable energy sources (i.e. grid storage) or electric transportation requires storage capabilities which allow the uptake and release of energy on a large range of different timescales. Thus, for applications where fast charging/discharging rates and long cycle lifetimes are required, supercapacitors are believed to partially replace, yet to a large extent complement Li ion technology. Today supercapacitors are used in transportation for the recovery of braking energy, in electric busses, cable cars or airplane doors.<sup>7</sup> Moreover, supercapacitors are believed to play an important role for microelectronic applications and in smart textiles in future.<sup>8</sup> Yet, the market represents currently (2016) only 400 million USD compared to 95 billion USD of the global battery market, but is believed to catch up significantly in the near future.<sup>9</sup> To widen the usage of supercapacitors the costs need to be reduced from currently 0.010 – 0.015 USD/F to 0.005 USD/F.<sup>10</sup> This goal appears reasonable, considering the predicted increase in supercapacitor production in near future.

A fundamental understanding about the mechanisms controlling ion electrosorption in charged nanopores is essential to improve energy densities, power densities and cycle lifetime of supercapacitors. Usually supercapacitors consist of high surface area electrodes immersed in (liquid) electrolyte. Ions are adsorbed at the oppositely charged electrodes, if a cell voltage is applied. The opposing charges of cations (or anions) at the electrolyte side and electrons (or holes) at the electrode side reveal the capacitive behavior. In this work nanoporous carbons with specific surface areas up to 2000 m<sup>2</sup>/g and an average pore size around 1 nm are used as electrode material. These pores are not much larger than the hydrated ion radius of the used alkali metal ions in aqueous solution. Pores, in which ions are highly confined, can lead to an increased capacitance and energy density; yet, the mutual blocking of ions during charging and discharging in such pores can lower ion transport and power densities. In general, atoms or molecules in spatial confinement of a size comparable to the size of a single atom or molecule are highly interesting from a scientific point of view. Unusual physical properties can be obtained such as a shift of the water freezing point<sup>11</sup>, enhanced ion diffusion<sup>12</sup> or the extreme densification of hydrogen<sup>13</sup>. The behavior of molecules and ions in nanoporous confinement not only determines properties of energy storage technologies like supercapacitors<sup>14</sup>, but also devices for capacitive de-ionization<sup>15</sup> (CDI) or applications in life science like nanopore DNA sequencing.<sup>16</sup>

The enhancement of energy densities in supercapacitors is currently attempted by different strategies<sup>17</sup>. Aqueous electrolytes have compared to organic electrolytes or ionic liquids the drawback of a small decomposition (voltage) window, which limits the amount of storable energy<sup>14</sup>. In most commercially available supercapacitors nowadays organic electrolytes are used. However, aqueous electrolytes are preferable

for future applications due to low costs, easy handling, environmental friendliness (“green technology”) and non-flammability.<sup>18</sup> Moreover, fast ion diffusion in aqueous electrolyte enables high power densities. Strategies for increasing the energy density in aqueous systems involve many times an increase in the capacitance, by either optimizing the electrical double-layer capacitance and/or introducing sources of fast faradaic reactions (so-called pseudocapacitance). Redox active aqueous electrolytes in combination with nanoporous carbon electrodes have recently drawn attention due to their potential energy density values of 50 Wh/kg (by keeping at the same time power densities high).<sup>19-21</sup>

Other sources of faradaic reactions might be functionalized carbon surfaces (pseudocapacitance) or “hybrid” battery and supercapacitor materials.<sup>14</sup> For any source of faradaic or non-faradaic capacitance, the subtle trade-off between increasing the energy densities and keeping high power densities requires a fundamental understanding of the key parameters governing ion charge storage in nanoporous carbons on an atomistic level.

The lack of suitable *in situ* experimental techniques on the one side and the increased computational capabilities on the other side has opened an increasing gap between detailed predictions of sophisticated simulations and their experimental verification.<sup>17,22</sup> Atomistic simulations have increasingly elucidated details about the charge storage mechanism of ions on an atomic scale, taking e.g. the full complexity of the carbon electrode structure into account. Predictions and explanations regarding ion diffusion, ion desolvation and ion concentration changes in different categories of pores could be retrieved. In contrast to that until recently *in situ* experimental techniques yielded only global cation and anion concentration changes as a function of the applied cell voltage. Hence, for a long time an experimental verification of atomistic simulations by comparing quantitative numbers seemed only possible by developing either simplified experimental model systems or simulations being as close as possible to the experimental reality. Alternatively, *in situ* scattering methods that allow retrieving structural information on the carbon pore structure and the spatial distribution of ions and solvent molecules within the pores might enable a direct verification of results from most recent molecular dynamics simulations. *In situ* small angle X-ray scattering (*in situ* SAXS) for example is a suitable technique to study concentration and structural changes of cations and anions within nanoporous carbon electrodes during charging and discharging. The *in situ* scattering data contains rich detail of structural and kinetic information, as obtained from preliminary studies to this work.<sup>23</sup> However, the complexity of the investigated system, consisting of carbon atoms, water molecules and two sorts of ions, makes the analysis of the SAXS data challenging.

---

In this thesis ion electrosorption in nanoporous carbons is studied by *in situ* small angle X-ray scattering. The developed *in situ* cell and experimental method allow recording and quantifying both global ion concentration changes and local (in-pore) ion rearrangements. Problems related to data interpretation due to the complexity of the system are overcome by novel data analysis strategies. One of these strategies involves atomistic Monte Carlo simulations and allows the study of voltage dependent ion rearrangements on a real space carbon nanopore model on the computer. The ability to study structural aspects of electrical double layer formation in nanopore confinement leads to conclusions regarding ion desolvation and optimized electrode pore geometries.



## 2 Fundamentals

### 2.1 Interaction of matter with X-rays

If an incident X-ray beam hits a material some of its initial intensity is attenuated. A number of different interactions between X-ray photons and electrons (and partially phonons) are responsible for a lowered intensity of the transmitted beam (Fig. 2.1). Depending on the incident photon energy and the material one or the other interaction dominates.<sup>24</sup>

Some of the incident X-ray photons are scattered, either elastically or inelastically. The elastic scattering process is discussed in detail in section 2.2. So-called Compton scattering involves an energy transfer to (from) an electron from (to) the incoming photon. As a consequence the inelastically scattered photon has a different energy than the incoming photon. Compton scattering is an incoherent scattering process; i.e. the scattered wave has no fixed phase relation to the incoming wave, resulting in a constant scattering intensity  $I(Q)$  (incoherent background).<sup>24</sup> Other inelastic scattering processes like Raman scattering and Brillouin scattering involve optical phonons and acoustic phonons in their scattering processes, respectively. Both processes concern photons mainly in the optical regime.<sup>24</sup>

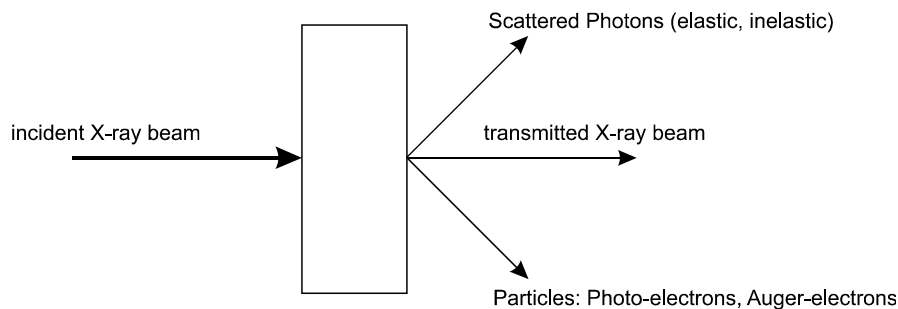


**Fig. 2.1:** Interaction of matter with light. Emitted particles/waves can be detected and used to study the irradiated material.

Besides coherently and incoherently scattered photons most of the X-ray primary beam intensity is attenuated due to photoelectric absorption. Energy of an incoming photon is absorbed by kicking an electron into the vacuum. Energy is in turn released by emitting fluorescence radiation due to the relaxation of an electron from a higher

shell to the empty state of the lower shell. Alternatively energy is released by emitting an Auger electron.<sup>24</sup>

In summary, the attenuation of the primary beam intensity can be splitted into three main contributions: coherently scattered photons, incoherently scattered photons and (in the X-ray regime predominantly) photon absorption due to the photoelectric effect.<sup>24-26</sup> According to Lambert-Beers law the primary beam intensity decays exponentially within the material  $I(x) = I_0 * e^{-\mu x}$ , depending on the material specific attenuation coefficient  $\mu$ .

## 2.2 Kinematic scattering theory

In a scattering experiment (Fig. 2.2a) the intensity of the scattered waves are recorded as a function of the scattering angle  $2\theta$ , or more general the scattering vector  $\vec{Q}$ , being defined as the difference between the wave vector of the scattered and incoming wave  $\vec{k}_2 - \vec{k}_1$ . To obtain structural information of the sample the incoming (usually) monochromatic waves need a fixed phase relation over a certain width significantly larger than the investigated structures (lateral or transversal coherence length). The differential scattering cross section  $\partial\sigma/\partial\Omega$  is proportional to the fraction of photon flux being scattered into the solid angle  $d\Omega$  around  $\Omega$ , which is  $(\partial\sigma/\partial\Omega) d\Omega$ . The scattering length  $b_e$  is the proportionality constant between the amplitude of the incoming and the scattered electromagnetic wave and corresponds to the classical electron radius (if polarization is neglected).<sup>23,24,27,28</sup>

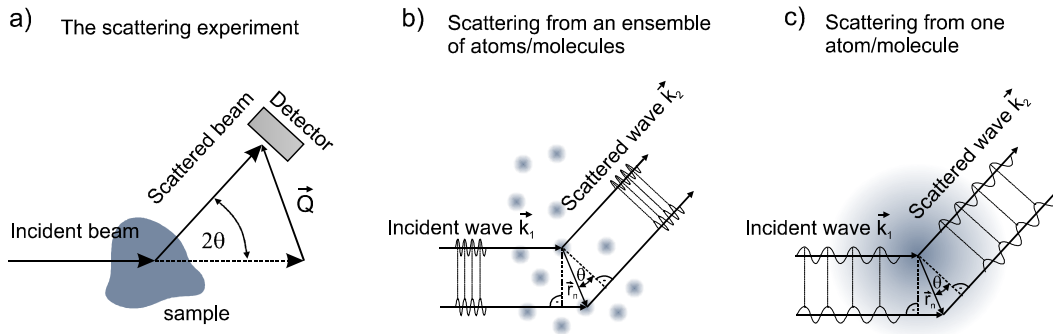


**Fig. 2.2:** Scattering experiment/process visualized on three different levels of magnification (a), (b), (c).

If a coherent electromagnetic wave  $\vec{k}_1$  is scattered by two electrons located at the origin and the position  $\vec{r}_n$  the total phase difference in the direction of  $\vec{k}_2$  corresponds to  $(\vec{k}_1 - \vec{k}_2) \cdot \vec{r}_n$ , as visualized in Fig. 2.2c. Thus the amplitude of the wave scattered at the position  $\vec{r}_n$  is proportional to  $\exp[i(\vec{k}_1 - \vec{k}_2) \cdot \vec{r}_n] = \exp[-i\vec{Q}\vec{r}_n]$ . Considering

the electron cloud of an atom the atomic formfactor can be written as a volume integral over all scattering centers.<sup>24,28</sup>

$$b_e f_0(Q) = b_e \int \rho(\vec{r}) e^{-i\vec{Q}\vec{r}} dV, \quad (2.1)$$

with  $b_e$  being the scattering length of a single electron and  $\rho(\vec{r})$  the number electron density within the atom. According to Eq. 2.1 the atomic formfactor corresponds to the Fourier transform of the real space electron density distribution. In the following, atoms (and not electrons) are considered as smallest scattering centers (Fig. 2.2b) with a scattering strength considered by the atomic form factor. More generally the atomic formfactor  $f(\omega, Q)$  can be defined as<sup>24,29,30</sup>

$$f(\omega, Q) = f_0 + f'(\omega) + if''(\omega). \quad (2.2)$$

The frequency dependent terms of the formfactor origins from the frequency dependent polarizability of a bounded electron, classically described by the forced oscillator model. The incoming electromagnetic wave causes an electron to oscillate and sending out dipole radiation. For that reason the amplitude of the scattered radiation is not equal for all angles, considered by the so-called Lorentz factor. The imaginary part changes the phase of the scattered wave and is (according to the optical theorem) related to the absorption within the material. Close to the resonance frequency of the bound electron the scattering signal is amplified significantly, enabling contrast variation experiments in materials consisting of more than one element (anomalous X-ray scattering<sup>29</sup>). The resonance frequency is related to the electron energy levels with respect to the vacuum level. At high photon frequencies the scattering length and thus the atomic formfactor becomes frequency independent; i.e.  $f'(\omega)$  and  $f''(\omega)$  become zero, so-called Thomson scattering dominates. All scattering data analyzed in this thesis relate to elastic, non-resonant Thomson scattering.<sup>24,30,31</sup>

Scattering from an ensemble of atoms/molecules gives a similar expression for the scattering amplitude as seen for the scattering of a single atom. The scattering intensity is proportional to the squared magnitude of the scattering amplitude and reads

$$I(Q) \cdot V / b_e^2 = f(Q)^2 \sum_n e^{i\vec{Q}\vec{r}_n} \sum_m e^{-i\vec{Q}\vec{r}_m} = f(Q)^2 \sum_n \sum_m e^{i\vec{Q}(\vec{r}_n - \vec{r}_m)}. \quad (2.3)$$

Separating the double summation, where  $m=n$  gives

$$I(Q) \cdot V/b_e^2 = Nf(Q)^2 + f(Q)^2 \sum_n \sum_{m \neq n} e^{i\vec{Q}(\vec{r}_n - \vec{r}_m)}. \quad (2.4)$$

Replacing the second summation by an integral, introducing the atomic number density  $n_n(\vec{r}_{nm})$  and  $\vec{r}_{nm} = \vec{r}_m - \vec{r}_n$  as the distance vector between  $\vec{r}_m$  and the reference atom at position  $\vec{r}_n$ , results in

$$\begin{aligned} I(Q) \cdot V/b_e^2 = Nf(Q)^2 + f(Q)^2 \sum_n \int_V [n_n(\vec{r}_{nm}) - n_0] e^{i\vec{Q}(\vec{r}_n - \vec{r}_m)} dV_m \\ + f(Q)^2 n_0 \sum_n \int_V e^{i\vec{Q}(\vec{r}_n - \vec{r}_m)} dV_m. \end{aligned} \quad (2.5)$$

Considering atom density fluctuations around the average atom density  $n_0$  results in an additive contribution (last term in Eq. 2.5) accounting for the scattering from a homogenous atom density. This scattering contribution takes fluctuations in the average density  $n_0$  on a higher level of hierarchy into account, contributing to the total scattering intensity at small Q-values. Most importantly, Eq. 2.5 reveals the formal splitting of atomic/molecular structure factor (first two terms) from the small angle scattering intensity (last term). The splitting is exact as long as correlations between atomic and superior structures at higher level do not exist. Practically this is always the case for crystal lattices with long range order and if the typical length scale of the superior structure is significantly larger than average atomic distances. However, even if differences in the length scale between atomic and higher order structure are small, correlations are often negligible.<sup>27,32</sup> The last term in Eq. 2.5 is denoted as small angle scattering intensity and treated separately in section 2.3.

Taking only the first two terms in Eq. 2.5 into account, replacing the sum in the structure factor term by a volume integral and replacing the atom density  $n_n(\vec{r}_{nm})$  (surrounding the reference atom  $n$ ) by its average over all atoms  $n(\vec{r})$  gives

$$I(Q) \cdot V/b_e^2 = Nf(Q)^2 + f(Q)^2 \int_V [n(\vec{r}) - n_0] e^{i\vec{Q}\vec{r}} dV. \quad (2.6)$$

Considering isotropy and the radial distribution function  $g(r) = n(r)/n_0$  results in the general expression for the structure factor<sup>27</sup>

$$S(Q) = \frac{I(Q)}{Nf(Q)^2} \cdot V/b_e^2 = 1 + \frac{4\pi}{Q} \int_0^\infty r[g(r) - 1] \sin(Qr) dr, \quad (2.7)$$

where  $g(r)$  can be calculated via the Fourier-integral theorem in 3D<sup>27</sup>



$$g(r) = 1 + \frac{1}{2\pi^2 r n_0} \int_0^\infty Q[S(Q) - 1] \sin(Qr) dQ. \quad (2.8)$$

For a multi-component system partial structure factors  $S_{\alpha\beta}$  have to be taken into account<sup>33,34</sup>

$$S_{multi}(Q) \cdot V/b_e^2 = \sum_\alpha \phi_\alpha f_\alpha^2 + \sum_\alpha \sum_{\beta \geq \alpha} (2 - \delta_{\alpha\beta}) \phi_\alpha \phi_\beta f_\alpha f_\beta [S_{\alpha\beta} - 1]. \quad (2.9)$$

### 2.3 Small angle X-ray scattering

Replacing the summation in the last term of Eq. 2.5 by an integral and introducing the scattering length density  $\rho_b(\vec{r}) = b_e f n_0$ , the small angle scattering intensity can be written as<sup>32</sup>

$$I_{SAS}(Q) = \iint_V \rho_b(\vec{r}_n) \rho_b(\vec{r}_m) e^{i\vec{Q}(\vec{r}_n - \vec{r}_m)} dV_m dV_n. \quad (2.10)$$

Since the atomic form factor corresponds approximately to the atomic electron number within the small angle scattering regime<sup>24</sup>, the scattering length density is roughly  $b_e$  times the electron density. Following a convention of Ref.<sup>32</sup> the constant scattering length  $b_e$  shall be neglected in section 2.3. Moreover, the scattering intensity is not normalized by the (irradiated) sample volume  $V$ . As a consequence the scattering length density is simply replaced by the electron density  $\rho(\vec{r})$ . Introducing the auto-correlation function  $\tilde{\rho}^2(r)$ , Eq. 2.10 can be rewritten to<sup>32</sup>

$$\tilde{\rho}^2(r) = \int_V \rho(\vec{r}_n) \rho(\vec{r} + \vec{r}_n) \quad \text{with } \vec{r} = \vec{r}_n - \vec{r}_m, \quad (2.11)$$

$$I_{SAS}(Q) = \int_V \tilde{\rho}^2(r) e^{i\vec{Q}\vec{r}} dV.$$

Assuming isotropy and absence of long range order gives

$$I_{SAS}(Q) = \int 4\pi r^2 \tilde{\rho}^2(r) \frac{\sin(Qr)}{Qr} dr \quad (2.12)$$

For  $r = 0$  the autocorrelation function  $\tilde{\rho}^2(r)$  equals  $V\langle\rho^2\rangle$ . The assumption of missing long range order further implies that  $\tilde{\rho}^2(r)$  approaches  $V\langle\rho\rangle^2$  at large  $r$ . This constant

background in the autocorrelation function does not contribute to the scattering intensity. It is convenient to subtract the mean electron density by considering density fluctuations only and introduce the correlation function  $\gamma(r)$ .

$$V\gamma(r) = \bar{\rho}^2(r) - V\langle\rho\rangle^2 \quad \text{with} \quad I_{SAS}(Q) = V \int 4\pi r^2 \gamma(r) \frac{\sin(Qr)}{Qr} dr \quad (2.13)$$

An inverse Fourier transform of Eq. 2.13 gives the correlation function from measured SAXS data.<sup>32</sup>

### 2.3.1 Non particulate systems

In isotropic non-particulate systems (e.g. interconnected porous systems, Fig. 2.3a) the correlation function can be written as

$$\gamma(r) = \langle \eta(r_1)\eta(r_1 + r) \rangle = \varphi(1 - \varphi)(\Delta\rho)^2\gamma_0(r), \quad (2.14)$$

with  $\eta$  being the electron density fluctuations  $\rho - \langle\rho\rangle$ ,  $\varphi$  the volume fraction of one phase (e.g. pores),  $\Delta\rho$  the electron density difference (Fig. 2.3b) and  $\gamma_0(r)$  the normalized correlation function with a maximum value of 1. As long as the typical length scale of the two-phase (Fig. 2.3a) and the atomic structure are different, or more generally, correlations between two-phase and atomic structure do not exist, the following picture is exact (see discussion in section 2.2). The (mean) electron density difference between the two phases  $\Delta\rho$  is a measure for the X-ray contrast.

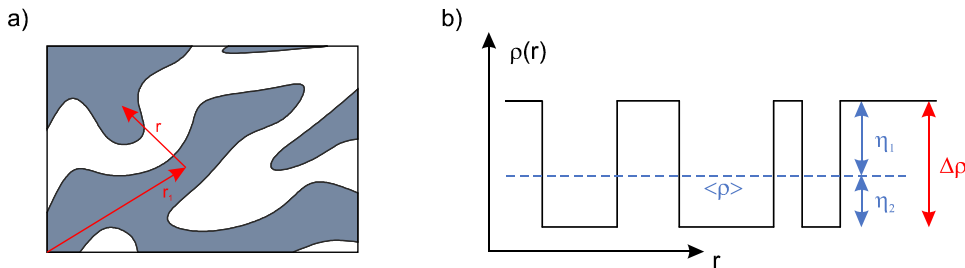


**Fig. 2.3:** Schematic representation of a disordered two-phase system (a). The electron density profile of a two-phase system is sketched in (b).

A systematic change of the electron density level of one the phases, e.g. by filling water into the pores or changing the magnitude of the complex formfactor (by changing the X-ray wavelength; anomalous SAXS; Eq. 2.2), can help to interpret SAXS data in the presence of a third or fourth phase. Such contrast variation approach is a common strategy for scattering experiments on complex multiphase systems.<sup>31</sup>

Considering Eq. 2.14, the small angle scattering intensity reads<sup>32</sup>

$$I_{SAS}(Q) = V \cdot \varphi(1 - \varphi)(\Delta\rho)^2 \int_0^\infty 4\pi r^2 \gamma_0(r) \frac{\sin(Qr)}{Qr} dr . \quad (2.15)$$

A simple analytical description of the scattering intensity of randomly shaped pore (or more generally two-phase) structures is provided by the Debye-Anderson-Brumberger (DAB) model<sup>35</sup>. The DAB model implies a random pore structure and consequently an exponentially decaying correlation function. The correlation length  $a$  is defined as the arithmetic average of the correlation function and corresponds to the  $1/e$  value of the exponentially decaying correlation function within the DAB model. It is related to the pore volume and the specific surface  $S/V$  as shown below.

$$\gamma_0(r) = e^{-r/a} \quad \text{with} \quad a = \frac{4V\varphi(1 - \varphi)}{S} \quad (2.16)$$

The scattering intensity is in this case an analytic function of the form<sup>35</sup>

$$I_{DAB}(Q) = \frac{2\pi(\Delta\rho)^2 * S}{(1/a^2 + Q^2)^2 * V} . \quad (2.17)$$

### The low Q regime

The scattering power at small Q-values results from Eq. 2.15 and is proportional to a so-called correlation volume  $v_c$ .

$$I_{SAS}(Q = 0) = V \cdot \varphi(1 - \varphi)(\Delta\rho)^2 \cdot v_c \quad \text{with} \quad v_c = \int_0^\infty 4\pi r^2 \gamma_0(r) dr \quad (2.18)$$

According to Eq. 2.16 and 2.17 the correlation volume for a random pore system equals  $8\pi$  times the third power of the correlation length  $a$ . Any change in the correlation length during the scattering experiment, e.g. due to strain, in this way significantly influences the scattering intensity at small Q.<sup>32</sup>

### The intermediate Q regime

The central part of the SAXS curve of *non-interacting particles* can be described by the Guinier formula:<sup>32</sup>

$$I_{SAS}(Q) = (\Delta\rho)^2 e^{-Q^2 R_g^2 / 3} . \quad (2.19)$$

The radius of gyration  $R_g$  is defined as the mean square distance from the center of gravity of the particle. It is derived by expanding the factor  $\cos(Qr)$  of the scattering amplitude by a power series up to the  $Q^2$  term. For non-particulate systems, as discussed here, the Guinier approximation is in principle not valid. However, a fit to the scattering intensity using Eq. 2.19 can still give an approximate measure for a mean correlation length in the two-phase system, as shown in section 5.3.

### The large Q regime

The Porod law comprises a power-law intensity decay being proportional to  $Q^{-4}$  at large Q. It is valid for an ideal two-phase system having sharp interfaces and a constant electron density within the phases.

$$I_{SAS}(Q \rightarrow \infty) = V\varphi(1 - \varphi)(\Delta\rho)^2 \cdot \frac{8\pi}{a} \cdot \frac{1}{Q^4} = (\Delta\rho)^2 \cdot \frac{2\pi}{Q^4} \cdot S \quad (2.20)$$

In microporous carbons different reasons might cause deviations from the ideal Porod behavior. A realistic electron density profile and its approximation according to the two-phase model are sketched in Fig. 2.4. First, the finite width of the smooth density transition between pore and carbon matrix (indicated by blue arrow in Fig. 2.4) influences the scattering intensity at large Q. A convolution of the 2-phase electron density and a smoothing function with a variance that is small compared to the average width of pores/matrix gives rise to the following approximation.<sup>36</sup>

$$I_{SAS}(Q) = I_{2-phase}(Q) \cdot (1 - \sigma^2 Q^2) \quad (2.21)$$

Density fluctuations within a single phase, as indicated by the red arrow (Fig. 2.4) could also lead to deviations from the Porod behavior. Ruland<sup>36</sup> has shown that one dimensional density fluctuations lead to an additive intensity term proportional to  $Q^{-2}$ . These fluctuations have been found in graphitic and non-graphitic carbons and are related to fluctuations in the graphene interlayer distance. Random and isotropically (in all three dimensions) distributed density fluctuations, that show no correlation with the actual pore structure, lead to a constant additive intensity contribution. All of these deviations from the ideal two-phase model might be treated as structure factor contributions as well. This seems reasonable, since smoothing functions and density fluctuations are in the typical size regime of atomic distances themselves. Alternatively nano- and sub-nanometer sized carbon pores (with a “rough” surface due to defects or in general “empty space” in the size regime below  $\approx 0.5$  nm) can be treated as a fractal. A fractal structure reveals a power-law intensity decay with an exponent between -2 and -4.<sup>37</sup>

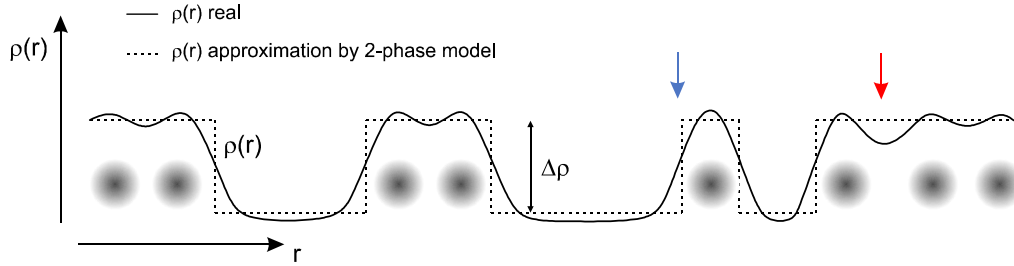


**Fig. 2.4:** Sketch of the electron density profile of a 1D cross-section of a nanoporous carbon structure. The shaded areas represent positions of carbon atoms.

In general, a significant number of pores in the sub-nanometer range (e.g. with  $\approx 0.5$  nm) cause some scattering power at very large  $Q$ -values. Theoretically, an ideal Porod decay of those small size-features could be visible at even larger  $Q$ , where the carbon structure factor intensity already dominates. This makes a clear splitting of the atomic structure (with atomic distances of  $\approx 0.3$  nm) impossible. It seems rather arbitrary whether the deviation of the  $Q^{-4}$  decay is considered within the actual nanopore scattering intensity (described by a power-law decay with an exponent smaller than four) or treated as additive term within the carbon structure factor. In general, the exact discrimination between contributions belonging to the nanopore scattering and those belonging to an additive structure factor is difficult for carbons with very small mean pore sizes (typically  $< 1$  nm in our case) and there are certainly several possible (and equally valid) approaches.<sup>36-38</sup>

### SAXS measurements and their spatial resolution

The spatial resolution in scattering experiments is restricted by the maximum measured scattering vector length value.<sup>39,40</sup> Generally speaking, the scattering power at large  $Q$ -values contains information about small spatial features and vice versa. The scattering amplitude  $A(Q)$  for a scattering experiment in a finite  $Q$ -regime can be expressed by

$$A(Q) = f(Q) \cdot g(Q) \quad \text{where} \quad g(Q) = \begin{cases} 1 & \text{for } Q \leq Q_{max} \\ 0 & \text{for } Q > Q_{max} \end{cases} . \quad (2.22)$$

This means that the theoretical scattering amplitude  $f(Q)$  of the scattering real space structure is multiplied by a rectangular function (Fig. 2.5a). The Fourier Transform of the scattering amplitude gives the real space structure (Fig. 2.5c), and corresponds to the convolution of the Fourier transformed functions  $f$  and  $g$ ,  $H(x) = F(x) * G(x)$ . As an example let's assume that the scattering amplitude  $f(Q)$  corresponds to the

amplitude of a rectangular slit, where  $F(x)$  gives a rectangular function and  $G(x)$  the spherical Bessel function of first kind and zeroth order (Fig. 2.5b).

$$F(x) \sim \begin{cases} 1 & \text{for } x_{min} < x \leq x_{max} \\ 0 & \text{for rest} \end{cases} \quad \text{and} \quad G(x) \sim \frac{\sin(xQ_{max})}{xQ_{max}}, \quad (2.23)$$

The convolution effectively smears out the rectangular real-space structure (Fig. 2.5c).  $G(x)$  can be approximated by a Gaussian function fitted to the primary peak of  $G(x)$ . Measuring the scattering intensity up to  $8 \text{ nm}^{-1}$  would give a Gaussian smearing function with a width of  $\approx 0.25 \text{ nm}$ . In other words, the scattering power of a rectangular scattering object measured up to  $Q < 8 \text{ nm}^{-1}$  would not be distinguishable from the same rectangular object smeared with a Gaussian of the width  $0.25 \text{ nm}$  (Fig. 2.5c). This perception of spatial resolution is patterned on the definition of microscopy and relates to the discriminability of two neighboring objects.

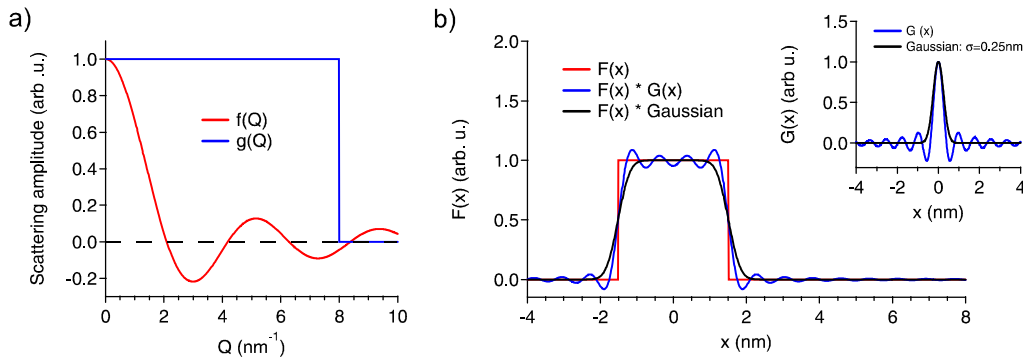


**Fig. 2.5:** The scattering amplitude as a function of the scattering vector length  $Q$  is given in (a). The real space object (rectangular function  $F(x)$ ) is convoluted with  $G(x)$  or by approximation with a Gaussian function (b). The inset shows the function  $G(x)$ , being the Fourier Transform of the rectangular function  $g(Q)$ . It can be approximated by a Gaussian (black curve).

However, in scattering experiments the scattering intensity and changes of the scattering intensity usually represent the time and spatial average of millions of scattering objects. This implies that structural changes of the two-phase system (e.g. mechanical strain) that are orders of magnitudes smaller than the actual spatial resolution (of e.g.  $0.25 \text{ nm}$ ) can be detected. In that case the resolution of structural changes is restricted by experimental parameters like the beam divergence, the detector pixel size and the monochromaticity of the X-ray beam.<sup>39,41</sup>

## 2.4 Supercapacitors

If two inert electrodes are immersed in liquid electrolyte an electrical double-layer will form at the electrode-electrolyte interface as a voltage is applied (Fig. 2.6a). In a simplified picture cations in the electrolyte are attracted to the negative electrode and anions are attracted to the positive electrode, which is equivalent to two capacitors in series. In a pure electrical double-layer capacitor (EDLC) no chemical reaction, i.e. no charge transfer across the electrode-electrolyte interface, takes place. The opposed charges at the interface represent the electrical double-layer and reveal the capacitive behavior.<sup>42</sup>

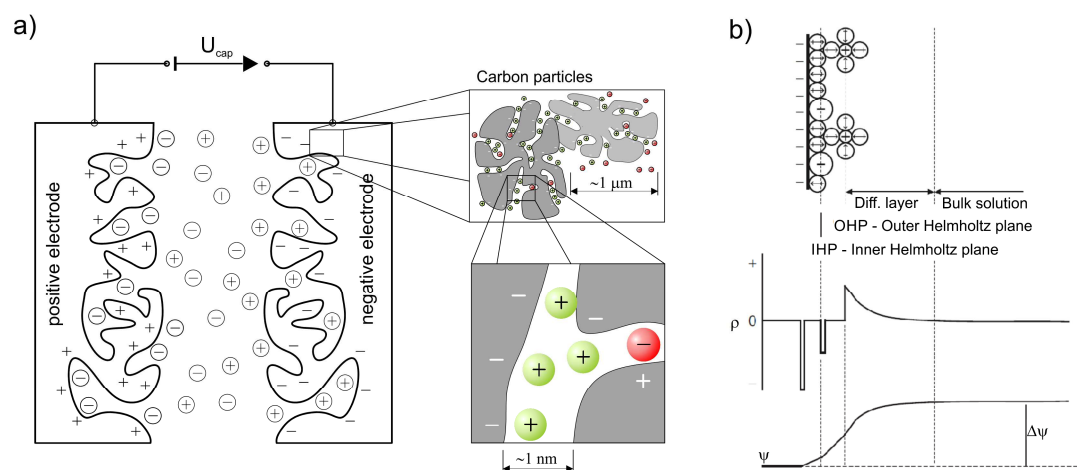


**Fig. 2.6:** (a) Sketch of an electrochemical double-layer capacitor (EDLC) at different levels of magnification. In (b) charge (center) and potential (bottom) of the electrical double-layer (top) across the electrode-electrolyte interface are shown. Reproduced with permission from Ref.<sup>42</sup>. © Wiley-VCH.

The electrical double layer at a planar electrode (Fig. 2.6b) was initially described by Helmholtz as a dense layer of counter-ions opposing the electronic charges in the electrode. Due to entropic reasons Gouy and Chapman considered a diffuse layer of counter-ions with a decaying concentration extending several atomic distances into the electrolyte. Within the Gouy-Chapman-Stern (GCS) theory a dense layer of physisorbed counter-ions at the outer Helmholtz plane are followed by a diffuse layer of counter-ions counterbalancing the electrode charges. In addition some specifically adsorbed ions are located at the inner Helmholtz plane. They lose parts of their solvation shell and are chemically bound to the electrode surface. Solvent molecules at the electrode surface may orient their dipole moment depending on the electrode polarization.<sup>42,43</sup>

The stored energy  $E$ , the maximum power output  $P_{max}$ , and the capacitance  $C$  of any system exhibiting capacitive behavior are defined as

$$E = \frac{1}{2}CU^2, \quad P_{max} = \frac{U^2}{4ESR}, \quad C = \varepsilon_0\varepsilon_r \frac{A}{d}, \quad (2.24)$$

where  $U$  is the applied voltage,  $ESR$  the equivalent serial resistance,  $A$  the surface area, and  $d$  the average distance of the opposed charges.

Since opposed charges in a supercapacitor are separated across the electrode-electrolyte interface,  $d$  is small and amounts at maximum to several atomic distances. In order to increase the capacitance the surface area of the electrode is made as large as possible. This is achieved by making the pores as small as possible. In commercial supercapacitors activated carbons or carbide-derived carbons (see section 2.5.1) with an average pore size around 1 nm and a particle size ranging from several hundred nanometers to several micrometers are deployed (Fig. 2.6a). Unexpected phenomena like the enhancement of the surface-normalized capacitance can occur if pores become as small as the bare ions themselves.<sup>44</sup> Ion transport in such pores becomes more and more difficult, since ions block each other, which lowers ion diffusion.<sup>45</sup> Besides these confinement effects, the influence of the electronic band structure of the electrode material or the potential desolvation of ions make the capacitance in general a complex function depending on voltage, scan rate, cell design and many more parameters.<sup>14,17,42</sup>

#### 2.4.1 Physical electrochemistry

The chemical potential  $\mu_i$  of a substance  $i$  represents the driving force for chemical reactions, redistributions of substances or phase changes and is defined as

$$\mu_i = \left( \frac{\delta G(T, p, n_j)}{\delta n_i} \right)_{T, p, n_{j \neq i}}, \quad (2.25)$$

with  $G$  being the Gibbs free energy of the system and  $n$  the amount of substance. The Gibbs free energy of a system consisting of more than one component is minimized if the chemical potentials of all substances are equal. Thereby the law of mass action is conserved. A difference in the chemical potentials of two or more species implies for example that a chemical reaction may take place or the composition will change. According to the Fermi-Dirac statistics  $f(E)$  the chemical (or electrochemical) potential of electrons in a solid is equal to the fermi level  $E_f$  and represents (for all temperatures) the energy where  $f(E)$  equals  $1/2$ .<sup>28,43</sup>



More generally, in a system with varying electric potentials, the electrochemical potential  $\tilde{\mu}_i$  is constant in equilibrium and defined as

$$\tilde{\mu}_i = \mu_i^0 + RT \ln \left( \frac{c_i}{c_{i,0}} \right) + z_i F \Phi, \quad (2.26)$$

with  $\mu_i^0$  being the standard chemical potential,  $c_i$  the concentration of the species,  $\Phi$  the potential,  $F$  the Faraday constant and  $z_i$  the number of elementary charges of species  $i$ . In equilibrium the electron transfer rate between the electrode and redox active species across the interface ( $O + ne^- \rightleftharpoons R$ ) is equal in back- and forward direction. We therefore write

$$\begin{aligned} \tilde{\mu}_{e,redox} &= \tilde{\mu}_{e,solid} = E_f \\ \mu_{e,redox}^0 + RT \ln \left( \frac{c_{ox}}{c_{red}} \right) + z_e F \Phi^{solv} &= \mu_{e,solid}^0 + z_e F \Phi^{solid} \end{aligned} \quad (2.27)$$

The so-called single electrode potential or Galvani potential  $E$  (don't confuse with the electron energy  $E$  used above) is then

$$E = \Phi^{solid} - \Phi^{solv} = \frac{\mu_{e,redox}^0 - \mu_{e,solid}^0}{z_e F} + \frac{RT}{z_e F} \ln \left( \frac{c_{ox}}{c_{red}} \right). \quad (2.28)$$

The first term on the right hand side of Eq. 2.28 is called the standard single electrode potential  $E^0$ . Thus, the difference of the electron chemical potential at the electrode-electrolyte interface is responsible for the onset of an electric potential drop across the interface (as visualized in Fig. 2.7).

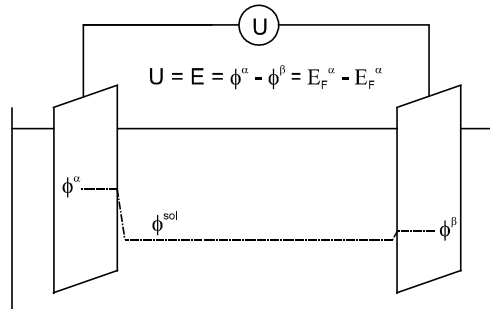


**Fig. 2.7:** Differences in the electrode's and electrolyte's chemical potential are responsible for an electric potential drop at the electrode electrolyte interface.

The potential shift during equilibration is realized via charges on the electrode side and the electrolyte side (electrical double-layer), as explained in detail further below.

The Galvani potential is not directly accessible to experiments; only potential differences vs. a reference electrode such as the standard hydrogen electrode (SHE) can be measured (Fig. 2.7). Standard single electrode potentials vs. SHE for different redox reactions are listed in electrochemical standard electrode tables.<sup>42,43</sup>

Combining the concepts of solid state physics and electrochemistry enables a microscopic understanding of chemical reactions, electrical double-layer formation and related effects at the electrode-electrolyte interface.<sup>46</sup> The electrode-electrolyte interface can be treated in analogy to semiconductor or metal heterojunctions (such as p-n junctions or Schottky junctions). In equilibrium the Fermi level of an n-type semiconducting electrode is equal to the electrochemical potential of the redox active species in the electrolyte in equilibrium (Fig. 2.8a). The so-called reorganization energy  $\lambda$  accounts for the different energies of reduced and oxidized species and is caused by the interaction of polar water molecules with the differently charged redox species. According to Marcus theory<sup>47</sup> the entropic fluctuations of water molecules in the hydration shell cause a Gaussian distributed density of states (DOS) of electron energy levels of oxidized and reduced species. This might be different in nanoporous electrodes, since the hydration behavior is influenced by strong confinement.<sup>48</sup> Charge transfer of an electron from the electrode to the oxidized species ( $\rightarrow$  reduction) can only take place if the electron energy level of the electrode is equal to the energy state of an oxidized species (i.e. to an empty state), since electron transfer across the interface corresponds to a tunneling process. For charge transfer at least parts of the DOS distribution of the oxidized species needs to overlap with some electron energies in the conduction band of the semiconductor. For oxidation electrons are transferred from the reduced species to empty states within the conduction band.<sup>46,49</sup>

If an appropriate electrode is inserted into an electrolyte a potential drop is built up at the interface during equilibration. Depending on the conductivity of the electrode and the ion concentration of the electrolyte either the space charge layer and/or the Helmholtz and diffuse layer of ions will contribute most to the potential drop. Both, ions within the double layer and electrons at the electrode side possess some capacitance. For the situation sketched in Fig. 2.8a electrons at the electrode are repelled from the surface, resulting in a band bending being consistent with electron depletion. The remaining positively charged atomic cores cause a positive potential on the electrode. On the electrolyte side a Helmholtz layer and a diffuse layer of ions contribute to the negative potential of the solvent with respect to the electrode. In the sketch of Fig. 2.8a the space charge layer contributes, due to its spatial extension, by far the most to the capacitance (  $1/C_{ges} = 1/C_{SC} + 1/C_H + 1/C_{DL}$  ). The potential therefore drops mainly on the electrode side and the bands are “pinned” with respect to their initial energies before equilibration. Having a metal or semi-metal electrode

(such as graphite, Fig. 2.8b) most of the potential will drop at the electrolyte side, due to the spatial extension of the Helmholtz layer and the diffuse layer of ions. In equilibrium the potential drop across the interface corresponds to the Galvani potential of the half cell. The open circuit voltage of two half-cells is the difference between the two Galvani potentials as mentioned above (Fig. 2.7).<sup>46,49,50</sup>

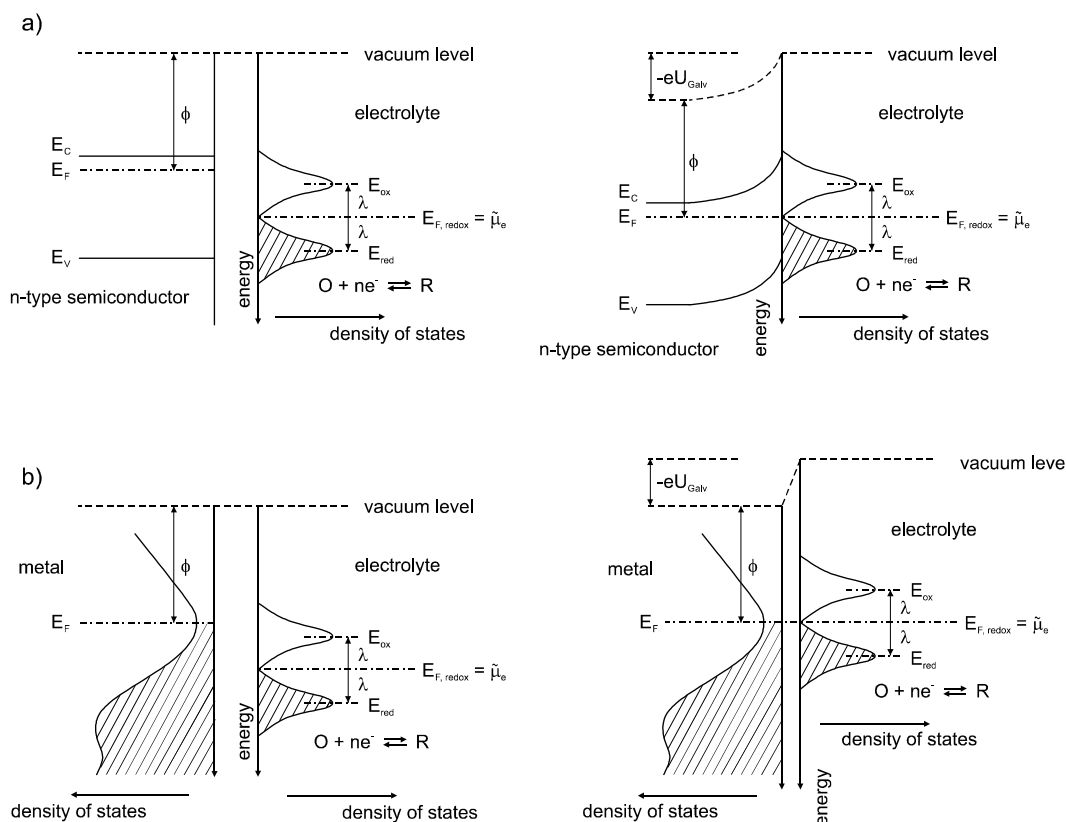


**Fig. 2.8:** (a) Energy levels of a n-type semiconductor electrode and some redox-active species within an electrolyte before (left) and after (right) equilibration (alignment of the electrochemical potentials or fermi levels). In (b) the same is sketched for a (semi-) metal electrode like graphite.<sup>46,50</sup>

## 2.4.2 Electrical double-layer capacitance

In contrast to batteries in pure EDLCs no charge is transferred across the electrode-electrolyte interface; the electrode is ideally polarizable within a certain voltage window. The Fermi level of a carbon electrode (such as activated carbon) and the energy levels of  $Cl^-$  and  $Cs^+$  (1 M aqueous  $CsCl$ : standard electrolyte in this work; see section 3) do not promote any chemical reaction at zero applied voltage (Fig. 2.9). Since single electrode potentials are given vs. SHE the energy scale (right) is different compared to the absolute scale referenced by the vacuum level (left).<sup>46,51</sup>

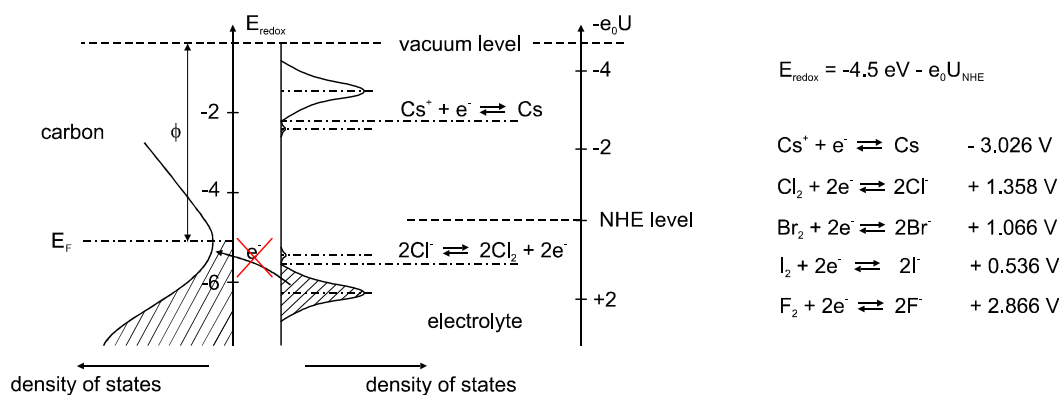


**Fig. 2.9:** Energy vs. electron density of states (DOS) sketched for a carbon electrode,  $\text{Cs}^+$  reduction and  $\text{Cl}^-$  oxidation. Note the different energy scales typically used in solid state physics (left) and electrochemistry (right). On the right single electrode potentials of other halide anions are listed.<sup>51</sup>

Apart from specifically adsorbed ions, charge is accumulated near the interface only if an external voltage is applied. Specific adsorption of anions or cations can however shift the potential of zero electrode charge (PZC). Anions like  $\text{Cl}^-$ ,  $\text{Br}^-$  or  $\text{I}^-$  have the tendency to loose parts of their hydration shell and chemically bind to the electrode surface, shifting the PZC to negative values. Electron transfer between electrode atoms and the adsorbed species is required for the change in the potential of zero charge. As shown in Fig. 2.9 the single electrode potentials of all halogen ions except of  $\text{F}^-$  are not far below the fermi level of the carbon. Due to surface defects and surface reconstruction, locally the Fermi level might differ slightly compared to the bulk value. Halide ions might adsorb specifically at those sites, aligning locally the redox Fermi level with the electrode Fermi level. If any ionic species shifts the PZC an opposed charge is needed to reach zero electrode charge. This is equivalent to applying a negative potential to the n-type semiconductor electrode in Fig. 2.8a, (right) until the so-called flat-band potential is reached (i.e. energy bands are flat).<sup>43,46,52,53</sup>

Pure double-layer capacitance or ideal polarizability occurs only within a voltage range, where ions and solvent molecules cannot react. As explained above, the ability to chemically react is solely determined by the specific electron energy levels of all species in the electrolyte and electrode. The theoretical voltage window of water is 1.23 V, indicated in Fig. 2.10. The fermi level of a carbon electrode level lies in the middle of the hydrogen and oxygen evolution potential. Therefore, in a symmetric supercapacitor a cell voltage larger than 1.23 V will cause hydrogen evolution at the negative electrode and oxygen evolution at the positive electrode. This so called voltage window limits the maximum applied voltage and therefore the stored energy.<sup>18,49</sup>

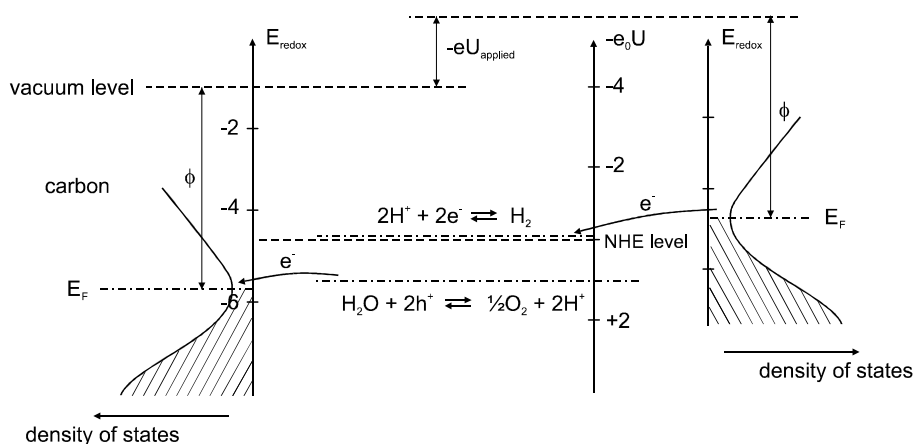


**Fig. 2.10:** Energy vs. density of states indicated for a symmetric aqueous supercapacitor. As the applied voltage exceeds the difference of hydrogen and oxygen evolution potentials the solvent is decomposed.<sup>49</sup>

### 2.4.3 Supercapacitors with nanoporous electrodes

In 2006 a so-called anomalous capacitance effect was proposed, claiming that the surface-normalized capacitance increases drastically as the pore size decreases towards the bare ion size (Fig. 2.11a).<sup>54</sup> In larger mesopores with a size of at least two ion diameters, the surface-normalized capacitance increases with increasing pore size. The Donnan model describes the potential in slit-like pores (of such size) as two overlapping double-layer potentials (Fig. 2.11b)<sup>55,56</sup>. The value of the potential minimum in the pore center is lower for larger pores. This implies that a greater amount of charge (in the form of ions) is present within larger pores. Consequently the surface normalized capacitance for mesopores increases with increasing pore size until a plateau value is reached. This plateau value corresponds to the surfaced-normalized capacitance of a planar electrode. Apart from that, ion packing effects might play a role in carbons with narrow pore size distributions, resulting in an oscillating behavior of the capacitance vs. pore size curve<sup>57</sup>. Those relations became apparent only a few years ago, when microporous carbons with well controllable and narrower pore size distribution could be synthesized. To get a complete picture of the relation between capacitance and pore width, the pore size dispersity needs to be taken into account.<sup>58,59</sup>

A first physical explanation of the anomalous capacitance increase was given by the theoretical work of Kondrat and Kornyshev using a simple slit-pore model.<sup>60</sup> Electronic charges on the conducting plates of a slit-like pore effectively screen the counter-ion counter-ion repulsion. The smaller the pore, the larger the screening effect becomes and the denser the counter-ions can be packed. For that reason the surface-normalized capacitance in the smallest accessible pores increases with

decreasing pore size. Using Molecular Dynamics Merlet et al. studied ion electrosorption for the first time in an atomistic structural carbide-derived carbon model.<sup>61</sup> The capacitance increase for ionic liquids was explained by a smaller average distance between carbon charge carriers and counter-ions in micropores with respect to planar graphite electrodes. On planar electrodes, the layer of co-ions following the first layer of counter-ions pulls away the first counter-ion layer from the carbon atoms. Since the second layer of co-ions is missing in sub-nanometer sized pores, counter-ions can approach the surface closer, leading to an enhanced capacitance. In a further modelling work the local arrangement of ions in the model pore structure was investigated as a function of the applied cell voltage. Conclusively the charge per coordinating carbon atom was found to be enhanced in sites where ions are most confined.<sup>62</sup>

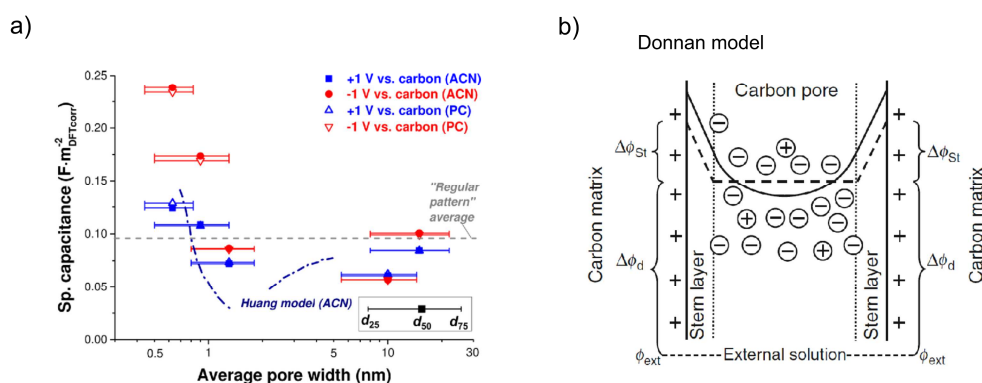


**Fig. 2.11:** (a) Specific capacitance vs. average carbon pore width. Reprinted with permission from Ref.<sup>59</sup>. © 2016, American Chemical Society. Electric double layer and potential decay in a carbon micropore according to the Donnan model. Reproduced with permission from Ref.<sup>56</sup>. © Springer.

Many assumptions based on experimental data imply that the supercapacitor is in equilibrium after charging. Depending on the kinetic behavior of the entire system (i.e. the entire cell) this assumption might be wrong. In principle a nanoporous supercapacitor electrode can be charged in different ways, as visualized in Fig. 2.12. Electronic charges of the electrode can be either counter-balanced by counter-ion adsorption, co-ion expulsion or so-called ion swapping, where the total ion concentration (cations plus anions) increases, decreases or remains constant, respectively. Which mechanism dominates might depend on the electrolyte salt concentration, the kinetics of charging and details on the atomic scale like ion-to-pore-size ratio or ion mobilities. In recent years some *in situ* experimental methods<sup>22</sup> have been developed, to measure cation and anion concentration changes as a function of the applied voltage or electrode charge. Electrochemical quartz crystal microbalance<sup>63</sup> (eQCM) for example measures the mass change of a thin electrode on

top of a quartz crystal via a shift of the crystals resonance frequency during charging and discharging. The ion flux in and out of the pores accompanied with an effective change of the solvent molecule number is responsible for the mass change within the electrode pores. *In situ* Nuclear magnetic resonance<sup>64</sup> (NMR) is a spectroscopic technique that can track element-specific concentration changes by analyzing the change of the corresponding peak area in the NMR spectrum during charging and discharging. The exact position of the peak is sensitive to its local environment. Therefore both the amount of in-pore and bulk ions can be determined. In a recent study ion dynamics was investigated using a dynamically changing magnetic field<sup>45</sup>. The increase of the total ion concentration within the pores was found to correlate inversely with the ion diffusion coefficient, providing evidence of mutual blocking of ions during diffusion. Interestingly, eQCM experiments<sup>63,65,66</sup> reveal a tendency for counter-ion adsorption where *in situ* NMR<sup>64,67-69</sup> shows a tendency for ion swapping. eQCM usually exhibits a significant increase of the total ion concentration, using a variety of electrolytes and salt concentrations. *In situ* NMR on the other hand reveals preferably ion swapping as the main charging mechanism; to a smaller extend also counter-ion adsorption or co-ion expulsion was found to contribute in NMR experiments.

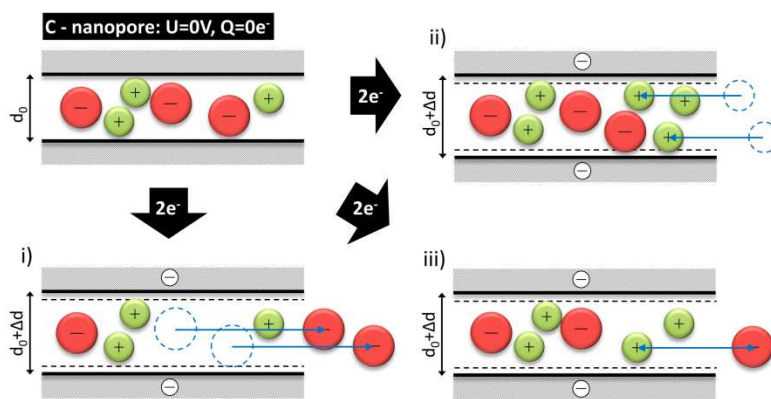


**Fig. 2.12:** Visualization of possible charge storage mechanisms; counter-ion adsorption (i), co-ion expulsion (ii), ion swapping (iii). Ref.<sup>70</sup> - Published by The Royal Society of Chemistry.

Another effect during charging a supercapacitor is electrosorption-induced electrode swelling, reducing cycle live time on the one hand, but utilized in electrochemical actuators on the other hand.<sup>71,72</sup> As the supercapacitor is charged, the concentration of ions within the (sub-) nanometer electrode pores is changing, as well as the electronic charge on the electrode. Several contributions, including the change of the osmotic

pressure or the electron-hole doping on the electrode surface atoms, might be responsible for the complex strain behavior as a function of applied cell voltage.<sup>73</sup>

#### 2.4.4 Faradaic contributions

The electrical double-layer capacitance at carbon particles (Fig. 2.13a) or in carbon nanopores (Fig. 2.13b) might be enhanced by fast and reversible redox reactions. Faradaic contributions that are fast enough to reveal capacitance-like behavior are called pseudocapacitive. Typical pseudocapacitive materials are  $\text{MnO}_2$  or  $\text{RuO}_2$  involving fast and reversible redox reactions occurring at or near to the surface (Fig. 2.13c). In batteries on the other hand reactions take place slowly due to phase transformation and intercalation of ions (e.g.  $\text{Li}^+$ ) into a host material (Fig. 2.13d), i.e. charging and discharging of the electrode is diffusion limited. Cyclic Voltammetry (CV) experiments of pseudocapacitive materials reveal the typical rectangular shape as shown in Fig. 2.13e. Batteries on the other hand exhibit distinct peaks of forward and backward reaction in the CV curve (Fig. 2.13f). As the supercapacitor is charged with a constant current load (galvanostatic cycling) the voltage steadily increases (Fig. 2.13g). In a battery the galvanostatic charging and discharging curve shows a distinct plateau region (Fig. 2.13h). In the case a typical battery material is made thin enough (several nanometers) the electrochemical response can again be capacitor-like. Such “extrinsic” pseudocapacitance is caused by the larger number of surface-near  $\text{Li}^+$  intercalation sites in nano-engineered electrode materials such as  $\text{V}_2\text{O}_5$ .<sup>74-76</sup>

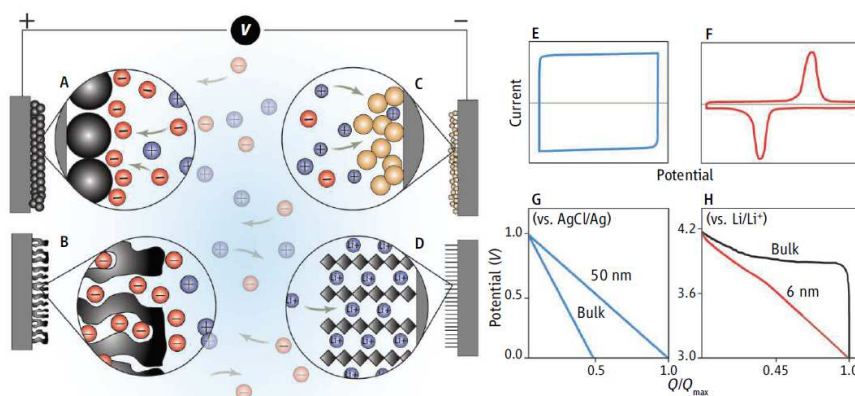


**Fig. 2.13:** Schematic visualization of electrical double layer capacitance on carbon particles (a) and in carbon nanopores (b), of pseudocapacitance at oxide particles (c), of  $\text{Li}^+$  intercalation in graphite. Cyclic voltamograms typical for supercapacitors (e) and batteries (f) and galvanostatic discharge cycles typical for supercapacitors (g) and batteries (h). From Ref.<sup>74</sup>. Reprinted with permission from AAAS.

Depending on the cell and electrode design, the applied scan rates and other non-material-specific conditions the electrochemical behavior may change from



capacitor-like to battery-like. As long as performance parameters are tested correctly and the underlying mechanisms explained adequately the discussion about the terminology is not essential.

A number of different sources of faradaic reactions can improve the performance of nanoporous electrodes<sup>14,17</sup>, such as redox active species decorating the electrode surface or reactions of redox active species within the electrolyte (redox electrolytes). As recently shown, the latter enables large energy densities (up to 50 Wh/kg) by maintaining a relatively high power density in aqueous systems. Considering the environmental friendliness, non-toxicity and easy handling of aqueous electrolytes the use of redox active species seems to be a promising way for future applications.<sup>19-21,77</sup>

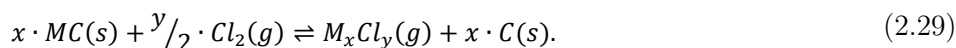
## 2.5 Materials

### 2.5.1 Carbon electrode materials

Due to their large specific surface areas and beneficial electronic properties, nanoporous carbons are widely used and studied as supercapacitor electrode material both in industry and academics. According to IUPACC, pores are classified into micropores (pore size  $< 2$  nm), mesopores ( $2 < \text{pore size} < 50$  nm) and macropores (pore size  $> 50$  nm). A big variety of highly porous carbon materials exists, however, most of them still only on a lab scale. Among all those materials activated carbon is by far the most attractive for industry, due to its cheap production and the beneficial structural, chemical and electronic properties.<sup>78,79</sup>

Activated carbons are made from (organic) raw-materials like charcoal, petroleum pitch or coconut husk. Two different types of activation processes exist. For physical activation the organic raw material is in a first step carbonized under inert gas atmosphere (Ar, N<sub>2</sub>) with temperatures ranging from 400 – 900 °C. In a second processing step, the carbon material is oxidized using steam or O<sub>2</sub> atmosphere usually at temperatures around 350 – 1000 °C. During chemical activation the carbonization and activation step takes place at the same time, where the raw material is infiltrated with strong acids or bases like phosphoric acid or potassium hydroxide. For both activation processes the oxidation reaction proceeds from outer regions towards the inside of the carbonaceous material, making most of the pores accessible for adsorption.<sup>80</sup> Depending on the exact processing parameters (like temperature) the resulting, highly disordered pore structure exhibits an average pore size typically ranging from 0.8 – 2 nm.<sup>78,79,81</sup>

Carbide-derived carbons<sup>82</sup> (CDCs) represent another class of disordered, nanoporous carbons. A huge number of carbides, like TiC, SiC, B<sub>4</sub>C, Mo<sub>2</sub>C (and many more) can be used as precursor material. Processing with Cl<sub>2</sub> (or other halogens) at elevated temperatures removes all atoms except those of carbon:



Depending on the temperature treatment, a microporous structure with well controllable pore size distribution remains. High resolution - TEM (HR-TEM) images of TiC derived carbons, synthesized at 600 °C (top), 800 °C (center) and 1200 °C (bottom) are shown in Fig. 2.14. Quenched molecular dynamics<sup>83</sup> was used to simulated 3D atomic structures of the three CDCs (right column). Modeled HR-TEM images of the simulated structures are shown in the center column. With increasing

temperature the carbon structure becomes more ordered, as confirmed by HR-TEM and Raman spectroscopy.<sup>83,84</sup> According to electron energy loss spectroscopy (EELS) the  $sp^2/sp^3$  ratio is rather constant and greater than 0.9 for Ti-CDCs synthesized at different processing temperatures.<sup>85</sup> The large amount of carbon double-bonds ( $sp^2$ ) compared to single-bonds ( $sp^3$ ) is responsible for the graphite-like electronic properties. Similar structural properties were observed for activated carbons.

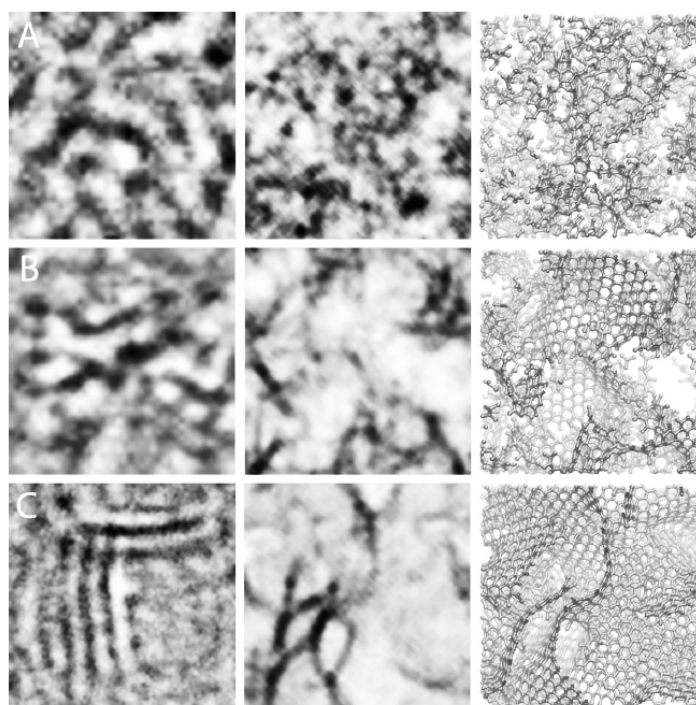


**Fig. 2.14:** Transmission electron microscope (TEM) images (left column), carbon atomic structures derived from quenched Molecular Dynamics simulations (right column) and modeled TEM images of the simulated structures (center column); of TiC-CDC at 600°C (a), TiC-CDC at 800°C (b) and TiC-CDC at 1200°C. Reproduced with permission from Ref.<sup>83</sup>. © Elsevier.

### Electronic properties

According to Robertson et al.<sup>86</sup> electronic conduction in amorphous carbon can be described by a hopping mechanism between  $sp^2$  (graphitic-like) domains. In between these domains  $sp^3$  bonds, with electronic states being higher in energy, form an energy barrier. Charge transport therefore requires activation energy, resulting in an Arrhenius-like temperature dependency of the electronic conductivity (Boltzmann factor).<sup>86,87</sup>

Besides the bulk conductivity the powder form of most nanoporous carbons significantly reduces the electronic conductivity. During electrode preparation the

carbon particles are pressed in a hot-roll press and held together with a polymer binder. The contact area in-between the rather large particles ( $0.1 - 5 \mu\text{m}$ ), is relatively small. Electric conduction in the electrode therefore corresponds to a percolation-like transport. Additives like carbon black with good conductivity and a small particle size can significantly increase the contact area and the electrode conductivity.<sup>88</sup>

The graphene band structure shows zero density of states (DOS) at the fermi level and a linear dispersion relation, symmetric in positive and negative direction (Dirac cone). The DOS in graphite is finite with a minimum around the fermi level (Fig. 2.15a). Although the band diagram of amorphous carbon reveals some differences, the minimum in the DOS is also close to the fermi level. A consequence of the finite density of states is a finite charge carrier density within the electrode. This leads to a space charge layer on the electrode side with a rather low capacitance. Compared to the Helmholtz capacitance of electrolytes with high salt concentrations the electrode space charge capacitance can limit the overall capacitance.<sup>89,90</sup>

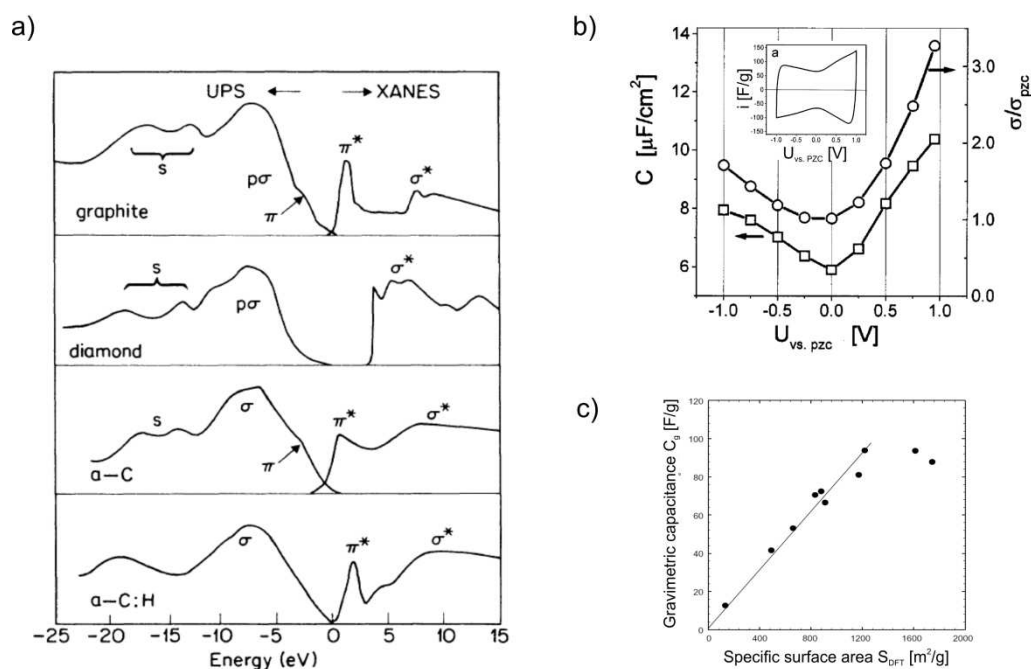


**Fig. 2.15:** (a) Density of states (DOS) vs. energy for graphite, diamond, amorphous carbon and amorphous carbonhydride. Reproduced with permission from Ref.<sup>86</sup>. © The American Physical Society. Surface-normalized capacitance and conductivity of activated carbon electrodes as a function of the electrode potential are shown in (b). The inset shows the corresponding cyclic voltammogram. Reprinted with permission from Ref.<sup>90</sup>. © 2003, The Electrochemical Society. The gravimetric capacitance as a function of specific surface area, using different nanoporous carbons as electrode materials, is given in (c). Reproduced with permission from Ref.<sup>91</sup>. © Elsevier.

Many theoretical studies consider ideal metallic behavior<sup>60,92</sup>, i.e. no electric field can penetrate into the electrode material. The electric field of ionic charges is entirely screened at an infinitely thin layer at the carbon surface, where the carbon capacitance contribution is infinitely high. Therefore all potential drops on the electrolyte side. In a slit-like pore the potential between two ions decays exponentially<sup>60</sup> instead of  $1/r^2$  (Coulomb potential); i.e. the ion interaction is effectively screened. Other studies have considered non-ideal conductivity by taking a finite thickness of electronic counter-charges on the electrode side into account<sup>93</sup> (Thomas-Fermi screening length). Depending on the charge carrier density, the electric field penetrates a finite width into the electrode material. The screened ionic potential still decays exponentially, but the characteristic length of the exponential decay has increased. This situation is equivalent to a perfectly conducting pore with larger width than the real pore with finite conductivity.<sup>93</sup>

Some recent theoretical studies have considered so-called quantum capacitance, where the charge carrier density is limited by the density of states and changes as a function of the electrode potential.<sup>94</sup> The increase in the electrode capacitance with an increasing magnitude of the electrode polarization was observed for a number of nanoporous carbons<sup>90</sup>, graphene<sup>95</sup> and graphite<sup>89</sup> electrodes. It can be explained by an increase of the density of states with increased positive or negative potential (see DOS, Fig. 2.15). The ion interaction potential in slit pores may be modeled with a scaling of  $1/r^3$ , making the screening much less effective compared to pure metallic electrodes.<sup>93,94</sup>

Quantum capacitance becomes apparent in cyclic voltamograms with the typical “butterfly shape”.<sup>95</sup> Also in common activated carbon electrodes for EDLCs quantum capacitance can play a major role.<sup>90</sup> The most prominent effect was observed in graphene electrodes and is attributed to the extremely low density of states and the slope of the dispersion relation around the Dirac point. The extremely high conductivity of graphene solely induced by the high mobility (but not by the high density) of charge carriers cannot support effective screening of ion - ion interactions.

The extended space charge layer in the electrode is also responsible for a saturation of the capacitance with increasing surface area of the electrode material (Fig. 2.15c). Since on average the pore walls become thinner with increasing surface area, the space charge layer of opposing interface overlap at some point and cannot compensate for a larger ionic charge within the pores.<sup>91</sup>

## 2.5.2 Aqueous electrolytes and ion hydration

The dielectric permittivity of water ( $\epsilon = 78$  at room temperature) is among the highest of all solvents. Strong interactions between ions and water molecules lead to

large hydration energies, controlling ion migration properties and the charge storage ability in carbon nanopores.

In the following the origins of the most important contributions to the hydration enthalpy in bulk solution are given. The ion-dipole model treats liquid water as a loose ice structure and takes the dipole moment of single water molecules into account. The hydration enthalpy  $\Delta H_{i-s}$  corresponds to the enthalpy change for transferring an ion from vacuum into the solvent. It can be splitted into the following contributions:<sup>42</sup>

- The formation of a cavity  $\Delta H_{cf}$  in the water means removing a cluster of five water molecules, involving the breaking of 12 hydrogen bonds.  $\Delta H_{cf} \cong 250 \text{ kJmol}^{-1}$
- Breaking the four hydrogen bonds of the removed cluster requires another  $\Delta H_{cb} \cong 84 \text{ kJmol}^{-1}$
- The electrostatic interaction between ions and water dipoles is attractive and can be written as  $\Delta H_{id} = -(nN_A\mu_W|ze|)/(4\pi\epsilon_0(r_i + r_W)^2)$ , with  $n$  being the number of water dipoles,  $\mu_W$  the dipole moment of a water molecule,  $|ze|$  the charge of the ion and  $r_i + r_W$  the distance between ion and water molecules.
- The Born Free enthalpy corresponds to the reversible work to bring an ion from the vacuum into a continuous dielectric medium and reads  $\Delta G_{i-s} = N_A(W_1 + W_2) \text{ Jmol}^{-1}$ , with  $W_1$  as the reversible work to discharge an ion in vacuum, and  $W_2$  the work to charge the ion in a continuous dielectric medium with the dielectric constant  $\epsilon$ . No work is needed to bring the discharged ion into the solvent. Thus the Born free enthalpy reads  $\Delta G_{i-s} = (-N_A(ze)^2/8\pi\epsilon_0r)(1 - 1/\epsilon_r)$ . Considering  $\Delta G = \Delta H - T\Delta S$  and  $\Delta S_{i-s} = \partial\Delta G_{i-s}/\partial T$  the Born enthalpy liberated when bringing an ion into a dielectric medium is  $\Delta H_{i-s} = (-N_A(ze)^2/8\pi\epsilon_0r)(1 - 1/\epsilon_r - T/\epsilon_r^2 d\epsilon_r/dT)$
- Finally, the energy that is liberated when water molecules are oriented within the cavity is  $\Delta H_{cp,cation} = -10 * 21 = -210 \text{ kJmol}^{-1}$  and  $\Delta H_{cp,anion} = -8 * 21 = -167 \text{ kJmol}^{-1}$ , where cations are able to form 10 hydrogen bonds and anions 8 hydrogen bonds.
- Returning the leftover water molecules to the bulk solution results in a heat of condensation of  $\Delta H_C = -42 \text{ kJmol}^{-1}$ .

Considering all these interactions, results in good correspondence between theoretical and experimental hydration enthalpies. Experimental hydration enthalpies are listed in Table 2.1. All values presented in Table 2.1 are intrinsically connected to each other. The hydration enthalpy shows a clear correlation to the bare ion size. Not surprisingly, water molecules in the first hydration shell of small ions like  $\text{Na}^+$  are

stronger bound compared to large ions. Moreover ion transport in aqueous solutions intrinsically depends on ion hydration. Both Stokes radius<sup>96</sup> (being a radius of a hypothetical hard sphere diffusing with the same speed as the actual solvated ion) and ion mobilities reveal systematic correlations to the hydration enthalpies.

Depending on the specific design of an electrochemical cell either the carbon electron transport or the electrolyte ion transport can limit the charging and discharging currents. The sheet resistance of an electrode with commercial activated carbons is in the order of 10  $\Omega\text{cm}$  and can be lowered by a factor of five when adding 10 % conductive additives.<sup>88</sup> Depending on the salt concentration and temperature the conductivity of a high molar aqueous electrolyte is in the range of 100 mS/cm corresponding to a resistivity of 10  $\Omega\text{cm}$ .<sup>18</sup>

**Table 2.1:** Properties of alkali metal cations and the chloride anions: Hydration enthalpies are taken from experiments. The hydrated ion radius corresponds to experimentally determined distance between ion and oxygen atoms of water molecules in the first hydration shell. Alternatively the hydrated ion radius is determined from ion transport properties. The bare ion radius corresponds to the crystal ion radius and the Stokes radius to an effective size value derived from limiting equivalent conductivities for diffusing ions. Ion mobilities are taken from a Molecular dynamics study in water at 25°C.

	Hydration enthalpy <sup>12</sup> (kJmol <sup>-1</sup> )	Hydr. ion radius: ion-oxygen distance <sup>97,98</sup> (nm)	Hydr. ion radius: obt. from ion diffusion <sup>96</sup>	Bare Ion radius <sup>96</sup> (nm)	Stokes radius <sup>96</sup> (nm)	Ion mobilities <sup>99</sup> (10 <sup>-8</sup> m <sup>2</sup> V <sup>-1</sup> s <sup>-1</sup> )
Cs <sup>+</sup>	-17.1	0.295	0.329	0.169	0.119	7.32±0.66
K <sup>+</sup>	-19.9	0.270	0.331	0.133	0.125	7.12±0.51
Na <sup>+</sup>	-24.5	0.250	0.358	0.95	0.184	4.98±0.19
Cl <sup>-</sup>	-19.5	≈ 0.315	0.332	0.181	0.121	6.88±0.31

## 2.6 Monte Carlo Simulation

The state of a (classical) many body system is defined by knowing positions and velocities of the particles. The state of the system at any given time point in the past or in the future could in principle be predicted using Hamilton's equations of motion. However such knowledge of microscopic quantities is of limited practical use. Thus, it is the aim of statistical physics to calculate macroscopic quantities like total energy or pressure by averaging over all possible microscopic configurations, weighted by the corresponding statistical distribution function. The law of large numbers (or the central limit theorem) implies that although microscopic variables corresponding to single particle values (like the kinetic energy of a specific atom) may fluctuate strongly, the corresponding macroscopic parameter that is a sum over many independent random variables (e.g. the total energy of the system) is normal distributed with extremely small relative variance ( $\sigma/E \sim 1/\sqrt{N}$ ).<sup>100-102</sup>

In classical statistical physics the average of an observable A (e.g. pressure, energy) is obtained by

$$\langle A(\mathbf{x}) \rangle = \frac{1}{Z} \sum_r A(\mathbf{x}_r) e^{-\beta \mathcal{H}(\mathbf{x}_r)}, \text{ where } Z = \sum_r e^{-\beta \mathcal{H}(\mathbf{x}_r)} \quad (2.30)$$

is defined as the partition sum. The vector  $\mathbf{x}_r$  in phase space stands for a particular configuration defined by all positions (and all velocities) of the particles. The Hamiltonian  $\mathcal{H}$  applied to the configuration  $\mathbf{x}_r$  gives the total energy of the system, where  $\beta = 1/kT$ . The sum runs over all possible configurations  $r$ , where the observable  $A(\mathbf{x}_r)$  is weighted by the Boltzmann factor. The partition sum is directly related to the free energy  $F(T,V,N)$  of the system and, thus, contains the entire physical information (like the energy  $E$ , the pressure  $p$ , the chemical potential  $\mu$ ).<sup>101,102</sup>

$$E = -\frac{\partial Z}{\partial \beta}, \quad \beta p = \frac{\partial Z}{\partial V}, \quad \beta \mu = \frac{\partial Z}{\partial N}, \quad \beta F = -\ln(Z) \quad (2.31)$$

An analytical calculation of the partition sum is possible only for very few and simple model systems, like the ideal gas, a harmonic crystal or non-interacting spins. Mostly one has to use numerical methods, one of these being Monte Carlo methods. In the simple sampling Monte Carlo approach the expectation value is estimated by summing up randomly chosen configurations. This is not very effective since the Boltzmann factor is sharply peaked and most configurations have negligible statistical weight. Thus, using simple-sampling the error of the estimated mean value might be large. To solve this problem a method is needed to sample mainly the configurations



of the phase space that are important (importance-sampling). Therefore Eq. 2.30 can be extended by a probability function  $P(\mathbf{x}_r)$  selecting points in phase space accordingly.<sup>101</sup>

$$\langle A(\mathbf{x}) \rangle = \frac{\sum_r A(\mathbf{x}_r) e^{-\beta \mathcal{H}(\mathbf{x}_r)} / P(\mathbf{x}_r)}{\sum_r e^{-\beta \mathcal{H}(\mathbf{x}_r)} / P(\mathbf{x}_r)} \quad (2.32)$$

The best choice for  $P(\mathbf{x}_r)$  would be a function proportional to the Boltzmann factor in Eq. 2.30. This is difficult to apply, since the knowledge about the Boltzmann factor essentially means to solve the problem in advance. An importance-sample Monte Carlo algorithm generates a so called Markov chain of states of the system. The defining property of a Markov chain is that the system has no memory, i.e. the next state depends only on the state directly preceding and not on any other states of the past. Within the algorithm the next state  $\mathbf{n}$  is generated from an old state  $\mathbf{o}$  with a certain transition probability between the two states. The algorithm has to ensure that (after some equilibration) the states of the Markov chain occur with the Boltzmann weight demanded by the canonical ensemble. This is achieved by applying the condition of detailed balance for the equilibrium case that ensures the stationarity of the limiting distribution, i.e. on average the number of moves from state  $\mathbf{o}$  to  $\mathbf{n}$  has to be cancelled by the reverse moves from state  $\mathbf{n}$  to  $\mathbf{o}$

$$P(\mathbf{o}) \cdot sel(\mathbf{o} \rightarrow \mathbf{n}) \cdot acc(\mathbf{o} \rightarrow \mathbf{n}) = P(\mathbf{n}) \cdot sel(\mathbf{n} \rightarrow \mathbf{o}) \cdot acc(\mathbf{n} \rightarrow \mathbf{o}), \quad (2.33)$$

where the probability of going from state  $\mathbf{i}$  to  $\mathbf{f}$  consists of the probability of selecting state  $\mathbf{i}$   $sel(\mathbf{i} \rightarrow \mathbf{f})$  and the probability of accepting this new state  $acc(\mathbf{i} \rightarrow \mathbf{f})$ . If  $sel(\mathbf{i} \rightarrow \mathbf{f})$  is chosen to be symmetric it cancels out on both sides of Eq. 2.33.  $P(\mathbf{o})$  is the mean number of simulations in state  $\mathbf{o}$

$$P(\mathbf{o}) = \frac{1}{Z} e^{-\beta \mathcal{H}(\mathbf{o})}. \quad (2.34)$$

Based on the condition of detailed balance it can be shown that for the ratio of the acceptance probabilities the partition function  $Z$  cancels out and only the energy difference between old and new state enters.

$$\frac{acc(\mathbf{o} \rightarrow \mathbf{n})}{acc(\mathbf{n} \rightarrow \mathbf{o})} = e^{-\beta(E(\mathbf{n})-E(\mathbf{o}))} = e^{-\beta \Delta E} \quad (2.35)$$

As a result the mean value of the desired observable can be calculated by summing up the values of the single particles.

$$\langle A(\mathbf{x}) \rangle = \frac{1}{M} \sum_i^M A_i . \quad (2.36)$$

Practically Eq. 2.35 is implemented via the Metropolis algorithm as follows. First,  $M$  particles are distributed randomly on a defined mesh. A randomly chosen new position of one particle defines the new state. The new state is accepted with the following probability.

$$acc(o \rightarrow n) = \begin{cases} e^{-\beta\Delta E} & E(n) > E(o) \\ 1 & \text{else} \end{cases} \quad (2.37)$$

In this way the system is updated fulfilling detailed balance. After many Monte Carlo steps an ensemble average over all configurations (Eq. 2.36) gives the equilibrium parameter of interest. Note that the Metropolis algorithm results in an equilibrium configuration and does not give a time-dependent evolution of the particle system.<sup>100-102</sup>

### 2.6.1 Long-range interactions (Ewald summation)

Calculating the total energy  $U$  of the system means summing up the coulombic potential  $\phi(r)$  between cations, anions and electrode charges.

$$U = \frac{1}{2} \sum_i q_i \phi(\mathbf{r}_i) \quad (2.38)$$

The factor  $\frac{1}{2}$  accounts for the fact that each pair interaction potential should be only counted once. Computing all pair interactions is computationally demanding in systems containing thousands of particles. Coulombic interactions are long-range interactions, the electric field decays with  $1/r^2$  and the potential with  $1/r$ . The contribution of the mean charge at a distance  $r$  scales with  $4\pi r^2$ , i.e. the contribution of a specific charge density to the potential increases linearly with the distance. Even in neutral solutions (e.g. bulk electrolyte with cations and anions in a dielectric medium) small charge fluctuations at large distances have large impacts. For that reason simple truncation of the potential induces significant errors.<sup>103,104</sup>

Ewald summation<sup>105-107</sup> is a method dealing accurately with the problem of long-range potentials. The following derivation is largely based on a theoretical introduction into Ewald summation presented in Ref.<sup>105</sup>. Let's assume a system containing point charges with periodic boundary conditions in three dimensions. The simulation box can be imagined as unit cell that is periodically arranged in all three dimensions. For the Ewald summation method a Gaussian counter charge is added to the electric point

charges, causing a fast decay of the coulombic interaction in real space (visualized in Fig. 2.16). In addition, the counter charge of the screening Gaussian charge cloud can easily be added in Fourier space, due to its periodicity and smooth variation in space. In summary the Coulomb potential at the position  $\mathbf{r}_i$  in the simulation box is calculated by adding up all contributions.<sup>105,107</sup>

$$\phi(\mathbf{r}_i) = \phi_{Fourier}(\mathbf{r}_i) - \phi_{self-int}(r=0) + \phi_{real}(\mathbf{r}_i) \quad (2.39)$$

$\phi_{Fourier}(\mathbf{r}_i)$  is the potential contribution of the counter charges of the screening Gaussian charge clouds, summed up in Fourier space. The Fourier contribution contains a potential caused by the interaction with the Gaussian charge of the charge  $q_i$  at  $r=0$ . This spurious self-interaction term is corrected by subtracting  $\phi_{self-int}(r=0)$ .  $\phi_{real}(\mathbf{r}_i)$  represents the potential of the screened point charges added up in real space up to a certain cut-off radius.

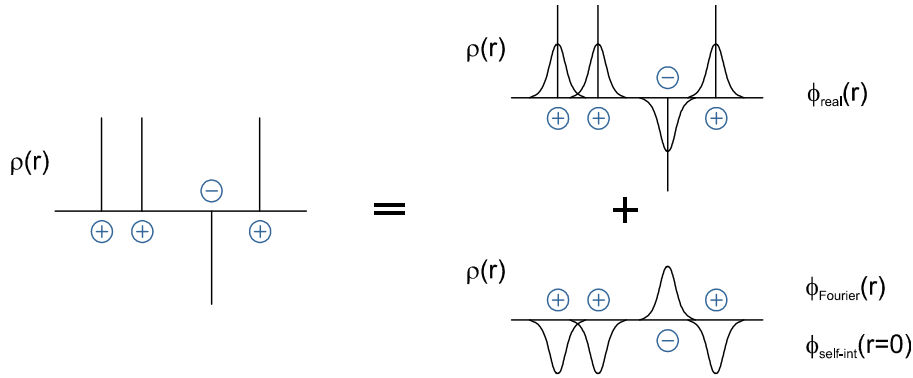


**Fig. 2.16:** The Ewald summation method requires periodic boundary conditions. Point charges are effectively screened by added Gaussian counter charges. These smoothly varying counter charges are corrected by summing up again the counter charges in Fourier space.<sup>105</sup>

The charge density creating the potential of the point charges (with charge  $q_j$ ) is a periodic function of period  $L$ , with  $L$  being the size of the simulation box.

$$\rho(\mathbf{r}_i) = \sum_n \sum_j q_j \delta(|\mathbf{r}_i - (\mathbf{r}_j + \mathbf{n}L)|) \quad (2.40)$$

The function is very sharp and would never converge in a Fourier representation. The charge distribution of the Gaussian counter charges can be written as

$$\rho_{Fourier}(\mathbf{r}_i) = \sum_n \sum_j q_j (\alpha/\pi)^{3/2} \cdot \exp(-\alpha|\mathbf{r}_i - (\mathbf{r}_j + \mathbf{n}L)|^2). \quad (2.41)$$

Using the Poisson equation  $k^2\phi(\mathbf{k}) = -\rho(\mathbf{k})/\varepsilon_0\varepsilon_r$  and the charge distribution in Fourier space the potential can be calculated.

$$\rho_{Fourier}(k) = \int_V \rho_{Fourier}(r)e^{-ikr} dr = \sum_j q_j \exp(-k^2/4\alpha) \cdot \exp(-ikr_j) \quad (2.42)$$

The potential in reciprocal space reads

$$\phi_{Fourier}(k) = \frac{1}{\varepsilon_0\varepsilon_r} \sum_{j=1}^N \frac{q_j}{k^2} \exp(-k^2/4\alpha) \cdot \exp(ikr_j). \quad (2.43)$$

The real space representation is the Fourier transform of the reciprocal representation. In addition, skipping the imaginary part gives for the real space representation<sup>107</sup>

$$\phi_{Fourier}(\mathbf{r}_i) = \frac{1}{\varepsilon_0\varepsilon_r} \sum_{k \neq i} \sum_{j=1}^N \frac{q_j}{k^2} \exp(-k^2/4\alpha) \cdot \cos(\mathbf{k} \cdot (\mathbf{r}_i - \mathbf{r}_j)). \quad (2.44)$$

The isotropic charge distribution of a three-dimensional Gaussian charge cloud can be written as

$$\rho_{Gauss}(r) = q_i(\alpha/\pi)^{3/2} \exp(-\alpha r^2). \quad (2.45)$$

Using the Poisson equation in real space  $\nabla^2\phi(r) = -\rho(r)/\varepsilon_0\varepsilon_r$  the potential can be calculated

$$\phi_{Gauss}(r) = \frac{1}{4\pi\varepsilon_0\varepsilon_r} \frac{q_i \operatorname{erf}(\sqrt{\alpha}r)}{r}. \quad (2.46)$$

The potential at the origin of the Gaussian charge cloud represents the spurious contribution that needs to be subtracted from  $\phi_{Fourier}(\mathbf{r}_i)$ .<sup>107</sup>

$$\phi_{self-int}(r=0) = \frac{1}{4\pi\varepsilon_0\varepsilon_r} 2q_i(\alpha/\pi)^{1/2} \quad (2.47)$$

The real space potential contribution consists of point charges and their screening Gaussian counter charges and reads

$$\phi_{real}(\mathbf{r}_i) = \sum_{j=1}^N \frac{1}{4\pi\epsilon_0\epsilon_r} \left( \frac{q_j}{r} - \frac{q_j \operatorname{erf}(\sqrt{\alpha}r_{ij})}{r_{ij}} \right) = \sum_{j=1}^N \frac{1}{4\pi\epsilon_0\epsilon_r} \frac{q_j \operatorname{erfc}(\sqrt{\alpha}r_{ij})}{r_{ij}} \quad (2.48)$$

The electric field acting on the particle corresponds to the gradient of the total electrostatic energy  $U$ .<sup>107</sup>

$$\mathbf{E}_i = -\frac{1}{q_i} \frac{\partial}{\partial \mathbf{r}_i} U = \mathbf{E}_{i,Fourier} + \mathbf{E}_{i,Real} \quad (2.49)$$

The self-interaction term of the total electrostatic energy is a constant and does not contribute to the electric field. The real-space term reads

$$\mathbf{E}_{i,Real} = \frac{1}{4\pi\epsilon_0\epsilon_r} \sum_n \sum_j q_j \left[ \frac{\operatorname{erfc}(\alpha|\mathbf{r}_{ij} + \mathbf{n}|)}{|\mathbf{r}_{ij} + \mathbf{n}|} + \frac{2\alpha}{\sqrt{\pi}} \exp(-\alpha|\mathbf{r}_{ij} + \mathbf{n}|^2) \right] \frac{\mathbf{r}_{ij} + \mathbf{n}}{|\mathbf{r}_{ij} + \mathbf{n}|^2}, \quad (2.50)$$

and the Fourier space term

$$\mathbf{E}_{i,Fourier} = \frac{1}{4\pi\epsilon_0\epsilon_r} \frac{4\pi}{V} \sum_{\mathbf{k} \neq 0} \sum_{j=1}^N \frac{\mathbf{k}}{k^2} \exp(-k^2/4\alpha) \cdot \sin(\mathbf{k} \cdot \mathbf{r}_{ij}). \quad (2.51)$$

In practice both the real space and reciprocal space contributions for the potential and electric field calculation need a cut-off distance. Pair interactions in real space are only counted for distances smaller than  $R_{real}$ . The reciprocal cut-off  $R_{Fourier}$  constrains the magnitude of the reciprocal space vector  $\mathbf{k}$ . The optimum values are defined as<sup>105-107</sup>

$$R_{real} = \sqrt{\frac{-\log \Delta_E}{\alpha^2}}, \quad R_{Fourier} = 2\alpha \sqrt{-\log \Delta_E}, \quad (2.52)$$

with  $\Delta_E$  as the assumed value of the relative precision of the energy. The parameter  $\alpha$  accounts for the width of the screening Gaussian charge clouds. Considering equal computation times for the real and imaginary part of the potential an optimum value can be estimated from<sup>105</sup>

$$\alpha \cong \sqrt{\pi} \left( \frac{N}{V^2} \right)^{\frac{1}{6}}. \quad (2.53)$$



## 3 Experimental

### 3.1 Electrodes and electrolytes

Parts of section 3.1 are not original and have been published in Ref.<sup>70,108,109</sup>. *In situ* scattering experiments in this thesis were realized on custom-built *in situ* supercapacitor cells with nanoporous carbons as electrode material and aqueous 1 M salt solutions as electrolyte. Three different nanoporous carbon electrodes (AC1, AC2, CDC) in combination with 1 M CsCl, KCl and NaCl aqueous electrolytes were investigated.

For electrode preparation, carbon powder was soaked with ethanol and agitated in a mortar. 10 mass% of dissolved polytetrafluoroethylene (PTFE, 60 mass% solution in water from Sigma Aldrich) were added as binder. The resulting dough-like material was rolled with a rolling machine (MTI HR01, MTI Corp.) to a  $300\pm 20$   $\mu\text{m}$  (AC1 and AC2) or  $200\pm 20$   $\mu\text{m}$  (CDC) thick free standing film electrode and finally dried at 120 °C at 2 kPa for 24 h. Details on the electrode preparation are given in Ref.<sup>110</sup>.

Pore size distributions and surface area values determined with N<sub>2</sub> and CO<sub>2</sub> sorption are given in Fig. 3.1. Sorption measurements and their data analysis were carried out by N. Jäckel from the Energy Materials Group, INM Saarbrücken. Nitrogen gas sorption on the carbon electrodes were conducted with an Autosorb iQ system (Quantachrome) at 77 K (-196 °C). All samples were degassed at 10<sup>2</sup> Pa and 150 °C for 10 h. The sorption isotherm was recorded at relative pressure ( $p/p_0$ ) from  $5 \cdot 10^{-7}$  to 1.0 in 68 steps. The specific surface area (SSA) and pore size distribution (PSD) were calculated via quenched-solid density functional theory (QSDFT) assuming slit pores between 0.56 nm and 37.5 nm.<sup>111</sup> In addition, carbon dioxide gas sorption was done at 0 °C in the relative pressure range from  $1 \cdot 10^{-4}$  to  $1 \cdot 10^{-2}$  in 40 steps. SSA and PSD values were calculated using non-local density functional theory (NLDFT) for pore sizes between 0.3 nm and 1 nm.<sup>112</sup> The combination of both PSDs into one pattern was performed as described elsewhere.<sup>58</sup>

AC1 is a commercially available activated carbon (YP-80F, Kuraray Chemicals Co), with an average pore size of 1.3 nm and a specific surface area of 1598 m<sup>2</sup>/g. AC2 is an activated carbon with average pore size of 0.9 nm and a specific surface area of 1707 m<sup>2</sup>/g (MSP20, Kansai Coke and Chemicals Co.). The third carbon (CDC) is a titanium carbide-derived carbon synthesized at the Energy Materials Group, INM Saarbrücken with an average pore size of 0.65 nm and a surface area of 1158 m<sup>2</sup>/g.

The AC particles have a size up to several  $\mu\text{m}$  (CDC particles up to several hundred nm), leading to an additional volume of macropores ( $>50$  nm) within the electrode for the space comprised between such particles; yet, in terms of the specific surface area their contribution is negligible ( $< 1$   $\text{m}^2/\text{g}$ ).

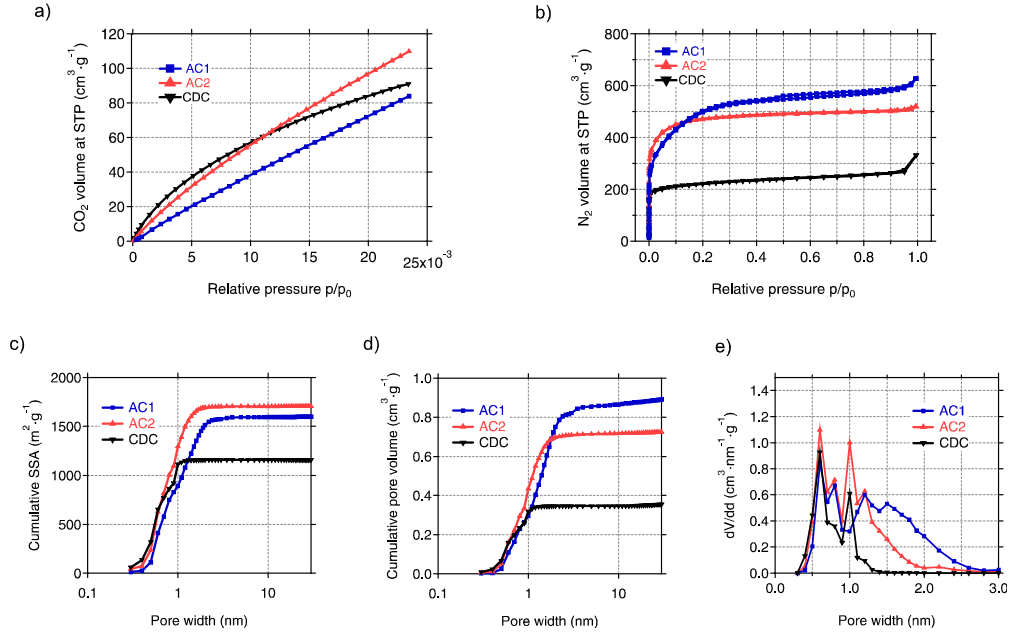


**Fig. 3.1:** Carbon-dioxide sorption isotherms (a) and nitrogen-sorption isotherms (b) carried out at 273 K and 77 K, respectively, for the three microporous carbons AC1, AC2, and CDC. (c)-(e) show the cumulative specific surface area, the cumulative specific pore volume, and the differential pore size distribution of the electrodes containing 10 mass% PTFE. Reproduced with permission from Ref.<sup>109</sup>. © Nature Publishing Group.

Specific surface areas, specific pore volumes, mean pore sizes and micropore volume fractions are listed in Table 3.1. The mean pore size corresponds to the arithmetic average of the volumetric differential pore size distribution. The micropore volume fraction is determined from the specific pore volume  $V_{spec}$ , obtained from gas sorption, and the carbon skeleton density, estimated from absolute SAXS measurements (see section 5.1.3), using the formula  $1.1 \cdot V_{spec} / (V_{spec} + 1/\rho_{skel})$ . The skeleton density for all carbons was estimated with  $1.9$   $\text{g}/\text{cm}^3$  and the factor of 1.1 originates from the 10 mass% of PTFE binder in the electrodes. Micropore volume fractions are further used as input for the carbon pore model generation from *ex situ* SAXS measurements (see section 5.1.5). Since the SAXS intensity cannot resolve spatial features larger than ca.  $7.5$  nm ( $\approx \pi/Q_{min}$ ), specific pore volumes in Table 3.1 (input for nanopore models) are taken from Fig. 3.1d at a pore width of  $7.5$  nm.



**Table 3.1:** Specific surface area, specific pore volume and mean pore size of all nanoporous carbon electrodes. The micropore volume fraction was determined by considering a carbon skeleton density of  $1.9 \text{ g} \cdot \text{cm}^{-3}$ .

	Specific surface area ( $\text{m}^2 \cdot \text{g}^{-1}$ )	Specific pore volume ( $\text{cm}^3 \cdot \text{g}^{-1}$ )	Mean pore size (nm)	Micropore volume fraction
AC1	1598	0.86	1.30	0.643
AC2	1707	0.72	0.90	0.600
CDC	1158	0.35	0.65	0.423

Electrolytes were prepared by mixing distilled water and salts with high purity (CsCl: 99.9 %; NaCl: 99.99%; both provided by Alfa Aesar). The 1M KCl aqueous solution was used as received (Alfa Aesar).

## 3.2 The in-situ experiment

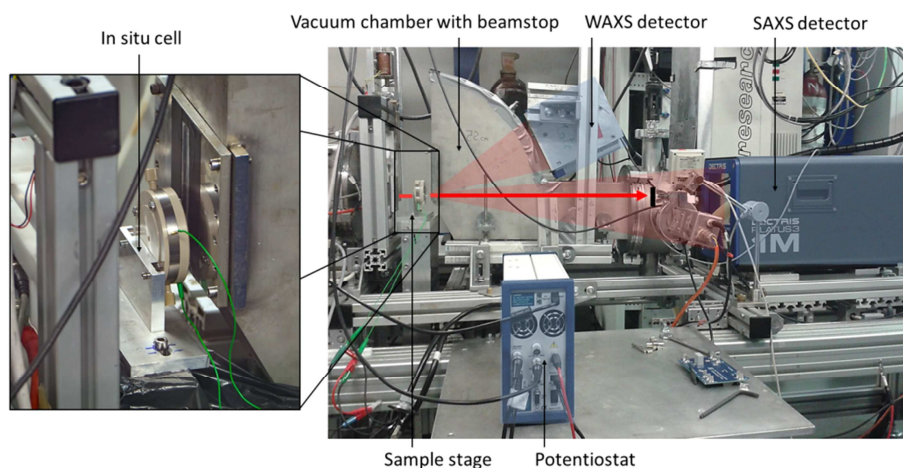


**Fig. 3.2:** Experimental set-up at the SAXS Beamline at the Synchrotron radiation facility ELETTRA in Trieste, Italy.

Parts of section 3.2 are not original and haven been published before.<sup>70,108,109</sup> *In situ* SAXS experiments were conducted at the Austrian SAXS beamline<sup>113</sup> at the synchrotron radiation source ELETTRA (Trieste, Italy) and partially at a laboratory SAXS instrument (NanoStar, Bruker AXS). They were realized on custom-built *in situ* supercapacitor cells connected to a potentiostat, using nanoporous carbon electrodes and aqueous electrolytes (Fig. 3.2). While applying the cyclic voltage signal via the potentiostat, at the Synchrotron transmission values and SAXS patterns are

measured in a period of 1 - 10 s. The small-angle scattering signal is recorded with a 2D position sensitive X-ray detector (SAXS: Pilatus 1M) and the transmission signal using an X-ray sensitive photodiode. In addition to the small angle data, the wide angle X-ray scattering (WAXS) intensity was recorded by a second 2D detector (Pilatus 100K) during Synchrotron experiments.

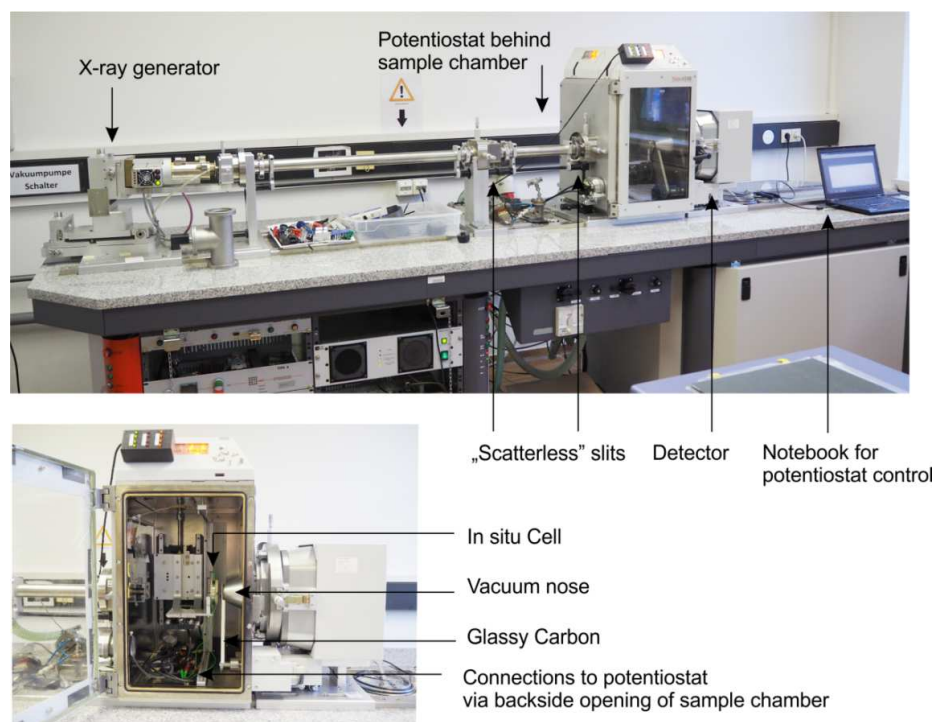


**Fig. 3.3:** Experimental set-up at the in-house SAXS/WAXS system.

*In situ* SAXS measurements with the laboratory SAXS instrument (NanoStar, Bruker AXS) were carried out using Cu K $\alpha$  radiation (45 kV and 0.650 mA), and a Vantec 2000 area detector (Fig. 3.3). The sample chamber is held under ambient conditions since the *in situ* cell is not perfectly sealed against a vacuum of 0.1 mbar, usually present in the Nanostar chamber. For this reason a vacuum nose is placed between sample and outer flange of the sample chamber (Fig. 3.3). In contrast to *in situ* experiments at the Synchrotron the transmission signal is measured using the Glassy carbon method.<sup>114</sup> Every time after a 2D scattering pattern is recorded the glassy carbon is positioned into the beam, right behind the *in situ* cell. In a good approximation the transmission signal corresponds to the integrated intensity of the 2D pattern of *in situ* cell plus glassy carbon divided by the integrated intensity of the glassy carbon alone. The flux of the laboratory X-ray source is several orders of

magnitudes lower than that of a typical Synchrotron beam. Therefore the charging cycles need to be slow (cyclic voltammetry with scan rates smaller than 0.2 mV/s) having a time resolution of about 900 s. Practically, this means that each scattering pattern of the *in situ* cell is recorded for about 900 s, and each transmission value (having *in situ* cell plus glassy carbon in the beam) for about 60 s. Data of *in situ* SAXS experiments carried out at the in-house SAXS system are shown in section 6.

Electrochemical measurements on the *in situ* cell were carried out using a Gamry Ref600 Potentiostat. Cyclic voltammetry was applied for all *in situ* measurements with a maximum voltage of  $\pm 0.6$  V (alternatively  $\pm 0.8$  V). Due to the oversized counter electrode (section 3.2.1) this corresponds approximately to the voltage dropping at the working electrode. Depending on the specific experiment, scan rates between 0.5 – 20 mV/s were used at the Synchrotron beamline and 0.05 – 0.2 mV/s were used at the laboratory SAXS instrument.

*Ex situ* SAXS measurements of the empty carbon electrode, the electrode filled with water and the electrode filled with electrolyte were carried out with the same set-up at the laboratory SAXS instrument (NanoStar, Bruker AXS).

X-ray diffraction (XRD) was carried out with a D8 Advance Eco (Bruker, AXS) diffractometer using Cu-K $\alpha$  radiation (40 kV, 25 mA). The XRD profile was recorded by a line-detector (LYNXEYE XE-T).

### 3.2.1 *In situ* cell design

The specific design of the *in-situ* supercapacitor cells allows the selective probing of only one electrode at a time, so that all data can be related just to the working electrode. This was achieved by having a hole in all materials except of the working electrode (WE) (Fig. 3.4). The oversized counter electrode (CE, about six times) was used as a quasi-reference electrode and guarantees that the capacitance is largely defined by the WE. The assembly of platinum current collector / working electrode / separator / counter electrode / platinum current collector was sandwiched in a polyether ether ketone (PEEK) housing and contacted with titanium end plates similar to the *in situ* cell developed by Ruch et al.<sup>115</sup> Moreover, two sticky polyimide (Kapton<sup>®</sup>) tapes sealed the cell at the X-ray entrance holes between the platinum current collectors and the titanium/PEEK casing. Since the polyimide tape produces a diffraction peak in the Q-range around 4 nm<sup>-1</sup>, in recent experiments a Tixo<sup>®</sup> or Scotch<sup>®</sup> tape was used preferably. For the cell assembly, a thin platinum paper (Dukatshop.de; ~200 nm) was used as current collector (CC) and a porous Whatman (GF/A) membrane as separator. The end plates consist of pure titanium in order to prevent corrosion. Similarly the platinum paper reveals (in contrast to gold or

stainless steel current collectors) no corrosion/chemical reactions within chlorine containing aqueous electrolytes.

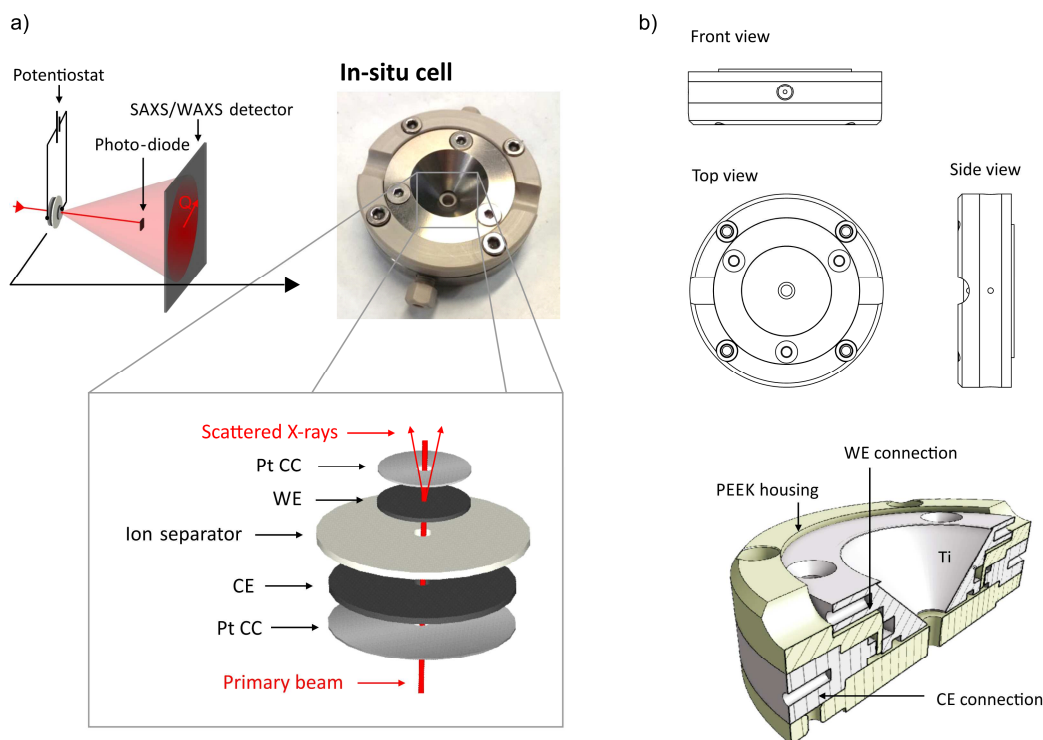


**Fig. 3.4:** Sketch of the in-situ experiment, with a photo of the *in situ* cell and a schematic representation of the cell assembly (a). 3D CAD drawings of the *in situ* cell are given in (b). Ref.<sup>108</sup> - Published by the PCCP Owner Societies.

A detailed drawing of all components as an assembly within the *in situ* cell is given in Fig. 3.5. The Pt current collectors don't necessarily require a hole, due to their negligible absorption ( $\tau \approx 0.92$ ). When studying ion electrosorption based on this cell design specific kinetic effects eventually need to be considered for certain experiments. The detail in Fig. 3.5 reveals the ion diffusion pathways for counter ions as blue arrows. In contrast to a conventional cell design the ion diffusion pathway into the center of the WE (position where the X-ray beam hits the WE) is longer. The kinetic behavior of ions tracked via the X-ray transmission signal and X-ray scattering intensity might be different from the overall (average) kinetic behavior of the WE. In fact X-ray transmission and scattering signal are always somewhat delayed compared to the electrochemical signal (averaged signal from the entire WE). For rather slow cycling and high molar electrolytes with a large ionic conductivity this effect has no big impact. However, for a hole in the CE and separator larger than 4mm, an increase in the time delay between X-ray signals and applied cyclic voltage signals from the

edge towards the center of the WE was observed. Moreover for the study of low molar (e.g. 0.01 M) electrolytes the X-ray signal cannot be quantitatively related to the overall electrochemical WE signal any longer.

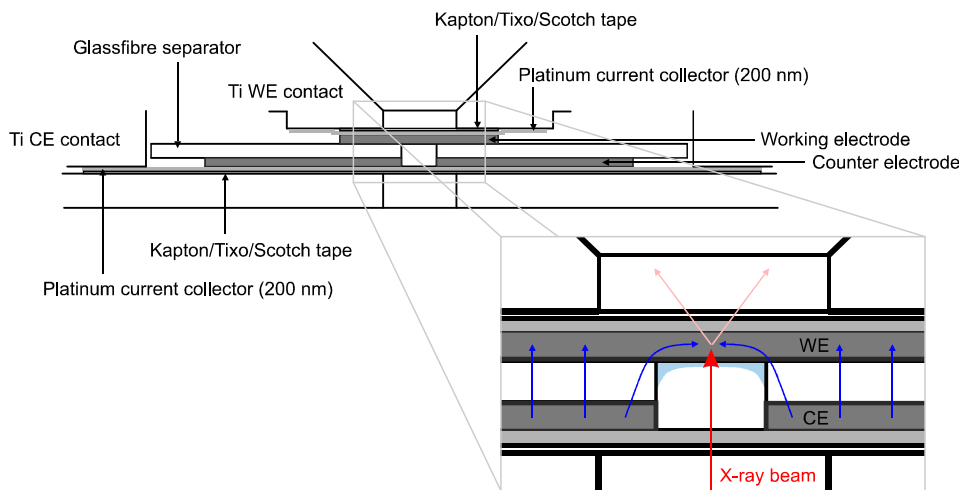


**Fig. 3.5:** Sketch of the cell assembly within the *in situ* supercapacitor cell. The detailed drawing indicates the ion diffusion pathways (blue arrows) and the X-ray beam (red) hitting the WE.

Depending on the wettability of the electrode a meniscus of the liquid electrolyte can occur in the hole of separator and CE (as indicated in Fig. 3.5). This needs to be considered for the quantitative analysis of the X-ray signals. In order to avoid this additional liquid film of bulk electrolyte on top of the WE a future cell design could be considered with counter and working electrode lying next to each other on the same level. Similar designs were frequently used for other *in situ* experiments<sup>22,116</sup>. However, ion diffusion pathways would increase even more, resulting in stronger kinetic effects and a large equivalent serial resistance of the *in situ* cell.

### 3.2.2 Primary SAXS data treatment

The following two paragraphs are not original and have been published in Ref. <sup>23</sup>. In particular for *in situ* experiments a transmission data correction is necessary because not only the scattering signal but also the absorption may change during the experiment. Without transmission correction the as-measured scattering intensity changes are overlaid by transmission changes and thus difficult to interpret.

An X-ray beam with the incident flux  $\phi_0$  in (photon/s/mm<sup>2</sup>) and a cross section  $A$  in (mm<sup>2</sup>) hits a sample with the thickness  $d$ , where  $\Delta\Omega = p^2/L^2$  represents a solid angle element of a detector pixel with the size  $p$  (mm) at a specimen-detector distance of  $L$  (mm) and  $\varepsilon(x,y)$  the detector efficiency. Before a photon of the incident beam gets

scattered at position  $x$  in the sample the beam is weakened by a factor  $e^{-\mu x}$ . After the scattering process the scattered beam is again weakened due to absorption, now by a factor of  $\exp(-\mu(d-x)) / \cos \theta$ . The integral over all possible  $x$ -positions gives the intensity which is recorded on the detector at the angle  $\theta$  ( $Q \sim \sin \theta$ ).<sup>117</sup>

$$I(\theta) = \int_0^d \phi_0 A \varepsilon(x, y) \Delta \Omega e^{-\mu x} \frac{e^{-\mu(d-x)}}{\cos \theta} \frac{d\Sigma}{d\Omega} dx \quad (3.1)$$

The instrumental constant  $K$  is defined as follows.

$$K = \phi_0 A \varepsilon(x, y) \Delta \Omega \quad (3.2)$$

At small angles  $\cos \theta \cong 1$ , the integration gives

$$I(\theta) = K d e^{-\mu d} \frac{d\Sigma}{d\Omega} = K d \tau \frac{d\Sigma}{d\Omega} \quad (3.3)$$

with  $\tau$  being the sample transmission.<sup>117</sup> Thus, the absorption process influences the absolute scattering intensity, although it is practically independent on the scattering angle in the case of small angles.

During charging and discharging the *in situ* supercapacitor cell cation and anion concentrations within the working electrode are expected to change. Due to the different electron numbers and absorption coefficients of cations and anions the scattering intensity and the transmission signal are going to change with time. A transmission correction of the as-measured scattering intensity is therefore absolutely required, which is realized by a simple division of the transmission  $\tau$ . The intensity modulation of the measured detector frames due to the changing transmission is thereby filtered out. Apart from *ex situ* SAXS measurements (section 5.1.3) carried out at the SAXS lab system, a calibration to absolute scattering units ( $\text{cm}^{-1}$ ) is not required, which makes the determination of the instrumental constant  $K$  obsolete.

For all SAXS measurements, each 2D detector pattern was spherically averaged using the software FIT2D<sup>118</sup>, and normalized by the measurement time and the corresponding transmission value. Constant background contributions to the scattering signal, originating from X-ray windows (polyimide, Scotch® or Tixo® tape) and air scattering were subtracted after transmission and time correction.

*Ex situ* spherically averaged SAXS pattern of the carbon electrodes were corrected for transmission, time and sample thickness, and calibrated to absolute scattering cross sections using distilled water as a calibration standard<sup>119</sup>. The calibration procedure

and further data treatment like analytical model fits or the determination of the liquid structure factor background are explained in section 5.1.

*In situ* data presented in section 5.3 (AC1 as electrode; 1M CsCl, KCl and NaCl as electrolyte) were treated as follows. The so-called radius of gyration is a parameter sensitive to any structural change within the system of ions, water molecules, and carbon pore structure. It is easily assessable from the SAXS signal by performing a conventional Guinier analysis.<sup>32,120</sup> The Guinier analysis was conducted for Q-values larger than  $1.2 \text{ nm}^{-1}$  in order to avoid any impact of the scattering contribution from the large carbon particles. Moreover, an ion concentration dependent background contribution originating from the carbon and electrolyte structure factor was subtracted from the SAXS intensity. This background was evaluated by a modified Porod analysis.<sup>32</sup> In a perfect two-phase material Porod has shown that the intensity at large Q decays with a power law  $I(Q) \sim Q^{-4}$  (see section 2.3.1). In disordered microporous carbons on the other hand the exponent might be significantly smaller than 4. This fact is explained by a breakdown of the validity of the ideal two-phase model with sharp interfaces due to the small size of the pores with rough or fractal surface.<sup>36,121 122</sup> From a power law fit, an exponent of -3.28 was obtained for Q-values between  $4 \text{ nm}^{-1}$  and  $8 \text{ nm}^{-1}$ . Assuming a SAXS intensity of the form  $AQ^{-3.28} + BG$ , the background was evaluated by the common Porod procedure and then subtracted from the data.

Apart from integral parameters like the radius of gyration, time-dependent information from *in situ* SAXS data can be analyzed via “heat plots”, as used in section 5.3 and 5.4 and shown in Fig. 3.6a. All azimuthally averaged and corrected SAXS patterns are normalized by a scattering curve representing the average of all scattering curves of the particular CV cycle. The resulting relative SAXS intensity change is plotted as a function of time and the scattering vector length Q in matrix form, where the relative intensity values are visualized as different colors (Fig. 3.6a). Alternatively the SAXS curves could be normalized by the first SAXS curve at zero applied voltage (section 5.3). However any noise of the first SAXS curve is in this case transferred to all other relative SAXS intensity curves, as visible by vertical lines in the heat plots of section 5.3. In section 5.4 heat plots were obtained by normalization with the average SAXS curve.

Relative intensity (“heat”) plots as a function of time are chosen as the best visualization of Q-dependent intensity changes. In order to verify the correspondence between measured and simulated scattering data (details see section 4 & 5) heat plots are simply compared “by eye”, which is reasoned as follows. The absolute intensity change of the scattering curve is very small (see Fig. 3.6b), which is problematic in the case of the rather noisy simulated scattering data. The normalized SAXS intensity

of both measured and simulated scattering curves at +0.6 V, -0.6 V and 0.0 V applied voltage are given in Fig. 3.6c. The information content in terms of quantitative numbers does not necessarily improve. The simulated curves reproduce the measured curves, however, the noise level due to the limited simulation box size is very high. Thus, “heat plots” seem to be the most convenient form of visualizing *in situ* scattering data and deviations between simulation and experiment.

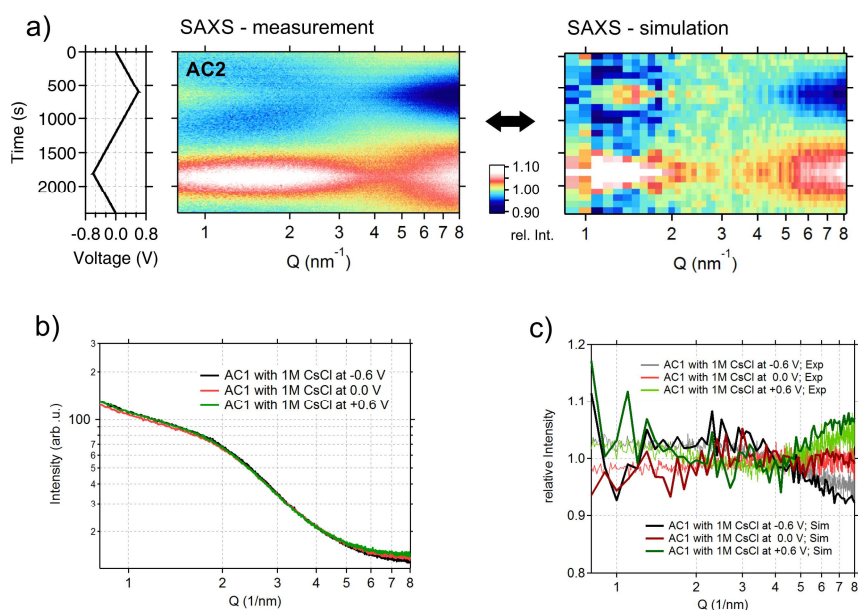


**Fig. 3.6:** Relative small angle scattering intensity change as a function of scattering vector length  $Q$  and time (or the cell voltage). In (b) the measured small angle scattering intensities of an *in situ* experiment at three different cell voltages is given as a function of  $Q$ . Measured and simulated scattering curves normalized by their average scattering intensity are shown in (c).



## 4 Simulating equilibrium ion positions in nanoporous carbons

In the framework of this thesis a novel SAXS data analysis tool was developed that includes a Monte Carlo simulation to obtain equilibrium ion positions within a modeled pore structure as a function of the electrode charge. The entire data analysis strategy is presented in section 5.4. Here, details on the developed Monte Carlo simulation are given. The specific design of the simulation is based on experimental outputs from the *in situ* XRT and *ex situ* SAXS experiments used as input for the simulation and on considerations for achieving satisfactory comparability between simulation output and *in situ* SAXS experiments. The 3D carbon model is obtained from *ex situ* SAXS measurements of the empty carbon electrode using so-called Gaussian random fields, as explained in detail in section 5.1. During charging and discharging the supercapacitor the X-ray transmission signal delivers the absolute cation and anion concentrations as a function of the applied cell voltage (section 5.2). These concentrations are used as an input for the Monte Carlo simulation. Only the cation and anion arrangement within the pore structure is obtained by the Monte Carlo simulation, their concentrations are predefined. For the simulations presented in this work aqueous CsCl was used as electrolyte, exploiting the fact that Cs<sup>+</sup> and Cl<sup>-</sup> ions reveal similar dehydrated and hydrated ion radii and consequently comparable hydration energies. This similarity is advantageous due to the symmetry at positive and negative electrode polarization. Once the equilibrium ion positions are obtained all phases in the system are weighted by their corresponding electron densities. The spherically averaged squared amplitude of a Fourier Transform of this structure reveals the scattering curve, which can be compared to the measured SAXS curve. As a consequence of the required noise level of the Fourier transformed scattering curve, the simulation box needs to be large, which has further implications on the structure of the simulation.

### 4.1 General structure

The following section is in parts not original and published in Ref.<sup>109</sup>. In a closed system containing conducting structures with a certain capacitance the conservation of charge is fundamental. Even for a charged conducting sphere in vacuum the

counter-charge can be imagined as being somewhere at infinite distance. If the sphere is grounded (sketched in Fig. 4.1) the counter charge in the ground exactly balances the charge of the sphere. Since the ground is per definition a huge conducting mass with a huge capacitance the voltage remains constant ( $Q = CU$ ). For a plate capacitor the amount of charge on a single electrode depends only on the potential *difference* between the two electrodes; absolute potentials of the single electrodes (i.e. whether the one of the electrodes is grounded or not) have no influence on the amount of charge. This is generally valid for a system containing conducting structures at different potentials (e.g. sphere and ground).

For a capacitor consisting of two perfect conductors (which allow no charge transfer between the two phases) the capacitance is defined by geometry and corresponds to the proportionality constant between voltage and charge. This means that for simulating equilibrium ion positions within the bulk of an electrode carbon particle using a canonical ensemble (as indicated by the subsection in red in Fig. 4.1b), the concentration of ionic (and electrode) charges have to be predefined. Alternatively, in a Grand canonical ensemble the electrode voltage could be defined, where the corresponding ion and electrode charge would result from the simulation. In Fig. 4.1c the potential landscape around a nanopore entrance is shown schematically. Since the ion concentrations within the simulation are pre-defined by XRT experiments only the relative potential landscape in the bulk of the nanopore structure is of interest. Consequently, there is no need to consider the drop (rise) in the potential energy (see red arrow in Fig. 4.1c) of counter-ions (co-ions) when entering the pores from the bulk electrolyte.

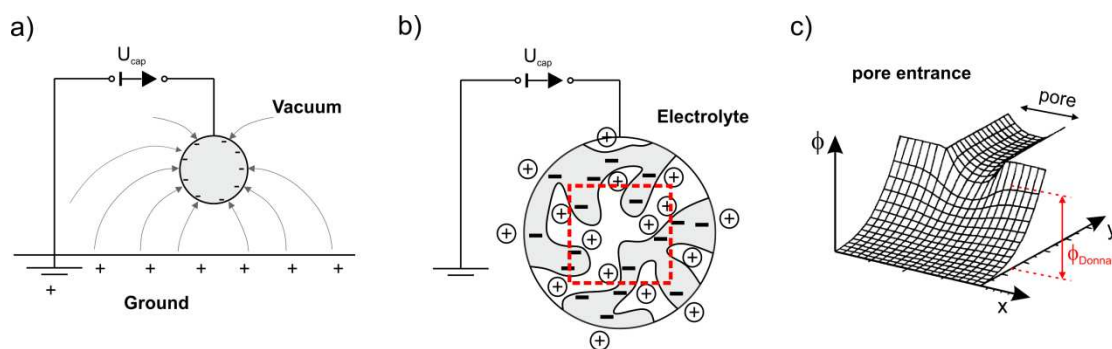


**Fig. 4.1:** (a) Sketch of a conducting sphere held at negative potential vs. the ground and the corresponding electric field lines. (b) Sketch of a porous structure held at a certain potential. The ionic charge exactly counterbalances the electrode charge and defines the potential applied to the pore structure. (c) Potential landscape around a nanopore entrance. According to the Donnan model the potential within a slit-like nanopore can be modeled by two overlapping double-layer potentials.<sup>56</sup> Fig. 4.1c adapted with permission from Ref.<sup>55</sup>. © Elsevier.

Practically the simulation in this work is implemented as follows. First, cations and anions are placed randomly within the pores in the corresponding carbon structure, where the number of cations and anions is obtained from the XRT signal for each voltage step (section 5.2). The positions of ions at a certain applied voltage are updated using a MC simulation considering coulombic ion-ion interactions and ion-carbon interactions due to induced electrode charges. Both, cations and anions are treated as hard spheres of radius  $0.18 \text{ nm}^{97,98}$ , water is introduced as a continuous dielectric medium, and the electrode is a continuous perfect conductor. In accordance with literature<sup>123</sup> best agreement between simulated and measured SAXS curves was achieved with a dielectric constant of  $\epsilon = 40$ , being significantly lower in nanopores than in bulk water ( $\epsilon = 78$ ). The correct treatment of the conducting electrode is essential for the arrangement of ions.<sup>124</sup> The ability to induce charges on the metal-like electrode represents the capacitive behaviour of the electrode-electrolyte interface on the one hand, and effectively screens the ion-ion coulombic interactions on the other hand. As sketched in Fig. 4.2 each charge in the system (cations, anions, and induced electrode charges) cause an electric field on a certain surface element of the electrode which consequently induces an electrode charge (per unit area)  $\sigma$  at this position.<sup>125</sup>

Cation and anion concentrations are set to fixed values obtained from XRT (see section 5.2), thus, corresponding to the (NVT) canonical ensemble. Specifically, from the (meso- and) micropore concentration changes, the fraction (cation and anion fraction = 0.5 at 0V) of cations and anions is calculated for each state of charge. To calculate the equilibrium positions of the ions, standard metropolis algorithm was implemented considering ions as hard spheres with coulombic interaction potentials. Because the electrode is conductive, ions induce surface charges on the electrode, leading to attractive forces. The electrode is modelled as a continuous triangulated surface with a point charge at the centre of each triangle (Fig. 4.2). These surface charges ensure that no electric field propagates through the electrode. This concept corresponds to a constant potential within the metallic electrode which is generally favoured in such simulations as compared to a constant charge density all over the surface.<sup>124</sup>

The box size used for the simulations is  $16.2 \times 16.2 \times 16.2 \text{ nm}^3$  corresponding to  $162 \times 162 \times 162$  voxels (of  $0.001 \text{ nm}^3$  size) to obtain a reasonable reduction of the noise level in the subsequently, re-calculated scattering curves. Periodic boundary conditions (PBCs) are implemented in all three dimensions requiring 3D PBCs in the GRF generated pore structures as well. In order to end up with manageable computation times, the simulation box is divided into cells with a size of  $2.7 \text{ nm}$  (AC1:  $3.24 \text{ nm}$ ; depending on the interaction radius described below) allowing the implementation of a neighbour list (linked-list method).<sup>100,102</sup> In the case of AC2, the

linked-list method<sup>100</sup> requires a splitting of the simulation box into 6 x 6 x 6 cells, each with a minimal size equal to the cut-off radius (2.7 nm). The chosen box size represents the minimum for comparing simulated with experimental SAXS data with reasonable accuracy and being an integer multiple of the required cell size.

For each MC step, a cation or anion is chosen randomly. Then a new position for this ion within the pore space is chosen randomly. The energy difference between current and new position is calculated considering contributions from all charges (cations, anions and electrode charges) within a specified interaction radius according to the pore structure of each carbon (AC1: 3.24 nm, AC2: 2.7 nm, CDC: 2.25 nm). The new position is accepted or rejected using a standard Metropolis algorithm.<sup>100</sup> The interaction radius was chosen large enough to ensure that the net contribution of all charges (i.e., cations, anions plus electrode charges) is essentially zero outside this sphere and small enough to not unnecessarily increase computational time. Methods that accurately deal with long-range forces (such as the Ewald summation method) are computationally too expensive for the required box sizes of 16.2 nm (containing about 160000 electrode charges and 3600 ions). In this system, the induced electrode charges and the complexly shaped pore confinement effectively screen the Coulombic interactions, as shown in previous work (known as ‘superionic state’, a term introduced by Kondrat and Kornyshev).<sup>60,126-128</sup> At distances significantly larger than the actual pore sizes, the potentials have basically fallen off to zero. Cross-checks applying simulations in small box sizes using Ewald summation and simulations with different interaction radii were carried out to confirm the validity of the time saving cut-off method (section 4.4).

To prevent the system from being trapped in local energy minima, the method of simulated annealing was used. In this method, the temperature is slowly decreased from a large value to the desired temperature of 300 K.

Besides coulombic interactions, the energy cost due to dehydration of ions approaching the carbon surface or other ions closer than their hydrated ion radius (0.33 nm<sup>97,98</sup>) was considered in a semi-quantitative way. The so-called degree of desolvation (DoDS, see section 5.4.2), representing the fraction of released water molecules in the hydration shell of a single ion due to geometrical confinement was multiplied by experimentally determined hydration energies from literature ( $\approx 30 \text{ kJ} \cdot \text{mol}^{-1}$ ).<sup>42</sup>

To calculate the energy of an ion, the induced electrode charges must be evaluated for each cation or anion move. The electrode is considered as perfect conductor meaning that the potential is constant and the electric field zero within the carbon phase. The induced surface charge density  $\sigma_{\text{ind},i}$  of the conducting electrode surface element  $i$  can be expressed as:<sup>129</sup>

$$\sigma_{ind,i} = -2 \cdot \sum_{j \neq i} \vec{n}_i \cdot \epsilon_i \vec{E}_{ij} . \quad (4.1)$$

where  $\vec{n}_i$  is the unit surface normal vector and  $\vec{E}_{ij}$  the electric field of cation/anion/electrode charge  $j$  at the surface element  $i$ . In order to calculate the surface charge the following fixed-point iteration was used.<sup>125</sup>

$$\sigma_{ind,i}^{(n+1)} = \omega \cdot \left[ -2 \sum_{j \neq i} \vec{n}_i \cdot \epsilon_i \vec{E}_{ij}^{(n)} \right] + (1 - \omega) \cdot \sigma_{ind,i}^{(n)} \quad (4.2)$$

where  $\omega$  was chosen to be 0.7 allowing the most effective conjugation<sup>125</sup>. The iteration was stopped when the relative change of the total induced charge is smaller than 0.015. Since the total induced electrode charge after each MC step compensates the total ion charge within the pores, it can be concluded that the iteration procedure works properly.

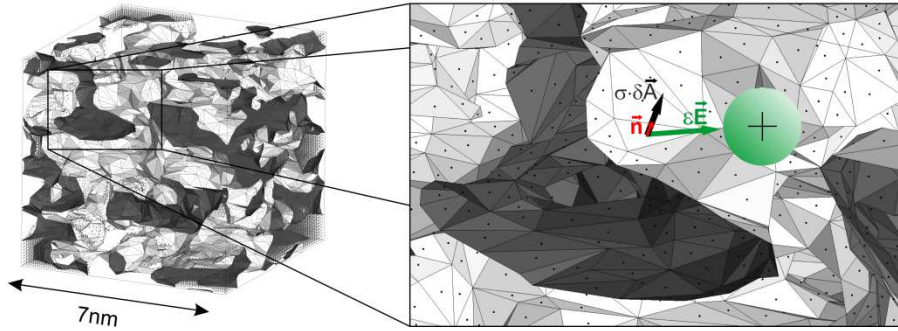


**Fig. 4.2:** Three dimensional visualization of a nanoporous carbon (here: 3D sub-volume with  $7 \times 7 \times 7 \text{ nm}^3$ ). The pore structure is populated with cations and anions in a homogeneous dielectric water phase with the ion concentration obtained from X-ray transmission (section 5.2). For each electrode voltage, ions are re-arranged according to a MC simulation. The electric field  $\epsilon \vec{E}$  caused by all surrounding charges (as an example cation in green electrode charges as black dots) induce a charge  $|\sigma \cdot \delta \vec{A}|$  in the center of each triangle (normal vector  $\vec{n}$ ) of the carbon pore-interface, as indicated in the zoomed view.

The coulombic potential between an ion and its image on a conducting electrode at constant potential contains an additional factor of  $\frac{1}{2}$ . Hence, for the potential originating from the electrode charges induced (only!) by the “moving” ion of the current Monte-Carlo step a factor of  $\frac{1}{2}$  has to be considered.<sup>130</sup> If an ion approaches a conducting plate at constant potential (which is equivalent to a grounded plate) the coulombic potential between the ion and its image can be written as  $\frac{1}{2} \cdot 1/(4\pi\epsilon_0 \epsilon_r) \cdot$

$q_{image}/r_{image-ion}$ . The factor of  $\frac{1}{2}$  can be explained by the fact that no work is needed for rearranging the image charges within the equipotential surface of the conducting plate, when the ion approaches the plate.

Details on the electrode charge calculation and the treatment of long-range coulombic interactions are given in section 4.2 and 4.4, respectively.

## 4.2 Induced electrode charges

In general, the computational time is the limiting factor regarding the electrode charge calculation using the iterative procedure. Already after two iteration steps the potential in several test geometries remained at a constant value. In Fig. 4.3 the calculated potential for a charge in front of a conducting and finite plate (4.7 x 4.7 nm) is plotted as a function of the distance. Only at larger distances (where the finite dimensions of the plate become important) deviations to the analytic potential of a charge in front of a grounded conducting plate are visible.

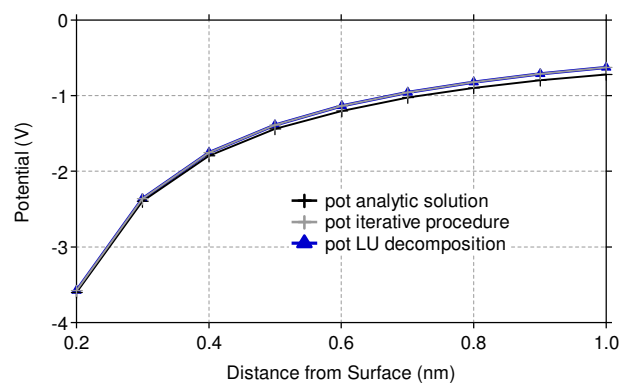


**Fig. 4.3:** Analytic and numerical solutions for the potential of a point charge in front of a conducting, 4.7 x 4.7 nm sized plate.

In the actual pore model the result of the iteration is found to fluctuate (at least for some numerically unfavorable electrode arrangements) between 4 -5 % around its real solution. Due to these rather strong fluctuations a second exit condition, regarding the total electrode charge (& considering for the high computational cost of each iteration step), was implemented in the code: If the relative change of the total induced electrode charge is smaller than 1.5% the iteration was stopped. This rather pragmatic exit condition gives in the end the correct value for the total induced electrode charge within an acceptable error. Since this second exit condition is the stronger one it actually applies most of the times during the simulation.

A further crosscheck of the iterative procedure was performed by rearranging Eq. 4.1 to a problem of solving a set of linear equations.<sup>125</sup> The electrode charge was then solved by using a linear Equation solver (LU decomposition).

$$(\delta_{ij} - K_{ij})q_i = E_i^{const} \quad , \quad \text{where} \quad K_{ij} = 2 \frac{1}{4\pi} \frac{1}{r_{ij}^2} \vec{e}_{rij} \cdot \vec{n}_i \quad , \quad (4.3)$$

with  $\delta_{ij}$  as the identity matrix. The matrix  $K_{ij}$  accounts for pair interactions between the electrode charge  $i$  and all surrounding electrode charges  $j$ .  $E_i^{const}$  is the electric field at the surface element  $i$  caused by all surrounding cations and anions and is calculated by Eq. 4.1. As visualized in Fig. 4.3 the potential reproduces perfectly the curve obtained from the iterative procedure. Compared to LU decomposition the iterative procedure is very fast. During a Monte Carlo step an ion is moved to new position, where all other ions remain at the same position. Therefore electrode charges in the surrounding are not affected too much. Consequently the iterative procedure has in many times already finished after two iteration steps.

Apart from the conducting plate the procedure was tested on simple geometries like a slit pore, a hollow sphere (with ions inside the sphere) and a conducting sphere (with ions outside the sphere). Apart from the conducting sphere, all geometries revealed equal electrode and ionic charge, reasonable charge distributions and potentials within some systematic error.

The iterative algorithm was initially developed for dielectric interfaces.<sup>125</sup> Although it is applicable for dielectric-metal interfaces as well, numerical inaccuracies can result in an incorrect total charge at sensitive geometries. For example the calculation of the surface charge distribution of a conducting sphere, with an ion being placed in front of the sphere, results in an incorrect total induced charge in the sphere (error up to 500% of the correct total charge). Moreover the total induced charge depends on the distance of the ion with respect to the sphere. The relative distribution of surface charges, however seem realistic and reproduces the dipole characteristics of the ion and its image within the sphere. Changing the distribution and density of the surface charges on the sphere gives a similar relative charge distribution but again a different total induced charge, confirming that numerical problems due to geometry are responsible for the error. In disordered, three dimensional pore structures the theoretically induced charge is exactly defined by the ionic charge. A correct induced charge might be generated by multiplying the point charges (correct relative charge distribution!) by a weighting factor.

A hollow sphere with an ion being placed inside the sphere, on the other hand, gives a correct relative charge distribution and a total induced charge being about 5% above

its correct value of  $1.602 \cdot 10^{-19}$  C. However a certain numerical error is induced, since the triangulated surface is not an exact representation of the real curvature. Charge induced by the curved surface in the direct surrounding to a point charge is, due to the finite width of the triangles, not accounted for. Direct surrounding means distances smaller than the average distance between neighboring point charges. This error induced by the finite size of the surface triangles can be corrected for by multiplying each surface charge by a correction factor. However in randomly shaped geometries this is difficult, since the error and the correction factor would depend on the local curvature. Concave surfaces, as present in a hollow sphere, result in a too large magnitude of the total induced surface charge. Convex surfaces, as described by the charged sphere example, are numerically more problematic.

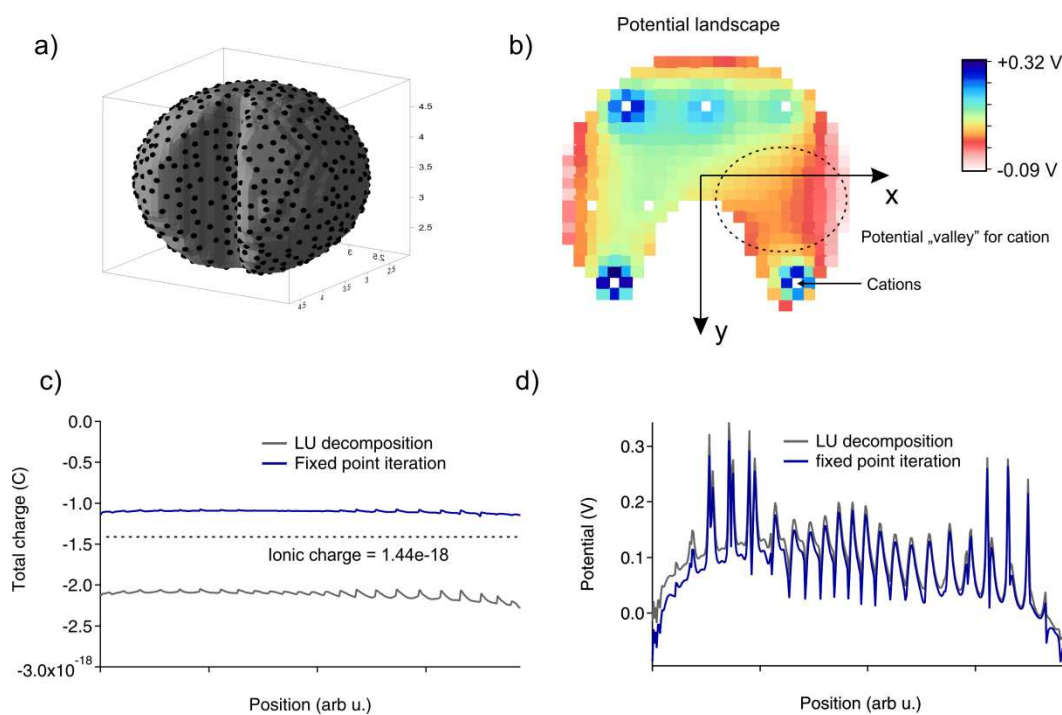


**Fig. 4.4:** 3D visualization of a test pore geometry (a) with pore dimensions and curvatures similar to the actual nanopore structures used in the simulations. In (b) the potential landscape in a horizontal cross section of the pore geometry is shown; where a positive test charge is scanned through the section and some additional test charges are placed randomly within the test geometry. The total charge (c) and the potential (d) are given as a function of the position in the cross section, using both the iterative approach and LU decomposition for calculating the electrode charge.

Though numerical errors of the total induced charge seem rather large, the test geometry shown in Fig. 4.4 should reveal the applicability of the algorithm to the nanopore model structures. A test charge (positive) was scanned through the hollow structure in order to determine the potential landscape. Eight additional positive



point charges were placed randomly within the pore structure, partially visible in the cross section of the potential in Fig. 4.4b. For the present point charge distribution the potential landscape seems realistic. An area of low energy is present in a narrow pore (with a rather high “degree of confinement”, see section 5.4.1) as indicated by the dashed ellipse. The magnitude of the total induced charge obtained from the iterative procedure (given in blue in Fig. 4.4c) is about 25% lower than its theoretical value. The total induced charge obtained from LU decomposition (given in grey in Fig. 4.4c) on the other hand is about 50% larger than the theoretical value. Given the large numerical errors of the total induced charge, the potentials (Fig. 4.4d) of both approaches are rather similar. Only the potential differences are critical for the acceptance probability of a Monte Carlo step, using the Metropolis algorithm. Those relative differences are nearly identical for both approaches. This implies that, as long the relative distribution of the surface charge is obtained correctly, and the absolute values lie within an error of 20 – 30 %, the potential landscape should be determined correctly.

Another problem occurs for point charges with opposed normal vectors lying too close to each other. For such unfavorable geometrical situation the two charges could mutually induce an opposed charge with unrealistic high magnitude. Therefore the pore model surface is triangulated in such a way that the minimum distance between neighboring point charges (in the center of triangles) is larger than a certain value (usually taken as 0.1 nm). Practically, the triangulation was performed in Matlab, since the roughness of the surface triangulation can be adjusted with a rather simple command. Subsequently the data was imported in IgorPro and triangles with a neighbor – neighbor distance smaller than 1 nm unified; i.e. the corresponding normal vectors weighted by the area of the triangle, were added vectorially. Apart from that a condition prohibiting too large magnitudes of point charges is implemented in the code of the Monte Carlo simulation.

Alternative strategies avoiding most of these errors in the electrode charge calculation could be a Finite boundary method.<sup>131,132</sup> Similar to the Finite element method the induced surface charge density would be approximated by a simple (e.g. linear) function within the triangles. To do so, a numerical integration over the triangle surface is required. The computing time is thus increased at least by a factor equal to the “number of integration elements per triangle”, assuming that the number of iteration steps per point charge remains the same.

### 4.3 Structure of C++ Code

Parts of the developed code are given in Appendix A. Code lines for DoDS-, potential-, energy- and electrode-charge- calculation are shown exemplarily.

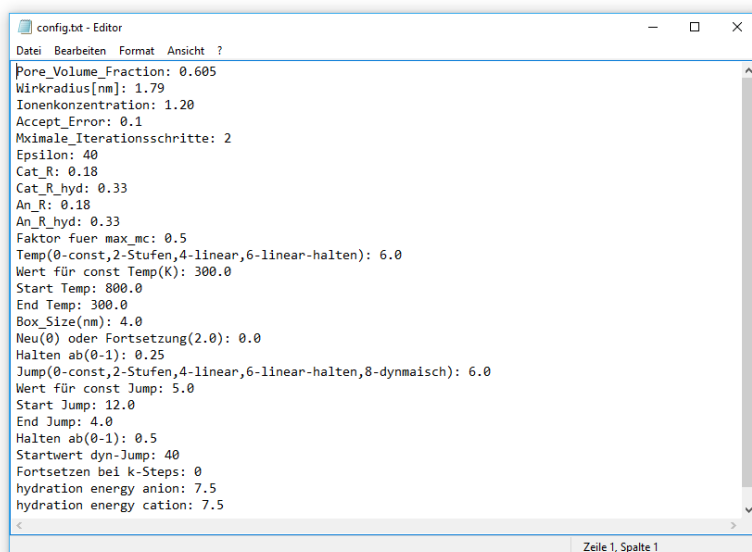
The simulation was initially implemented in the data analysis software, numerical computing environment and programming language Igor Pro, where the language is based on C. The code was then translated into a C++ code for reasons of computational time. The simulation box has a size of 162 x 162 x 162 voxels and is divided into individual cells in order to apply a linked list method (Appendix A). The linked list algorithm ensures a nearly linear scaling of computational time with the simulation box volume. The simulation for a certain cell voltage (or state of charge) was conducted at least five times in order to reduce the noise level by averaging the resulting scattering curves. All simulations were conducted at the EVA HPC Cluster (Institute of Mechanics, Montanuniversitaet Leoben) using more than 100 cores in parallel for about one week. In order to perform effective input parameter studies a single simulation was also optimized for the calculation on the GPU of a single PC, using CUDA programming.<sup>133</sup> Translation into C++ and the optimization of computational time was largely performed by Christian Koczwar. The general structure of the code is given in the following.

#### Set parameters

##### 1 Input via text files:

- position, surface area and normal vectors of surface elements
- volumetric data of 3D pore structure

Input parameters from Config file:



```
config.txt - Editor
Datei Bearbeiten Format Ansicht ?
Pore_Volume_Fraction: 0.605
Wirkradius[nm]: 1.79
Ionenkonzentration: 1.20
Accept_Error: 0.1
Maximale_Iterationsschritte: 2
Epsilon: 40
Cat_R: 0.18
Cat_R_hyd: 0.33
An_R: 0.18
An_R_hyd: 0.33
Faktor fuer max_mc: 0.5
Temp(0-const,2-Stufen,4-linear,6-linear-halten): 6.0
Wert fuer const Temp(K): 300.0
Start Temp: 800.0
End Temp: 300.0
Box_Size(nm): 4.0
Neu(0) oder Fortsetzung(2.0): 0.0
Halten ab(0-1): 0.25
Jump(0-const,2-Stufen,4-linear,6-linear-halten,8-dynmais): 6.0
Wert fuer const Jump: 5.0
Start Jump: 12.0
End Jump: 4.0
Halten ab(0-1): 0.5
Startwert dyn-Jump: 40
Fortsetzen bei k-Steps: 0
hydration energy anion: 7.5
hydration energy cation: 7.5
Zeile 1, Spalte 1
```

2 Declaration of all vectors and variables

### **Generate starting configuration**

- 3 Fill ions into pore structure with random arrangement  
Always check, whether position can be accepted (ion-ion distances, ion-carbon distances, position inside a pore?)
- 4 Calculate Degree of desolvation (DoDS) for all ions
- 5 Calculate energy for all ions in this random configuration
  - 5.1 Therefore calculate electrode charges
  - 5.2 Sum up potential contributions of surrounding cations, anions and electrode charges
  - 5.3 Add hydration energy by multiplying the DoDS by hydration enthalpy

### **Start of metropolis algorithm**

- 6 First, random draw of an ion (cation or anion)
- 7 If an ion is chosen, choose a new position for this ion (jump length decreases during the simulation to keep the acceptance probabilities roughly constant); check whether new position is possible (is the new position still in the pore? Is any other ion already placed on the new position?) If a new position cannot be found after 50 attempts choose a new ion.
- 8 Then calculate energy and potential (“get ion potential old”)
  - 8.1 First calculate electrode charges
  - 8.2 Sum up potential contributions of cations, anions and electrode charges
  - 8.3 Add hydration energy by multiplying the DoDS by hydration enthalpy
- 9 Calculate DoDS of ion on new position
- 10 Calculate electrode charges
- 11 Sum up potential contributions of surrounding cations, anions and electrode charges
- 12 Calculate energy by adding the hydration contribution
- 13 Accept new position according to a Boltzmann probability if the energy is higher; and in any case if the energy is lower (Metropolis)
- 14 After a certain number of MC steps, when the total energy remains constant the Metropolis algorithm is stopped.

## Output

15 Calculation of output parameters, like Degree of Confinement (see section 5.4.1), energies, induced electrode charges, ...

Parts of the code are given in Appendix A and are available by request from the author.

## 4.4 Control parameters

The Monte Carlo simulation is stopped after the system has equilibrated. In Fig. 4.5 the mean degree of confinement (DoC, details section 5.4.1) and the total energy of cations and anions for different states of charge are plotted as a function of Monte Carlo steps. For this particular simulation the system has equilibrated after roughly 100000 Monte Carlo steps.

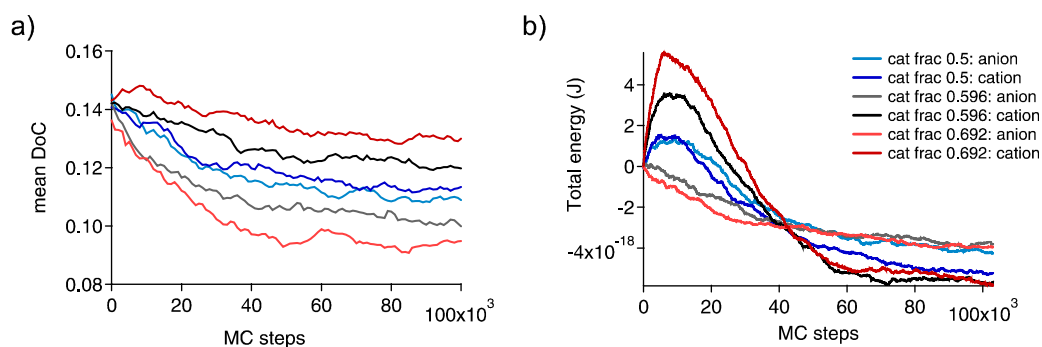


**Fig. 4.5:** Mean DoC values (a) and total energy (b) of cations and anions as a function of the Monte Carlo step number (or equivalently simulation time) for different cation fractions (states of charge).

As discussed in section 4.2 the iterative algorithm for calculating the electrode charge brings some numerical error, depending on the shape of the pores and the point charge distribution. As visualized in Fig. 4.6 the local electrode charge induced by the ion performing the actual Monte Carlo jump is somewhat lower than its theoretical value of  $1.602 \cdot 10^{-19}$  C. Moreover the resulting electrode charge shows some spreading around a mean value. The mean value (histogram in Fig. 4.6b) obviously depends on the ratio between counter- and co-ions.

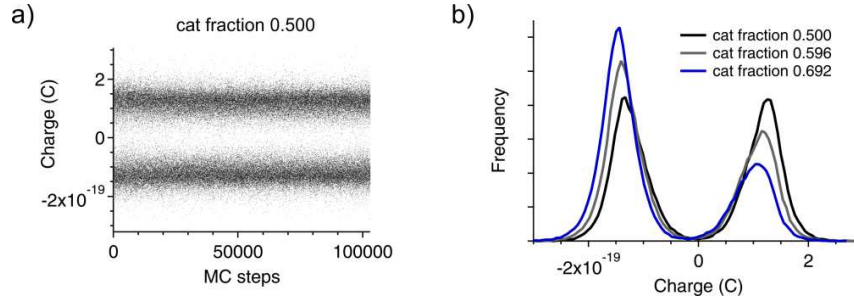


**Fig. 4.6:** Local charge (within the cut-off radius) as a function of Monte Carlo step number, induced by the specific ion performing the Monte Carlo step (a). The same is shown in form of histograms (b) for different cation fractions (states of charge).

The radial pair distribution function  $g(r)$  accounts for ion-ion correlations and measures the probability to find an ion  $B$  in a certain distance  $r$  from an ion  $A$ :

$$g_{A-B}(r) = \left\langle \frac{N_{r,r+dr}}{4\pi r^2 dr} \cdot \frac{1}{n} \right\rangle_A \quad (4.4)$$

$n$  is the mean number density of ion  $B$  within the simulation box,  $N_{r,r+dr}$  is the number of species  $B$  in the spherical shell with the thickness  $dr$  at the distance  $r$  from ion  $A$ . The cation-anion (and anion-cation) correlations depend on the fraction of counter- and co-ions (Fig. 4.7). Rather strong attraction is present between ions of different sign; repulsion between ions of the same sign. The radial pair distribution function looks similar for all states of charge.

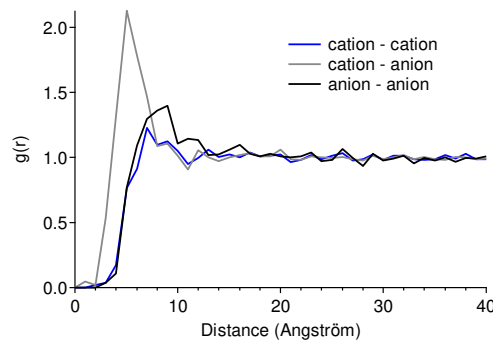


**Fig. 4.7:** Radial pair distribution functions of cation-cation, anion-anion and cation-anion correlations.

Coulombic interactions are long range (discussion see section 2.4.1) and small deviations from the ideal screening behavior of the conducting phase boundary either due to (locally occurring) large pores or numerical errors in the electrode charge determination can have a big impact. The obtained electrode charge of the studied

pore structures is, depending on the average pore size (and other factors), about 3 – 10 % too small. For this reason the pair distance distribution function shows some distinct cut-off effects as indicated in Fig. 4.8 (here  $g(r)$  is not normalized by the mean number density). Ions of the same sign have a higher probability of being located at distance just outside the cut-off radius; ions of opposite sign just inside the cut-off radius. These humps in the ion – ion correlations occur at distances relevant for the SAXS scattering regime. A distinct peak is present for the simulated *in situ* scattering data without correction around  $Q = 2\pi/R_{\text{cut-off}}$ . Therefore, the coulombic potential of each charge (cations, anions and electrode charges) was modified. The potential is now subtracted by its constant value at the cut-off distance (indicated in Fig. 4.8b). Doing so, the potentials are shifted by an absolute value to go towards zero at the cut-off distance. The relative potential landscape within the cut-off sphere remains the same. Considering the isotropy and the homogeneity of the 3D pore structure the relative errors in the electrode charge determination (which are corrected for) should be similar for all MC steps. With this assumption the potential correction represents only a shift in the absolute scale in the potential landscape, not affecting the equilibrium configuration. Simulated *in situ* scattering data with and without cut-off correction are shown in Fig. 4.8c.

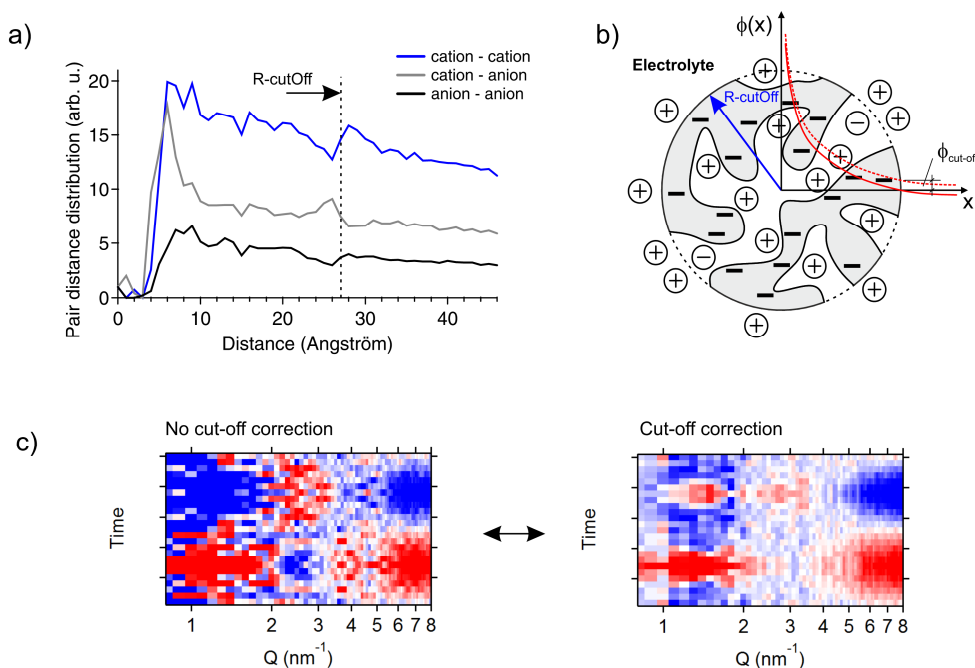


**Fig. 4.8:** (a) Radial pair distribution functions (without normalization to the mean number density of the corresponding ion) for the simulation without potential correction. The “cut-off sphere” and the coulombic potential are sketched in (b). In (c), the relative scattering intensity changes of the simulated structures for one cyclic voltammetry period without (left) and with (right) potential correction, is indicated.

## 4.5 Long range interactions

Due to the required low noise level of the simulated scattering curve for comparison with the experimental SAXS data, the simulation box needs a size of at least  $16.2 \times 16.2 \times 16.2 \text{ nm}^3$ , containing roughly 160000 electrode charges and 3600 ions. The size of the box defines the resolution in reciprocal space and the noise level in the scattering curves obtained from Fourier Transformation of the simulation box (see section 5.4).

Although “only” 3600 ions are rearranged during the simulation, for each MC step the electrode charges have to be updated. Using a cut-off of 2.7 nm and a linked-list method, the entire computational time scales roughly as  $\mathcal{O}(N_{\text{ions}} \cdot n_{\text{el}_c}^2)$  where  $N_{\text{ions}}$  is the number of ions and  $n_{\text{el}_c}$  the average number of electrode charges within the cut-off ( $n_{\text{el}_c} \approx 3000$  in the case of AC2 and 2.7 nm as cut-off). The iteration procedure to calculate the electrode charge is thereby the limiting time step ( $\mathcal{O}(n_{\text{el}_c}^2)$ ). The computational time to reproduce three *in situ* experiments with three carbons (plus averaging several simulations) takes about 300 CPU weeks (without parameter studies).

Using the Ewald summation method, again the iterative procedure to calculate electrode charges (Eq. 4.2) would be the limiting time step. For conventional Ewald summation (at least for the reciprocal contribution) the sum to calculate a single electrode charge must run over all charges within the simulation box (unit cell) and all k-vectors within the reciprocal cut-off. Again this has to be done for each electrode charge. In summary, the conventional Ewald summation and even faster methods dealing with long-range forces (particle mesh Ewald, fast multipole method, etc.) are computational extremely expensive and not suitable to calculate systems with the required size in reasonable time.

As discussed in section 2.4.1 significant errors potentially arise when using Coulomb potentials in combination with a simple cut-off. However, in the nanopore system used here, the surface (or electrode) charges (that are updated for each MC step) effectively screen the coulombic ion-ion interactions. In combination with sub-nanometer pore structures an ion within the pores is practically not able to “see” ionic or electrode charges for distances significantly larger than the actual pore size. Moreover, the pore structure defining the position of cation, anion and electrode charges is disordered but isotropic in all three dimensions. This means that at large enough distances the probability to find a positive charge (cation or positive electrode charge) is equal to the probability to find a negative charge (anion or negative electrode charge), which means that the net potential contribution is effectively zero at distances larger than

the cut-off. The cut-off therefore depends on the pore size and was chosen at distances significantly larger than the average pore size of AC1, AC2, and CDC.

To confirm this point, simulations were conducted using different cut-off radii. As shown in Fig. 4.9, the mean DoC change (Degree of confinement, see section 5.4.1) for the AC2 carbon is basically the same for all three cut-off radii (1.8 nm, 2.025 nm and 2.7 nm). In this work a cut-off radius of 3.0 nm for AC1, 2.7 nm for AC2, and 2.25 nm for CDC was used in order to minimize computational time, but accounting for similar accuracy in the potential calculation (different cut-offs because the potential is more effectively screened if the pore size becomes smaller).

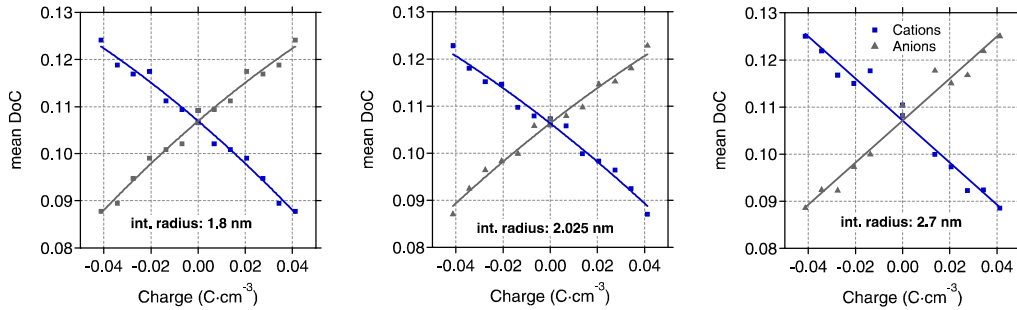


**Fig. 4.9:** Mean DoC changes as a function of the electrode charge using different cut-off radii, as indicated.

The effective screening of the coulombic potentials due to the conducting electrode forming a randomly shaped, but isotropic confinement obviously allows a simple cut-off after a certain distance. The argumentation is similar to the cut-off used for the real space term in the Ewald summation method, which is only allowed because of a (Gaussian) screening charge density (with opposite sign) around the ions (section 2.4.1). A general discussion about the applicability of cut-off based methods can be found in Ref. <sup>103</sup>.

To further cross-check the validity of the presented method, a simulation on a small simulation box (4.8 x 4.8 x 4.8 nm) using Ewald summation for both the electrode charge calculation and the potential calculation of the ions were carried out (formulas for potential and electric field see section 2.6.1).<sup>105,107</sup> Though, it is not possible to calculate meaningful scattering curves using such a small simulation box, the mean DOC values (Degree of confinement, see section 5.4.1) as a function of the electrode charge can be used as control parameter. Indeed, the change of the mean DOC was found to be equivalent to the cut-off method, as shown in Fig. 4.10 for AC2 (compare the linear fit through data points of both simulations). The absolute values are slightly shifted to lower values for the Ewald method, which is most probably a size



effect of the small simulation box. The pore structures (generated by GRFs) require periodic boundary conditions, resulting in a large scatter of pore volume fractions around the actual value for too small boxes. This has the consequence of a larger scatter of absolute DoC values, depending on the actual pore structure in the small box. Moreover, the structural correlation functions (of the pore two-phase pore structure) are certainly influenced by the required PBCs (also during the GRF based pore generations) in those small boxes. Within the range of these errors, Ewald and cut-off based simulations yield the same result.

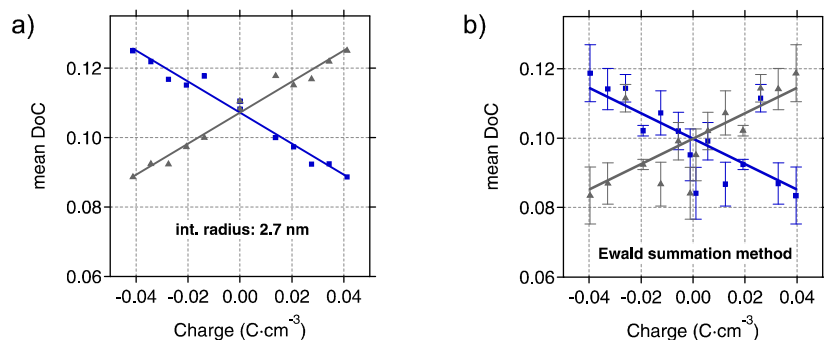


**Fig. 4.10:** Mean DoC change as a function of charge, using the cut-off method with a simulation box with a size of 16.2 x 16.2 x 16.2 nm (a), and using the Ewald summation method with a simulation box of 4.8 x 4.8 x 4.8 nm.

Considering the large box sizes needed and the high computational cost for Ewald methods, the cut-off method is probably the only possibility to deal with these problems. Two independent cross checks (1) using different cut-off radii and (2) a simulation in a small box size using Ewald summation confirm the validity of the chosen approach.



## 5 Results and Discussion

In general *in situ* scattering data of ion electrosorption in nanoporous carbons are rich on information, but complex to interpret. Knowledge about the empty carbon structure and the nanopore morphology is essential to understand ion rearrangements during charging and discharging. *Ex situ* small angle and wide angle scattering data are presented in section 5.1, including a simple analytical model to fit the scattering data from empty carbons and a strategy to generate 3D pore models on the computer. Beginning with section 5.2, results of the *in situ* SAXS experiments, during charging and discharging the *in situ* supercapacitor cell, are presented. First, it is demonstrated how the X-ray transmission signal can be used to quantify the global cation and anion flux in and out from the working electrode. In section 5.3 a simple two-phase model to describe the *in situ* SAXS data is presented. The model allows extracting information about voltage-induced ion rearrangement on a local scale. Cations were varied using three different electrolytes (CsCl, KCl, NaCl), representing a contrast variation of the cation. Yet, the proposed model fails in describing the data of other carbons than AC1 and does not give a closer insight regarding physical explanations of the local ion rearrangement. For this reason a novel data analysis approach was developed (section 5.4), where the 3D carbon pore models (section 5.1) were further used in Monte Carlo simulations to determine equilibrium ion positions in the nanopore structure. The subsequent generation of simulated scattering intensities allows a direct comparison between measured and simulated *in situ* scattering data and a quantification of ion confinement and desolvation during charging and discharging the supercapacitor. Large parts of section 5 are not original and have been published in Ref.<sup>70</sup>, Ref.<sup>109</sup> and Ref.<sup>108</sup>.

### 5.1 *Ex situ* characterization of disordered nanoporous carbons

Nanoporous carbons used in this work (AC1, AC2, CDC) differ in pore size and morphology due to the different production routes. To preserve comparability all *ex situ* characterisations are carried out on the electrodes rather than the pure carbon powders.

In the following sections (5.1.1 and 5.1.2) a more general explanation of the scattering curves for empty and electrolyte-filled microporous carbons is given, based on data of

the AC2 electrode. In sections 5.1.3 - 5.1.6 the atomic and nanopore structure of all used carbons is analyzed by means of ex-situ SAXS, X-ray diffraction and gas sorption analysis (GSA).

### 5.1.1 SAXS on empty disordered nanoporous carbons

Small angle scattering of X-rays (SAXS) or neutrons (SANS) has been widely used to describe porous carbons.<sup>38,134-138</sup> The scattering curve of the empty carbon (AC2) electrode (i.e., carbon plus binder) is given in Fig. 5.1. As shown in section 2.2, the scattering intensity can in general be split into two additive terms: one accounting for *electron-density fluctuations* on the molecular level (atomic structure factor) and another one accounting for fluctuations of a *mean electron density* on a larger length scale (SAXS intensity).<sup>27</sup> Neglecting cross-correlations between the carbon atomic structure and the nanopore structure for a typical activated carbon powder one can write:<sup>27,134,139</sup>

$$I(Q) = I_{particle}(Q) + I_{NP}(Q) + SF_C(Q) \quad (5.1)$$

At very small Q-values, a power-law term  $I_{particle}(Q) = C/Q^\alpha$  (see Fig. 5.1) accounts for the scattering contribution of the carbon powder particles (in the size range from 0.1-1  $\mu\text{m}$ ).<sup>134</sup> This term depends on the mean electron density difference between the carbon particles and the (meso- and macro-) pores surrounding these particles. In addition, also the binder adds a small, but non-negligible power-law contribution at low Q, as was verified by measurement of the binder alone. Since particularly the carbon particle surfaces are rough the exponent  $\alpha$  has typically a value smaller than four (section 2.3). At intermediate Q-values, the scattering  $I_{NP}(Q)$  from the actual nanopore structure within the carbon particles is most prominent for the empty carbon. This contribution depends on a constant factor  $I_{NP}(Q) \propto (\Delta\rho)^2$  with  $\Delta\rho$  being the electron density difference of the carbon phase and the “pore phase” (where  $\rho_{pore}$  is zero for the carbon in vacuum). The dense packing of carbon particles within the (compacted) electrode is found to induce some additional interparticular mesoporosity as compared to the loosely packed pure AC powder. This results in a slight intensity increase around 1-2  $\text{nm}^{-1}$  and a slight increase of  $I_{particle}(Q)$ . Therefore, for the carbon pore model described in the next section, the scattering data of the AC electrode is used. The scattering power of the PTFE binder is negligibly small for  $Q > 1 \text{ nm}^{-1}$ . Finally, the carbon structure factor  $SF_C(Q)$  in Eq. 5.1 can be approximated by a constant contribution ( $BG$ ) in the SAXS regime ( $Q < 8\text{nm}^{-1}$ ). Due to the breakdown of the Porod condition of sharp interfaces in sub-nanometer pores and/or density fluctuations within the carbon phase<sup>36</sup>, for the analysis presented in section 5.1.6 the

constant carbon structure factor was subtracted by using a power law fit of the form  $I(Q) = AQ^{-\beta} + BG$  in the range  $5 \text{ nm}^{-1} < Q < 8 \text{ nm}^{-1}$ .

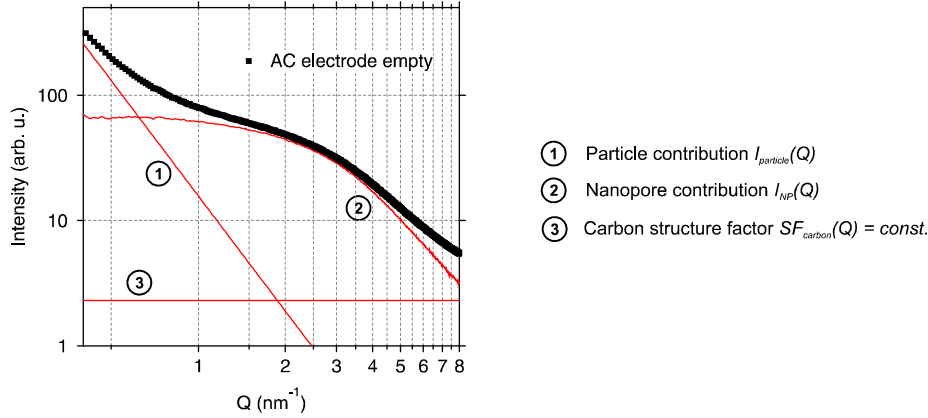


**Fig. 5.1:** The SAXS intensity vs. the scattering vector length  $Q$  is given for the carbon (AC2) electrode in vacuum. The red lines show the additive scattering contributions (as given in Eq. 5.1) obtained from power-law fits in the low  $Q$  and high  $Q$  regime as explained in section 5.1.1. Ref.<sup>108</sup> - Published by the PCCP Owner Societies.

### 5.1.2 SAXS on disordered nanoporous carbons filled with liquid

The scattering curves of the empty carbon electrode in vacuum and filled with electrolyte (no voltage applied) are given in Fig. 5.2. As explained in more detail in section 5.3, the reduced scattering contrast between the carbon phase and the electrolyte filled pores is responsible for the decreased scattering intensity in the SAXS regime of the carbon soaked with electrolyte. At larger scattering angles (WAXS regime), the structure factor of the electrolyte plays a more dominant role, leading to an increase in intensity compared to the empty electrode. In accordance with Eq. 5.1, one can write for the electrolyte filled carbon (Ref. <sup>27,134,139</sup>):

$$I(Q) = I_{particle}(Q) + I_{NP}(Q) + SF_C(Q) + SF_{el}(Q). \quad (5.2)$$

In addition to the terms occurring for the empty carbon the electrolyte structure factor  $SF_{el}(Q)$  contributes to  $I(Q)$ . During charging and discharging the supercapacitor these contributions except  $SF_C(Q)$  (neglecting deformation effects) may change their intensities as a function of the scattering vector length  $Q$  due to the redistribution of ions in the pore space at all scales. First, electrical double layer formation near the AC particle surface can effectively flatten out the rough particle surface and influence both the pre-factor  $C$  and the exponent  $\alpha$  of the particle term. The exact interpretation of these changes is complex but their contribution to the

electrical double-layer capacitance is negligibly small. Therefore this contribution is determined empirically by a power law fit for each state of charge, without assessing its physical origin in more detail.

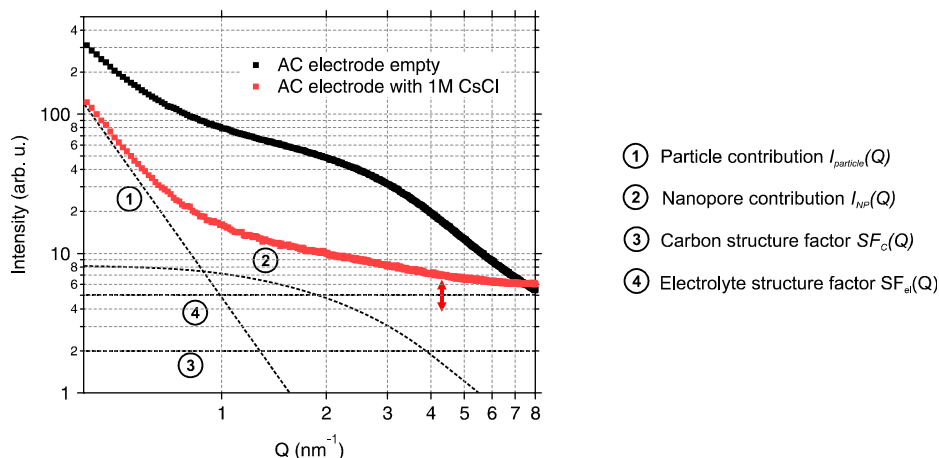


**Fig. 5.2:** The SAXS intensity vs. the scattering vector length  $Q$  is given for the carbon electrode in air and soaked with electrolyte (at zero cell voltage). The dashed lines indicate the additive scattering contributions for the electrolyte filled carbon as given in Eq. 5.2 (guide for the eye, no real data). The red arrow indicated the changes of the electrolyte structure factor contribution upon charging and discharging the supercapacitor. Except of contribution 3, all other contributions depend on the ion concentrations within the working electrode, and change upon changing the voltage. The nanopore contribution (2) can also change its shape due to local ion redistribution within the pores. Ref.<sup>108</sup> - Published by the PCCP Owner Societies.

At intermediate  $Q$ -values, the scattering  $I_{NP}(Q)$  from the actual nanopore structure within the carbon particles is most prominent for the empty carbon. For the electrolyte filled carbon, this contribution strongly decreases because  $I_{NP}(Q) \propto (\Delta\rho)^2$  with  $\Delta\rho$  being the electron density difference between the carbon phase and the electrolyte. This is only true, however, if the electrolyte within the pores can be considered as a homogeneous phase, resulting in a simple two-phase system. As shown in section 5.2 - 5.4 this contribution contains information about global ion concentration changes within all electrode pores and additional local ion rearrangement across the nanopores when applying a voltage (see section 5.3). This local structural re-arrangement can be interpreted as a preferred movement of counter-ions from the pore center towards the pore walls. Obviously, in this case the ions within the electrolyte are not randomly distributed across the pores anymore, and a simplified two-phase model for the SAXS contribution is not sufficient anymore. Although possible in principle, a full analytical multiphase SAXS approach would have to be very specific, thus lacking any generality. Therefore, another approach for the *in situ* SAXS data analysis is chosen, which is described below (section 5.3-5.4).

The additive structure factor term  $SF_{el}(Q)$  in Eq. 5.2 accounts only for correlations between individual ions and/or water molecules (corresponding to a “bulk” electrolyte). Correlations caused by the fact that the electrolyte is confined within the nanopore structure are accounted for within the contribution  $I_{NP}(Q)$ .

An important aspect regarding the interpretation of the *in situ* SAXS data is the correct treatment of the electrolyte structure factor  $SF_{el}(Q)$ , which will change upon charging and discharging of the cell. For the SAXS Q-regime, the mean electrolyte structure factor can be treated in good approximation as a constant contribution (see Fig. 5.2), with a magnitude depending on the cation and anion concentration within the irradiated electrolyte volume. Here a brief derivation of this contribution is given. The scattering cross section (being proportional to the measured intensity) of an aqueous electrolyte consisting of cations, anions, and solvent (water) molecules can be expressed by Eq. 5.3.<sup>33,34</sup>

$$SF_{el}(Q) \cdot V/b_e^2 = \sum_{\alpha} \phi_{\alpha} f_{\alpha}^2 + \sum_{\alpha} \sum_{\beta \geq \alpha} (2 - \delta_{\alpha\beta}) \phi_{\alpha} \phi_{\beta} f_{\alpha} f_{\beta} [S_{\alpha\beta} - 1] \quad (5.3)$$

$S_{\alpha\beta}$  represent the partial structure factors (section 2.2) which cover the cross-correlations of species  $\alpha$  with species  $\beta$ .  $f$  and  $\phi$  are the atomic/molecular formfactors and the number fractions, respectively, and  $\delta_{\alpha\beta}$  is the Kronecker delta ( $\delta_{\alpha\beta} = 0$  for  $\alpha \neq \beta$ ;  $\delta_{\alpha\alpha} = 1$ ). At small Q-values the atomic/molecular form factors can be replaced by the respective electron numbers per atom/molecule  $n$  (effective electron numbers, see section 5.3). For a random distribution of the ions within the solvent, the ion-ion partial structure factors can be set to 1. Although a 1 M solution is not dilute, the ratio between the number of water molecule per cation/anion is high enough to make the following additional approximations:  $\phi_{H_2O} \cong 1$ ,  $1 - \phi_{an} \cong 1$ ,  $1 - \phi_{cat} \cong 1$ ,  $1 - \phi_{H_2O} \cong \phi_{cat} + \phi_{an}$  and  $\phi_{cat}\phi_{an} \cong 0$ . With this, Eq. 5.3 simplifies to:

$$SF_{el}(Q) \cdot V/b_e^2 \cong \phi_{cat} [(n_{cat} - n_{H_2O})^2 + 2n_{cat}n_{H_2O}S_{catH_2O}] \\ + \phi_{an} [(n_{an} - n_{H_2O})^2 + 2n_{an}n_{H_2O}S_{anH_2O}] + n_{H_2O}^2 S_{H_2OH_2O} \quad (5.4)$$

The last term corresponds to the structure factor of water, the other terms depend on the cation and anion concentrations. Changes of the water-water correlation ( $S_{H_2OH_2O}$ ) and water-ion correlations ( $S_{catH_2O}$ ,  $S_{anH_2O}$ ) are assumed to be small in the SAXS regime. Moreover, it is also reasonable that the partial structure factors within the SAXS regime are much smaller than 1. Hence, Eq. 5.4 can be further simplified to:

$$SF_{el}(Q) \cdot V/b_e^2 \cong \phi_{cat}(n_{cat} - n_{H_2O})^2 + \phi_{an}(n_{an} - n_{H_2O})^2 + n_{H_2O}^2 S_{H_2O H_2O} \quad (5.5)$$

The approximation in Eq. 5.5 describes the diffuse scattering contribution of dilute, non-correlated ions within a water matrix (similar to the so-called Laue scattering in solid solutions)<sup>139</sup> and the water structure factor. Since both, cation and anion concentration are changing during charging or discharging the supercapacitor, the electrolyte structure factor  $SF_{el}(Q)$  in the SAXS regime is changing as well during the *in situ* experiment (indicated by the red arrow in Fig. 5.2). Although ion-ion correlations might change this behavior for very high concentrations, in the case of the 1M electrolyte no distinct peak formation was observed during the *in situ* experiment, justifying the assumptions experimentally.

The carbon structure factor  $SF_C(Q)$  is not expected to depend on ion concentration and thus, gives just a constant baseline contribution as discussed earlier. Yet, this approximation may break down for strong structural changes in the carbon, for instance due to electrosorption induced swelling.<sup>73</sup>

### 5.1.3 Absolute SAXS measurements on disordered nanoporous carbons

*Ex situ* SAXS measurements of the carbon electrodes calibrated against absolute scattering units<sup>119</sup> ( $\text{cm}^{-1}$ ) were carried out to estimate the carbon skeleton densities. Measurements of the carbon electrode filled with distilled water and a 1M CsCl aqueous solution should indicate whether pores of different size are entirely filled or not (open vs. closed porosity). To further crosscheck the quality of the estimated numbers a fourth micro- and mesoporous carbon was measured (called BP2000); that is a carbon black with significant microporosity due to an additional activation step.

In order to calibrate the scattering intensity to absolute units distilled water is used as a calibration standard.<sup>119</sup> The time and thickness normalized, background and transmission corrected, scattering intensity is shown in Fig. 5.3 (black curve) and has a constant value of  $\approx 2.1 \cdot 10^{-3}$  throughout the SAXS Q-regime. The theoretical scattering cross section of water at small Q is  $d\Sigma/d\Omega = \rho^2 kT \chi_T$ , with  $\rho^2$  being the squared scattering length density of water and  $\chi_T$  as the isothermal compressibility. At 301.15 K the scattering cross section is  $0.016881919 \text{ cm}^{-1}$ . The ratio between theoretical cross section and measured water scattering intensity (in arbitrary units) is then used as calibration factor for all SAXS measurements (background and transmission corrected, time and thickness normalized).



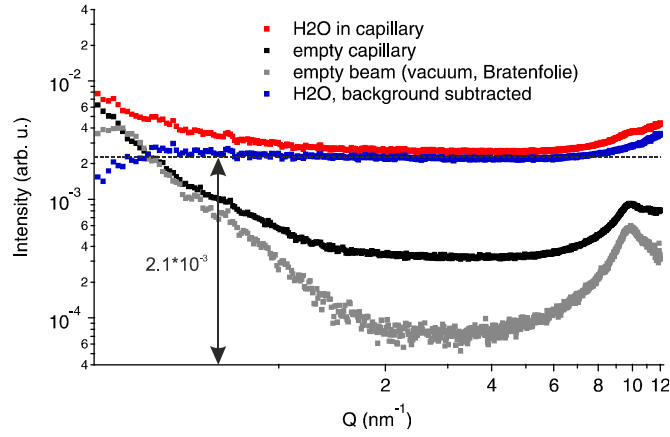


**Fig. 5.3:** SAXS intensity as a function scattering vector length  $Q$  for  $H_2O$  in a capillary, for the empty beam, the empty capillary and the corrected  $H_2O$  signal.

Absolute SAXS intensities of four different carbon electrodes empty, filled with water and filled with a 1M CsCl electrolyte are shown in Fig. 5.4. The measured scattering curves are fitted by the following analytical model (black curves in Fig. 5.4)<sup>134</sup>

$$I_{fit}(Q) = \frac{P}{Q^4} + \frac{8\pi\langle\eta^2\rangle a^3}{(1 + Q^2 a^2)^2} + BG, \quad (5.6)$$

where  $P$ ,  $\langle\eta^2\rangle$ ,  $a$  and  $BG$  are the parameters determined from the model fit. The second term in Eq. 5.6 corresponds to the DAB-model (see section 2.3.1) and describes the nanopore scattering contribution approximated by an exponentially decaying correlation function. The unconventional representation of  $1/\text{cm}$  for the scattering vector length  $Q$  was chosen to obtain the fit parameters already in the correct unit.

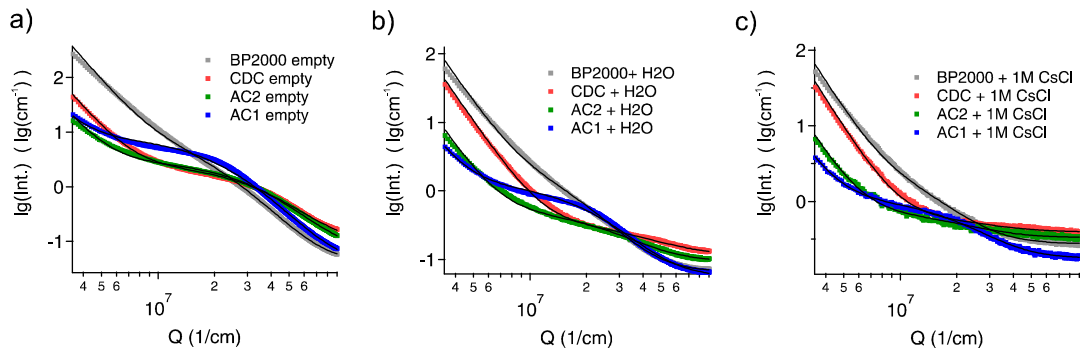


**Fig. 5.4:** Logarithm of the absolute scattering intensity as a function of the scattering vector length  $Q$  in units of  $\text{cm}^{-1}$  for the empty carbon electrodes (a), the electrodes filled with water (b) and the electrodes filled with a 1M CsCl aqueous electrolyte (c). The model fits are indicated as black lines.

All fit parameters obtained from the fits shown in Fig. 5.4 are listed in Table 5.1a-c.

**Table 5.1a:** Fit parameters of empty carbon electrodes

	P	$\langle \eta^2 \rangle$	a	BG
BP2000	5.46E+28	2.49E+21	4.85E-08	0.0407748
CDC	7.13E+27	6.47E+21	2.41E-08	0.0902292
AC2	2.62E+27	6.09E+21	2.63E-08	0.0639236
AC1	1.86E+27	4.35E+21	4.14E-08	0.0367044

**Table 5.1b:** Fit parameters of carbon electrodes filled with water

	P	$\langle \eta^2 \rangle$	a	BG
BP2000	1.20E+28	5.82E+20	5.08E-08	0.0659828
CDC	6.43E+27	1.29E+21	1.90E-08	0.116533
AC2	1.13E+27	6.89E+20	2.84E-08	0.0941914
AC1	4.99E+26	8.06E+20	3.87E-08	0.0559896

**Table 5.1c:** Fit parameters of empty carbon electrodes filled with 1M CsCl.

	P	$\langle \eta^2 \rangle$	a	BG
BP2000	9.68E+27	4.58E+20	5.54E-08	0.276145
CDC	5.79E+27	5.59E+20	2.50E-08	0.391588
AC2	1.05E+27	3.72E+20	3.41E-08	0.332733
AC1	4.42E+26	6.55E+20	3.77E-08	0.175969

As introduced in section 2.3.1 the parameter  $\langle \eta^2 \rangle$  is equal to  $\varphi(1 - \varphi)(\Delta\rho)^2$ , resulting in carbon skeleton densities as listed in Table 5.2 (first line).

**Table 5.2:** Skeleton densities obtained from the model fits (first line), and the ratio between empty and water filled carbon electrodes (second and third line).

	BP2000	CDC	AC2	AC1
Skeleton density (g/cm <sup>3</sup> )	2.2	1.9	1.9	1.6
$\Delta I_{empty}/I_{H2O}$	4.4	8.1	8.0	6.1
Skeleton density alt. (g/cm <sup>3</sup> )	2.2	1.54	1.55	1.7

The porosities are estimated from the specific micropore volume obtained from gas sorption measurements (section 3.1, Table 3.1). The error induced by closed porosity, which is detected by SAXS but not by gas sorption analysis, is believed to be small in the carbons used here.<sup>80</sup> The cross-calibration of the SAXS data might contain additional sources of error, like temperature fluctuations, uncertainties in background

subtraction, transmission correction or thickness normalization. Errors from data corrections are particular critical for thin capillaries as used here. However, the obtained skeleton density values seem realistic. The carbon black BP2000 has a density close to the graphite density. AC2 and CDC have a lower skeleton density, consistent with Helium pycnometry data and literature values of microporous carbons.<sup>80,136</sup> whereas the value of AC1 seems rather low. Surface functional groups (oxygen) are known to be responsible for the excellent wetting properties of AC1 which might be responsible for the affinity of water molecules to remain within the pores. Hence, some rest of water might be present in the micropores of AC1 during the *ex situ* SAXS measurement, causing the lowered electron density difference.

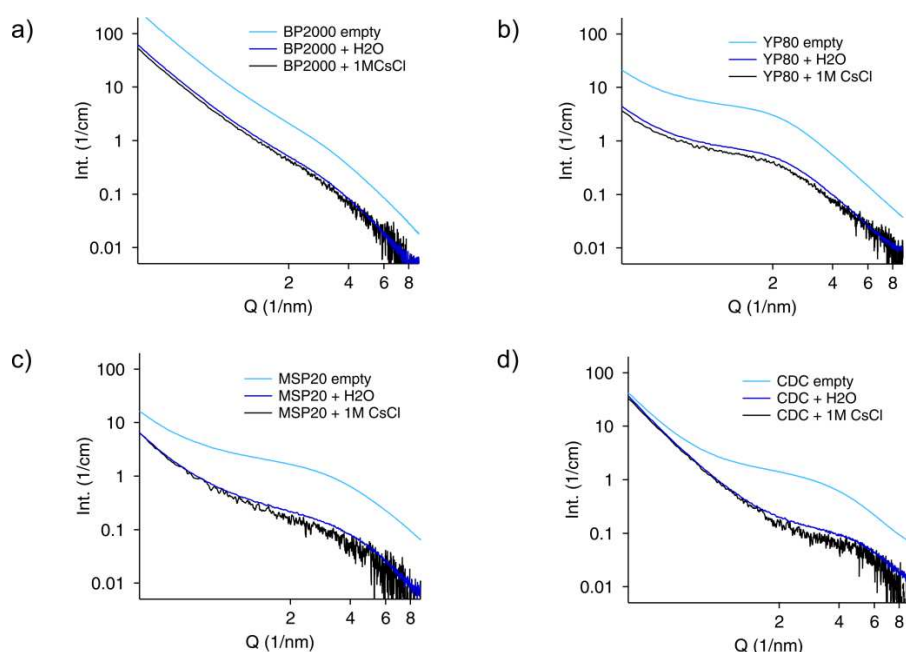


**Fig. 5.5:** (a-d), Scattering intensities in absolute scattering units of  $\text{cm}^{-1}$  as a function of the scattering vector length  $Q$  for all carbons (empty, filled with water, filled with electrolyte), where the background BG obtained from the model fit of Eq. 5.6 was subtracted from all curves.

Subtracting the constant background BG obtained from the fit results in scattering curves as shown in Fig. 5.5. Apart from the CDC electrode the infiltration with water and electrolyte seem to lower the intensity by a constant factor. This indicates complete wetting and a small (negligible) amount of closed porosity, consistent with literature.<sup>80</sup> Deviations from this behavior, as observed for CDC, could be caused by a breakdown of the ideal two-phase behavior, the incorrect assumption of a constant background BG or incomplete wetting. Since the background is particular high for CDC (see Fig. 5.4, right) errors in the data correction or inaccuracies of the analytical

model function have a big impact. Nevertheless, in the light of the small average pore size of all nano- and sub-nanoporous carbons used here, the two-phase model works surprisingly well. The ratio between empty and water filled carbon intensities at intermediate Q-regimes can give a further estimate of the carbon skeleton density, assuming a bulk water density of  $1.0 \text{ g/cm}^3$ . This ratio is equal to the ratio of the squared electron density contrast. Values obtained from the SAXS intensities shown in Fig. 5.5 are given in Table 5.2 (second, third line).

Again there are multiple sources of error, like incomplete wetting, breakdown of the two-phase model or densified water in the sub-nanometer confinement. From both estimations it becomes evident, that the carbon skeleton density in the largely microporous carbons CDC, AC2 and AC1 is significantly lower than the graphite density.

#### 5.1.4 X-ray diffraction

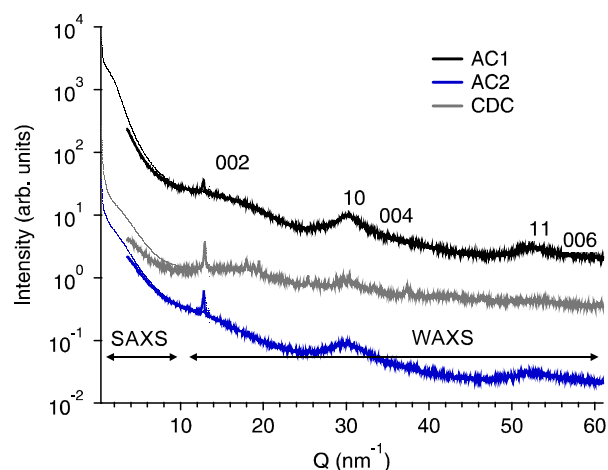


**Fig. 5.6:** X-ray diffraction profile (scattering intensity vs. scattering vector length  $Q$ ) for the AC1, AC2 and CDC electrode (10 % PFTE binder). At small  $Q$  ex-situ SAXS data is plotted as thin data points. Intensities are shifted in y-direction for better visualization.

The X-ray diffraction profile of the AC1, AC2 and CDC electrode reveal a rather disordered atomic structure in all three carbons (Fig. 5.6). For both AC1 and AC2 the out-of-plane (002) peak is relatively weak, where the in plane (10) peak is more distinct. Relatively high in-plane and low out-of-plane order suggests a structure with extended graphene-like sheets which are randomly bended to form a disordered, interconnected pore structure (see e.g. Fig. 2.14 in section 2.5.1). CDC shows a relatively low in-plane ordering (10 peak), suggesting generally a strong disorder with randomly shaped pores. A sharp peak around  $12.5 \text{ nm}^{-1}$  is present in XRD profiles of

all carbon electrodes and origins from the PTFE binder. Additional sharp peaks observed for the CDC electrode are caused by the sample holder (glas).

### 5.1.5 Generating a 3D model of the pore structure

Absolute ex-situ SAXS measurements of the empty carbon electrode can be used to derive a three-dimensional model of the real space pore structure. In the following, a comprehensive theoretical description of the carbon pore model generation is presented and visualized using the experimental data of the empty AC2 electrode. The primary SAXS data treatment of the ex-situ SAXS curves shown in this section is described in section 5.1.1.

A three-dimensional scalar field, known as Gaussian random field (GRF) is generated using the following expression (vectorial quantities are given in bold):<sup>140-143</sup>

$$y(\mathbf{x}) = \sqrt{\frac{2}{N}} \sum_{i=1}^N \cos(\mathbf{k}_i \cdot \mathbf{x} - \varphi_i) \quad (5.7)$$

Here each spatial coordinate  $\mathbf{x}$  is assigned to a GRF value  $y(\mathbf{x})$  (Fig. 5.7a) and the phase factors  $\varphi_i$  are randomly distributed between 0 and  $2\pi$ . The values  $y(\mathbf{x})$  are Gaussian distributed as shown in Fig. 5.7c. The two-point correlation function of the GRF<sup>141</sup>

$$g(r) = \langle y(\mathbf{x} + \mathbf{r})y(\mathbf{x}) \rangle, \quad (5.8)$$

is used to calculate the probability function  $P(k)$

$$P(k) = \frac{2}{\pi} k \int_0^{\infty} r g(r) \sin(kr) dr. \quad (5.9)$$

The vectors  $\mathbf{k}_i$  in Eq. 5.7 are now isotropically distributed with a magnitude given by Eq. 5.9. A suitable two-point correlation function containing statistical information about size and morphology of the actual pore structure for the AC pore structure is

$$g(r) = \frac{1}{\cosh(r/\xi)} \cdot \frac{\sin(2\pi r/d)}{(2\pi r/d)} \quad (5.10)$$

where  $\xi$  is a correlation parameter related to the mean size of the pores and  $d$  a parameter accounting for ordering effects in-between pores, that is, the ‘‘damping’’

term in Eq. 5.10 is related to the mean pore size and the “oscillation” term to the pore arrangement. Inserting Eq. 5.10 into Eq. 5.9 results in the following analytic function:

$$P(k) = \frac{k}{\pi} \xi d \frac{\sinh(\pi k \xi / 2) \sinh(\pi^2 \xi / d)}{\cosh(\pi k \xi) + \cosh(2\pi^2 \xi / d)}. \quad (5.11)$$

The vectors  $\mathbf{k}_i$  are generated by a Monte Carlo based approach using the function  $P(k)$ . After a certain k-vector is produced, a random number between 0 and 1 is generated. A k-vector magnitude is accepted if the random number is smaller than the normalized probability function  $P(k)/P_{max}$  at this point. The resulting distribution of the k-vector magnitudes is shown in Fig. 5.7c.

Because the generated pore structures are used in a subsequent Monte-Carlo simulation (Section 5.4) periodic boundary conditions are implemented by allowing only a specific set of  $\mathbf{k}_i$  vectors fulfilling

$$\mathbf{k}_i = \sum_{k=1}^3 \frac{2\pi n_k^i}{L} \mathbf{j}_k \quad \text{with } n_k^i \in N \quad \langle \mathbf{j}_l \cdot \mathbf{j}_k \rangle = \delta_{l,k}, \quad (5.12)$$

and  $L$  being the box-size of the resulting pore structure. To produce a pore structure made up from two phases (carbon matrix and pore) threshold values  $\alpha$  and  $\beta$  are defined in the continuous GRF histogram (Fig. 5.7b), assigning each  $y(x)$  values to pore or carbon matrix. The cut-off levels are indicated by the black arrows in Fig. 5.7b, resulting in a pore structure as shown in Fig. 5.7a. The two threshold values are related to the porosity  $\phi_1$  via:

$$\phi_1 = \frac{1}{\sqrt{2\pi}} \int_{-\infty}^{\beta} \exp\left(-\frac{t^2}{2}\right) dt - \frac{1}{\sqrt{2\pi}} \int_{-\infty}^{\alpha} \exp\left(-\frac{t^2}{2}\right) dt. \quad (5.13)$$

Thus, the area under the curve of Fig. 5.7b within  $\alpha$  and  $\beta$  represents the porosity  $\phi_1$ . In order to generate a scattering curve from the two-phase pore structure a so-called two-point probability function  $P_{11}(r)$  is necessary.<sup>140,144</sup>

$$P_{11}(r) = \frac{1}{2\pi} \int_0^{g(r)} \frac{1}{\sqrt{1-t^2}} \left[ \exp\left(-\frac{\alpha^2}{1+t}\right) - 2\exp\left(-\frac{\alpha^2 - 2\alpha\beta t + \beta^2}{2(1-t^2)}\right) + \exp\left(-\frac{\beta^2}{1+t}\right) \right] dt + \phi_1^2 \quad (5.14)$$

As a final step, a realistic three-dimensional pore structure with an interconnected matrix phase is produced by intersecting two independently generated GRF pore structures after the thresholding procedure just described. This intersecting-approach promotes a highly interconnected carbon phase and avoids “free floating” pieces of carbon and closed porosity to a large extend. The pore volume fraction and the two-point probability function of the final, intersected pore structure (upper index I) are then defined as:<sup>141</sup>

$$\phi_1^I = (\phi_1)^2, P_{11}^I(r) = [P_{11}(r)]^2 \quad (5.15)$$

The correlation function  $\gamma(r) = P_{11}^I(r) - \phi_1^{I2}$  is now used to calculate the model scattering curve from the nanoporous carbon:

$$I_{NP}^{GRF}(Q) = (\Delta\rho \cdot b_e)^2 \int_0^\infty \gamma(r) \frac{\sin(Qr)}{Qr} 4\pi r^2 dr \quad (5.16)$$

$I_{NP}^{GRF}(Q)$  is the absolute scattering intensity (scattering cross section) in units of  $\text{cm}^{-1}$  and is fitted to the measured intensity  $I_{NP}(Q)$  (Eq. 5.1) of the empty carbon, using  $\xi$ ,  $d$  and the threshold value  $\beta$  as fitting parameters ( $\alpha$  is related to  $\beta$  via Eq. 5.13 and the pore volume fraction  $\phi_1^I$  is used as input from gas sorption measurements). Closed porosity is usually rather small in highly activated carbons<sup>80</sup> and its influence is neglected here. Eq. 5.16 gives excellent fits to the measured SAXS data, as shown in Fig. 5.7d. The slope at small Q-values  $I_{particle}(Q)$  corresponds to the additive power-law term as described above. This term was evaluated from an independent fit at smallest possible Q-values and added to  $I_{NP}^{GRF}(Q)$  for the fit in Fig. 5.7d. The scattering length density  $\Delta\rho \cdot b_e$  is determined from absolute SAXS measurements of the carbon in vacuum plus the carbon soaked with water (section 5.1.3). The resulting real space structure for the AC is shown in Fig. 5.7 as a three-dimensional visualization (Fig. 5.7e) and 2D cross section (Fig. 5.7f).

The squared amplitude of the discrete Fourier Transformation (FFT) of the real space pore structure reads as

$$|\hat{\rho}_{k,l,m}|^2 = \left| \sum_{n=0}^{N-1} \sum_{o=0}^{O-1} \sum_{p=0}^{P-1} \rho_{n,o,p} \cdot e^{-2\pi i \frac{nk}{N}} \cdot e^{-2\pi i \frac{ol}{O}} \cdot e^{-2\pi i \frac{pm}{P}} \right|^2. \quad (5.17)$$

$\rho_{n,o,p}$  represents the real space electron density of the voxel  $n, o, p$  ( $n, o, p$  representing coordinates in  $x, y, z$  direction of the simulation box) and  $\hat{\rho}_{k,l,m}$  are three-dimensional Fourier coefficients in reciprocal space. The spherical average of the

squared amplitude of the FFT of the pore structure weighted by the carbon (and pore) electron densities yields again the original scattering curve (Fig. 5.7d, blue curve). This confirms the suitability of the statistical description of the real space structure, derived from an *ex situ* SAXS measurement of the empty carbon electrode material. Though, the model fit to the measured and rather featureless SAXS curve is certainly not unique. Alternative correlation functions than the one in Eq. 5.10 might lead to a similar fit accuracy. Therefore, some additional knowledge about the carbon pore morphology (e.g., from HRTEM, XRD, or Raman scattering) is important to choose the most realistic correlation function. Also the XRD pattern (section 5.1.4) indicate a highly disordered structure typical for activated carbons. Thus, our approach of an isotropic pore model as described by the correlation function Eq. 5.10 is justified. As will be shown below (section 5.4), the pore model can be further used for a detailed analysis of the *in situ* SAXS data. For this use the typical size and shape features of the structure must be reproduced correctly only in a statistical sense, which is the case for the chosen system.

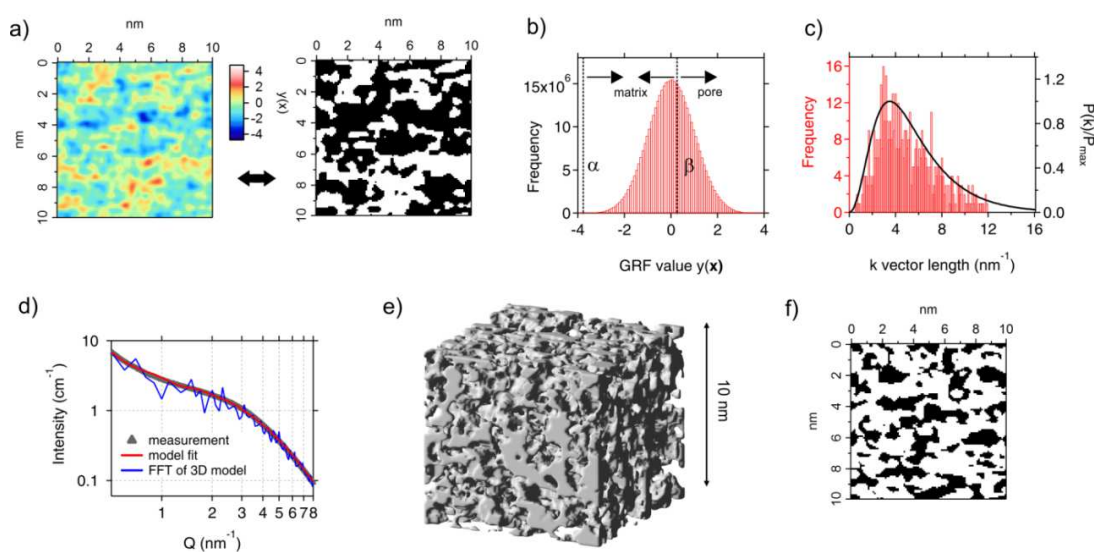


**Fig. 5.7:** a) 2D section of a 3D Gaussian Random Field (GRF) and the resulting two-phase pore structure (right). b) Histogram of the GRF values  $y(\mathbf{x})$ . c) Distribution of the  $k$ -vector magnitude of the GRF (analytical  $P(k)$  function in black, MC generated values in red). d) measured SAXS intensity of the AC (grey), GRF model fit using Eq. 5.16 (red), and re-calculated scattering curve of the finite real space structure using FFT (e) (blue). In e) and f) the intersected pore structure resulting from two independent GRF's is visualized in 3D and as a 2D cross section. Ref.<sup>108</sup> - Published by the PCCP Owner Societies.

### 3.3 Pore characteristics

To investigate pore size distributions of the microporous carbon, nitrogen and carbon-dioxide sorption measurements were performed and evaluated on the AC electrode as



described in section 5.1.5. The NLDFT kernel suffers from idealization assumptions (infinitely flat, homogenous carbon) which results in sharp maxima in the pore size distributions.<sup>145</sup> Nevertheless, CO<sub>2</sub> adsorption is the most favorable method for the determination of pores below 1 nm.<sup>146,147</sup> In agreement with literature,<sup>58</sup> the calculated PSD was incremented by a linear approximation of the calculated pore volume (CO<sub>2</sub>-sorption derived PSD was used up to a pore size of 0.9 nm and PSD derived from N<sub>2</sub>-sorption for pores larger than 0.9 nm). Since the SSA and pore volume obtained from CO<sub>2</sub> sorption was higher than the one calculated from nitrogen sorption at the intercept-spot 0.9 nm, the corresponding offset was added to the nitrogen sorption derived PSD.<sup>58,148</sup> This procedure resulted in an average pore size of 0.9 nm and a specific surface area of 1707 m<sup>2</sup> · g<sup>-1</sup> for AC2. The cumulated and specific pore volume obtained from gas sorption are given in Fig. 5.8 as a function of the pore size assuming slit pores.

Gas sorption derived PSDs from nanoporous carbons are widely used in the current literature. Their calculation with given DFT-kernels<sup>149</sup>, however, requires a-priori knowledge of a defined pore shape. When considering the disordered and randomly shaped 3D pore structure from the GRF in Fig. 5.7, the definition of a unique pore shape is difficult and that it is not intuitive why to assume for instance ideal slit pores to describe this structure. In general, if the pore shape is unknown, either more generic distributions like the autocorrelation function<sup>32</sup>, chord-length distributions<sup>136</sup> or size distributions with alternative ways of defining pore sizes<sup>150</sup> can be derived from X-ray scattering data.

Alternatively, a specific pore size characteristic of the AC electrode can be obtained using the 3D pore structure derived from the GRF methodology (Fig. 5.8a-b). The slit pore model used for the calculation of the PSD from the sorption isotherm assumes one-dimensional confinement (in contrast to cylindrical model with a two-dimensional confinement). A PSD assuming no specific pore shape can be derived from the 3D GRF data by the following algorithm (see Fig. 5.8c). First, the carbon surface is triangulated and the normal vector is calculated in the center of each triangle. The surface elements are chosen to have a mean size of 0.01 nm<sup>2</sup> and the normal vector  $\mathbf{n}$  points towards the inside of the pore. Along this direction, the distance to the next opposing carbon surface is measured. Doing this for all surface elements, a histogram ( $df/dD$ ) can be calculated where each measured distance is weighted by the surface area of the corresponding triangle. The cumulated distance distribution is then approximated by integrating the histogram  $df/dD$ .

As shown in Fig. 5.8b, the PSD obtained from GSA is quite well reproduced by this histogram. The mean pore size, being defined as the size where 50% of the maximum value of the cumulative PSD is reached, is very similar for both approaches (0.91 nm

for GSA as indicated in Fig. 5.8a vs. 0.87 nm for SAXS). The size distribution is somewhat broader in the curves derived from GRFs (see cumulative plot Fig. 5.8a), but this deviation is acceptable considering the generic differences of the two approaches. The PSDs derived from *ex situ* SAXS measurements as described here represent a new possibility to cross-verify outcomes and to test the limits of GSA results on micro- and sub-microporous carbons.

The small fraction of pores with a size of 0.3-0.4 nm as indicated by the PSD derived from SAXS should probably not be labeled as “pores”. Those small normal distances naturally occur within the random two-phase pore model, and must relate to the details of the SAXS curves at large  $Q$  already discussed earlier (e.g., density fluctuations). This should not be confused with any real pores physically accessible to ions or molecules.

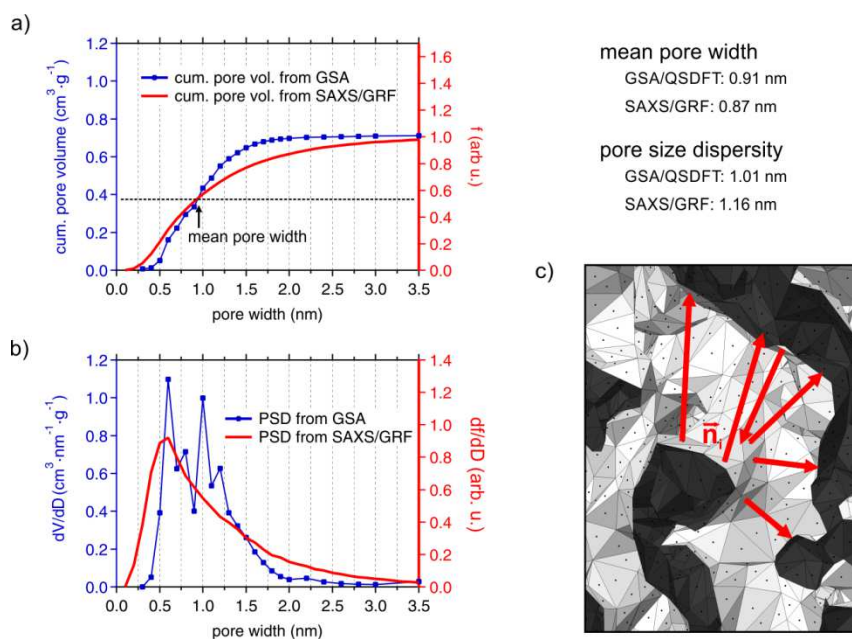


**Fig. 5.8:** (a) and (b) show the cumulative pore volume, and the differential pore size distribution (PSD) of the electrode AC2 obtained from gas sorption analysis (GSA) and SAXS measurements (using the concept of Gaussian random fields). The black arrow in (a) indicates the mean pore width of the GSA/QSDFT approach. Red arrows in the three-dimensional sub-section of the pore structure (c) indicate the normal distances from some surface elements to the opposing pore wall. Counting these distances and classifying them in a histogram represents a reasonable approximation to the PSD obtained from GSA. Ref.<sup>108</sup> - Published by the PCCP Owner Societies.

Scattering curves and the resulting pore models for all three carbons are given in Fig. 5.9. The carbons differ mainly in the average pore size and pore volume fractions. Since the same correlation function (Eq. 5.10) was used for the generation of all three

carbon models the shape or morphology of pores are comparable. The model fit and the scattering curve obtained from the Fourier transformation of the real space structure reproduces the measured scattering curves sufficiently well.

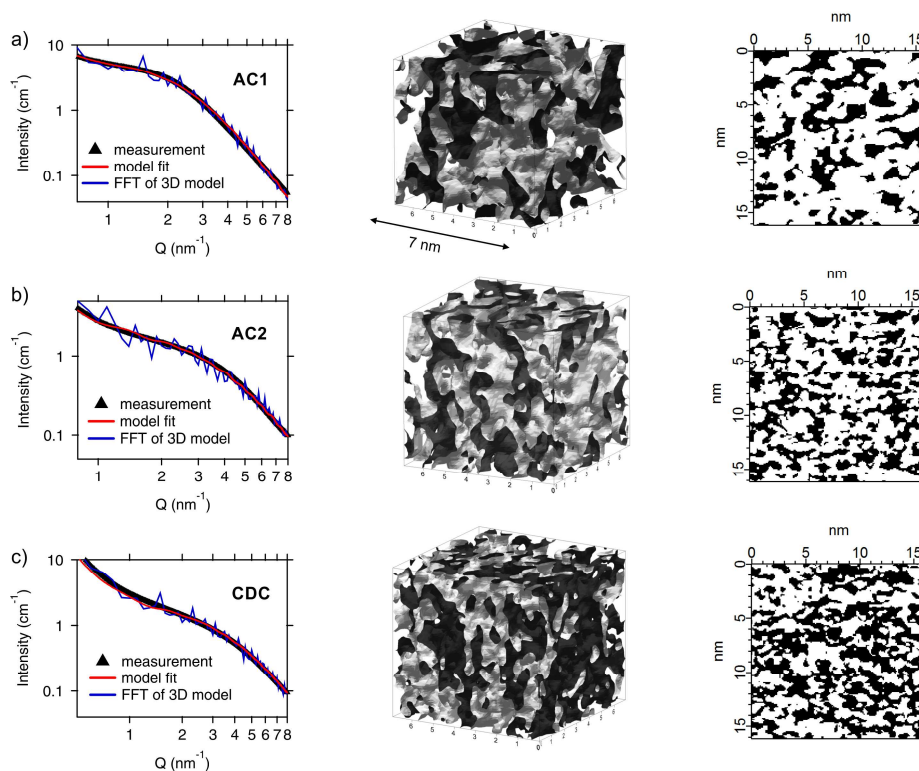


**Fig. 5.9:** Measured SAXS intensities (black data points) as a function of the scattering vector length  $Q$  are given for AC1 (a), AC2 (b) and CDC (c). Analytical fits (red) yield statistical parameters serving as input to produce 3D pore structures using the concept of Gaussian random fields (GRFs). 3D visualizations ( $7 \times 7 \times 7 \text{ nm}^3$ ) and cross sections ( $16.2 \times 16.2 \text{ nm}^2$ ) are given in the centre column and right column, respectively. Blue curves in the left column represent the spherical averaged amplitude square of the discrete Fourier Transformation (FFT) of the real space pore structures.

The pore size distribution obtained from the SAXS/GRF approach reproduce the PSDs obtained from  $\text{N}_2$  and  $\text{CO}_2$  gas sorption reasonably well for all three carbons (Fig. 5.10). Indeed, the PSDs obtained from SAXS seem to have in general a broader size distribution, where the average pore size is comparable. A reason for that could be the different ways of defining the size of a pore. The SAXS PSDs correspond to histograms of normal distances, whereas for the PSDs obtained from gas sorption the relative vapour pressure in the sorption isotherms is related to the width of a slit-like pore.

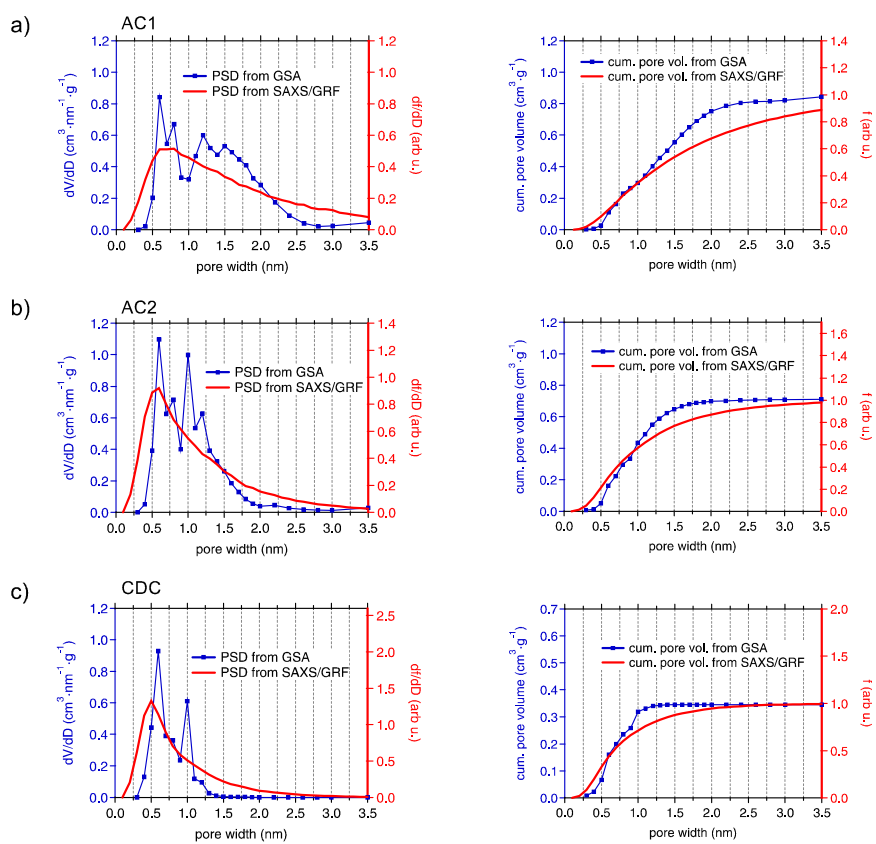


**Fig. 5.10:** Differential (left) and cumulative (right) pore size distribution obtained from gas sorption analysis (blue curves) and small angle scattering (red curves) for AC1 (a), AC2 (b) and CDC (c).

## 5.2 *In situ* X-ray transmission to quantify global ion concentration

In the following the X-ray transmission (XRT) signal is used in combination with the electric current signal (Fig. 5.11) to calculate the global cation and anion flux in and out of the WE as a function of the electrode charge. The procedure is described with data from a cell using AC2 as working electrode and a 1M CsCl electrolyte. As shown in Fig. 5.11a the cell shows mainly electrical double-layer capacitance with minor faradaic contributions. Large parts in section 5.2 are not original and have been published in Ref.<sup>108</sup>.

The transmission  $\tau$  of the X-ray beam through the working electrode is determined by the photoelectric absorption of the X-rays by all atomic species in the sample. According to the Lambert-Beer law, the X-ray intensity  $I(d)$  decays exponentially within the penetrated material:

$$\tau_{c+el} = \frac{I(d)}{I_0} = \prod_i e^{-\mu_i d_i} = e^{-\left[\sum_i w_i \left(\frac{\mu}{\rho}\right)_i\right]_{el} \rho_{el} d_{el}} * e^{-\left(\frac{\mu}{\rho}\right)_c \rho_c d_c}, \quad (5.18)$$

where  $d_i$  corresponds to the thickness,  $\rho_i$  to the mass densities,  $\mu_i$  to the linear X-ray attenuation coefficients and  $\left(\frac{\mu}{\rho}\right)_i$  to the mass attenuation coefficients of the different species. The mass attenuation coefficient of the electrolyte is the sum of all species, weighted by their mass fraction  $w_i$ . Since the contribution of the carbon material (index C) is constant during voltage cycling, its logarithm is subtracted from the logarithm of the experimental transmission value. Then, the logarithm of the electrolyte transmission contribution  $\tau_{el}$  reads:

$$-\ln(\tau_{el}) = \mu_{el} d_{el} = \left[ c_{cat} M_{cat} \left(\frac{\mu}{\rho}\right)_{cat} + c_{an} M_{an} \left(\frac{\mu}{\rho}\right)_{an} + \rho_{H2O} \left(\frac{\mu}{\rho}\right)_{H2O} \right] d_{el}, \quad (5.19)$$

where  $c_i$  correspond to the ion concentration in mol/l,  $M_i$  is the molar mass and  $\rho_{H2O}$  is the mass density of water. Thus, the change in electrolyte transmission is the sum of cation and anion concentration changes weighted by their respective X-ray mass attenuation coefficients<sup>25</sup> (see Fig. 5.11b). The changes in water contribution are negligible for the ions used in this work.

In order to discriminate between cation and anion concentration changes, additional information is needed. Since the WE volume is significantly smaller than the CE volume the current signal integrated over time gives essentially the accumulated charge on the WE as a function of time (see Fig. 5.11b). The electroadsorbed charge  $N_Q$

(in units of mol of elementary charges per  $\text{cm}^3$ ) on the other hand is given by the difference between cation  $c_{cat}$  and anion concentration  $c_{an}$ .

$$N_Q(t) = \frac{1}{V_{el} \cdot |q_e| \cdot N_A} \int i(t) dt = -(c_{cat} - c_{an}) \quad (5.20)$$

Combining Eq. 5.19 and Eq. 5.20, the two unknown ion concentrations can be obtained. Note that a certain amount of bulk electrolyte (i.e., electrolyte volume which is not confined in nanopores) within the irradiated volume is always present (in macropores and possibly on top of the WE as a thin wetting film). The thickness of this film may vary from cell to cell due to different electrode wetting properties. This unknown contribution is accounted for by normalizing the integrated current signal  $\int i(t) dt$  by an effective electrolyte volume  $V_{el}$ , which was calculated from the absolute transmission value at 0 V. Assuming a 1 M concentration of cations and anions within all pores and the possible electrolyte film on top of the WE, the electrolyte thickness  $d_{el}$  and subsequently the electrolyte volume can be calculated using Eq. 5.19. The actual, calculated electrolyte thickness is therefore used as a correction factor for the theoretical pore volume to obtain  $V_{el}$ . This also means that the absolute ion concentration changes shown in Fig. 5.11c correspond to concentration changes within the entire electrolyte volume and not only within the micropores.

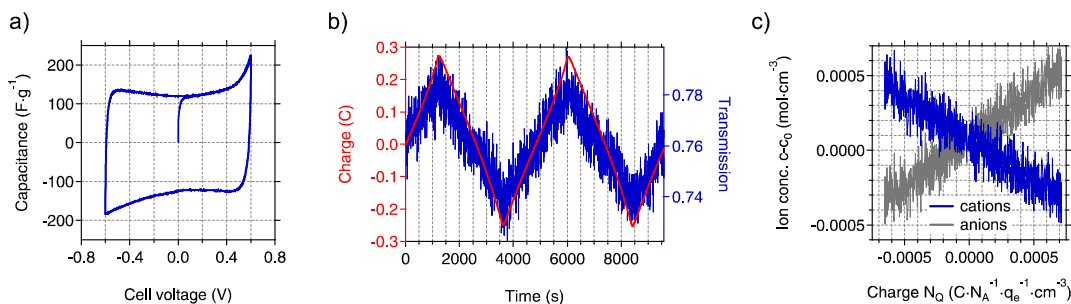


**Fig. 5.11:** a) Cyclic voltammogram (CV) of the AC2 electrode in 1 M CsCl with a scan rate of 0.5 mV/s. b) Charge (integration of current signal) in red and transmission signal in blue. c) Calculated cation (blue) and anion (grey) concentration change as a function of the electrode charge. Ref.<sup>108</sup> - Published by the PCCP Owner Societies.

In accordance with recent *in situ* experiments on highly concentrated electrolytes,<sup>64,68</sup> the electrical double-layer is found to be formed by ion swapping. As soon as the system is charged, the balance between cations and anions is disturbed, but the total number of ions remains constant within the electrodes. This also implies that both cation and anion concentration within the bulk electrolyte remains fairly constant during charging and discharging. To calculate the absolute concentrations within the

---

micropores only, the numbers normalized to the effective electrolyte volume  $V_{el}$  are corrected by multiplying  $V_{micro}/V_{el}$ , where the micropore volume  $V_{micro}$  is determined from gas sorption experiments (Table 3.1, section 3.1). These experimentally determined cation and anion concentrations are further used as input for the Monte Carlo simulation (see section 5.4).

### 5.3 A two-phase model approach to interpret the *in situ* SAXS data

The content presented in section 5.3 is to a large extent not original and has been published in Ref.<sup>70</sup>. In order to understand the relative changes of the SAXS intensity upon charging and discharging, the aqueous electrolyte is varied systematically. A 1 M CsCl, KCl and NaCl aqueous solution was used as electrolyte and AC1 as electrode material. First the changes in the cation and anion concentration are analyzed quantitatively using the XRT signal and the concept presented in section 5.2. While the electrochemical data for all three tested electrolytes were roughly identical, the X-ray transmission data during charging and discharging exactly differentiates the different ionic systems (Fig. 5.12b). Since only the positive ion is varied for the different electrolytes, the X-ray scattering contrast of positive ions is expected to change while the actual electrosorption mechanism remains equal. Therefore the experiment presented in section 5.3 represents a contrast variation approach, which serves as additional source of information.

#### Integral ion concentrations from XRT

Changes in the measured transmission signal correspond to the sum of cation ( $c_{\text{cat}}$ ) and anion concentration ( $c_{\text{an}}$ ) changes weighted by their mass attenuation coefficients and molar masses (Eq. 5.19, section 5.2). The mass attenuation coefficient of  $\text{Cs}^+$  is much larger than the one of  $\text{Cl}^-$  (see Table 5.3). Hence, the transmission decreases at negative voltages since the cation concentration is increasing and the anion concentration is decreasing (and vice versa at positive voltages; cf. Fig. 5.12). The situation is different for NaCl, where the  $\text{Cl}^-$  attenuation coefficient is larger than the one of  $\text{Na}^+$ . Consequently, the periodic transmission signal behaves just oppositely. Since the attenuation coefficients of  $\text{K}^+$  and  $\text{Cl}^-$  are similar, cyclic variations of the transmission signal are much smaller. Yet, the charge signal for all three systems is very similar (blue curves in Fig. 5.12). It is calculated by integrating the current signal over time and normalized by the electrolyte volume, which was estimated from the transmission value at zero applied voltage (Eq. 5.20, section 5.2).

Using the concept explained in section 5.2 quantitative information on the ion concentration change as a function of the electrode charge was obtained. Evidently, the data for all three electrolytes follow the same general trend (Fig. 5.15a). An increase in counter-ions with increasing electrode charge results in an equal decrease in co-ions. For the investigated system so-called ion swapping is the main mechanism by which charge storage is accomplished. Accordingly, the total number of ions (i.e., the number of cations plus anions) stays constant while the anion or cation concentration changes to compensate a certain applied charge. This result aligns well with recent



findings from NMR using organic electrolytes.<sup>68</sup> A transition towards preferred counter-ion adsorption would also depend on other factors like the total ionic strength of the electrolyte as known from theoretical work for capacitive deionization.<sup>56</sup>

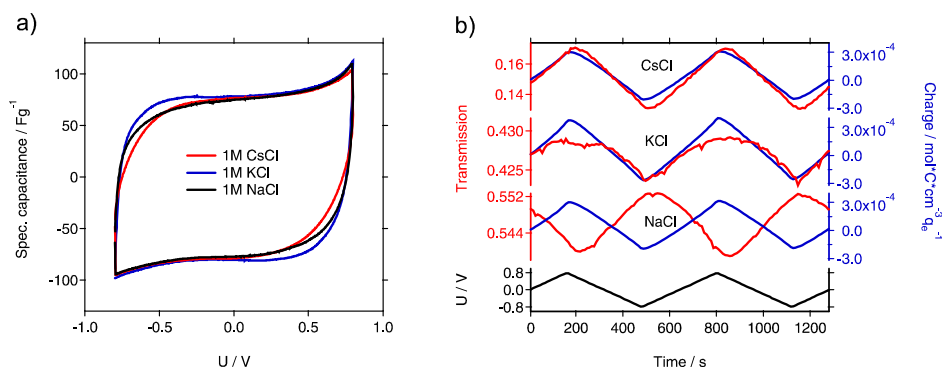


**Fig. 5.12** a) Cyclic voltammograms (CVs) of the in-situ measurements (AC1 with 1 M CsCl, KCl and NaCl) using a scan rate of 5 mV/s. b) Measured X-ray transmission (left scale, red color) and total charge  $Q$  obtained from the time integration of the electrical current and normalized by the electrolyte volume (right scale, blue color) for all three electrolytes. Note the different scaling on the transmission axes. On the bottom the voltage applied to the working electrode using a scan rate of 5 mV/s is given. Ref.<sup>70</sup> - Published by The Royal Society of Chemistry.

### Local information from SAXS

Beyond information on the ion concentration from X-ray transmission, SAXS allows to unravel more details about the ion electrosorption mechanism. The SAXS curves from carbon electrodes in air or when soaked with electrolyte are shown in Fig. 5.13. As explained in detail in section 5.1.1 and 5.1.2 these curves can be categorized into three main regions, having their origin in different levels of hierarchy of the carbon structure. At very small  $Q$ -values ( $Q < 0.7 \text{ nm}^{-1}$ ), the power law decay of the SAXS intensity is partly attributed to large pores between the micrometer-sized AC particles ( $I_{\text{particle}}(Q)$ ).<sup>134</sup> Scattering from disordered nanopores  $I_{\text{NP}}(Q)$  dominates the intermediate region between  $0.7 \text{ nm}^{-1}$  and  $5 \text{ nm}^{-1}$ . This region is often described by the Debye-Anderson-Brumberger (DAB) model<sup>35</sup> (see section 2.3.1 and 5.1.3) to obtain average correlation parameters that are related to the size and surface area of the pores.<sup>134</sup> At larger  $Q$ -values (i.e.,  $Q > 5 \text{ nm}^{-1}$ ), the molecular structure factors of the carbon matrix  $SF_C(Q)$  and the electrolyte  $SF_{el}(Q)$  dominate, corresponding to the correlation of individual carbon atoms and electrolyte ions.<sup>139</sup>

When the electrode is infiltrated with electrolyte, the SAXS intensity (Fig. 5.14b, blue curve) at low and medium  $Q$  significantly decreases due to the decreased electron density difference (SAXS contrast)  $(\Delta\rho)^2 = (\rho_c - \rho_{el})^2$  between carbon matrix and electrolyte-filled pores (Fig. 5.14a).<sup>32</sup> At the same time, the intensity at large  $Q$

increases due to the contribution of the electrolyte molecular structure factor in addition to the carbon structure factor. If ions are randomly distributed within the water matrix, the electrolyte structure factor contribution is constant in the SAXS regime<sup>151</sup> (indicated in Fig. 5.13b), its value being determined by the concentration and type of ions within the irradiated sample volume (section 5.1.2).<sup>152</sup> In addition to the SAXS signal ( $Q$ -range from 0.3 - 8  $\text{nm}^{-1}$ ) the wide angle regime (WAXS,  $Q$ -range from 9.5 - 20  $\text{nm}^{-1}$ ) is included here. The WAXS signal was measured by an additional detector simultaneously with the SAXS signal. The carbon structure factor (002)-peak and the first water structure factor peak around 20  $\text{nm}^{-1}$  are visible for AC1 in air and AC1 wetted with 1 M NaCl, respectively.<sup>153</sup> In Fig. 5.14b the SAXS intensity for all three electrolytes is shown. Note the difference in intensity in particular at larger  $Q$ -values ( $Q > 5\text{nm}^{-1}$ : electrolyte structure factor).

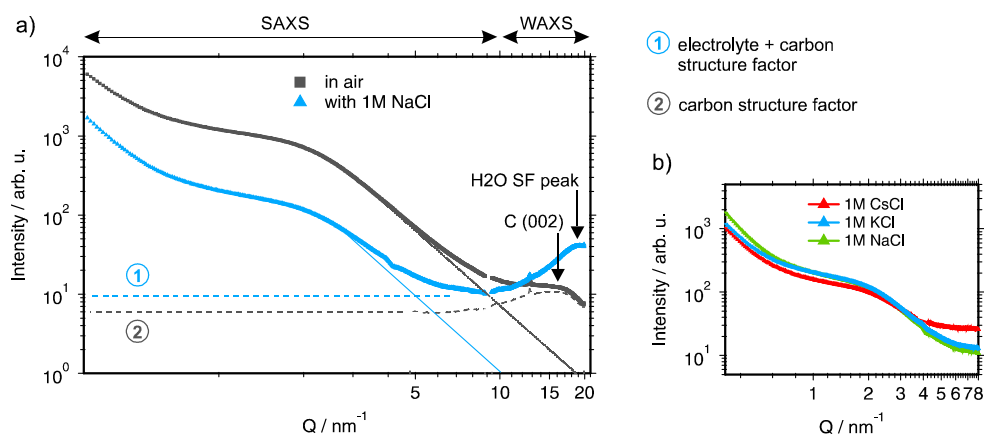


**Fig. 5.13** a) SAXS and WAXS intensity for the activated carbon (AC1) in air (grey) and filled with a 1M NaCl electrolyte (blue). The thin (grey and blue) lines indicate the power law decay of the SAXS intensity at larger  $Q$ -values. The horizontal dashed lines (both blue and grey) indicate the constant contribution of the carbon and electrolyte structure factors in the SAXS regime. b) SAXS intensity for the AC filled with three different electrolytes: 1 M CsCl, 1M KCl, NaCl. The scattering curves were measured at 0 V cell potential. Ref.<sup>70</sup> - Published by The Royal Society of Chemistry.

When a voltage is applied to the electrolyte-filled carbon electrode, the change in the electron density contrast in the pores (red arrow in Fig. 5.14a) is expected to lead to a change in the SAXS intensity, as was previously demonstrated.<sup>115,116,154</sup> However, besides the mean electron density change within the pores, structural changes like the rearrangement of ions within the pores or an electrosorption induced swelling of the pore structure might occur. Qualitatively, this would cause a change in the shape of the SAXS curve, which goes beyond a simple vertical shift of the intensity due to an average contrast change considered widely in the literature so far.

In order to visualize the voltage-dependence of the SAXS signal, all SAXS curves were normalized by the first curve measured at 0 V and displayed in Fig. 5.14c-e as color-coded relative intensity versus time and  $Q$  (see section 3.2.2). As the very low- $Q$  region (where mainly  $I_{particle}(Q)$  contributes) is not of primary interest here, the scattering curves were conveniently classified into two main regions Q-A ( $< 5 \text{ nm}^{-1}$ ) and Q-B ( $> 5 \text{ nm}^{-1}$ ) (indicated in Fig. 5.14c-e), emphasizing essentially the SAXS region and the onset of the molecular structure factor region.

As shown in section 5.1.2 the electrolyte structure factor for the given systems can be approximated by Eq. 5.21:

$$SF_{el}(Q_B) \cong A[\phi_{cat}(n_{cat} - n_{H_2O})^2 + \phi_{an}(n_{an} - n_{H_2O})^2 + C], \quad (5.21)$$

where  $\phi_i$  are the number fractions and  $n_i$  the electron numbers of the corresponding species, and  $A$  and  $C$  are constants. This signal contains similar information on the ion concentration as the transmission signal, the behavior of the SAXS intensity in the region Q-B being linked quantitatively to ion concentration via Eq. 5.21 with the electron numbers of the ions given in Table 5.3. In the case of CsCl, the change of the electrolyte scattering is dominated by the cation concentration due to the much higher number of electrons of the  $\text{Cs}^+$  ion (Table 5.3). Thus, the scattering intensity increases if  $\text{Cs}^+$  is inserted at negative voltages. The intensity will decrease at positive voltages because a large number of  $\text{Cs}^+$  ions is expelled due to ion swapping. This is in perfect agreement with the experimental data (Fig. 5.14c). A qualitatively similar behavior of the scattering intensity in the Q-B region is observed also for the KCl electrolyte (Fig. 5.14d). In this case, both the  $\text{K}^+$  and the  $\text{Cl}^-$  ion have 18 electrons (Table 5.3). Therefore, the electrolyte structure factor should stay constant in case of ion swapping (as implied from XRT data). Interestingly, the intensity changes of the NaCl electrolyte are qualitatively similar to experiments with KCl and CsCl (Fig. 5.14e). In the case of NaCl, the number of electrons in the cation (10) is considerably smaller than the one of the anion (18) and, consequently, ion swapping should result in an inversion of the scattering signal in the Q-B region as compared to the CsCl electrolyte.

A possible explanation for this unexpected behavior of the scattering intensity for KCl and NaCl can be given by considering the role of the solvent, that is, exchange or densification of water. An increased amount of water molecules transported by small cations has been proposed in a recent eQCM study.<sup>65</sup> Instead of just considering the bare ions in Eq. 5.21, a densified water layer surrounding each ion is taken into account.<sup>151</sup> This leads to the concept of an effective electron number. The numbers of tightly bounded water molecules evaluated by Levi et al.<sup>65</sup> for carbon nanopores were used to calculate these effective values, which are listed in Table 5.3. The effective

electron number of the  $K^+$  and  $Na^+$  ions are now similar, and both are larger than the one of the  $Cl^-$  ion, in qualitative agreement with the experimental observation.

**Table 5.3:** X-ray mass attenuation coefficients<sup>25</sup> at a photon energy of 8 keV, electron numbers of the bare ions and effective electron numbers of the hydrated ions within the micropores (using values from Ref. <sup>65</sup>). Effective electron numbers in parenthesis are the values used for the modeled data shown in Fig. 5.17.

	$Cs^+$	$K^+$	$Na^+$	$Cl^-$	$H_2O$
Mass attenuation coefficients ( $cm^2/g$ )	330	151	31	111	10
Electron number of dehydrated ions $n$	54	18	10	18	10
Effective electron number $n_{eff}$	59	31(40)	32(40)	24	10

In the following the SAXS intensity in region Q-A is discussed (Fig. 5.14). If a simple two-phase model of a homogeneous electrolyte within the pores of the carbon matrix were applicable, the intensity in the SAXS regime should behave just opposite as the electrolyte structure factor in Q-B, since it is determined by the scattering contrast  $(\Delta\rho)^2 = (\rho_c - \rho_{el})^2$ . This is obviously not the case for any of the used electrolytes (Fig. 5.14c-e). Again, for CsCl the situation should be the simplest one, since the scattering intensity changes will be dominated by the  $Cs^+$  concentration changes. When assuming pure ion swapping, one would expect an intensity increase at positive voltage (when  $Cs^+$  is expelled) and a decrease at negative voltage (when  $Cs^+$  is adsorbed). However, at negative voltage not a minimum, but a strong intensity maximum is observed experimentally, which cannot be simply related to ion concentration changes. In the case of the KCl electrolyte at intermediate Q-values ( $1\text{ nm}^{-1} < Q < 5\text{ nm}^{-1}$ ), the intensity signal reveals maxima at positive and minima at negative voltages (Fig. 5.14d). This behavior would be consistent with the simple two-phase model considering the results from the electrolyte scattering. However, similar to the CsCl sample, an additional intensity maximum is observed at negative voltages at  $Q < 1\text{ nm}^{-1}$ , although this maximum is less pronounced. Finally, considering the effective electron number of  $Na^+$  ions (Table 5.3) and the measured concentration changes (Fig. 5.15a), the intensity change in the Q-A region should be rather similar to KCl, which is obviously the case (Fig 5.14d,e).

Conclusively, a simple two-phase model with an essentially homogeneous electron density distribution of the electrolyte within the micropores is not able to explain the behavior of the SAXS intensity within the Q-A regime. A peculiar feature, namely an intensity maximum at negative voltages, occurs for all electrolytes at medium to low

Q-values. This maximum scales roughly with the effective electron number of the cations adsorbed, being largest for  $\text{Cs}^+$  and smaller for  $\text{K}^+$  and  $\text{Na}^+$ .

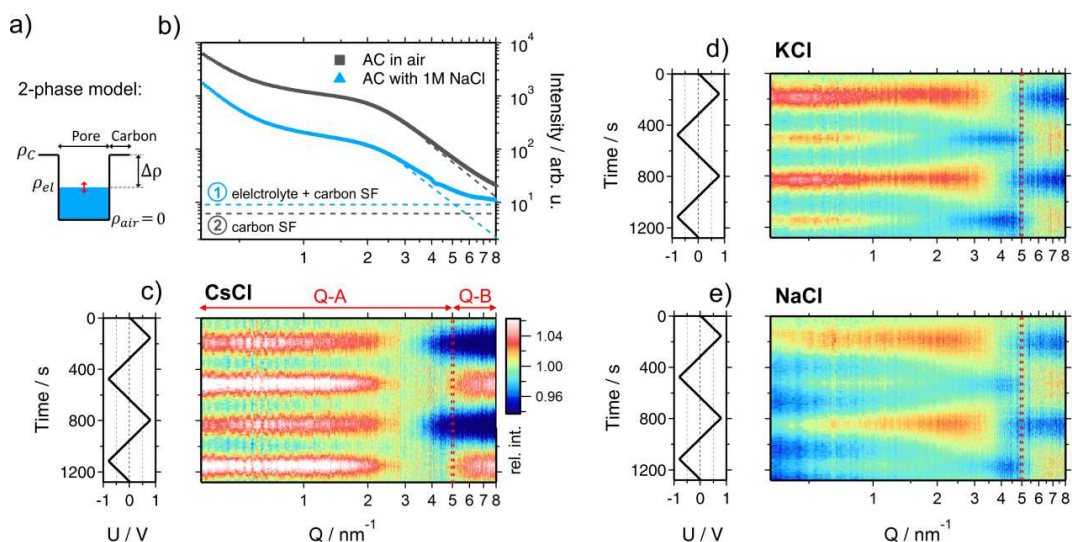


**Fig. 5.14** a) Sketch of the electron density profile in an electrolyte filled pore assuming a fully homogeneous electrolyte (2-phase model). b) Double logarithmic representation of the scattering intensity  $I(Q)$  of the AC1 electrode in air (grey) and infiltrated with a 1 M aqueous NaCl electrolyte (blue) without external voltage applied. The dashed thin lines indicate the molecular contributions of carbon and electrolyte to the measured scattering intensity. c)-e) Left rows: applied voltage signal as a function of time. Right row: Scattering intensity (color coded scale) normalized to the intensity at 0V as a function of time and the scattering vector length  $Q$ . Note the indicated Q-regions Q-A and Q-B. c) CsCl, d), KCl, e) NaCl. Ref.<sup>70</sup> - Published by The Royal Society of Chemistry.

### The radius of gyration as a correlation length parameter

The deviation from a simple two-phase model is not unexpected, since - at least for large enough pores - the counter-ions are expected to accumulate close to the pore walls during double-layer formation (section 2.4.3). Yet, SAXS from a multiphase system in connection with the complex disordered pore structure of activated carbons is not treatable without introducing too many ad-hoc assumptions. Therefore, in order to understand the basic features of the structural arrangement of the ions within the pore space, Guinier analysis (see experimental section 3.2.2) of the SAXS data is a convenient tool.<sup>120</sup> As the Guinier approximation is strictly applicable only for particulate systems of low volume fraction, the radius of gyration obtained from this analysis is merely a correlation length parameter without direct connection to a real size in the system.

In Fig. 5.15b the relative change of the radius of gyration ( $R_g$ ) is plotted as a function of the applied charge, the values being normalized to the  $R_g$  value at zero voltage. The

magnitude of the normalized radius of gyration is high for CsCl and lower for KCl and NaCl at maximum negative voltage. Going from zero to maximum positive charge, all electrolytes show an increase of  $R_g$ . Interestingly, the increase of  $R_g$  left and right to the minimum is correlated to the effective electron number (Table 5.3) of the individual counter-ions ( $\text{Cs}^+$ ,  $\text{K}^+$ , or  $\text{Na}^+$  at negative charge and  $\text{Cl}^-$  at positive charge). Hence, the change of the correlation length rather than the change of the intensity seems to open a way to a better understanding of the in-situ SAXS signals. This will be discussed in the following section.

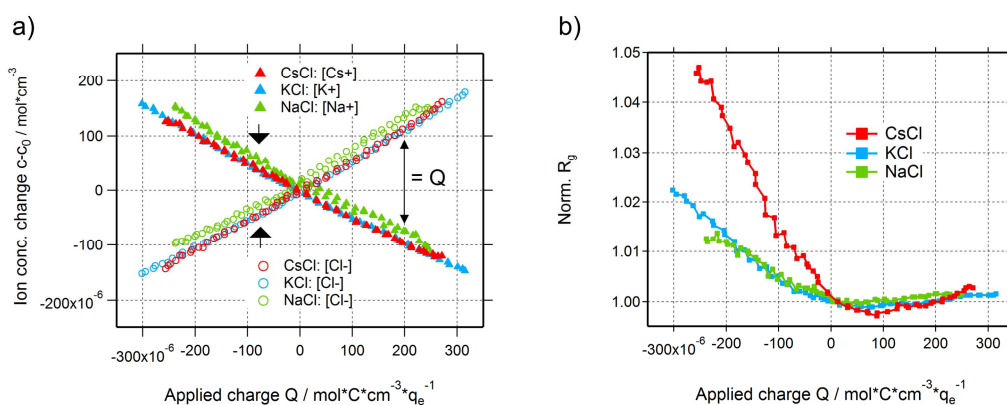


**Fig. 5.15** (a) Cation and anion concentration changes of all three electrolytes as a function of the applied charge. Note that the difference between cation and anion concentration corresponds to the applied charge (indicated by the black arrow on the right). (b) Relative change of the radius of gyration for all three electrolytes as a function of the applied charge. The shape of the curves in (a) and (b) reveal the characteristic differences regarding global and local ion rearrangement. Ref.<sup>70</sup> - Published by The Royal Society of Chemistry.

### Probing local ion arrangement

As seen from gas sorption data (see section 3.1), the volume fraction of micropores (and mesopores) in the AC1 electrode is 65% (Table 3.1, section 3.1) and the average pore size is about 1.3 nm. Hence, on average, there is enough space for two solvated ions next to each other to build up a layer of electroadsorbed ions at the charged carbon surface. Such preferred arrangement of ions should lead to a significant change of the electrolyte electron density close to the carbon surface in particular in the case of  $\text{Cs}^+$  ions, but also for  $\text{K}^+$  and  $\text{Na}^+$  taking their effective electron numbers into account. Yet, the resolution of the SAXS setup is not sufficient to deduce unambiguously the real electron density profile.

As sketched in Fig. 5.17a, the increase of the actual electron density near the surface may be represented within a two-phase model by an effective decrease of the pore size. Upon charging, an excess amount of counter-ions will be attracted by the pore walls

leading to an electron density profile as sketched in Fig. 5.17a on the bottom. The green dashed line represents this profile within the pore for heavy cations like  $\text{Cs}^+$  (large effective electron number) and the red dashed line indicates the electron density profile caused by light ions like  $\text{Cl}^-$  (having a small effective electron number). In the resolution limited SAXS experiment, the electron density near the pore walls can be replaced by the black line to represent again a two-phase model, leading to an effective decrease of the pore volume fraction. Furthermore, the average electrolyte electron density  $\rho_{\text{el}}$  is changing upon changing the average ion concentrations within the pore. This model is very useful and may be employed even for pores smaller than the double-hydrated ion diameter, as the probability of ions in proximity to the pore wall is still higher compared to the pore center.

Within this two-phase approximation, the radius of gyration can now be related to the actual volume fraction of pores and the carbon matrix. Within the Debye-Anderson-Brumberger (DAB) model (section 2.3.1), which has been used extensively to describe the structure of disordered carbons, this relation is explicitly given by:<sup>35,134,155</sup>

$$R_g = \sqrt{6} * \frac{\varphi(1 - \varphi) * V}{S}, \quad (5.22)$$

with the volume fractions of pores ( $\varphi$ ) and carbon ( $1 - \varphi$ ), and  $S/V$  being the surface area per unit volume. Hence an effective decrease of the pore volume fraction  $\varphi$  would for  $\varphi > 0.5$  lead to an increase of the product  $\varphi \cdot (1 - \varphi)$ . For our micropore structure, this product can theoretically increase from  $0.65 \times 0.35$  to  $0.5 \times 0.5$ , corresponding to an increase of roughly 9%. Assuming the volume fraction to be the only parameter that changes in Eq. 5.22, the radius of gyration increases significantly upon decreasing the pore volume fraction. Hence the effective pore width within the sketch of Fig. 5.17a changes according to the  $R_g$  signal, while the average electrolyte density within the pore  $\rho_{\text{el}}$  is changing due to pure ion swapping (vertical shift of the profile in Fig. 5.17). Using these two independent parameters,  $R_g$  from Fig. 5.15b and  $\rho_{\text{el}}$  from Fig. 5.15a, as an input for model calculations with the DAB model, the scattering curves can be re-calculated (modeled) as a function of the applied charge. As a starting point the fit parameters needed to describe the scattering curve at 0 V were evaluated (Fig. 5.16). Following this, the relative changes of all fit parameters were calculated using the effective electron numbers (Table 5.3), the cation and anion concentration changes from the XRT evaluation (Fig. 5.15a) and the radius of gyration signal (Fig. 5.15b) as an input. The generation of the modeled *in situ* SAXS curves is described in the following.

### Modelling the scattering intensity change

The so-called Debye-Anderson-Brumberger (DAB)<sup>35</sup> model represents an analytical expression describing the scattering of random pore systems with an exponentially decaying correlation function. The corresponding scattering cross section is analytically given by:

$$I_{DAB}(Q) = \frac{2\pi(\Delta\rho)^2 \cdot S}{(6/R_g^2 + Q^2)^2 \cdot V}, \quad (5.23)$$

where  $R_g$  corresponds to the radius of gyration,  $(\Delta\rho)^2$  to the electron density contrast and  $S/V$  to the surface to volume ratio of the pore structure. In the case of activated carbons an additional term has to be considered, covering the contribution of the significant volume of large pores in between the carbon particles, leading to a power law behavior of the intensity at small  $Q$ .<sup>134</sup> To fit the measured scattering intensity the following expression was used:

$$I_{fit}(Q) = \frac{A}{Q^{3.5}} + \frac{B}{(6/R_{g,0}^2 + Q^2)^2} + C, \quad (5.24)$$

with  $A$ ,  $B$ , and  $C$  together with  $R_{g,0}$  being the fit parameters. The first term corresponds to the contribution of the carbon particles  $I_{particle}(Q)$  which was found to decay with a power law exponent of -3.5 from a fit of the SAXS intensity of dry AC at low  $Q$ -values. The second term corresponds to the nanopore scattering  $I_{NP}(Q)$  (DAB-model), and the third term covers the  $Q$ -independent contributions of the electrolyte structure factor  $SF_{el}(Q)$  and the carbon structure factor  $SF_C$ . The parameter  $C$  can be further splitted into the carbon structure factor contribution  $SF_C$  (known from measurements of the bare AC) and the electrolyte structure factor contribution  $SF_{el}$ . In Fig. 5.16a, the fit is shown for the CsCl sample at 0 V. Although the fit is not perfect, the model covers the basic features of the system which allows simulating the relative intensity changes of the scattering curves as observed from the experimental data in Fig. 5.14c-e. The input is given by the relative changes of the radius of gyration  $R_{g,0}$  and the electrolyte structure factor  $SF_{el,0}$  from the SAXS data, and the electron density contrast  $(\Delta\rho)^2$  between micropores and carbon matrix calculated from the known concentrations from XRT and the effective electron numbers in Table S3. To this end, Eq. 5.24 was rewritten as Eq. 5.25:

$$I_{sim}(Q) = \frac{A}{Q^{3.5}} + \frac{(\Delta\rho)_{rel}^2 \cdot B}{(6/(R_{g,rel}^2 R_{g,0}^2) + Q^2)^2} + SF_{El,rel} \cdot SF_{el,0} + SF_C. \quad (5.25)$$



The parameters  $A$ ,  $B$  and  $SF_C$  are kept constant for all simulated scattering curves.  $A$  and  $B$  are known from the fit at 0 V (Fig. 5.16a) and  $SF_C$  corresponds to the carbon structure factor evaluated from the scattering intensity of the bare AC (“AC in air”, Fig. 5.14a). Changes of all other parameters are considered by multiplying a relative value  $((\Delta\rho)_{rel}^2, R_{g,rel}, SF_{El,rel})$  to the initial parameters at 0V ( $B, R_{g,0}, SF_{El,0}$ ).

The electrolyte structure factor contribution  $SF_{El,rel}$  is calculated according to Eq. 5.5 in section 5.1.2 using the ion concentration from the transmission calculations and the effective electron numbers of the cations  $n_{eff,cat}$  and anions  $n_{eff,an}$  (Table 5.3) as an input. In order to obtain relative changes these values are normalized by the value at 0V.

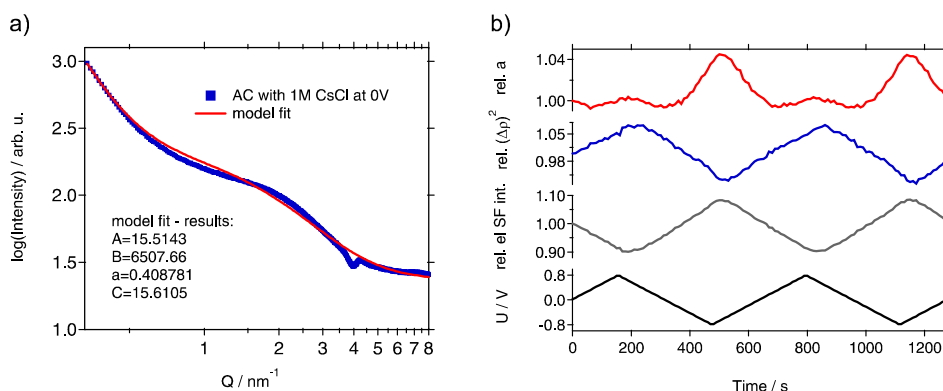


**Fig. 5.16** In a) the SAXS intensity of the AC1 filled with the 1M CsCl electrolyte at 0V is given (red data points). In black the model fit according to Eq. 5.24 is indicated. In b) the changing parameters needed for the simulation of the relative CsCl scattering intensity according to equation 5.24 are shown. The result of the re-calculated scattering data is shown in Fig. 5.17b. Ref.<sup>70</sup> - Published by The Royal Society of Chemistry.

The electron density contrast change  $(\Delta\rho)^2$  is estimated by assuming ion concentration changes  $c_i$  within the micropores proportional to the calculated ones (Fig. 5.16a). The global ion concentration changes calculated from the XRT evaluation cover changes within the entire electrolyte volume of the WE including both macropores and micropores. Due to the low macropore surface area all concentration changes can be reduced to changes within the micropores. Hence the actual micropore concentration change has to be multiplied by a factor corresponding to the ratio of total to micropore volume  $\phi_{total}/\phi_{micro}$ . The total pore volume is estimated from the transmission measurement at 0V (section C) and the micropore volume from the gas sorption measurements (section 3.1). The carbon matrix electron density  $\rho_c$  is estimated by comparing the height difference between the SAXS intensity (intermediate regime) of the AC in air with the AC infiltrated with

electrolyte at 0V. Hence the electron density difference shown in Fig. 5.16b is written as Eq. 5.26:

$$(\Delta\rho)_{rel}^2 = \frac{1}{(\Delta\rho_0)^2} \left( \rho_c - \left( \frac{\phi_{total}}{\phi_{micro}} c_{cat} n_{eff,cat} + \frac{\phi_{total}}{\phi_{micro}} c_{an} n_{eff,an} + c_{H_2O} n_{eff,H_2O} \right) \right)^2 \quad (5.26)$$

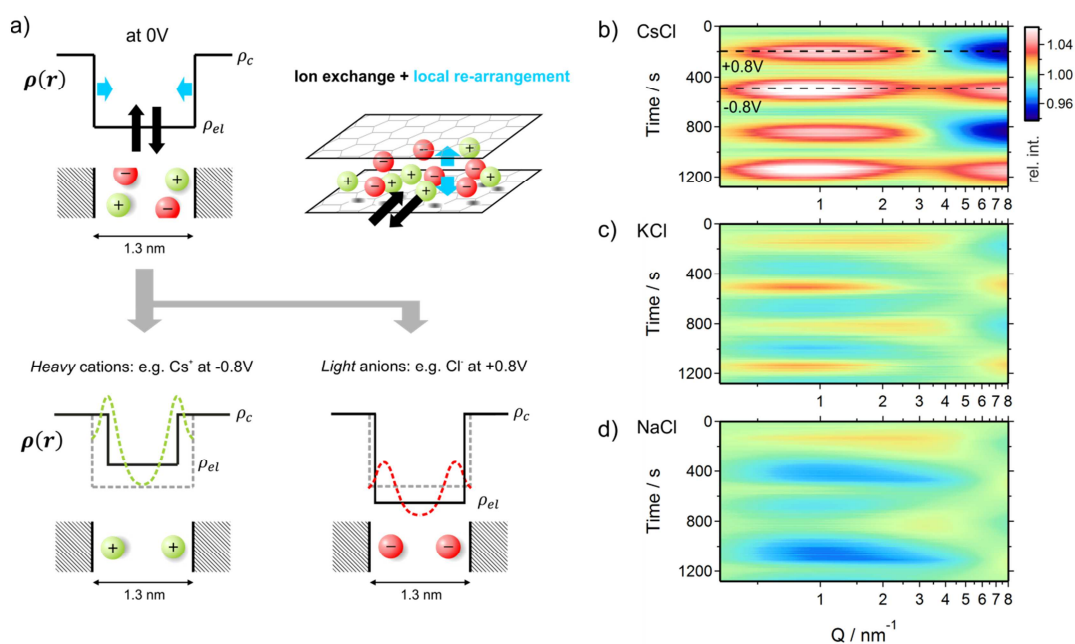
All time (or voltage) dependent parameters needed as an input for the simulations are shown exemplarily for CsCl in Fig. 5.16b. The resulting simulated scattering curves for all electrolytes are given in Fig. 5.17b-d.

Fig. 5.17 shows that indeed the scattering intensity increases at small Q-values when the radius of gyration is increased (in particular at negative voltages). The simulations of all three electrolytes are in good agreement with the measured scattering data (Fig. 5.14). Using only two independent signals from the XRT evaluations (ion concentrations) and the SAXS measurements ( $R_g$ ) as an input for a simple model, the complex changes of the SAXS intensity could be fully reproduced. Hence, the relative change of the radius of gyration in Fig. 5.15b can be understood as a measure for ions preferably adsorbed on the pore walls and weighted by a factor related to the effective electron number (see sketch in Fig 5.17a). Qualitatively, Fig. 5.15b is a measure of the local ion concentration close to the pore walls.

Interestingly, the local ion concentration near to the pore walls (Fig. 5.15b) behaves quite differently as compared to the global ion concentration (Fig. 5.15a) which was interpreted as pure ion swapping. The radius of gyration increases strongly at negative applied charge, but only slightly at positive values. In the simplest scenario, the local ion concentration near the pore walls is expected to behave similar to the globally measured ion swapping. In this case, an increase of  $R_g$  at negative and a decrease of  $R_g$  at positive applied charge should be present, since the  $R_g$  signal is dominated by the local ion concentration changes of cations (having a larger effective electron number). This is obviously not the case, as an increase in both directions of the applied charge has been observed. In fact, the  $R_g$  signal suggests the preferred arrangement of counter-ions locally close to the pore walls, depending on the polarization of the electrode. However, on a global scale, the ion transport in and out of the pores on the other hand is accommodated by ion swapping.

Moreover,  $R_g$  (Fig. 5.15b) and eQCM data (i.e., mass change vs. charge) reveal a noticeable similarity. So far eQCM has mainly shown counter-ion adsorption as the dominant charge compensating mechanism for a variety of electrolytes and salt concentrations. Yet, pure ion swapping has not been observed so far at large enough potentials.<sup>63,65,156</sup> For these experiments only counter-ions are involved in the local re-arrangement, which explains the similarity between the  $R_g$  and eQCM data. On the

other hand, the ion exchange in and out of the micropores is realized by pure ion swapping, which corresponds to the actual mechanism counterbalancing the electrode charge. The minimum of the curves in Fig. 5.15b might be taken as an indication for the point of zero charge (PZC), similar as proposed in recent eQCM studies.<sup>66</sup> However, since the actual charge compensating mechanism seems to be ion swapping, the  $R_g$  signal (local ion redistribution) is probably not suitable for the determination of the “overall” (global) PZC.



**Fig. 5.17** a) Sketch of the electron density profile of a carbon pore filled with electrolyte at 0 V (top). The size of the sketched ions corresponds roughly to the dehydrated ion size with respect to the average pore size of 1.3 nm. Water molecules in the hydration shell and the solvent are not visualized. When applying a voltage the average ion concentration within the pores will change (ion exchange in and out of the pores: indicated as black arrows on the top). Moreover the ions will re-arrange locally within the nanopore (local re-arrangement: blue arrows on the top). These changes lead to electron density profiles as sketched on the bottom. In the case of heavy ions (large effective electron number), the preferably adsorbed ions next to the pore walls will lead to a significant increase of the electron density close to the pore walls. The sketch of the real electron density across the pore (green dashed line) can be replaced by the profile shown by the black solid line suggesting an apparent decrease of the pore size. The same argument is valid for negative voltages when  $\text{Cl}^-$  ions are situated preferably near the pore walls, but due to their lower effective electron number the apparent decrease of the effective pore width is smaller. The sketched profiles on the bottom describe the situation exemplarily for -0.8V and +0.8V. These two points are indicated as dashed lines within the simulated scattering intensities in Fig. 5.17b. b)-d) Simulated scattering intensities of all three electrolytes, covering changes of the pore volume fraction, the average electrolyte density and the electrolyte structure factor. b) CsCl, c) KCl, d) NaCl. The simulations reproduce the main features of the measured scattering intensity changes (Fig. 5.14c-e). Ref.<sup>70</sup> - Published by The Royal Society of Chemistry.

Since only relative changes of  $R_g$  are discussed, the arrangement of ions at 0 V conditions can be only estimated. Hence, the presented electron density profiles and ion concentrations represent excess values with respect to the 0 V situation. MD simulations have shown the preferred position of ions near to the pore walls already at 0 V.<sup>157</sup> However, independent on the distribution of ions across the pore at 0 V, the change of  $R_g$  corresponds to a local re-arrangement of ions from the center towards the pore walls. Using combined in-situ SAXS and XRT one is sensitive to both the global ion concentration (corresponding to the average ion concentration within the micropores) and the local ion arrangement within the pores.

The profiles in Fig. 5.17c,d were modeled by using effective electron numbers of 40 electrons for both, the hydrated  $\text{Na}^+$  and  $\text{K}^+$  ions. When using instead the literature values of 31 and 32 electrons, respectively (see Table 5.3), the basic features are qualitatively reproduced, but the correspondence between Fig. 5.14d,e and Fig. 5.17c,d is not as good. Detailed confinement effects, being different for different carbons, may be responsible for this deviation. Furthermore deviations might be induced by the different nature of the methods used for estimating the effective electron numbers.

### Conclusions of section 5.3

Local ion rearrangement has, so far, only been accessible via simulation<sup>157</sup> or on flat plates with X-ray reflectometry<sup>158</sup> which is difficult to translate to the complex situation in confinement of carbon nanopores inside activated carbon particles. The data presented in section 5.3 help to draw a clearer picture of ion electrosorption in aqueous media with high ionic strength (1 M). Globally, charge accommodation is accomplished without changing significantly the global number of ions in the pores, that is, cations plus anions. Effectively, this corresponds to what is known as ion swapping. Yet, ion electrosorption also entails a second component, namely local in pore ion rearrangement. Compared to the uncharged state, counter-ions move much closer to the pore wall and facilitate the formation of a dense ion layer. This process is intimately tied with the ionic system and the solvent. In particular, it has been shown that a much “denser” hydration shell needs to be considered with an increased amount of water molecules transported by small cations. This experimental fact should further motivate to take the solvent (water) properly into account in atomistic simulations.<sup>159-161</sup>

## 5.4 A new data analysis approach

Large parts presented in section 5.4 are not original and have been published in Ref.<sup>108,109</sup>. The two-phase model approach (section 5.3) could explain the scattering data of the AC1 electrode infiltrated with different aqueous electrolytes. Beside global ion concentration changes, for the first time ions were found to rearrange locally upon charging and discharging the supercapacitor. In the two-phase model picture, local rearrangement implies counter-ions preferably moving from the center towards the pore walls as a voltage is applied. However, *in situ* SAXS data of other nanoporous carbons like CDCs, with an average pore size of only 0.65 nm, still exhibit characteristic features of local ion rearrangement. With an average pore size of 0.65 nm cations and anions have to be at least partially desolvated or distorted already for entering the pores of the CDC. A local rearrangement across the pore within the slit-pore picture sketched in Fig. 5.17 is not possible. Similar contradictions were observed for the activated carbon AC2, with an average pore size of 0.9 nm. The simple interpretation used in section 5.3 cannot be applied to the scattering data of nanoporous carbons with pores smaller than AC1 and it does not provide comprehensive physical explanations for local ion rearrangement. Evidently, in complex multiphase systems like carbon nanopores filled with electrolyte (cations, anions, and solvent molecules like water) no analytical models are available to describe changes of the scattering intensity caused by positional changes of ions and solvent molecules during charging and discharging.

In this section a strategy how to overcome this limitation is presented.<sup>109</sup> The data analysis strategy relies on atomistic computer simulations, enabling a mutual cross-verification of experimentally measured and simulated data sets. In the first step, the concept of Gaussian random fields (GRFs)<sup>142</sup> is used to produce a real space three-dimensional pore structure of nanoporous carbon from *ex situ* SAXS measurements (details section 5.1.5). In the second step, the virtual 3D pore structure is populated with ions in a dielectric medium and their equilibrium positions for a given applied voltage are evaluated using a Monte Carlo based algorithm (details section 4). In the third step, a Fast Fourier Transformation of this calculated real space model yields a calculated scattering curve which can be compared to the measured SAXS pattern. Repeating this procedure for different electrode charges (i.e., applied voltages), measured *in situ* SAXS intensities can be quantitatively compared to the simulations. Referring to the work of Merlet et al.<sup>62</sup>, a parameter called degree of confinement (DoC) is introduced, which allows quantifying the local ion concentration changes in nanoconfinement. Also a second parameter is established, the degree of desolvation (DoDS) of ions, to quantify the influence of local pore environment on the (partial)

removal of the solvation shell. The voltage dependence of these two parameters provides a clear physical description of the local behaviour of ions in different confining environments directly from experiment, helping to significantly advance our understanding on the intricacies of ion electrosorption in nanoporous carbons. Moreover length scale dependent ion kinetics is studied by investigating *in situ* data applying cyclic voltammetry with different scan rates. Apart from Monte Carlo simulations, ions can alternatively be rearranged within the model carbons following an empirical algorithm.

Three predominantly microporous carbons with different average pore sizes were investigated: activated carbons, AC1 (1.3 nm) and AC2 (0.9 nm), and titanium-carbide derived carbon, CDC (0.65 nm) (section 5.1.4). Cyclic voltammograms of the *in situ* measurements of all three cells are shown in Fig. 5.18a. Highest gravimetric performance is observed for the AC2 electrode. The mean pore size in AC2 is significantly smaller as compared to the AC1 electrode; yet increased ohmic losses due to limited ion mobility within the smaller pores are still negligible. A slightly smaller gravimetric capacitance is observed for the CDC electrode.

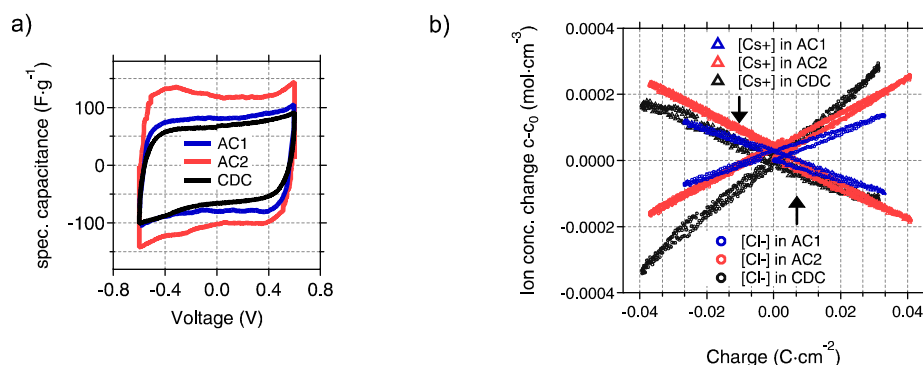


**Fig. 5.18:** a) Cyclic voltammograms (CVs) of the in-situ measurements using a scan rate of 1 mV/s. b) Ion concentration change as a function of the electrode charge. Reproduced with permission from Ref.<sup>109</sup>. © Nature Publishing Group.

Following the procedure described in section 5.2, cation and anion concentration changes as a function of charge are quantified by the analysis of the simultaneously recorded X-ray transmission signal through the electrode (section 5.2). The absolute values of cation and anion concentration changes differ for the three carbons due to their specific capacitance values and the specific conditions within each of the in-situ cells (Fig. 5.18b). In accordance with results of section 5.3 and results on supercapacitors using organic electrolytes with high ionic strength<sup>68</sup>, ion electrosorption in all three carbons is accomplished by failure of the permselectivity, also known as ion swapping<sup>162</sup> (Fig. 5.18). The total concentration of cations plus

anions remains constant; only the balance of anion-to-cation ratio is disturbed. A transition towards preferred counter-ion adsorption is predicted for electrolytes with lower ionic strengths and/or larger applied voltages.<sup>56</sup>

Concentration changes for CDC are slightly asymmetric (black curves, Fig. 5.18b) caused by slow ion diffusion in CDC and the long diffusion pathways from the CE towards the (X-ray) irradiated WE volume due to the specific design of the in-situ cell (section 3.2.1). Although the asymmetry introduces a certain error within the ion concentration calculation procedure, this has no impact on the conclusions and assumptions drawn below.

Fig. 5.19a shows the SAXS intensity vs. scattering vector length  $Q$  for the empty AC2 electrode. The SAXS profiles reveal characteristic changes when the electrodes are infiltrated with 1 M CsCl in water and the voltage was cycled (Fig. 5.19e). They indicate changes of counter- and co-ion concentration (large  $Q$ ), as well as their locations within the pores (low  $Q$ ), as discussed in section 5.3.

Besides the global ion concentration change within all electrode pores, ions re-arrange locally across the nanopores upon applying a voltage causing the  $Q$ -dependent intensity changes in Fig. 5.19e. The SAXS data show collective structural rearrangements in all three carbons, notably also in CDC, where the hydrated ion size fits almost exactly the average pore size. In section 5.3 the local structural rearrangement in AC1 was interpreted as a preferred movement of counter-ions from the pore centre towards the pore walls using a simple two-phase approximation for the SAXS data. However, this simple model fails to explain the in-situ data from AC2 and CDC. In particular, this is true for local ion rearrangement that can be observed even in the smallest pores (CDC, Fig. 5.20). To overcome these limitations, a novel data analysis strategy was developed to extract more intuitive local physical information from the comprehensive data in Fig. 5.20 (left column).

Using the GRF<sup>141,142</sup> based concept explained in section 5.1.5, the real space 3D representations of the (empty) pore structures were generated on the computer from an accurate model fit of the SAXS data in Fig. 5.19a (see section 5.1.5). In Fig. 5.19b (AC2) and in Fig. 5.9, the resulting 3D micropore morphologies of the three different carbons are shown. The most distinct differences are the decreasing average pore size as well as the decreasing micropore volume fraction in the sequence AC1, AC2, CDC in good agreement with gas sorption analysis (Fig. 5.10). The statistical resemblance of the obtained morphologies by the measured SAXS data is validated by discrete Fast Fourier Transformation (FFT) of the 3D pore morphology (Fig. 5.19a).

In the next step ions are randomly placed within the 3D real space carbon pore model and redistributed for different applied voltages to sample the equilibrium

configurations of the system. This is done using a Monte Carlo (MC) based algorithm considering coulombic ion-ion and ion-electrode interactions (see section 4). Simple FFT of each simulated charge configuration allows to reconstruct a simulated counterpart (Fig. 5.19d) of the measured in-situ SAXS intensity changes with the applied voltage (Fig. 5.19e). The main features of the measured SAXS patterns are well reproduced (Fig. 5.19d-e), even though the simulation was kept simple to capture the essential physics of the process.

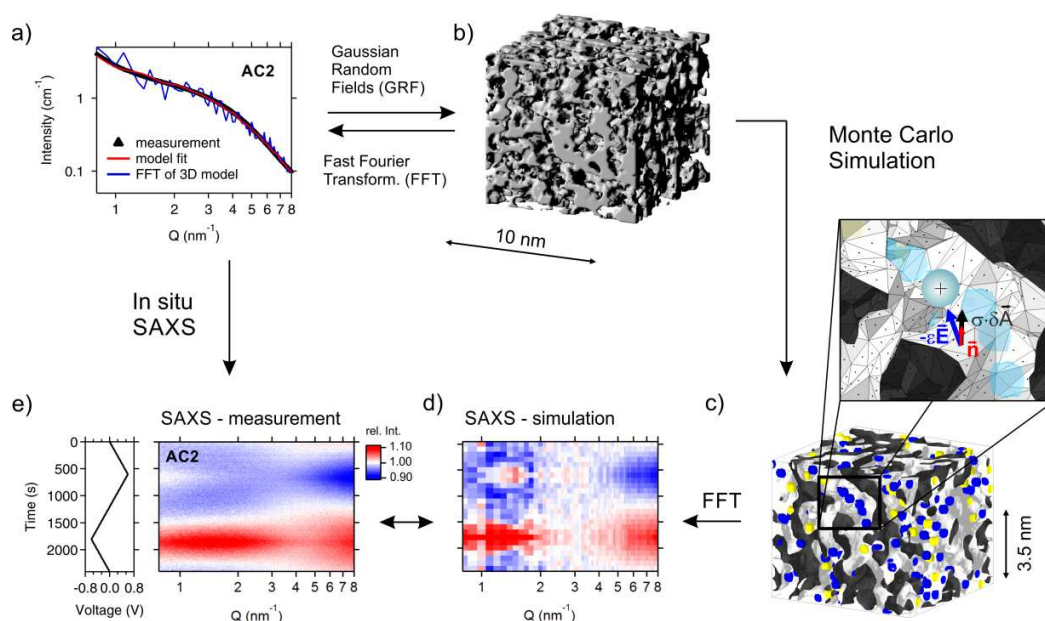


**Fig. 5.19:** a, SAXS intensity versus scattering vector length ( $Q$ ) of measured data (black) for sample AC2 in vacuum and an accurate model fit (red), (b) resulting in a real space pore structure (here:  $10 \times 10 \times 10 \text{ nm}^3$ ) using the concept of Gaussian random Fields (GRFs). Numerical Fast Fourier Transformation (FFT) of the real space structure results again in a scattering curve (blue curve in a), see section 5.1.5. c, The pore structure (here: 3D sub-volume with  $7 \times 7 \times 7 \text{ nm}^3$ ) is populated with cations (blue) and anions (yellow) in a homogeneous dielectric water phase with the ion concentration obtained from X-ray transmission (section 5.2). For each electrode voltage, ions are re-arranged according to a MC simulation. The electric field  $\epsilon \vec{E}$  caused by all surrounding charges (cations in blue, anions in yellow and electrode charges as black dots) induce a charge  $|\sigma \cdot \delta \vec{A}|$  in the center of each triangle (normal vector  $\vec{n}$ ) of the carbon pore-interface, as indicated in the zoomed view and explained in detail in section 4. Ions, water and carbon phase are then weighted by their respective electron density and subsequent FFT yields the simulated SAXS intensity of the carbon-electrolyte system. Simulated relative SAXS curves (d) are compared to the measured relative SAXS intensities with the applied voltage signal shown in (e). Reproduced with permission from Ref.<sup>109</sup>. © Nature Publishing Group.

A strength of the approach is, that the major input into the simulation consists of the empty carbon structure and the global ion concentration, both taken directly from experimental data. The only additional parameters entering the simulation are the



dielectric permittivity of water, the radii of hydrated and dehydrated ions, and an estimate of their hydration energy (details see section 4). It is well known that the dielectric permittivity varies with the pore size which may have distinct effects on charge storage.<sup>163</sup> Parameter studies suggest that the agreement between experiment and simulation could indeed be further improved by introducing pore size dependent dielectric permittivity and hydration energy. Yet, taking water molecules into account goes beyond this work as it is computationally extremely expensive for the required box sizes. For similar reasons, the carbon electrodes were treated as perfect conductors, although deviations from ideal metallic behaviour might influence the results.<sup>94,126,164</sup>

The simulation accounts for the ion-ion and ion-electrode coulombic interactions and for ion hydration. Water apart from the ion hydration shell is treated as a continuous dielectric phase,<sup>123</sup> and the carbon electrode is taken as a perfect conductor. The dielectric constant of water in nanopore confinement needs to be significantly reduced (to 40) compared to bulk water (78), a fact that is well known from literature.<sup>123</sup> To keep the complexity of the system as low as possible, cations and anions are taken to be identical in size. Therefore, both,  $\text{Cs}^+$  and  $\text{Cl}^-$  ions are considered as hard spheres with a radius of 0.18 nm.<sup>97,98</sup> The electrode charge is modeled via point charges in the center of the triangulated carbon-pore interface (see Fig. 5.19c). The surrounding cations, anions and electrode charges induce a charge with opposite sign at these points, ensuring that no electric field can propagate into the conductive electrode. This corresponds to a constant potential within the electrode. The ability to induce electrode (surface) charges which counterbalance the ionic charge within the pores, causes the actual capacitive behavior of the electrode. If ions approach the carbon surface closer than their hydrated ion diameter (taken to be 0.33 nm for both ion species<sup>97,98</sup>), the energy cost of releasing parts of the ion's hydration shell is considered in a semi-quantitative manner, i.e., by multiplying the volume fraction of carbon penetrated with the hydration shell with the experimentally determined hydration energy taken from literature.<sup>42</sup>

Once the equilibrium ion positions are evaluated by the Monte Carlo simulation, all species within the structure are weighted by their electron densities. The carbon phase as well as the water within the pore is treated as a continuum and weighted by their mean electron density levels. A mass density of  $1.9 \text{ g/cm}^3$  was taken for the carbon phase, in accordance with literature<sup>80</sup> and absolute SAXS measurements of AC without electrolyte. The water density was assumed to be the bulk water density ( $1.0 \text{ g} \cdot \text{cm}^{-3}$ ), although it is known that confinement can influence these values considerably.<sup>165</sup> This corresponds to a scattering length density (proportional to the electron density) of  $1.6 \cdot 10^{-9} \text{ cm}^{-2}$  and  $0.94 \cdot 10^{-9} \text{ cm}^{-2}$  for the carbon and water phases,

respectively. Both cations and anions are treated as three-dimensional Gaussian electron clouds. These three-dimensional Gaussian electron clouds contain an effective number of electrons (section 5.3, Table 5.3) considering the densified hydration shell around the ions. A possible change in the effective electron number due to partial dehydration within the smallest pores is negligibly small and does not need to be considered explicitly. The width of the Gaussian distribution is adjusted in such a way that the scattering intensity of a single ion fits its theoretical form factor.<sup>166</sup> Finally, in order to obtain the correct relative intensity changes a constant power law term ( $I_{particle}(Q)$  in section 5.1.2) and a constant background accounting for carbon and water structure factor. Due to the continuum treatment of water and carbon both the carbon and water structure factor are not considered in the initial simulated scattering curve. This background is obtained by adjusting measured and simulated scattering intensities at large  $Q$ -values.

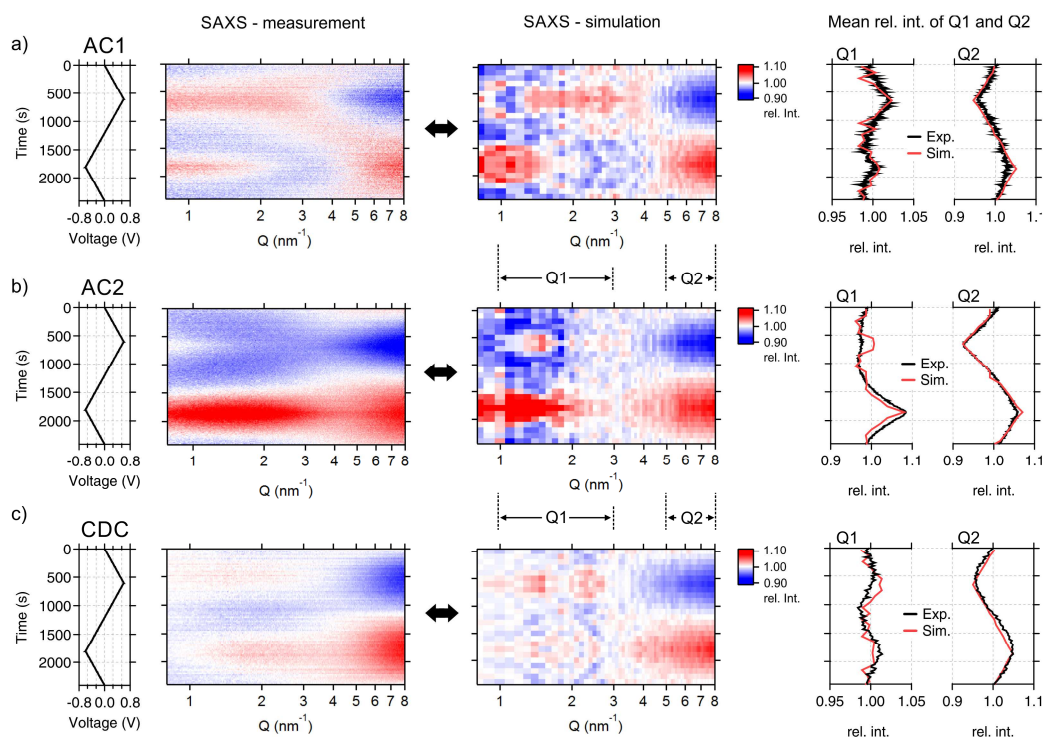


**Fig. 5.20:** Measured and simulated relative SAXS intensity changes as a function of the scattering vector length  $Q$  (horizontal) and time (vertical) for all three carbons (a, b, c). The applied voltage signal (CV,  $1 \text{ mV} \cdot \text{s}^{-1}$ ) is given on the left. On the right mean intensities changes within the  $Q$ -regions Q1 and Q2 are given as a function of time for both experiment and simulation. Reproduced with permission from Ref.<sup>109</sup>. © Nature Publishing Group.

Fig. 5.20 reveals the good agreement between simulated and measured *in situ* SAXS data for all three carbons. On the right the average intensities for the regions Q1 and

Q2 for measured and simulated data were plotted as a function of time, confirming the good correspondence.

#### 5.4.1 Quantifying the local rearrangement and the degree of confinement

More quantitative information can be extracted from the charge dependence of two parameters introduced in the following. To classify the local positions of ions within a complex nanoporous structure, Merlet et al. have established a degree of confinement (DoC)<sup>62</sup> characterizing the spatial environment of an ion. The DoC is a direct measure of how ions “see” the carbon pore structure. Considering the continuum treatment of electrode and solvent in our case (Fig. 5.21), the DoC had to be defined in a slightly different way:

$$DoC = \frac{\sum_i 1/R_{i,C}^2}{\sum_i 1/R_i^2} \text{ for } R_i < R_{cut-off} \quad (5.27)$$

Here,  $R_{i,C}$  is the distance between the centre of the ion and a voxel assigned to the carbon phase within a pre-defined cut-off radius  $R_{cut-off}$  (Fig. 5.21), and the sum runs over all voxels smaller than the cut-off radius and larger than the bare ion radius. The denominator normalizes the expression by its maximum possible value considering distances  $R_i$  between the centre and any voxel within the cut-off radius.

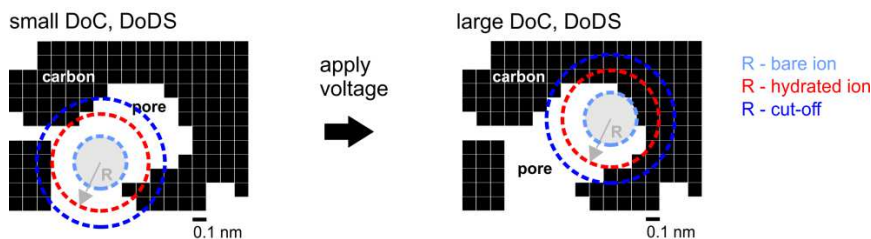


**Fig. 5.21:** A sketch of a two dimensional (2D) cross section of the 3D pore structure is shown to visualize the concepts of degree of confinement (DoC) and degree of desolvation (DoDS). Light blue, red and, dark blue circles represent the bare ion, the hydrated ion, and the cut-off radius for which the DoC is determined, respectively. The ions treated as hard spheres can approach carbon voxels as close as their bare ion radius leading to partial desolvation, which increases the DoDS. Reproduced with permission from Ref.<sup>109</sup>. © Nature Publishing Group.

Fig. 5.22a-c shows that for zero voltage the mean DoC is generally larger for carbons with smaller pore size. If a cell voltage is applied, the mean DoC of counter-ions increases and the one of co-ions decreases. This means that as the number of counter-ions is increased due to ion swapping, they also tend to occupy sites with a higher degree of confinement. Correspondingly, the number of co-ions is decreased and sites

with high DoC become more unlikely. This suggests that ions move preferentially to sites with a specific local surrounding depending on the electrode charge. The shapes of the mean DoC curves in Fig. 5.22a-c show important differences when comparing AC1, AC2, and CDC. In AC1, the increase of the counter-ion DoC tends to be larger than the decrease in the co-ion DoC level, leading to a slightly asymmetric curve. In contrast, the smaller pores in CDC lead to a DoC decrease of co-ions being larger than the counter-ion DoC increase, which may be indicative of a saturation of sites with high DoC.

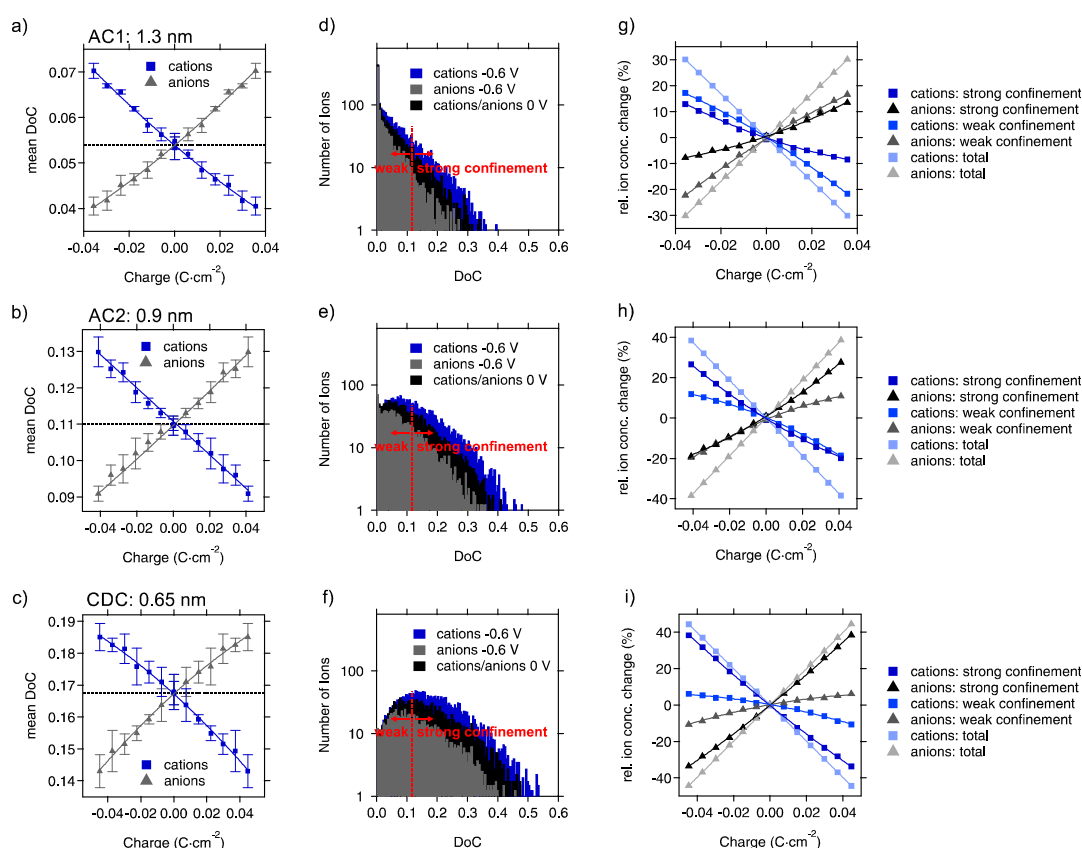


**Fig. 5.22:** a-c, Mean degree of confinement (i.e., mean value of DoC histograms, shown in (d-f) for selected voltages) for cations ( $\text{Cs}^+$ ) and anions ( $\text{Cl}^-$ ) as a function of the electrode charge for AC1 (a), AC2 (b), and CDC (c). Error bars correspond to the standard deviation of mean DoC values from five independent Monte Carlo simulations. Selected DoC histograms of cations and anions are shown for 0 V and for -0.6 V in (d-f). The vertical dotted line separates ions into two groups corresponding to “small” and “large” DoC, representing qualitatively “large” and “small” pores as indicated. g-i, The cation and anion concentration changes relative to their concentration at 0 V are given as a function of the SOC for the two classes of confinement. Reproduced with permission from Ref.<sup>109</sup>. © Nature Publishing Group.

In Fig. 5.22d-f, the number of cations and anions assigned to a specific DoC at 0 V and at -0.6 V cell voltage are plotted in a DoC histogram. The histograms do not only

change their absolute height (depending on the ion concentration) but also their overall shape. Ions on sites with high DoC can be conceptualized as ions in smaller pores. Accordingly, ions were classified in the DoC histogram into two categories, representing ions in either strong confinement ( $\text{DoC} > 0.11$ ) or weak confinement ( $\text{DoC} < 0.11$ ). The value of 0.11 is the mean DoC value of AC2 at 0V and assures that roughly 50% of ions are assigned to strong and the other 50% to weak confinement. This permits to quantify the number of counter- and co-ions in two differing confining environments as a function of the SOC from one single data set, allowing to quantitatively separate the local rearrangement in strong and weak confinement. In Fig. 5.22g-i, the relative change of the cation and anion concentration within the two environments is shown as a function of the SOC, together with the total cation and anion concentration changes. Obviously, the charge dependent ion concentration profile is strongly influenced by the confining environment. When a voltage is applied, the counter-ion concentration increase is smaller (or even inhibited) within pores in weak confinement, while it is strongly increased within the strong confinement (i.e., the smallest pores). While this effect is pronounced for AC2 and particularly for CDC, for AC1, the onset of counter-ion adsorption in small pores is visible (dark blue and black curve bending upwards), involving co-ion expulsion in larger nanopores (blue and grey curve bending downwards). Hence, the overall charge compensating mechanism remains ion swapping (light blue and light grey curve), but the local ion rearrangement occurs in a completely different manner.

Interestingly, the mean DoC value at 0V is significantly lower than the DoC value of a complete random ion arrangement within the pores (shown exemplarily on AC2: red dashed line in Fig. 5.23a). This means that in the actual configuration at 0 V ions are preferably located in the center of the pore or in pores where they are less confined. The hydration energy causes an additional energy expense, when ions move into sites with high DoC (introduction of hydration energy in the simulation see section 5.4.2 and 4). Applying a voltage increases the in-pore counter-ion concentration and therefore the repulsive interactions in-between counter-ions, which in turn makes sites of high DoC more favorable. This finding is in good agreement with a molecular dynamics study of aqueous electrolytes in slit-like pores.<sup>160</sup>

An important aspect is the correct interpretation of a DoC change (Fig. 5.23b). The separation into strong and weak confinement in Fig. 5.22 might be interpreted as a separation into “smaller” and “larger” pores. This implies that it is indeed possible to track and differentiate ion populations in smaller and larger pores within a very narrow size regime. However, the classification into “small” and “large” pores in a complex, disordered 3D network is somewhat arbitrary. As sketched in Fig. 5.23b an increase in the DoC does not necessarily mean that ions move into a different category

of smaller pores. Equivalently the ion could remain essentially in the same pore; it only approaches the surface, as visualized on the top of Fig. 5.23b. An actual relocation into a different category of smaller pores causing the same change in the DoC is sketched on the bottom of Fig. 5.23b. According to the DoC values these geometrically different situations are equivalent. The DoC is an extremely sensitive measure of “how ions see their local surrounding” in terms of physical interactions. Although the two situations are geometrically different, they might be equivalent in terms of physical interactions (which are uniquely tracked by the DoC).

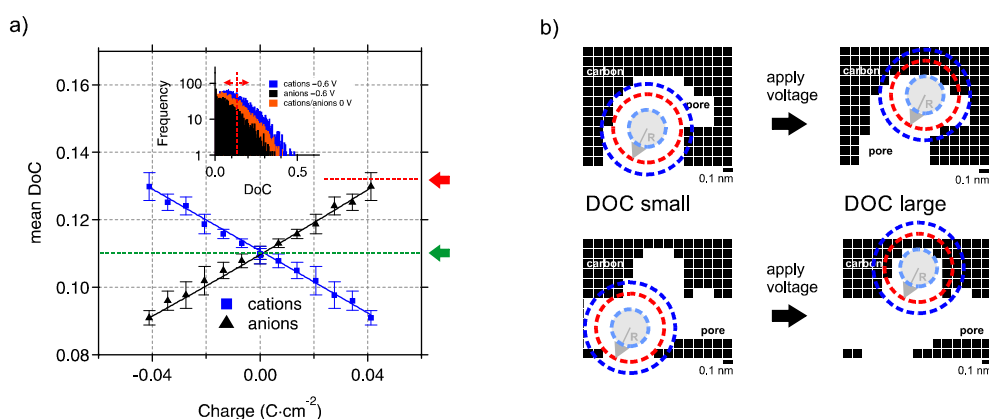


**Fig. 5.23:** The mean degree of confinement (DoC) as a function of electrode charge for AC2, with a DoC histogram in the inset, is given (a). The DoC of a random ion arrangement (red arrow) is larger than the DoC at 0V. In (b) two geometric situations for the same DoC increase are sketched. Blue dashed, red dashed and light blue dashed circles correspond to the cut-off, the hydrated ion and the bare ion radius.

In general, within such 3D pore systems the definition of “small” and “large” pores is a difficult issue. Sub-nanometer pore size distributions are calculated from a single adsorption isotherm of CO<sub>2</sub> molecules (using GSA). A certain amount of physisorbed molecules at a specific pressure in the sorption isotherm is assigned to a certain pore size. This pressure and consequently the calculated pore size may depend more accurately on the DoC of the CO<sub>2</sub> molecules than a difficult-to-define pore size. As a consequence when talking about smaller and larger pores in the sense of the PSDs obtained from gas sorption, it seems more convenient to think about strong and weak confinement, as discussed above. Geometrical constraints like a slit- or cylindrical pore shape do not describe the reality in disordered microporous carbons.

A first important conclusion from the experimental observations in Fig. 5.22 is that the preferred movement of counter ions into sites with high DoC can be explained solely by electrostatic interactions, and is not (necessarily) connected with any specific chemical functionalities of the carbon surface. As visualized in Fig. 5.24, the electrode surface charge density is particularly high around sites with high DoC. In AC1, pores

are generally larger and the mostly negative (red) charge is more equally distributed on the electrode as compared to CDC, where strongly localized regions with high negative charge are visible (compare regions indicated by the dashed lines). Thus, the electrode charge induced by an ion is more localized at sites with high DoC and the electric interaction is most effectively screened at such sites. Once the system is charged, the balance between cations and anions is disturbed and the concentration of counter-ions increases. This means that the energy cost due to counter-ion repulsion is most effectively minimized if more ions move to places with high DoC. The DoC is extremely sensitive to in-pore ion rearrangement from lower- to higher confinement (Fig. 5.22). This process is detectable even in CDC, where the *average* pore size of 0.65 nm represents roughly the hydrated ion size of both  $\text{Cs}^+$  and  $\text{Cl}^-$  ions. This underlines that the average pore size is insufficient to derive quantitative conclusions and the size dispersity of the 3D pore network needs to be considered.<sup>58,167</sup>

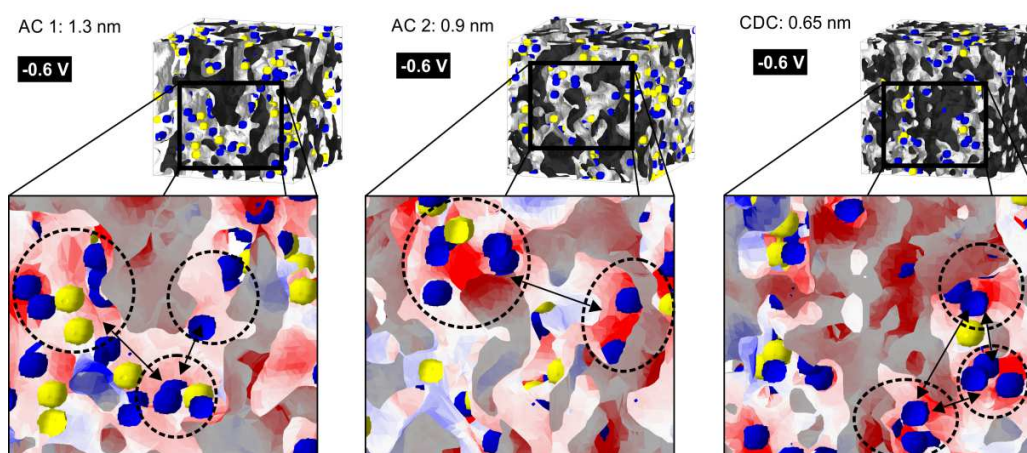


**Fig. 5.24:** a, Cations (blue) and anions (yellow) are visualized for maximum negative applied cell voltage (-0.6 V) for AC1, AC2, and CDC. The magnitude of the local electrode charge density is visualized in the zoomed views. Red means high negative surface charge density, which is generally found close to cations. In contrast, anions induce a positive electrode charge visualized in blue. Between these regions, white areas indicate regions with zero electric field. The charge storage is most localized for the CDC electrode. Compare regions indicated by the dashed lines and arrows; a quantification is given in Fig. 5.26a. Reproduced with permission from Ref.<sup>109</sup>. © Nature Publishing Group.

#### 5.4.2 Quantifying desolvation and the local electrode charge

Quantitative agreement between the SAXS-simulations and the SAXS-experiments was only found (Fig. 5.20) if ions could approach the carbon surface closer than their hydrated radius. Therefore, the required magnitude of the DoC increase is only achieved if at least some of the water molecules in their first hydration shell are distorted or released. This was realized in the MC simulation by allowing the ions to

approach the carbon surface up to the de-hydrated ion radius, and taking an additional energy term for dehydration explicitly into account. To quantify desolvation of ions due to confinement, the degree of desolvation (DoDS) is defined, representing a measure for the number of water molecules lost by an ion as compared to the bulk hydrated ion (Fig. 5.21).

$$DoDS = \frac{\sum_i V_i}{V_{HS}} \text{ for } R_i < R_{HS} \quad (5.28)$$

where  $V_{HS}$  corresponds to the volume of the entire hydration shell and  $\sum_i V_i$  to the volume of all voxels belonging to the carbon phase within the hydration radius  $R_{HS}$ . With this definition, the DoDS covers the range from zero (all ions fully hydrated) to one (all ions fully dehydrated). The energy cost for the partial de-hydration is considered in a semi-quantitative manner by multiplying the hydration energy for a single ion<sup>42</sup> by its DoDS value. A roughly linear correlation is found between DoDS and DoC, independent of the average pore size and pore volume fraction of the carbon electrode (Fig. 5.25a). Assuming an average number of 8 water molecules in the first hydration shell<sup>97</sup>, DoDS histograms can be calculated to reveal the frequency of released water molecules at maximum electrode charge (Fig. 5.25b). As expected, the average number of stripped-off water molecules (black, red and blue arrows in Fig. 5.25b) increases for decreasing average pore size.

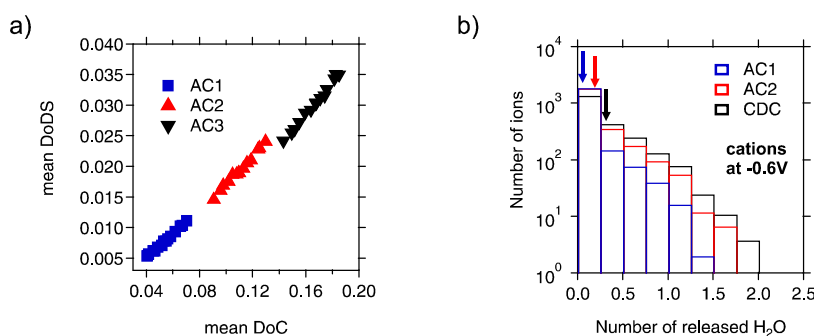


**Fig. 5.25:** The DoDS correlating linearly with the DoC is shown in (b). In (c), a histogram of the number of desolvated water molecules is given for cations in the three carbon electrodes at -0.6 V. Arrows indicate the average number of released water molecules. Reproduced with permission from Ref.<sup>109</sup>. © Nature Publishing Group.

The data demonstrate clearly that some few ions are partially desolvated even in AC1 where the average pore size is considerably larger than the hydrated ion size. Although on average only about 1% of the water molecules are stripped off, the extremely high sensitivity of the approach demonstrates that even AC1 exhibits sites with a high DoC, where it is energetically favourable to strip-off parts of the



hydration shell. Ion desolvation seems to be a universal phenomenon for virtually all nanoporous carbons because of the pore size dispersion and presence of ultranarrow (subnanometer) pores.

The fact that partial de-solvation of ions is quantified from a *structural* viewpoint in this work is different to recent eQCM studies. Those studies investigated aqueous electrolytes in activated carbons with comparable pore size<sup>65</sup> The average number of released water molecules per single ion is much smaller in our investigation. In this work the first hydration shell is considered as the sum of water molecules coordinating the ion (*structural* viewpoint) rather than the sum of water molecules bound with a certain binding energy to the ion (*energetic* viewpoint). While the water molecules in the first hydration shell are in confinement certainly weaker bound to the ion than in bulk (among other reasons due to the decreased dielectric constant of water in confinement), in this work the hydration shell is strictly defined as the nearest (neighboring) water molecules coordinating the ion.

For large ions like Cs<sup>+</sup> the remaining number of water molecules within the hydration shell was found to be zero in the eQCM studies, while in our study even for the carbon with the smallest average pore size on average only one molecule out of eight was released from the first shell. One reason for this apparent contradiction might be the strategy how the number of hydrated water molecules is calculated. The relevant eQCM study<sup>65</sup> inherently assumes that the total number of in-pore water molecules (apart from those in the hydration shell) remains constant during electrosorption. In this work on the other hand a constant *water density* within the pore is assumed, allowing the exchange of some water molecules if the total number of (partially hydrated) ions is increased during electrosorption. It appears being a physically more realistic assumption that each additional counter-ion occupying a part of the pore volume leads necessarily to the expulsion of some water molecules from the pore. Effectively, the assumption of confined, non-exchangeable water molecules might lower the actual hydration number for the relevant eQCM study, since a significant increase in the total ion concentration (permselectivity or counter-ion adsorption) was observed there. Small influences from water molecules on the measured quantities (mass or electron density contrast for eQCM and SAXS, respectively) should, within our picture, only occur due to the denser hydration shell compared to the bulk water. Only by considering such a model the scattering data can be described properly, first introduced in section 5.3 (Table 5.3). The tracking of the position of the individual ions within the pores along with the quantification of de-solvation from a *structural* point of view indicates that a complete loss of the solvation shell seems unlikely within such nanopore structures.

On the other hand, the continuum (non-atomistic) treatment of water and carbon molecules implies that the entire volume within the carbon pore is rather equally occupied by water, which might be wrong in reality. Hence the number of released water molecules extracted from this experiment certainly represents a lower limit.

As visualized in Fig. 5.24, the magnitude of stored electrode charge within the cut-off radius ( $R_{cut-off}$ , Fig. 5.21) increases for ions with higher DoC. Accordingly, the *local* electrode charge ( $\Delta q/V$ ) coordinating the ion also increases with increasing DoC (Fig. 5.26a). The correlation between *local* electrode charge and DoC (Fig. 5.26b) implies that also the integral capacitance per micropore volume ( $C/V = \Delta q/(V \cdot \Delta U)$ ) should closely correlate with the DoC. In physical terms, this means that the electric field of highly confined ions is screened most effectively, representing the actual mechanism responsible for the enhanced area normalized capacitance<sup>54</sup>, as was already outlined for a more simple geometrical situation by Kondrat et al.<sup>168</sup>. The results predict that this effect represents an inherent mechanism of electrical double-layer formation within different microporous carbons. The correlation between DoDS and DoC infers that the performance difference between different carbons involves not only differences in the DoC level but also in the number of released solvent molecules. Therefore, with DoC and DoDS being experimentally accessible parameters, a performance prediction of nanopore structures for EDLC systems is possible.

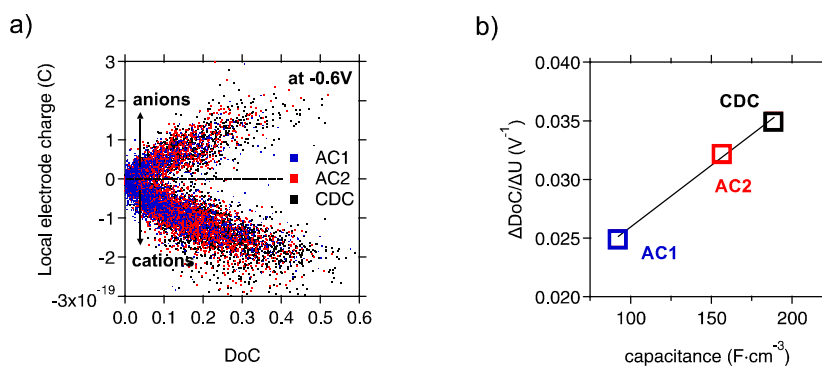


**Fig. 5.26:** In (a), a histogram of the number of desolvated water molecules is given for cations in the three carbon electrodes at -0.6 V. Arrows indicate the average number of released water molecules. The graph quantifies the visualization of the electrode charge in Fig. 5.24. As shown in (b), the magnitude of the local electrode charge (charge on coordinating carbon) increases for cations or anions sitting on sites with larger DoC. Therefore, the slope of the mean DoC (Fig. 5.22a) correlates linearly with the experimentally determined capacitance normalized by the micropore volume (b). Reproduced with permission from Ref.<sup>109</sup>. © Nature Publishing Group.

### 5.4.3 Arrangement and kinetics of ions

In the following, *in situ* SAXS experiments dealing with ion kinetics are presented and discussed, by applying the data analysis strategy explained above on *in situ*

experiments using an AC2 electrode and a 1 M CsCl aqueous electrolyte. Since the simulated data represent the equilibrium configuration of ions for a certain electrode charge, the experimental CV cycles should be performed with slowest possible scan rate (here 0.5 mV/s was used). As visualized in Fig. 5.27a-b the experimental (a) and simulated (b) SAXS intensity as a function of the applied voltage signal agree well on a quantitative level. As the DoC is very sensitive to the local environment of ions it can be used as a quantity describing the voltage dependent *local* ion rearrangement (section 5.4.1). In Fig. 5.27c, the mean DoC and the global ion concentration (calculated from Eq. 5.19-5.20) of cations and anions are plotted as a function of time. As the concentration of counter-ions increases their mean DoC increases as well. It was discussed in section 5.4.3 that the tendency of counter ions to adsorb in sites with high confinement upon charging is a consequence of the optimized screening of repulsive ion-ion interactions by free electrode charges (electrons or holes) of the conducting carbon in those sites.

In the intermediate Q-regime (denoted Q1 in Fig. 5.27a-b) a strong and a weak intensity maximum occur at maximum negative and positive voltage, respectively. The strong maximum can be assigned to the local rearrangement as quantified by the DoC. The weak maximum is an effect caused by the global ion concentration change, as explained in detail in section 5.3. Using the knowledge about global and local ion rearrangement, the dynamics and scan rate dependency of ion rearrangement can be studied. The average intensity of the intermediate Q-regime Q1 is plotted as a function of time in Fig. 5.27d for three different CV scan rates (0.5, 2.0, and 5.0 mV/s). A time lag between the maxima of the average SAXS intensities and the applied voltage signal (indicated by orange and green arrows) is clearly observed, which becomes larger for faster cycling. This phenomenon is tentatively explained as follows: As visualized in the experimental section 3 all cell materials except of the investigated WE contain a hole of 3 mm, which makes the ion diffusion pathway between the irradiated WE volume and the CE rather large, explaining the larger time shift at higher scan rates. Most interestingly, the time shift is not equal for the strong (assigned to local rearrangement) and the weak intensity maxima (assigned to global concentration change), as shown in Fig. 5.27e. They were calculated as the difference between the center of mass of the relative intensity peaks and the voltage maxima/minima beforehand. The difference between local and global time shifts is further supported by the fact that the weak maxima in Fig. 5.27d become increasingly asymmetric for larger scan rates (see black curve). Obviously, the global ion transport in and out of the WE is less dependent on the scan rate than the local ion rearrangement. In other words, the global cation and anion concentration is accommodated faster than the local ion arrangement. In the following some first tentative explanations for this observation are discussed.

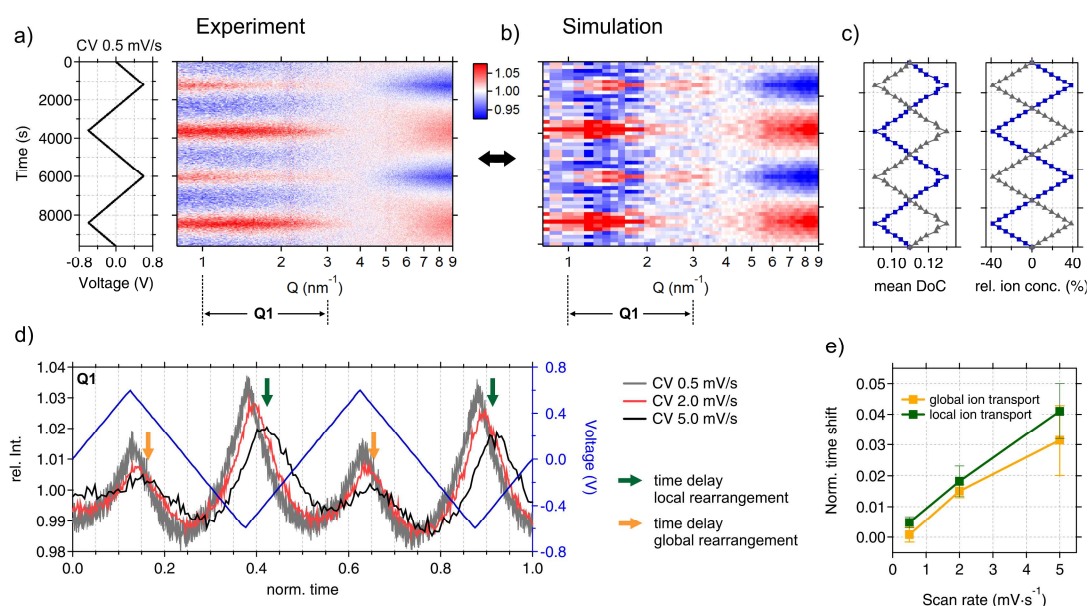


**Fig. 5.27:** Relative scattering intensity as a function of the scattering vector length  $Q$  and time during two full CV cycles from SAXS (a) and from the FFT of the MC simulations (b). The mean Degree of Confinement (DoC) of cations (blue) and anions (grey) and the global ion concentration change of cations and anions are plotted vs. time in (c). The average intensity change within the selected  $Q$ -regime  $Q_1$  is shown for CV cycles with three different scan rates (0.5, 2.0, 5.0 mV/s) (d). The time on the x-axis is normalized by the double period, and the applied voltage signal is given in blue. Orange and green arrows indicate intensity maxima assigned to global and local ion rearrangement, respectively. The time delay of the global rearrangement is smaller than for the local rearrangement, as shown in (e). Ref.<sup>108</sup> - Published by the PCCP Owner Societies.

As explained in section 5.4.1 the local rearrangement of counter-ions into sites with high DoC happens as a response to the global increase of counter-ions and decrease of co-ions. The repulsion between counter-ions and optimized screening by the conducting electrode makes sites with high DoC energetically favorable. During fast voltage cycling the global concentration is accommodated relatively fast compared to the equilibrium arrangement of ions. Moreover the rearrangement towards highest confinement is often accompanied with partial desolvation of ions. This energy barrier could cause an increase of the diffusion coefficients in strong confinement and therefore qualitatively explain the time lag between global and local rearrangement. A decrease of the ion diffusion coefficient in confinement was recently confirmed by Molecular dynamics simulations<sup>169</sup> and *in situ* NMR experiments.<sup>45</sup> Another aspect is the characteristics of the electrochemical potential distribution within the pore system. The energy gain for counter-ions to generally move into the micropores is rather large (equivalently for co-ions leaving these pores). Consequently, the gradient in the electrochemical potential and the driving force for counter-ions moving into these

pores is large. The energy gain for the correct structural (local) arrangement within the pores is relatively small, which means that the driving force for ions to rearrange at the local scale is rather small and slow in time. This might also explain the differences in the kinetic behavior.

This behavior implies that during fast cycling the system is far from the equilibrium configuration for a given cell voltage. Globally, the counter-ion (co-ion) concentration increases (decreases) rather fast, although their configuration on a local scale has not yet reached its equilibrium configuration of lowest energy.

#### 5.4.4 Empirical ion rearrangement algorithm

Apart from the simulation based ion arrangement using physical interactions, ions could be arranged within the carbon models (section 5.1.5) based on an empirical algorithm (details see Appendix B). Subsequent Fourier Transformation yields the *in situ* scattering data, which can be compared to the measured one. Input parameters for the empirical algorithm are then iteratively adapted to achieve best correspondence between measured and modeled scattering curves. As mentioned, the degree of confinement is a parameter that precisely depicts the local surrounding of each ion and the degree of carbon atoms coordinating the ion. Considering the screening effects of conducting pore walls it seems reasonable that ions preferably move into sites with highest possible degree of confinement as the counter-ion concentration increases. This is accounted for by arranging ions within the pore structure in such a way, that the probability for an ion to be located at a certain position is enhanced for a site with higher degree of confinement.

Ions are arranged within the pore structure similar to the Monte Carlo simulation discussed in section 4. Instead of accepting a Monte Carlo move according to the Metropolis criterion, a certain position is accepted by assigning the corresponding DoC with an empirically defined acceptance probability. This is implemented in an algorithm, written in the programming language Igor Pro. The structure of this algorithm along with the most important code lines are given in Appendix B.

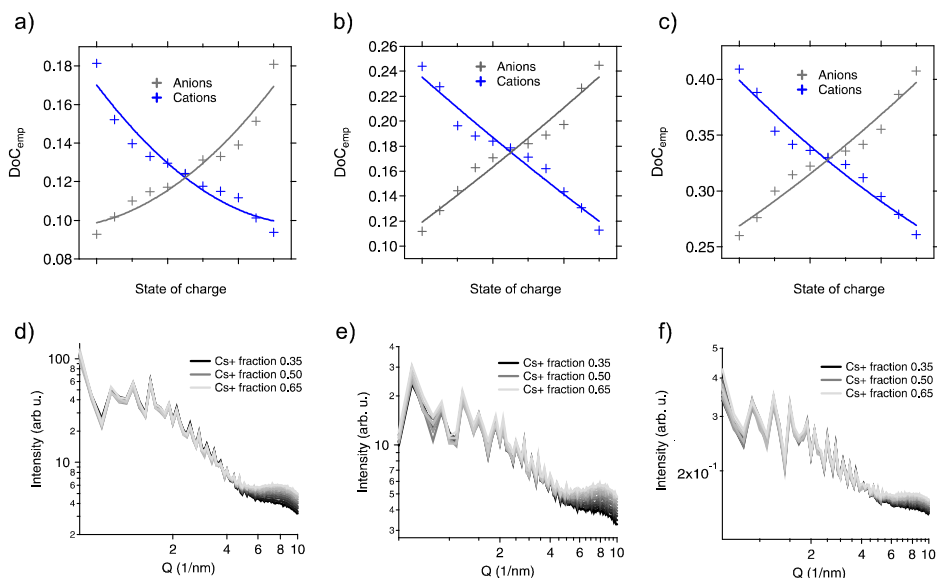


**Fig. 5.28:** Mean DoC curves as a function of the state of charge (SOC) for the three different carbons AC1 (a), AC2 (b), and CDC (c). Input parameters of the algorithm are adjusted in such a way that a certain mean DoC curve gives modelled scattering curves (Fig. 5.29) with good correspondence to the measured scattering curves. Modelled SAXS intensities vs. the scattering vector length  $Q$  for different states of charge for AC1, AC2 and CDC are given in (d), (e) and (f) respectively.

Applying this algorithm to the three different carbons, results in mean DoC curves as shown in Fig. 5.28a-c (empirically determined input parameters: factors in point 2, Appendix B). Ion concentrations are predefined from XRT measurements, equivalent to the Monte Carlo simulation. The spherical average of the amplitude of the Fourier transformed electron-density-weighted real space structure gives the modeled scattering curves (Fig. 5-28d-f). Normalization results in the time (or voltage) dependent heat plots of the *in situ* scattering data (section 3.2.2). Considering the rather simplistic model of reducing all local ion rearrangement effects to the change of a single parameter (namely the DoC) the modeled and measured scattering data agree reasonably well (Fig. 5.29). This further confirms that ion – ion correlations seem to play a minor role regarding the structural arrangement within such disordered nanopores. Local ion rearrangement towards sites with high DoC (accompanied with partial desolvation) seems to be the main effect, apart from global ion concentration changes, that is traceable in the SAXS  $Q$ -regime.

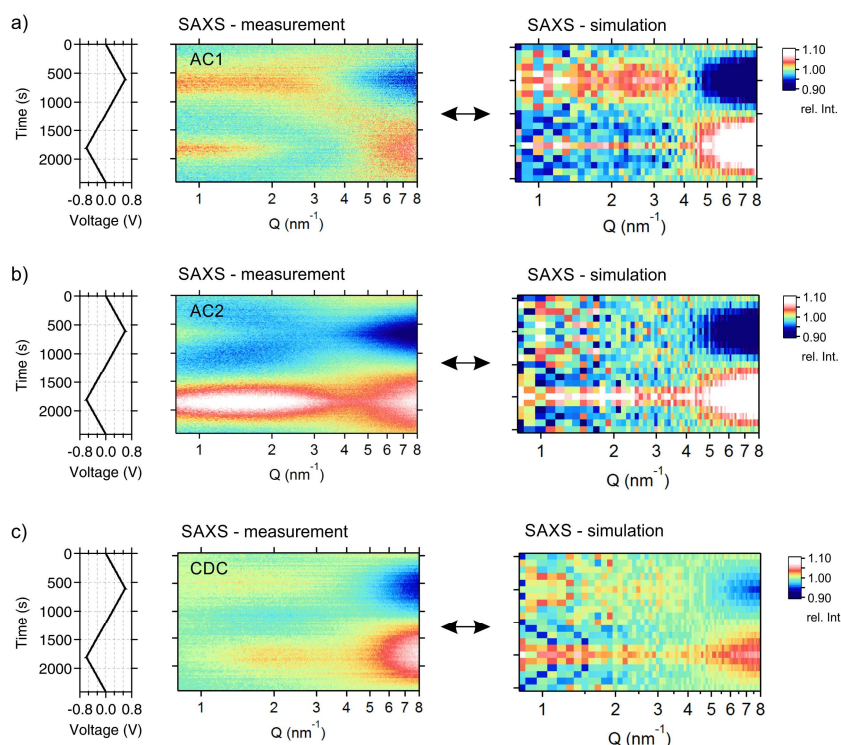


**Fig. 5.29:** Measured and modelled relative SAXS intensities as a function of the scattering vector length  $Q$  and the time (applied voltage) for AC1 (a), AC2 (b) and CDC (c).

#### 5.4.5 The data analysis strategy – summary

Parts of chapter 5.4.5 are not original and have been published in Ref.<sup>108,109</sup>. Fig. 5.30 and Table 5.4 visualize and summarize the developed data analysis strategy.

**Table 5.4:** Data analysis - summary

1	Primary SAXS data treatment; Plot relative change of the SAXS intensity as a function of time during cyclic voltammetry.
2	Generate pore structures (GRF approach; fit of <i>ex situ</i> SAXS data from empty carbon)
3	Fill structure with cations and anions (water and carbon are treated as continuum phases); Rearrange ions properly as a function of the electrode charge (Monte-Carlo simulation or empirical algorithm)  Weight carbon, water and ions with their corresponding electron densities; Calculate the Fourier Transform (FFT) square of the electron density map and perform a spherical average.
4	Compare resulting simulated intensity changes as a function of time or the applied voltage with the measured <i>in situ</i> SAXS data

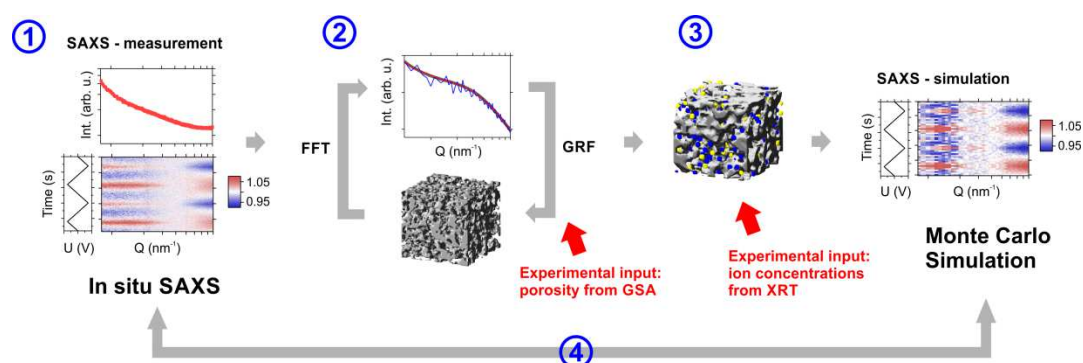


**Fig. 5.30:** Visualization of the data analysis strategy, called SuSan (Supercapacitor Sandbox toolkit). Ref.<sup>108</sup> - Published by the PCCP Owner Societies.

Since the SAXS intensity changes during voltage cycling are relatively small (a few percent only), all SAXS curves are normalized by the average of all SAXS curves. After this step, the relative SAXS intensity changes can be plotted as a function of time and the scattering vector length  $Q$  (step 1 in Fig. 5.30). A three-dimensional real-space structure of the nanoporous carbon is then calculated from the SAXS curve of the empty carbon using the concept of GRFs as described in section 5.1.5 (step 2). In step 3, ions are artificially placed into the GRF-based real-space pore structure, and rearranged via Monte Carlo simulation. The simulations include electrostatic ion-ion and ion-electrode interactions, with the carbon phase assumed as perfect conductor and the water solvent as a continuous dielectric phase (section 4). The number of cations and anions in the simulation box are an experimental input (see section 5.2 above). Alternatively ions could be arranged following an empirical algorithm (see section 5.4.4). After reaching equilibrium, the entire real-space structure (carbon, water, cations and anions) are weighted by the corresponding electron densities, and the squared amplitude of the spherically averaged FFT is calculated. Doing this for several states of charge, relative simulated SAXS intensity changes (step 4) can be plotted.

In conclusion, the comprehensive data analysis methodology presented in this work allows retrieving time-resolved real-space information on the structure and kinetics of ion electrosorption from *in situ* SAXS experiments. If an analytical correlation function can be employed to describe the scattering curve, the concept of GRFs can be used to produce a 3D real space model of the nanoporous carbon. Using this structure, guest phases can be virtually placed into the pore structure and arranged properly using a convenient algorithm describing the physical process (usually simulation based, e.g., molecular dynamics or Monte Carlo simulations). Weighting the resulting multiphase real space structure with the corresponding electron densities



and subsequent FFT allows re-calculating and perhaps even fitting experimentally measured *in situ* SAXS data. This general strategy will be applicable also for other systems or processes apart from ion electrosorption, for instance for gas adsorption as a function of vapor pressure.

The data obtained from this analysis allow not only quantifying the degree of confinement and the degree of desolvation but also subtle differences between local and global kinetics of ion rearrangement. Although the two-phase carbon pore model does not account for fine structural details on the atomic scale, it seems to be extremely sensitive for describing *in situ* ion redistribution in supercapacitor electrodes. As an important consequence, this implies that many structural details do not actually matter for processes regarding ion electrosorption, if the nanopore structure is correctly described in its statistical sense.



## 6 Conclusions and Outlook

Parts of section 6 are not original and have been published in Ref.<sup>70,108,109</sup>. In the framework of the present thesis small angle X-ray scattering was established as a novel *in situ* method to study structural aspects of ion electrosorption in nanoporous carbons, which were so far not accessible to any other technique. In contrast to other methods, such as *in situ* NMR or eQCM<sup>22</sup>, scattering data provide information on structural details of ions within carbon nanopores. Moreover the high brilliance of modern Synchrotron radiation sources enables time resolutions in the milliseconds regime. Thus, the rearrangement of ions, their global concentration change and ion kinetics can be studied during charging and discharging an *in situ* supercapacitor cell. Simplified two-phase models opened a first way to interpret the rather complex SAXS data (section 5.3). However, for a comprehensive description of *in situ* data, using other carbon electrodes and electrolytes, a more sophisticated approach was needed. The multiphase nature of the system carbon, water, cations and anions makes a derivation of an analytical model extremely difficult. To overcome this problem a two-phase model of the bare carbon structure was derived, the third and fourth phase (cations and anions) placed at convenient positions in the structure, and a scattering curve calculated using a Fast Fourier Transformation. Considering the fact that an actual physical model was used to position cations and anions (Monte Carlo simulation), which gave in turn simulated scattering curves that are in good correspondence to the measured scattering curves, the model description and their results appear to be close to reality. As a big advantage of the developed approach details about the ion structure can now be studied in real space, which dramatically simplifies the interpretation.<sup>70,108,109</sup>

Specifically, counter-ions were found to move into sites with highest possible degree of confinement, even to the energetic expense of the (partial) hydration energy (section 5.4.1 - 5.4.2). Thereby the repulsive coulombic interactions in-between counter-ions are effectively screened by the conducting carbon. At the same time co-ions move into sites with weaker confinement. Local ion rearrangement was found to be accompanied with the partial desolvation of ions, and was detected even in carbons with rather large mean pore size (e.g. AC1: 1.3 nm). Conclusively, the degree of local ion rearrangement turned out to be intrinsically linked to the amount of stored charge in a nanopore. Atomistic details on the ion charge storage mechanism could explain differences in the macroscopic performance of different electrode materials. Thus, in

order to find out which electrolyte-electrode combination is beneficial (i.e. cation and anion concentration changes must be large), the study of structural aspects regarding ion packing within the nanopore confinement contains the crucial information. This underlines the high potential of *in situ* scattering techniques to unravel physical mechanisms in functional, complex porous materials.<sup>108,109</sup>

Having in mind one of the main results of the present work, namely counter-ions can be packed most densely in pore structures where the local rearrangement and consequently the geometrical confinement is highest (section 5.4.1), idealized pore structures could be developed on the computer and serve as a model for synthesizing new carbons. Although ion packing within the available pore volume was found to work most effectively in the CDC electrode, the overall surface, the pore volume fractions and consequently the gravimetric capacitance are relatively low compared to AC2. Thus, pore structures allowing a large local rearrangement of ions upon charging and discharging reveal an effective screening of the counter-ion - counter-ion repulsion. However the pore volume fractions in such optimized pore morphologies need to be large in order reach beneficial macroscopic performance values. Too small carbon matrix fractions on the other hand could lead to an overlap of electronic space charge regions, lowering again the surface normalized capacitance (saturation effect discussed in section 2.5.1).<sup>91</sup>

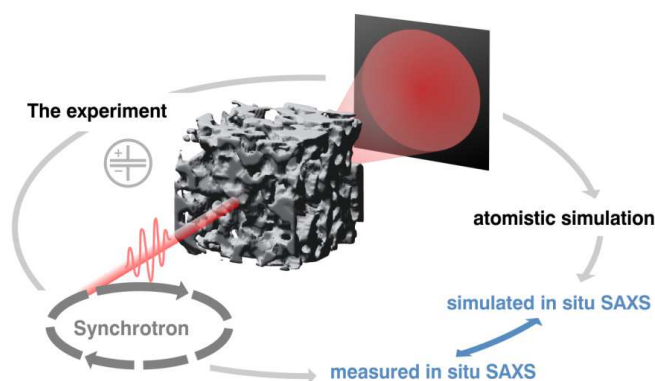


**Fig. 6.1:** Schematic representation of the developed method called Super Capacitor Sandbox (SuSan)

The developed method in this way represents a major step towards a better predictability of the performance of nanoporous carbons for supercapacitor systems on the one hand, and the possibility of experimental validation of theoretical simulation attempts to describe EDLC related phenomena on the other hand. The level of complexity of the simulation may be extended to take, for instance, surface

functionality, local dielectric water behaviour, or locally differing electrical conductivity of the carbons into account.

*In situ* SAXS data shown in section 5 are all recorded at a Synchrotron radiation source. However, for slow cycling high-quality *in situ* SAXS data can be recorded even at a laboratory SAXS system (Fig. 6.2) with a conventional X-ray micro-source (experimental details, section 3.2). The ability to perform high-quality *in situ* experiments in well-equipped X-ray labs is a big advantage, since Synchrotron beamtime is in any case limited and slow cycling more likely corresponds to the equilibrium ion configurations obtained from Monte Carlo simulations. Thus, similar experimental and data analysis approaches might find applications in many fields of supercapacitor research and beyond, where ion adsorption or molecule physisorption within confined geometry plays an important role, for example in the field of electrochemical water treatment or carbon hydrogen storage.

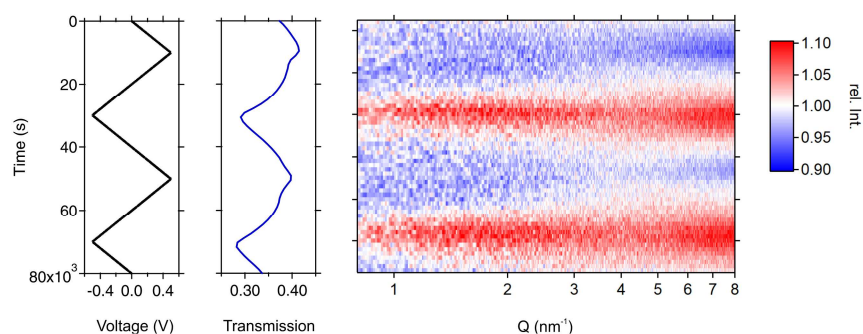


**Fig. 6.2:** *In situ* SAXS experiment (with AC2 and 1 M CsCl) carried out at the in-house SAXS/WAXS system, applying cyclic voltammetry ( $\pm 0.5$  V) with a scan rate of 0.05 mV/s. More specifically, the applied voltage signal, the transmission signal and the normalized SAXS curves (rel. intensity vs. scattering vector length  $Q$ ) are given as a function of time. The noise level of the measured relative SAXS intensity is comparable to (faster) Synchrotron measurements, shown in section 5.

To further increase the accuracy and precision of the developed method contrast variation experiments are planned in near future. Anomalous X-ray scattering allows the splitting of the individual cation and anion scattering contributions by varying the incident X-ray energy close to an absorption edge of the corresponding ions. This gives on the one hand more precise structural information of ions but on the other hand a better knowledge about changes in the water structure factor and structural changes of the carbon due to electrosorption induced strain.

Using different nanoporous carbons, the concept of Gaussian random fields was successfully applied to obtain 3D real space structural models (section 5.1). A simple algorithm was developed to deduce a specific pore size distribution. The size

distribution was found to agree reasonably well with the one obtained from gas sorption analysis under the assumption of slit-like pores, although the actual pore structure is far from being slit-like. This underlines the importance of having some a-priori information on the pore shape when interpreting size distributions from GSA.

Being able to accurately measure local and global ion rearrangements, second order effects like electrosorption induced pore swelling could be understood on a more fundamental basis in future. So far explanations for electrode swelling in supercapacitor electrodes were contradicting.<sup>73</sup> In a collaborative work between the Institute of Physics (MU Leoben), the University of Salzburg and the INM Saarbrücken, we could show that ion rearrangement in micropores play a dominant role in determining macroscopic electrode swelling, using *in situ* SAXS on hard templated carbon “model materials”.<sup>170</sup> The magnitude of DoC change during charging might be intrinsically linked to the electrode strain.

In general the degree of confinement is a parameter accurately accounting for interactions between ions, atoms or molecules and a confining host. Even more it seems to be a universal parameter to determine the actual physical interaction of confined species with its surrounding. More accurately than any other approaches which include an assumption about the pore shape (e.g. slit-like), the DoC is related to how the molecule or ion “sees” its local surrounding in terms of physical interactions. As discussed in section 5.4.1 different geometrical situations could cause a similar DoC value or a similar change of the DoC during a local rearrangement. In terms of physical interactions, (e.g. Coulombic interactions between ion and conducting carbon or van der Waals interactions in the case of molecule physisorption), these two situations might be equivalent. Gas sorption analysis for micropores<sup>146</sup> for instance involves the recalculation and assignment of these physical interactions (measured in the form of a relative pressure in the sorption isotherm) into a pore width of a slit-like pore (distance between two infinitely extended plates). Evidently, a specific pore size in a PSD obtained from gas sorption cannot uniquely be assigned to a specific pore with a certain size and shape and does not necessarily cover the correct geometrical situation. The PSDs obtained from SAXS measurements on the other hand do not require any a-priori assumption about the pore shape. In future work a direct verification of PSDs from gas sorption analysis and their errors could be performed by combining SAXS, the GRF derived pore model and an algorithm involving the DoC parameter. A DoC histogram of Argon atoms placed randomly into the GRF pore model could be translated to a DoC histogram of slit-pores and directly compared to a PSD obtained from GSA with slit-pore assumption.

The data presented in this thesis also help to draw a clearer picture of how electrode charge is counterbalanced in aqueous media with high ionic strength (section 5.2).

Globally, charge accommodation is accomplished without changing significantly the total number of ions in the pores (cations plus anions). Effectively, this corresponds to what is known as ion swapping. As known from capacitive deionization lower salt concentrations should lead to a transition towards preferred counter-ion adsorption. First test experiments showed that this is indeed the case. However, it turned out that the particular cell design and the ion kinetics, which in turn depends on the salt concentration and the scan rate, play a crucial role in the actual charge storage formation on the atomic scale.

In particular X-ray transmission experiments were performed on *in situ* cells with an increased electrolyte reservoir (5 x separator) by varying salt concentrations and scan rates of the applied CV cycles. The logarithm of the transmission signal is proportional to the sum of cation and anion concentration change weighted by their mass attenuation concentration change (section 5.2, Eq. 5.19). An exact quantification of cation and anion concentration changes in absolute numbers is problematic for low salt concentrations due to the slow ion transport in the bulk electrolyte and the particular cell design (discussion see section 3.2.1). As visualized in Fig. 6.3 a clear transition towards preferred counter-ion adsorption could be observed with decreasing salt concentration. However, increasing the scan rate causes even at lowest salt concentrations a transition towards ion swapping. Conclusively this means that the actual mechanism of ion electroadsorption depends inherently on the kinetic properties of the whole system (the entire cell).

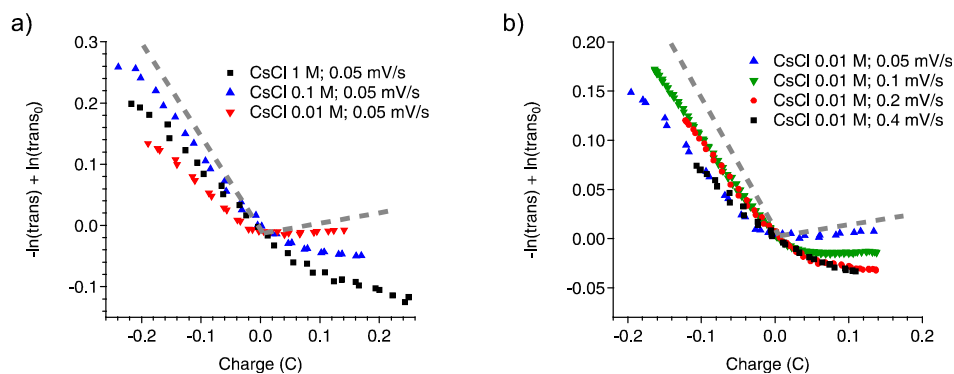


**Fig. 6.3:** Logarithm of the transmission signal as a function of the electrode charge, using *in situ* cells with different electrolyte salt concentrations (a), and using a cell with a salt concentration of 0.01 M at different scan rates (b). The grey dashed line indicate the theoretical transmission change for pure counter-ion adsorption, neglecting any exchange of water molecules.

This further implies that not only the comparability between different *in situ* techniques (all using very specific cell designs), but also between sophisticated experiments and commercial devices is limited. Specific charge storage mechanisms

---

detected on the smallest accessible length scale, should be only named as “fundamental and general” as long as the particular cell design, scan rate and salt concentrations are considered. This further emphasizes a well-known issue in supercapacitor research. It is extremely difficult (and requires extremely long charging times) to obtain a stable equilibrium ion configuration in the nanoporous electrodes of a supercapacitor. In an experimental situation the particular behavior of ions on the atomic scale usually have to be drawn from metastable ion configurations that can change significantly by slightly changing e.g. the temperature, the size of the electrolyte reservoir or the salt concentration. Therefore a systematic investigation of the supercapacitor’s metastability properties is essential to improve the comparability between fundamental studies using atomistic simulations and *in situ* experiments and consequently the performance of commercial devices in future.



## 7 Bibliography

- 1 Meinshausen, M. *et al.* Greenhouse-gas emission targets for limiting global warming to 2 °C. *Nature* **458**, 1158-1162 (2009).
- 2 Raftery, A.E. *et al.* Less than 2 °C warming by 2100 unlikely. *Nature Clim. Change* advance online publication, 10.1038/nclimate3352 (2017).
- 3 van Vuuren, D.P. *et al.* The representative concentration pathways: an overview. *Clim. Change* **109**, 5 (2011).
- 4 Schmidt, O., Hawkes, A., Gambhir, A. & Staffell, I. The future cost of electrical energy storage based on experience rates. *Nat. Energy* **6**, nenergy2017110 (2017).
- 5 Whittingham, M.S. History, evolution, and future status of energy storage. *Proceedings of the IEEE* **100**, 1518-1534 (2012).
- 6 Kato, Y. *et al.* High-power all-solid-state batteries using sulfide superionic conductors. *Nat. Energy* **1**, 16030 (2016).
- 7 Lu, M., Beguin, F. & Frackowiak, E. *Supercapacitors: materials, systems and applications*. 509-526 (John Wiley & Sons, 2013).
- 8 Jost, K. *et al.* Knitted and screen printed carbon-fiber supercapacitors for applications in wearable electronics. *Energy Environ. Sci.* **6**, 2698-2705 (2013).
- 9 TTI Europe, *The Global Supercapacitor Market is Facing Unique Challenges in 2016*, <http://www.ttieurope.com/object/me-zogbi-20161003.html>, 2016, (accessed 28.07.2017).
- 10 Lu, M., Beguin, F. & Frackowiak, E. *Supercapacitors: materials, systems and applications*. 307-371 (John Wiley & Sons, 2013).
- 11 Raviv, U., Laurat, P. & Klein, J. Fluidity of water confined to subnanometre films. *Nature* **413**, 51-54 (2001).
- 12 Chathoth, S.M. *et al.* Fast diffusion in a room temperature ionic liquid confined in mesoporous carbon. *Europhys. Lett.* **97**, 66004 (2012).
- 13 Ting, V.P. *et al.* Direct Evidence for Solid-like Hydrogen in a Nanoporous Carbon Hydrogen Storage Material at Supercritical Temperatures. *ACS Nano* **9**, 8249-8254 (2015).
- 14 Béguin, F., Presser, V., Balducci, A. & Frackowiak, E. Carbons and Electrolytes for Advanced Supercapacitors. *Adv. Mater.* **26**, 2219-2251 (2014).
- 15 Suss, M.E. *et al.* Water desalination via capacitive deionization: what is it and what can we expect from it? *Energy Environ. Sci.* **8**, 2296-2319 (2015).
- 16 Shi, W., Friedman, A.K. & Baker, L.A. Nanopore Sensing. *Anal. Chem.* **89**, 157-188 (2017).
- 17 Salanne, M. *et al.* Efficient storage mechanisms for building better supercapacitors. *Nat. Energy* **1**, 16070 (2016).

- 18 Fic, K., Lota, G., Meller, M. & Frackowiak, E. Novel insight into neutral medium as electrolyte for high-voltage supercapacitors. *Energy Environ. Sci.* **5**, 5842-5850 (2012).
- 19 Chun, S.-E. *et al.* Design of aqueous redox-enhanced electrochemical capacitors with high specific energies and slow self-discharge. *Nat. Commun.* **6**, 7818 (2015).
- 20 Lee, J. *et al.* Nanoconfinement of redox reactions enables rapid zinc iodide energy storage with high efficiency. *J. Mater. Chem. A* **5**, 12520-12527 (2017).
- 21 Lee, J. *et al.* Tin/vanadium redox electrolyte for battery-like energy storage capacity combined with supercapacitor-like power handling. *Energy Environ. Sci.* **9**, 3392-3398 (2016).
- 22 Forse, A.C., Merlet, C., Griffin, J.M. & Grey, C.P. New Perspectives on the Charging Mechanisms of Supercapacitors. *J. Am. Chem. Soc.* **138**, 5731-5744 (2016).
- 23 Prehal, C. *In-situ SAXS study on the ion dynamics in microporous carbon based supercapacitors*. Master of Science thesis, Montanuniversitaet Leoben, (2014).
- 24 Als-Nielsen, J. & McMorrow, D. in *Elements of Modern X-ray Physics* 1-28 (John Wiley & Sons, Inc., 2011).
- 25 Chantler, C.T. *et al.* *Detailed Tabulation of Atomic Form Factors, Photoelectric Absorption and Scattering Cross Section, and Mass Attenuation Coefficients for Z = 1-92 from E = 1-10 eV to E = 0.4-1.0 MeV*, <<http://physics.nist.gov/PhysRefData/FFast/html/form.html>>, NIST, Physical Measurement Laboratory (1995, 1996, 2001).
- 26 Als-Nielsen, J. & McMorrow, D. in *Elements of Modern X-ray Physics* 239-273 (John Wiley & Sons, Inc., 2011).
- 27 Als-Nielsen, J. & McMorrow, D. in *Elements of Modern X-ray Physics* 113-146 (John Wiley & Sons, Inc., 2011).
- 28 Kittel, C. *Introduction to solid state physics*. 23-43 (Wiley, 2005).
- 29 Sztucki, M., Di Cola, E. & Narayanan, T. Instrumental developments for anomalous small-angle X-ray scattering from soft matter systems. *J. Appl. Crystallogr.* **43**, 1479-1487 (2010).
- 30 Sturm, K. in *Streumethoden zur Untersuchung kondensierter Materie (IFF Ferienkurs, Vorlesungsmanuskripte)* Ch. A2, 1-30 (1996).
- 31 Als-Nielsen, J. & McMorrow, D. in *Elements of Modern X-ray Physics* 275-303 (John Wiley & Sons, Inc., 2011).
- 32 Glatter, O. & Kratky, O. *Small angle X-ray scattering*. 17-51 (Academic Press Inc. Ltd., 1982).
- 33 Neilson, G. Diffraction studies of aqueous electrolyte solutions. *Pure Appl. Chem.* **60**, 1797-1806 (1988).
- 34 Bowron, D.T. & Diaz Moreno, S. Using synchrotron X-ray and neutron methods to investigate structural aspects of metal ion solvation and solution structure: An approach using empirical potential structure refinement. *Coord. Chem. Rev.* **277-278**, 2-14 (2014).
- 35 Debye, P., Anderson, H.R. & Brumberger, H. Scattering by an Inhomogeneous Solid. II. The Correlation Function and Its Application. *J. Appl. Phys.* **28**, 679-683 (1957).

- 36 Ruland, W. Small-angle scattering of two-phase systems: determination and significance of systematic deviations from Porod's law. *J. Appl. Crystallogr.* **4**, 70-73 (1971).
- 37 Kalliat, M., Kwak, C. & Schmidt, P. in *New Approaches in Coal Chemistry* Vol. 169 Ch. 1, 3-22 (American Chemical Society, 1981).
- 38 Smarsly, B., Antonietti, M. & Wolff, T. Evaluation of the small-angle x-ray scattering of carbons using parametrization methods. *J. Chem. Phys.* **116**, 2618-2627 (2002).
- 39 Glatter, O. & Kratky, O. *Small angle X-ray scattering*. 136-139 (Academic Press Inc. Ltd., 1982).
- 40 Glatter, O. *Arbeitskriptum zu mathematische Behandlung chemischer Probleme*. Vol. 2, 126-130 (Institut für physikalische Chemie, Universität Graz, Graz, 1978).
- 41 Als-Nielsen, J. & McMorrow, D. in *Elements of Modern X-ray Physics* 29-67 (John Wiley & Sons, Inc., 2011).
- 42 Lu, M., Beguin, F. & Frackowiak, E. *Supercapacitors: materials, systems and applications*. 1-68 (John Wiley & Sons, 2013).
- 43 Bard, A.J. & Faulkner, L.R. *Electrochemical Methods: Fundamentals and Applications*. Vol. 2nd edition (John Wiley & Sons, 2000).
- 44 Simon, P. & Gogotsi, Y. Materials for electrochemical capacitors. *Nat. Mater.* **7**, 845-854 (2008).
- 45 Forse, Alexander C. *et al.* Direct observation of ion dynamics in supercapacitor electrodes using in situ diffusion NMR spectroscopy. *Nat. Energy* **2**, 16216 (2017).
- 46 Gerischer, H. The impact of semiconductors on the concepts of electrochemistry. *Electrochim. Acta* **35**, 1677-1699 (1990).
- 47 Marcus, R.A. On the Theory of Oxidation-Reduction Reactions Involving Electron Transfer. I. *J. Chem. Phys.* **24**, 966-978 (1956).
- 48 Li, Z. *et al.* Confinement Effects on an Electron Transfer Reaction in Nanoporous Carbon Electrodes. *J. Phys. Chem. Lett.* **8**, 1925-1931 (2017).
- 49 Nozik, A.J. & Memming, R. Physical Chemistry of Semiconductor–Liquid Interfaces. *J. Phys. Chem.* **100**, 13061-13078 (1996).
- 50 Conway, B.E. *Electrochemical Supercapacitors: Scientific Fundamentals and Technological Applications*. Vol. 6 (Springer, 1999).
- 51 Haynes, W.M. *CRC handbook of chemistry and physics*. - (CRC press, 2014).
- 52 Golub, D., Soffer, A. & Oren, Y. The electrical double layer of carbon and graphite electrodes: Part V. Specific interactions with simple ions. *J. Electroanal. Chem.* **260**, 383 - 392 (1989).
- 53 Kosmulski, M. *Surface charging and points of zero charge*. Vol. 145 12-15 (CRC Press, 2009).
- 54 Chmiola, J. *et al.* Anomalous Increase in Carbon Capacitance at Pore Sizes Less Than 1 Nanometer. *Science* **313**, 1760-1763 (2006).
- 55 Müller, M. & Kastening, B. The double layer of activated carbon electrodes: Part 1. The contribution of ions in the pores. *J. Electroanal. Chem.* **374**, 149-158 (1994).

- 56 Biesheuvel, P.M., Porada, S., Levi, M. & Bazant, M.Z. Attractive forces in microporous carbon electrodes for capacitive deionization. *J. Solid State Electr.* **18**, 1365-1376 (2014).
- 57 Jiang, D.-e., Jin, Z. & Wu, J. Oscillation of Capacitance inside Nanopores. *Nano Lett.* **11**, 5373-5377 (2011).
- 58 Jäckel, N. *et al.* Anomalous or regular capacitance? The influence of pore size dispersity on double-layer formation. *J. Power Sources* **326**, 660-671 (2016).
- 59 Jäckel, N., Simon, P., Gogotsi, Y. & Presser, V. Increase in Capacitance by Subnanometer Pores in Carbon. *ACS Energy Letters*, 1262-1265 (2016).
- 60 Kondrat, S. & Kornyshev, A.A. Superionic state in double-layer capacitors with nanoporous electrodes. *J. Phys. Condens. Matter* **23**, 022201 (2011).
- 61 Merlet, C. *et al.* On the molecular origin of supercapacitance in nanoporous carbon electrodes. *Nat. Mater.* **11**, 306-310 (2012).
- 62 Merlet, C. *et al.* Highly confined ions store charge more efficiently in supercapacitors. *Nat. Commun.* **4**, 2701 (2013).
- 63 Levi, M.D. *et al.* Application of a quartz-crystal microbalance to measure ionic fluxes in microporous carbons for energy storage. *Nat. Mater.* **8**, 872-875 (2009).
- 64 Griffin, J.M. *et al.* In situ NMR and electrochemical quartz crystal microbalance techniques reveal the structure of the electrical double layer in supercapacitors. *Nat. Mater.* **14**, 812-819 (2015).
- 65 Levi, M.D., Sigalov, S., Aurbach, D. & Daikhin, L. In Situ Electrochemical Quartz Crystal Admittance Methodology for Tracking Compositional and Mechanical Changes in Porous Carbon Electrodes. *J. Phys. Chem. C* **117**, 14876-14889 (2013).
- 66 Levi, M.D. *et al.* The Effect of Specific Adsorption of Cations and Their Size on the Charge-Compensation Mechanism in Carbon Micropores: The Role of Anion Desorption. *Phys. Chem. Chem. Phys.* **12**, 854-862 (2011).
- 67 Griffin, J.M. *et al.* FD 176: Ion Counting in Supercapacitor Electrodes using NMR Spectroscopy. *Faraday Discuss.* **FD 176** (2014).
- 68 Deschamps, M. *et al.* Exploring electrolyte organization in supercapacitor electrodes with solid-state NMR. *Nat. Mater.* **12**, 351-358 (2013).
- 69 Wang, H. *et al.* In Situ NMR Spectroscopy of Supercapacitors: Insight into the Charge Storage Mechanism. *J. Am. Chem. Soc.* **135**, 18968-18980 (2013).
- 70 Prehal, C. *et al.* Tracking the structural arrangement of ions in carbon supercapacitor nanopores using in situ small-angle X-ray scattering. *Energy Environ. Sci.* **8**, 1725-1735 (2015).
- 71 Shao, L.-H. *et al.* Electrically Tunable Nanoporous Carbon Hybrid Actuators. *Adv. Funct. Mater.* **22**, 3029-3034 (2012).
- 72 Torop, J. *et al.* Flexible supercapacitor-like actuator with carbide-derived carbon electrodes. *Carbon* **49**, 3113-3119 (2011).
- 73 Hantel, M.M., Weingarh, D. & Kötze, R. Parameters determining dimensional changes of porous carbons during capacitive charging. *Carbon* **69**, 275-286 (2014).
- 74 Simon, P., Gogotsi, Y. & Dunn, B. Where Do Batteries End and Supercapacitors Begin? *Science* **343**, 1210-1211 (2014).

- 75 Brousse, T., Bélanger, D. & Long, J.W. To be or not to be pseudocapacitive? *J. Electrochem. Soc.* **162**, A5185-A5189 (2015).
- 76 Lukatskaya, M.R., Dunn, B. & Gogotsi, Y. Multidimensional materials and device architectures for future hybrid energy storage. *Nat. Commun.* **7**, 12647 (2016).
- 77 Frackowiak, E., Fic, K., Meller, M. & Lota, G. Electrochemistry Serving People and Nature: High-Energy Ecocapacitors based on Redox-Active Electrolytes. *ChemSusChem* **5**, 1181-1185 (2012).
- 78 Frackowiak, E. & Beguin, F. Carbon materials for the electrochemical storage of energy in capacitors. *Carbon* **39**, 937-950 (2001).
- 79 Marsh, H. & Reinoso, F.R. *Activated carbon*. 1-86 (Elsevier Science, 2006).
- 80 Jafta, C.J. *et al.* Correlating pore size and shape to local disorder in microporous carbon: A combined small angle neutron and X-ray scattering study. *Carbon* **123**, 440-447 (2017).
- 81 Sevilla, M. & Mokaya, R. Energy storage applications of activated carbons: supercapacitors and hydrogen storage. *Energy & Environ. Sci.* **7**, 1250-1280 (2014).
- 82 Presser, V., Heon, M. & Gogotsi, Y. Carbide-Derived Carbons - From Porous Networks to Nanotubes and Graphene. *Adv. Funct. Mater.* **21**, 810-833 (2011).
- 83 Palmer, J.C. *et al.* Modeling the structural evolution of carbide-derived carbons using quenched molecular dynamics. *Carbon* **48**, 1116-1123 (2010).
- 84 Urbonaite, S., Hälldahl, L. & Svensson, G. Raman spectroscopy studies of carbide derived carbons. *Carbon* **46**, 1942-1947 (2008).
- 85 Urbonaite, S. *et al.* EELS studies of carbide derived carbons. *Carbon* **45**, 2047-2053 (2007).
- 86 Robertson, J. & O'Reilly, E.P. Electronic and atomic structure of amorphous carbon. *Phys. Rev. B* **35**, 2946-2957 (1987).
- 87 Kastening, B. *et al.* Electronic properties and double layer of activated carbon. *Electrochim. Acta* **42**, 2789 - 2799 (1997).
- 88 Jäckel, N. *et al.* Performance evaluation of conductive additives for activated carbon supercapacitors in organic electrolyte. *Electrochim. Acta* **191**, 284-298 (2016).
- 89 Gerischer, H., McIntyre, R., Scherson, D. & Storck, W. Density of the electronic states of graphite: derivation from differential capacitance measurements. *J. Phys. Chem.* **91**, 1930-1935 (1987).
- 90 Hahn, M. *et al.* Interfacial Capacitance and Electronic Conductance of Activated Carbon Double-Layer Electrodes. *Electrochem. Solid State Lett.* **7**, A33-A36 (2004).
- 91 Barbieri, O., Hahn, M., Herzog, A. & Kötz, R. Capacitance limits of high surface area activated carbons for double layer capacitors. *Carbon* **43**, 1303-1310 (2005).
- 92 Merlet, C. *et al.* The Electric Double Layer Has a Life of Its Own. *J. Phys. Chem. C* **118**, 18291-18298 (2014).
- 93 Skinner, B., Chen, T., Loth, M.S. & Shklovskii, B.I. Theory of volumetric capacitance of an electric double-layer supercapacitor. *Phys. Rev. E* **83**, 056102 (2011).
- 94 Lee, A.A., Vella, D. & Goriely, A. Quantum capacitance modifies interionic interactions in semiconducting nanopores. *EPL* **113**, 38005 (2016).

- 95 Xia, J., Chen, F., Li, J. & Tao, N. Measurement of the quantum capacitance of graphene. *Nat. Nano* **4**, 505-509 (2009).
- 96 Nightingale, E.R. Phenomenological Theory of Ion Solvation. Effective Radii of Hydrated Ions. *J. Phys. Chem.* **63**, 1381-1387 (1959).
- 97 Ohtaki, H. & Radnai, T. Structure and dynamics of hydrated ions. *Chem. Rev.* **93**, 1157-1204 (1993).
- 98 Marcus, Y. Ionic radii in aqueous solutions. *Chem. Rev.* **88**, 1475-1498 (1988).
- 99 Koneshan, S., Rasaiah, J.C., Lynden-Bell, R.M. & Lee, S.H. Solvent Structure, Dynamics, and Ion Mobility in Aqueous Solutions at 25 °C. *J. Phys. Chem. B* **102**, 4193-4204 (1998).
- 100 Allen, M.P. & Tildesley, D.J. *Computer simulation of liquids*. 110-180 (Oxford university press, 1989).
- 101 Binder, K. *et al. Monte Carlo simulation in statistical physics*. Vol. 7 (1993).
- 102 Landau, D.P. & Binder, K. *A guide to Monte Carlo simulations in statistical physics*. 1-134 (Cambridge university press, 2014).
- 103 Fukuda, I. & Nakamura, H. Non-Ewald methods: theory and applications to molecular systems. *Biophys. Rev.* **4**, 161-170 (2012).
- 104 Fennell, C.J. & Gezelter, J.D. Is the Ewald summation still necessary? Pairwise alternatives to the accepted standard for long-range electrostatics. *J. Chem. Phys.* **124**, 234104 (2006).
- 105 Frenkel, D. & Smit, B. *Understanding molecular simulation: from algorithms to applications*. Vol. 1 291-320 (Academic press, 2001).
- 106 A.C. Maggs, *Laboratory de Physicochimie th'eorique CNRS-ESPCI Paris, Optimizing Ewald summation for Monte Carlo simulations*. <https://turner.pct.espci.fr/~acm/ewald/ewald.pdf> (accessed 04.08.2017).
- 107 Toukmaji, A.Y. & Board, J.A. Ewald summation techniques in perspective: a survey. *Comput. Phys.* **95**, 73-92 (1996).
- 108 Prehal, C. *et al.* A carbon nanopore model to quantify structure and kinetics of ion electrosorption with in situ small angle X-ray scattering. *Phys. Chem. Chem. Phys.* **19**, 15549 (2017).
- 109 Prehal, C. *et al.* Quantification of ion confinement and desolvation in nanoporous carbon supercapacitors with modelling and in situ X-ray scattering. *Nat. Energy* **2**, 16215 (2017).
- 110 Schönmaier, H. *In-situ Röntgentransmissionsmessungen zur Untersuchung der Ionenkonzentration in nanoporösen, kohlenstoffbasierten Superkondensatoren*. Bachelor of Science thesis, Montanuniversitaet Leoben, (2016).
- 111 Gor, G.Y., Thommes, M., Cychosz, K.A. & Neimark, A.V. Quenched solid density functional theory method for characterization of mesoporous carbons by nitrogen adsorption. *Carbon* **50**, 1583-1590 (2012).
- 112 Ravikovitch, P.I., Vishnyakov, A. & Neimark, A.V. Density functional theories and molecular simulations of adsorption and phase transitions in nanopores. *Phys. Rev. E* **64**, 011602 (2001).

- 113 Amenitsch, H. *et al.* First performance assessment of the small-angle X-ray scattering  
beamline at ELETTRA. *J. Synchrotron Radiat.* **5**, 506-508 (1998).
- 114 Pedersen, J. A flux- and background-optimized version of the NanoSTAR small-angle  
X-ray scattering camera for solution scattering. *J. Appl. Crystallogr.* **37**, 369-380  
(2004).
- 115 Ruch, P.W. *et al.* A dilatometric and small-angle X-ray scattering study of the  
electrochemical activation of mesophase pitch-derived carbon in non-aqueous  
electrolyte solution. *Carbon* **48**, 1880 - 1888 (2010).
- 116 Boukhalfa, S., He, L., Melnichenko, Y.B. & Yushin, G. Small-Angle Neutron  
Scattering for InSitu Probing of Ion Adsorption Inside Micropores. *Angew. Chem. Int.  
Ed.* **52**, 4618-4622 (2013).
- 117 P., L. Neutron, X-rays and Light. Scattering Methods Applied to Soft Condensed  
Matter. *Mater. Today* **5**, 38 (2002).
- 118 Hammersley, A. FIT2D: an introduction and overview. *ESRF Internal Report  
ESRF97HA02T* (1997).
- 119 Orthaber, D., Bergmann, A. & Glatter, O. SAXS experiments on absolute scale with  
Kratky systems using water as a secondary standard. *J. Appl. Crystallogr.* **33**, 218-225  
(2000).
- 120 Guinier, A. & Fournet, G. *Small angle scattering of X-rays.* 5-82 (Wiley, 1955).
- 121 Perret, R. & Ruland, W. The microstructure of PAN-base carbon fibres. *J. Appl.  
Crystallogr.* **3**, 525-532 (1970).
- 122 Diduszko, R., Swiatkowski, A. & Trznadel, B.J. On surface of micropores and fractal  
dimension of activated carbon determined on the basis of adsorption and SAXS  
investigations. *Carbon* **38**, 1153-1162 (2000).
- 123 Senapati, S. & Chandra, A. Dielectric constant of water confined in a nanocavity. *J.  
Phys. Chem. B* **105**, 5106-5109 (2001).
- 124 Merlet, C. *et al.* Simulating Supercapacitors: Can We Model Electrodes As Constant  
Charge Surfaces? *J. Phys. Chem. Lett.* **4**, 264-268 (2013).
- 125 Tyagi, S. *et al.* An iterative, fast, linear-scaling method for computing induced charges  
on arbitrary dielectric boundaries. *J. Chem. Phys.* **132**, 154112 (2010).
- 126 Rochester, C.C., Lee, A.A., Pruessner, G. & Kornyshev, A.A. Interionic Interactions  
in Conducting Nanoconfinement. *ChemPhysChem* **14**, 4121-4125 (2013).
- 127 Goduljan, A. *et al.* Screening of ions in carbon and gold nanotubes — A theoretical  
study. *Electrochem. Commun.* **45**, 48-51 (2014).
- 128 Mohammadzadeh, L. *et al.* Nanotubes for charge storage – towards an atomistic  
model. *Electrochim. Acta* **162**, 11-16 (2015).
- 129 Levrel, L. & Maggs, A. Boundary conditions in local electrostatics algorithms. *J.  
Chem. Phys.* **128**, 214103 (2008).
- 130 Hua, W., Sprung, D.W.L. & Martorell, J. Potential energy of a point charge in a  
grounded conducting cavity. *Eur. J. Phys.* **21**, 413 (2000).
- 131 Purisima, E.O. & Nilar, S.H. A simple yet accurate boundary element method for  
continuum dielectric calculations. *J. Comput. Chem.* **16**, 681-689 (1995).

- 132 Yoon, B.J. & Lenhoff, A.M. A boundary element method for molecular electrostatics  
with electrolyte effects. *J. Comput. Chem.* **11**, 1080-1086 (1990).
- 133 Hall, C., Ji, W. & Blaisten-Barojas, E. The Metropolis Monte Carlo method with  
CUDA enabled Graphic Processing Units. *J. Comput. Phys.* **258**, 871-879 (2014).
- 134 Gibaud, A., Xue, J.S. & Dahn, J.R. A small angle X-ray scattering study of carbons  
made from pyrolyzed sugar. *Carbon* **34**, 499-503 (1996).
- 135 Calo, J.M. & Hall, P.J. The application of small angle scattering techniques to  
porosity characterization in carbons. *Carbon* **42**, 1299-1304 (2004).
- 136 Mascotto, S. *et al.* Poly(ionic liquid)-derived nanoporous carbon analyzed by  
combination of gas physisorption and small-angle neutron scattering. *Carbon* **82**, 425-  
435 (2015).
- 137 He, L. *et al.* Small-angle neutron scattering characterization of the structure of  
nanoporous carbons for energy-related applications. *Microporous Mesoporous Mat.*  
**149**, 46-54 (2012).
- 138 Wang, S. *et al.* Distorted Graphene Sheet Structure-Derived Latent Nanoporosity.  
*Langmuir* **32**, 5617-5622 (2016).
- 139 Guinier, A. *X-ray diffraction in crystals, imperfect crystals, and amorphous bodies.*  
27-184 (Courier Dover Publications, 1994).
- 140 Roberts, A.P. Statistical reconstruction of three-dimensional porous media from two-  
dimensional images. *Phys. Rev. E* **56**, 3203-3212 (1997).
- 141 Gommès, C.J. & Roberts, A.P. Structure development of resorcinol-formaldehyde gels:  
Microphase separation or colloid aggregation. *Phys. Rev. E* **77**, 041409 (2008).
- 142 Berk, N. Scattering properties of a model bicontinuous structure with a well defined  
length scale. *Phys. Rev. Lett* **58**, 2718 (1987).
- 143 Berk, N. Scattering properties of the leveled-wave model of random morphologies.  
*Phys. Rev. A* **44**, 5069 (1991).
- 144 Levitz, P. Off-lattice reconstruction of porous media: critical evaluation, geometrical  
confinement and molecular transport. *Adv. Colloid Interface Sci.* **76**, 71-106 (1998).
- 145 Jagiello, J. & Thommes, M. Comparison of DFT characterization methods based on  
N<sub>2</sub>, Ar, CO<sub>2</sub>, and H<sub>2</sub> adsorption applied to carbons with various pore size distributions.  
*Carbon* **42**, 1227-1232 (2004).
- 146 Thommes, M. *et al.* Physisorption of gases, with special reference to the evaluation of  
surface area and pore size distribution (IUPAC Technical Report). *Pure Appl. Chem.*  
**87**, 1051-1069 (2015).
- 147 Silvestre-Albero, J., Silvestre-Albero, A., Rodríguez-Reinoso, F. & Thommes, M.  
Physical characterization of activated carbons with narrow microporosity by nitrogen  
(77.4 K), carbon dioxide (273K) and argon (87.3 K) adsorption in combination with  
immersion calorimetry. *Carbon* **50**, 3128-3133 (2012).
- 148 Presser, V., McDonough, J., Yeon, S.-H. & Gogotsi, Y. Effect of pore size on carbon  
dioxide sorption by carbide derived carbon. *Energy Environ. Sci.* **4**, 3059-3066 (2011).
- 149 Puziy, A.M., Poddubnaya, O.I., Gawdzik, B. & Sobiesiak, M. Comparison of  
heterogeneous pore models QSDFT and 2D-NLDFT and computer programs ASiQwin  
and SAIEUS for calculation of pore size distribution. *Adsorption* **22**, 459-464 (2016).



- 150 Gommès, C. Small-angle scattering and scale-dependent heterogeneity. *J. Appl. Crystallogr.* **49**, 1162-1176 (2016).
- 151 Waluyo, I. *et al.* The structure of water in the hydration shell of cations from x-ray Raman and small angle x-ray scattering measurements. *J. Chem. Phys.* **134**, 1-10 (2011).
- 152 Pings, C.J. & Waser, J. Analysis of Scattering Data for Mixtures of Amorphous Solids or Liquids. *J. Chem. Phys.* **48**, 3016-3018 (1968).
- 153 Bellissent-Funel, M. Structure of confined water. *J. Phys.: Condens. Matter* **13**, 9165 (2001).
- 154 Stevens, D.A. & Dahn, J.R. An In Situ Small-Angle X-Ray Scattering Study of Sodium Insertion into a Nanoporous Carbon Anode Material within an Operating Electrochemical Cell. *J. Electrochem. Soc.* **147**, 4428-4431 (2000).
- 155 Laudisio, G. *et al.* Carbide-Derived Carbons: A Comparative Study of Porosity Based on Small-Angle Scattering and Adsorption Isotherms. *Langmuir* **22**, 8945-8950 (2006).
- 156 Tsai, W.-Y., Taberna, P.-L. & Simon, P. Electrochemical Quartz Crystal Microbalance (EQCM) Study of Ion Dynamics in Nanoporous Carbons. *J. Am. Chem. Soc.* **136**, 8722-8728 (2014).
- 157 Wander, M.C.F. & Shuford, K.L. Molecular Dynamics Study of Interfacial Confinement Effects of Aqueous NaCl Brines in Nanoporous Carbon†. *J. Phys. Chem. C* **114**, 20539-20546 (2010).
- 158 Zhou, H. *et al.* Nanoscale Perturbations of Room Temperature Ionic Liquid Structure at Charged and Uncharged Interfaces. *ACS Nano* **6**, 9818-9827 (2012).
- 159 Kalluri, R.K. *et al.* Unraveling the potential and pore-size dependent capacitance of slit-shaped graphitic carbon pores in aqueous electrolytes. *Phys. Chem. Chem. Phys.* **15**, 2309-2320 (2013).
- 160 Feng, G. *et al.* Ion Distribution in Electrified Micropores and Its Role in the Anomalous Enhancement of Capacitance. *ACS Nano* **4**, 2382-2390 (2010).
- 161 Merlet, C., Salanne, M., Rotenberg, B. & Madden, P.A. Influence of solvation on the structural and capacitive properties of electrical double layer capacitors. *Electrochim. Acta* **101**, 262-271 (2013).
- 162 Wu, P. *et al.* Voltage Dependent Charge Storage Modes and Capacity in Subnanometer Pores. *J. Phys. Chem. Lett.* **3**, 1732-1737 (2012).
- 163 Kondrat, S., Kornyshev, A.A., Stoeckli, F. & Centeno, T.A. The effect of dielectric permittivity on the capacitance of nanoporous electrodes. *Electrochem. Commun.* **34**, 348-350 (2013).
- 164 Weingarh, D. *et al.* Graphitization as a Universal Tool to Tailor the Potential-Dependent Capacitance of Carbon Supercapacitors. *Adv. Energy Mater.* **4**, 1400316 (2014).
- 165 Erko, M. *et al.* Density minimum of confined water at low temperatures: a combined study by small-angle scattering of X-rays and neutrons. *Phys. Chem. Chem. Phys.* **14**, 3852-3858 (2012).
- 166 Brown, P. *et al.* in *International Tables for Crystallography Volume C: Mathematical, physical and chemical tables* (ed E. Prince) 554-595 (Springer Netherlands, 2006).

- 
- 167 Kondrat, S. *et al.* Effect of pore size and its dispersity on the energy storage in nanoporous supercapacitors. *Energy Environ. Sci.* **5**, 6474-6479 (2012).
- 168 Kondrat, S., Georgi, N., Fedorov, M.V. & Kornyshev, A.A. A superionic state in nanoporous double-layer capacitors: insights from Monte Carlo simulations. *Phys. Chem. Chem. Phys.* **13**, 11359-11366 (2011).
- 169 Péan, C. *et al.* Confinement, Desolvation, And Electrosorption Effects on the Diffusion of Ions in Nanoporous Carbon Electrodes. *J. Am. Chem. Soc.* **137**, 12627-12632 (2015).
- 170 Koczwarra, C. *et al.* In Situ Measurement of Electrosorption-Induced Deformation Reveals the Importance of Micropores in Hierarchical Carbons. *ACS Appl. Mater. Interfaces* **9**, 23319-23324 (2017).

# Abbreviations

SAXS	small angle X-ray scattering
WAXS	wide angle X-ray scattering
EDLC	electrical double-layer capacitor
WE	working electrode
CE	counter electrode
CC	current collector
AC1	electrode material (activated carbon YP-80)
AC2	electrode material (activated carbon MSP20)
CDC	TiC derived carbon (TiC-CDC)
CV	cyclic voltammetry
PZC	point of zero charge
DoC	degree of confinement
DoDS	degree of desolvation
SOC	state of charge (equivalent to electrode charge)
MC	Monte Carlo (simulation)
NMR	nuclear magnetic resonance
eQCM	electrochemical quartz crystal microbalance
DOS	(electron) density of states
GSA	gas sorption analysis
SSA	specific surface area
PSD	pore size distribution



## List of publications

- N. Kostoglou, C. Koczwarra, **C. Prehal**, V. Terziyska, B. Babic, B. Matovic, G. Constantinides, C. Tampaxis, G. Charalambopoulou, T. Steriotis, S. Hinder, M. Baker, K. Polychronopoulou, C. Doumanidis, O. Paris, C. Mitterer and C. Rebholz, *Nanoporous activated carbon cloth as a versatile material for hydrogen adsorption, selective gas separation and electrochemical energy storage*. Nano Energy 2017, accepted, <https://doi.org/10.1016/j.nanoen.2017.07.056>.
- C. Koczwarra, S. Rumswinkel, **C. Prehal**, N. Jäckel, M. Elsaesser, H. Amenitsch, V. Presser, N. Huesing, O. Paris, *In situ measurement of electrosorption-induced deformation reveal the importance of micropores in hierarchical carbons*, ACS Applied Materials & Interfaces 2017, 9(28), 23319-23324.
- S. Choudhury, B. Krüner, P. Massuti-Ballester, A. Tolosa, **C. Prehal**, I. Grobelsek, O. Paris, L. Borchardt, V. Presser, *Microporous novolac-derived carbon beads/sulfur hybrid cathode for lithium-sulfur batteries*, J. Power Sources 2017, 357, 198.
- C. Prehal**, C. Koczwarra, N. Jäckel, H. Amenitsch, V. Presser and O. Paris, *A carbon nanopore model to quantify structure and kinetics of ion electrosorption with in situ small-angle X-ray scattering*, Phys. Chem. Chem. Phys., 2017, 19, 15549.
- C. Prehal**, C. Koczwarra, N. Jäckel, A. Schreiber, M. Burian, H. Amenitsch, M. A. Hartmann, V. Presser, O. Paris, *Quantification of ion confinement and desolvation in nanoporous carbon supercapacitors with modelling and in situ X-ray scattering*, Nature Energy, 2017, 2, 16215.
- C. Prehal**, D. Weingarth, E. Perre, R.T. Lechner, H. Amenitsch, O. Paris and V. Presser, *Tracking the structural arrangement of ions in carbon supercapacitor nanopores using in situ small-angle X-ray scattering*, Energy & Environmental Science, 2015, 8, 1725-1735.



# Appendix A

## C++ Code - Monte Carlo simulation

The presented code was developed by Christian Prehal and Christian Koczwarra at the Institute of Physics, Montanuniversität Leoben, Austria in 2015 - 2016.

The following code lines are not complete. The structure for DoDS-, potential-, energy- and electrode-charge- calculation is only shown exemplarily. Each of these calculations is carried out several times on different positions in the code, only with slight modifications of some variables. Since the general structure remains the same, representative code lines are only shown once.

### 1 Input via text files:

- position, surface area and normal vectors of surface elements
- volumetric data of 3D pore structure

Input parameters from Config file;

### 2 Declaration of all vectors and variables

## Generate starting configuration

### 3 Fill ions into pore structure with random arrangement

Always check, whether position can be accepted (ion-ion distances, ion-carbon distances, position inside a pore?)

```
    random_shuffle(ion_pos_begin(), ion_pos_end());
    for (int i = 0; i < number_of_ions; i++)
    {
        x_pos = 0; y_pos = 0; z_pos = 0;
        int x_pos_n = 0; int y_pos_n = 0; int z_pos_n = 0;
        if (ion_pos[i] < number_of_cations){cat_an = true;}
        else{}
        if (cat_an)
        {
            do
            {
                x_pos = rand() % ((int)(box_s)); y_pos = rand() % ((int)(box_s)); z_pos = rand() % ((int)(box_s));
                if (pore_structure_is[x_pos][y_pos][z_pos] == 0)
                {
                    count1 = 0;
                    for (int i = -3; i < 4; i++)
                    {
                        for (int j = -3; j < 4; j++)
                        {
                            for (int k = -3; k < 4; k++)
                            {
                                distance1 = sqrt(pow((0.1*i), 2) + pow((0.1*j), 2) + pow((0.1*k), 2));
                                if (distance1 < r_cat)
                                {
                                    x_pos_new = x_pos + i; y_pos_new = y_pos + j; z_pos_new = z_pos + k;
                                    pbc2(x_pos_new, y_pos_new, z_pos_new);
                                    count1 = count1 + pore_structure_is[x_pos_new][y_pos_new][z_pos_new];
                                }
                            }
                        }
                    }
                }
            }
        }
        if (count1 == 0)
```

```

{
cat_x_pos[u] = x_pos; cat_y_pos[u] = y_pos; cat_z_pos[u] = z_pos;
for (int i = -3; i < 4; i++)
{
for (int j = -3; j < 4; j++)
{
for (int k = -3; k < 4; k++)
{
distance1 = sqrt(pow((0.1*i), 2) + pow((0.1*j), 2) + pow((0.1*k), 2));
if (distance1 < r_cat)
{
x_pos_new = x_pos + i; y_pos_new = y_pos + j; z_pos_new = z_pos + k;
pbc2(x_pos_new, y_pos_new, z_pos_new);
pore_structure_is[x_pos_new][y_pos_new][z_pos_new] = pore_structure_is[x_pos_new][y_pos_new][z_pos_new] + 2;
}
}
}
}
break;
}
else{continue;}
}
} while (1);
u++;
}
else
{
do
{
x_pos = rand() % ((int)(box_s)); y_pos = rand() % ((int)(box_s)); z_pos = rand() % ((int)(box_s));
if (pore_structure_is[x_pos][y_pos][z_pos] == 0)
{
count1 = 0;
for (int i = -3; i < 4; i++)
{
for (int j = -3; j < 4; j++)
{
for (int k = -3; k < 4; k++)
{
distance1 = sqrt(pow((0.1*i), 2) + pow((0.1*j), 2) + pow((0.1*k), 2));
if (distance1 < r_an)
{
x_pos_new = x_pos + i; y_pos_new = y_pos + j; z_pos_new = z_pos + k;
pbc2(x_pos_new, y_pos_new, z_pos_new);
count1 = count1 + pore_structure_is[x_pos_new][y_pos_new][z_pos_new];
}
}
}
}
}
}
if (count1 == 0)
{
an_x_pos[v] = x_pos; an_y_pos[v] = y_pos; an_z_pos[v] = z_pos;
for (int i = -3; i < 4; i++)
{
for (int j = -3; j < 4; j++)
{
for (int k = -3; k < 4; k++)
{
distance1 = sqrt(pow((0.1*i), 2) + pow((0.1*j), 2) + pow((0.1*k), 2));
if (distance1 < r_an)
{
x_pos_new = x_pos + i; y_pos_new = y_pos + j; z_pos_new = z_pos + k;
pbc2(x_pos_new, y_pos_new, z_pos_new);
pore_structure_is[x_pos_new][y_pos_new][z_pos_new] = pore_structure_is[x_pos_new][y_pos_new][z_pos_new] + 3;
}
}
}
}
}
}
break;
}
else{continue;}
}
} while (1);
v++;
}
}

```

#### 4 Calculate Degree of desolvation (DoDS) for all ions

```

for (long int c = 0; c < number_of_cations; c++)
{
DOS_cat[c] = 0;
u = cat_x_pos[c]; v = cat_y_pos[c]; w = cat_z_pos[c];
for (int i = -3; i < 4; i++)

```



```

{
  for (int j = -3; j < 4; j++)
  {
    for (int k = -3; k < 4; k++)
    {
      distance1 = sqrt(pow(0.1*i, 2) + pow(0.1*j, 2) + pow(0.1*k, 2));
      if (distance1 < r_cat_hyd)
      {
        x_pos = (u + i); y_pos = (v + j); z_pos = (w + k);
        pbc2(x_pos, y_pos, z_pos);
        if (pore_structure_is[x_pos][y_pos][z_pos] == 1) { DOS_cat[c] = DOS_cat[c] + 0.001; }
      }
    }
  }
  DOS_cat[c] = DOS_cat[c] / DOS_max_cat;
}
for (long int c = 0; c < number_of_anions; c++)
{
  DOS_an[c] = 0; u = an_x_pos[c]; v = an_y_pos[c]; w = an_z_pos[c];
  for (int i = -3; i < 4; i++)
  {
    for (int j = -3; j < 4; j++)
    {
      for (int k = -3; k < 4; k++)
      {
        distance1 = sqrt(pow(0.1*i, 2) + pow(0.1*j, 2) + pow(0.1*k, 2));
        if (distance1 < r_an_hyd)
        {
          x_pos = (u + i); y_pos = (v + j); z_pos = (w + k);
          pbc2(x_pos, y_pos, z_pos);
          if (pore_structure_is[x_pos][y_pos][z_pos] == 1) { DOS_an[c] = DOS_an[c] + 0.001; }
        }
      }
    }
  }
  DOS_an[c] = DOS_an[c] / DOS_max_an;
}

```

## 5 Calculate energy for all ions in this random configuration

### 5.1 Therefore calculate electrode charges

```

do
{
  int p = 0;
  help = 0;
  for (int i = 0; i < grid_length; i++)
  {
    E_n_contr[i] = 0; E_n_contr_mit[i] = 0; e_field_x_cat[i] = 0; e_field_y_cat[i] = 0; e_field_z_cat[i] = 0;
    (...)
  }
  for (int i = 0; i < number_of_el_c; i++)
  {
    sigma[i][n + 1] = q_el_charge[i]; sigma_mit[i][n + 1] = q_el_charge_mit[i];
  }
  for (int k = 0; k < i_list_num; k++)
  {
    int i;
    i = i_list[k]; dx = ((el_c_x[i] - u)*0.1); dy = ((el_c_y[i] - v)*0.1); dz = ((el_c_z[i] - w)*0.1);
    distance1 = pbc(dx, dy, dz);
    if (distance1 < wr)
    {
      el_c_vector[i] = p; p_wave[p] = i;
      p++;
    }
  }
  el_c_size = p;
  #pragma omp parallel for schedule(static)
  private(dx,dy,dz,distance_cat,distance_an,distance1,p,distance_el_c,ex_el_c,ey_el_c,ez_el_c,ex_an,ey_an,ez_an,ex_cat,ey_cat,ez_cat) num_threads(core_num)
  for (int k = 0; k < el_c_size; k++)
  {
    int count_omp = 0; int i;
    p = k; i = p_wave[p];
    for (int m = 0; m < cell_control; m++)
    {
      int o;
      o = head_cat[cell_num[m]];
      do
      {
        dx = ((cat_x_pos[o] - el_c_x[i])*0.1); dy = ((cat_y_pos[o] - el_c_y[i])*0.1); dz = ((cat_z_pos[o] - el_c_z[i])*0.1);
        distance_cat = pbc(dx, dy, dz);
        if (distance_cat > 0)

```

```

{
ex_cat = (-dx / distance_cat); ey_cat = (-dy / distance_cat); ez_cat = (-dz / distance_cat);
dx = ((cat_x_pos[o] - u)*0.1); dy = ((cat_y_pos[o] - v)*0.1); dz = ((cat_z_pos[o] - w)*0.1);
distance1 = pbc(dx, dy, dz);
if (distance1 < wr && o != c)
{
e_field_x_cat[i] = (((1 / (epsilon_h2o * 4 * M_PI))*q_cation*(1e18) / (pow(distance_cat, 2)))*ex_cat);
e_field_y_cat[i] = (((1 / (epsilon_h2o * 4 * M_PI))*q_cation*(1e18) / (pow(distance_cat, 2)))*ey_cat);
e_field_z_cat[i] = (((1 / (epsilon_h2o * 4 * M_PI))*q_cation*(1e18) / (pow(distance_cat, 2)))*ez_cat);
E_n_contr[i] = E_n_contr[i] + (e_field_x_cat[i] * n_surf_x[i] + e_field_y_cat[i] * n_surf_y[i] +
e_field_z_cat[i] * n_surf_z[i]);
E_n_contr_mit[i] = E_n_contr_mit[i] + (e_field_x_cat[i] * n_surf_x[i] + e_field_y_cat[i] * n_surf_y[i] +
e_field_z_cat[i] * n_surf_z[i]);
}
if (distance1 < wr && o == c)
{
e_field_x_cat[i] = (((1 / (epsilon_h2o * 4 * M_PI))*q_cation*(1e18) / (pow(distance_cat, 2)))*ex_cat);
e_field_y_cat[i] = (((1 / (epsilon_h2o * 4 * M_PI))*q_cation*(1e18) / (pow(distance_cat, 2)))*ey_cat);
e_field_z_cat[i] = (((1 / (epsilon_h2o * 4 * M_PI))*q_cation*(1e18) / (pow(distance_cat, 2)))*ez_cat);
E_n_contr_mit[i] = E_n_contr_mit[i] + (e_field_x_cat[i] * n_surf_x[i] + e_field_y_cat[i] * n_surf_y[i] +
e_field_z_cat[i] * n_surf_z[i]);
}
}
o = list_cat[o];
} while (o != 0);
}
for (int m = 0; m < cell_control; m++)
{
int o;
o = head_an[cell_num[m]];
do
{
dx = ((an_x_pos[o] - el_c_x[i])*0.1); dy = ((an_y_pos[o] - el_c_y[i])*0.1); dz = ((an_z_pos[o] - el_c_z[i])*0.1);
distance_an = pbc(dx, dy, dz);
if (distance_an > 0)
{
ex_an = (-dx / distance_an); ey_an = (-dy / distance_an); ez_an = (-dz / distance_an);
dx = ((an_x_pos[o] - u)*0.1); dy = ((an_y_pos[o] - v)*0.1); dz = ((an_z_pos[o] - w)*0.1);
distance1 = pbc(dx, dy, dz);
if (distance1 < wr)
{
e_field_x_an[i] = (((1 / (epsilon_h2o * 4 * M_PI))*q_anion*(1e18) / (pow(distance_an, 2)))*ex_an);
e_field_y_an[i] = (((1 / (epsilon_h2o * 4 * M_PI))*q_anion*(1e18) / (pow(distance_an, 2)))*ey_an);
e_field_z_an[i] = (((1 / (epsilon_h2o * 4 * M_PI))*q_anion*(1e18) / (pow(distance_an, 2)))*ez_an);
E_n_contr[i] = E_n_contr[i] + (e_field_x_an[i] * n_surf_x[i] + e_field_y_an[i] * n_surf_y[i] + e_field_z_an[i] *
n_surf_z[i]);
E_n_contr_mit[i] = E_n_contr_mit[i] + (e_field_x_an[i] * n_surf_x[i] + e_field_y_an[i] * n_surf_y[i] +
e_field_z_an[i] * n_surf_z[i]);
}
}
o = list_an[o];
} while (o != 0);
}
for (int m = 0; m < el_c_size; m++)
{
int o;
o = p_wave[m];
dx = ((el_c_x[o] - el_c_x[i])*0.1); dy = ((el_c_y[o] - el_c_y[i])*0.1); dz = ((el_c_z[o] - el_c_z[i])*0.1);
distance_el_c = pbc(dx, dy, dz);
if (i != o)
{
count_omp++;
ex_el_c = (-dx / distance_el_c);
ey_el_c = (-dy / distance_el_c);
ez_el_c = (-dz / distance_el_c);
e_field_x_el_c[i] = (((1.0 / (epsilon_h2o * 4 * M_PI))*q_el_charge[o] * (1e18) / (pow(distance_el_c,
2)))*ex_el_c);
e_field_y_el_c[i] = (((1.0 / (epsilon_h2o * 4 * M_PI))*q_el_charge[o] * (1e18) / (pow(distance_el_c,
2)))*ey_el_c);
e_field_z_el_c[i] = (((1.0 / (epsilon_h2o * 4 * M_PI))*q_el_charge[o] * (1e18) / (pow(distance_el_c,
2)))*ez_el_c);
E_n_contr[i] = E_n_contr[i] + (e_field_x_el_c[i] * n_surf_x[i] + e_field_y_el_c[i] * n_surf_y[i] +
e_field_z_el_c[i] * n_surf_z[i]);
e_field_x_el_c[i] = (((1.0 / (epsilon_h2o * 4 * M_PI))*q_el_charge_mit[o] * (1e18) / (pow(distance_el_c,
2)))*ex_el_c);
e_field_y_el_c[i] = (((1.0 / (epsilon_h2o * 4 * M_PI))*q_el_charge_mit[o] * (1e18) / (pow(distance_el_c,
2)))*ey_el_c);
e_field_z_el_c[i] = (((1.0 / (epsilon_h2o * 4 * M_PI))*q_el_charge_mit[o] * (1e18) / (pow(distance_el_c,
2)))*ez_el_c);
E_n_contr_mit[i] = E_n_contr_mit[i] + (e_field_x_el_c[i] * n_surf_x[i] + e_field_y_el_c[i] * n_surf_y[i] +
e_field_z_el_c[i] * n_surf_z[i]);
}
}
sigma[i][n + 1] = omega*(2 * epsilon_h2o)*(E_n_contr[i]) + (1 - omega)*sigma[i][n];
sigma_mit[i][n + 1] = omega*(2 * epsilon_h2o)*(E_n_contr_mit[i]) + (1 - omega)*sigma_mit[i][n];
if (sigma[i][n + 1] < (-1.0*ulimit_load)) { sigma[i][n + 1] = -1.0*ulimit_load; }
}

```

```

    if (sigma[i][n + 1] > (ulimit_load)) { sigma[i][n + 1] = ulimit_load; }
    if (sigma_mit[i][n + 1] < (-1.0*ulimit_load)) { sigma_mit[i][n + 1] = -1.0*ulimit_load; }
    if (sigma_mit[i][n + 1] > (ulimit_load)) { sigma_mit[i][n + 1] = ulimit_load; }
}
test_time++;
for (int i = 0; i < number_of_el_c; i++)
{
    q_el_charge[i] = sigma[i][n + 1];
    q_el_charge_mit[i] = sigma_mit[i][n + 1];
}
n++;
if (help_mit > help) { help = help_mit; }
} while ( n <= max_it);

```

## 5.2 Sum up potential contributions of surrounding cations, anions and electrode charges

```

//Now, sum up the potential contribution of all charges surrounding the specific cations
for (int m = 0; m < cell_control; m++)
{
    int o;
    o = head_cat[cell_num[m]];
    do
    {
        dx = ((cat_x_pos[o] - u)*0.1); dy = ((cat_y_pos[o] - v)*0.1); dz = ((cat_z_pos[o] - w)*0.1);
        distance_cat = pbc(dx, dy, dz);
        if (distance_cat < wr && o != c && distance_cat > 0)
        {
            potential_cat[c] = potential_cat[c] + (1 / (epsilon_h2o * 4 * M_PI)*(1e9)*(q_cation / distance_cat)) -
                potential_shift*q_cation;
        }
        o = list_cat[o];
    } while (o != 0);
}
for (int m = 0; m < cell_control; m++)
{
    int o;
    o = head_an[cell_num[m]];
    do
    {
        dx = ((an_x_pos[o] - u)*0.1); dy = ((an_y_pos[o] - v)*0.1); dz = ((an_z_pos[o] - w)*0.1);
        distance_an = pbc(dx, dy, dz);
        if (distance_an < wr)
        {
            potential_cat[c] = potential_cat[c] + (1 / (epsilon_h2o * 4 * M_PI)*(1e9)*(q_anion / distance_an))-
                potential_shift*q_anion;
        }
        o = list_an[o];
    } while (o != 0);
}
for (int m = 0; m < cell_control; m++)
{
    int o;
    o = head_el_c[cell_num[m]];
    do
    {
        dx = ((el_c_x[o] - u)*0.1); dy = ((el_c_y[o] - v)*0.1); dz = ((el_c_z[o] - w)*0.1);
        distance_el_c = pbc(dx, dy, dz);
        if (distance_el_c < wr)
        {
            potential_cat[c] = potential_cat[c] + (1 / (epsilon_h2o * 4 * M_PI)*(1e9)*(q_el_charge[o] / distance_el_c))-
                potential_shift*q_el_charge[o];
            potential_cat[c] = potential_cat[c] + corr_f_el_p*(1 / (epsilon_h2o * 4 * M_PI)*(1e9)*((q_el_charge_mit[o] -
                q_el_charge[o]) / distance_el_c))-(q_el_charge_mit[o] -
                q_el_charge[o])*potential_shift*corr_f_el_p;
        }
        o = list_el_c[o];
    } while (o != 0);
}

```

## 5.3 Add hydration energy by multiplying the DoDS by hydration enthalpy

```

energy_cat[c] = potential_cat[c] * q_cation;
energy_cat[c] = energy_cat[c] + (DOS_cat[c] * hydr_energy_cat);
}

```

## Start of metropolis algorithm

6 First, random draw of an ion (cation or anion)

```

random_number = rand() % number_of_ions;
if (random_number < number_of_cations) // then take a cation; otherwise an anion
{
  c = random_number;
  DOS_cat_old = DOS_cat[c];
  (...)
}

```

- 7 If an ion is chosen, choose a new position for this ion (jump length decreases during the simulation to keep the acceptance probabilities roughly constant); check whether new position is possible (is the new position still in the pore? Is any other ion already placed on the new position?) If a new position cannot be found after 50 attempts choose a new ion.

```

(...)
do
{
  get_cells(cat_x_pos[c], cat_y_pos[c], cat_z_pos[c], box_s, cell_num);
  cell_num_old = cell_num;
  u1 = ((int)(-(int)(0.5 + jump_length[MC_step]) + (rand() % ((int)(jump_length[MC_step] * 2 + 0.5)))));
  v1 = ((int)(-(int)(0.5 + jump_length[MC_step]) + (rand() % ((int)(jump_length[MC_step] * 2 + 0.5)))));
  w1 = ((int)(-(int)(0.5 + jump_length[MC_step]) + (rand() % ((int)(jump_length[MC_step] * 2 + 0.5)))));

  if (u1 == 0 && v1 == 0 && w1 == 0) { /*cout << "0-Runde" << endl;*/ continue; }
  u2 = cat_x_pos[c] + u1; v2 = cat_y_pos[c] + v1; w2 = cat_z_pos[c] + w1;
  pbc2(u2, v2, w2);
  get_cells(u2, v2, w2, box_s, cell_num);
  count1 = 0; count2 = 0; count3 = 0; DOS_cat[c] = 0;
  for (int j = 0; j < cell_control; j++)
  {
    int i; i = head_cat[cell_num[j]];
    do
    {
      dx = ((cat_x_pos[i] - u2)*0.1); dy = ((cat_y_pos[i] - v2)*0.1); dz = ((cat_z_pos[i] - w2)*0.1);
      distance_cat = pbc(dx, dy, dz);
      if (distance_cat < (2 * r_cat_hyd) && i != c)
      {
        if (distance_cat >= (2 * r_cat))
        {
          height = (2.0*r_cat_hyd - distance_cat) / 2.0;
          DOS_cat[c] = DOS_cat[c] + (2.0*height*height*M_PI / 3.0*(3.0*r_cat_hyd - height));
        }
        if (distance_cat < (2 * r_cat)) { count3++; }
      }
      i = list_cat[i];
    } while (i != 0);
    i = head_an[cell_num[j]];
    do
    {
      dx = ((an_x_pos[i] - u2)*0.1); dy = ((an_y_pos[i] - v2)*0.1); dz = ((an_z_pos[i] - w2)*0.1);
      distance_an = pbc(dx, dy, dz);
      if (distance_an < (r_cat_hyd + r_an_hyd))
      {
        if (distance_an >= (r_cat + r_an))
        {
          height = (2.0*r_cat_hyd - distance_an) / 2.0;
          DOS_cat[c] = DOS_cat[c] + (2.0*height*height*M_PI / 3.0*(3.0*r_cat_hyd - height));
        }
        if (distance_an < (r_cat + r_an)) { count3++; }
      }
      i = list_an[i];
    } while (i != 0);
  }
  for (int i = -3; i < 4; i++)
  {
    for (int j = -3; j < 4; j++)
    {
      for (int k = -3; k < 4; k++)
      {
        distance1 = sqrt(pow(0.1*i, 2) + pow(0.1*j, 2) + pow(0.1*k, 2));
        if (distance1 < r_cat_hyd)
        {
          x_pos = (u2 + i); y_pos = (v2 + j); z_pos = (w2 + k);
          pbc2(x_pos, y_pos, z_pos);
          count1 = count1 + pore_structure_is[x_pos][y_pos][z_pos];
          if (pore_structure_is[x_pos][y_pos][z_pos] == 1) { DOS_cat[c] = DOS_cat[c] + 0.001; }
        }
        if (distance1 < r_cat)
        {
          x_pos = (u2 + i); y_pos = (v2 + j); z_pos = (w2 + k);
          pbc2(x_pos, y_pos, z_pos);

```

```

        count2 = count2 + pore_structure_is[x_pos][y_pos][z_pos];
    }
}
}
DOS_cat[c] = DOS_cat[c] / DOS_max_cat;
l++;
if (l > 50) { break; }
} while ((count2 != 0 || count3 != 0));
if (l > 50)
{
    DOS_cat[c] = DOS_cat_old;
    continue;
}
(...)

```

- 8 Then, calculate energy and potential of the old ion position (“get ion potential old”)
  - 8.1 First calculate electrode charges
  - 8.2 Sum up potential contributions of cations, anions and electrode charges
  - 8.3 Add hydration energy by multiplying the DoDS by hydration enthalpy
- 9 Calculate DoDS of ion on new position
- 10 Calculate electrode charges
- 11 Sum up potential contributions of surrounding cations, anions and electrode charges
- 12 Calculate energy by adding the hydration contribution
- 13 Accept new position according to a Boltzmann probability if the energy is higher; and in any case if the energy is lower (Metropolis)

```

(...)
acceptance = 0;
energy_cat_new = (potential_cat_new * q_cation) + (DOS_cat[c] * hydr_energy_cat);
if (energy_cat_new < energy_cat_old)
{
    cat_x_pos[c] = u; cat_y_pos[c] = v; cat_z_pos[c] = w;
    potential_cat[c] = potential_cat_new;
    energy_cat[c] = energy_cat_new;
    for (int i = 0; i < grid_length; i++)
    {
        q_el_charge[i] = q_el_charge_new[i];
    }
    movement++; acceptance = 1; acc_moves++; q_el_loc_time[MC_step] = q_el_loc_neu;
}
else //accept displacement according to Boltzmann statistics
{
    random_num2 = (rand() % 1001) / 1000.0;
    if (random_num2 < exp(-(energy_cat_new - (energy_cat_old)) / (k_b*temp_v[MC_step])))
    {
        cat_x_pos[c] = u; cat_y_pos[c] = v; cat_z_pos[c] = w;
        potential_cat[c] = potential_cat_new; energy_cat[c] = energy_cat_new;
        for (int i = 0; i < grid_length; i++)
        {
            q_el_charge[i] = q_el_charge_new[i];
        }
        movement++; acceptance = 1; acc_moves++; q_el_loc_time[MC_step] = q_el_loc_neu;
    }
}
if (acceptance == 0)
{
    cat_x_pos[c] = cat_x_pos[c] - u1; cat_y_pos[c] = cat_y_pos[c] - v1; cat_z_pos[c] = cat_z_pos[c] - w1;
    pbc2(cat_x_pos[c], cat_y_pos[c], cat_z_pos[c]); DOS_cat[c] = DOS_cat_old; q_el_loc_time[MC_step] = q_el_loc_alt;
}
(...)

```

- 14 After a certain number of MC steps, when the total energy remains constant the Metropolis algorithm is stopped.

```
(..)
} while (MC_step < max_mc_steps);
(..)
```

## Output

15 Calculation of output parameters, like Degree of Confinement (see section 5.4.1), energies or induced electrode charges.

Periodic boundary conditions are implemented in the form of header functions:

```
double pbc(double& dx1, double& dy1, double& dz1)
{
    double xsize = box_si / 10; double ysize = box_si / 10; double zsize = box_si / 10;

    if (dx1 > xsize / 2) { dx1 = dx1 - xsize; }
    if (dx1 <= -xsize / 2) { dx1 = dx1 + xsize; }
    if (dy1 > ysize / 2) { dy1 = dy1 - ysize; }
    if (dy1 <= -ysize / 2) { dy1 = dy1 + ysize; }
    if (dz1 > zsize / 2) { dz1 = dz1 - zsize; }
    if (dz1 <= -zsize / 2) { dz1 = dz1 + zsize; }

    return(sqrt(pow(dx1, 2) + pow(dy1, 2) + pow(dz1, 2)));
}

void pbc2(double& x_pos_new1, double& y_pos_new1, double& z_pos_new1)
{
    double xsize = box_si / 10; double ysize = box_si / 10; double zsize = box_si / 10;

    if ((x_pos_new1*0.1) < 0) { x_pos_new1 = x_pos_new1 + (xsize * 10); }
    if ((x_pos_new1*0.1) >= xsize) { x_pos_new1 = x_pos_new1 - (xsize * 10); }
    if ((y_pos_new1*0.1) < 0) { y_pos_new1 = y_pos_new1 + (ysize * 10); }
    if ((y_pos_new1*0.1) >= ysize) { y_pos_new1 = y_pos_new1 - (ysize * 10); }
    if ((z_pos_new1*0.1) < 0) { z_pos_new1 = z_pos_new1 + (zsize * 10); }
    if ((z_pos_new1*0.1) >= zsize) { z_pos_new1 = z_pos_new1 - (zsize * 10); }
}
```

The linked list method requires two header functions, “cell update” and “get cells”:

```
void cell_update(vector<double>& x_pos_c, vector<double>& y_pos_c, vector<double>& z_pos_c, double box_size, vector<int>& head, vector<int>& list)
{
    vector<vector<vector<int>>> cell_number;
    int p; int dim_c = round(box_size / sub_bx_si); int cell_number2 = 0;
    cell_number.resize(dim_c);
    for (int i = 0; i < dim_c; ++i)
    {
        cell_number[i].resize(dim_c);
        for (int j = 0; j < dim_c; ++j)
        {
            cell_number[i][j].resize(dim_c);
        }
    }
    p = 0;
    for (long int i = 0; i < dim_c; i++)
    {
        for (long int j = 0; j < dim_c; j++)
        {
            for (long int k = 0; k < dim_c; k++)
            {
                cell_number[i][j][k] = p; p++;
            }
        }
    }
    int u; int v; int w;
    int list_length; list_length = list.size(); int head_length; head_length = head.size();
    for (int i = 0; i < head_length; i++)
    {
        head[i] = 0;
    }
    for (int i = 0; i < list_length; i++)
    {
        u = (int)(x_pos_c[i] / sub_bx_si); v = (int)(y_pos_c[i] / sub_bx_si); w = (int)(z_pos_c[i] / sub_bx_si);
        cell_number2 = cell_number[u][v][w];
        list[i] = head[cell_number2];
        head[cell_number2] = i;
    }
}
```

```

    }
}

void get_cells(double x_pos_gc, double y_pos_gc, double z_pos_gc, double box_size, vector<int>& cell_num)
{
    vector<vector<vector<int>>> cell_number; int dim_c = round(box_size / sub_bx_si);
    cell_number.resize(dim_c);
    for (int i = 0; i < dim_c; ++i)
    {
        cell_number[i].resize(dim_c);
        for (int j = 0; j < dim_c; ++j)
        {
            cell_number[i][j].resize(dim_c);
        }
    }
    int p; p = 0;
    for (long int i = 0; i < dim_c; i++)
    {
        for (long int j = 0; j < dim_c; j++)
        {
            for (long int k = 0; k < dim_c; k++)
            {
                cell_number[i][j][k] = p; p++;
            }
        }
    }
    int u, v, w; int va1, va2, va3; int o = 0;
    u = (int)(x_pos_gc / sub_bx_si); v = (int)(y_pos_gc / sub_bx_si); w = (int)(z_pos_gc / sub_bx_si);
    if (box_size == sub_bx_si)
    {
        va1 = w; va2 = v; va3 = u;
        if ((w) < 0) { va1 = va1 + box_size / sub_bx_si; }
        if ((w) >= box_size / sub_bx_si) { va1 = va1 - box_size / sub_bx_si; }
        if ((v) < 0) { va2 = va2 + box_size / sub_bx_si; }
        if ((v) >= box_size / sub_bx_si) { va2 = va2 - box_size / sub_bx_si; }
        if ((u) < 0) { va3 = va3 + box_size / sub_bx_si; }
        if ((u) >= box_size / sub_bx_si) { va3 = va3 - box_size / sub_bx_si; }
        cell_num[0] = cell_number[va3][va2][va1];
    }
    else
    {
        for (int i = -1; i < 2; i++)
        {
            for (int j = -1; j < 2; j++)
            {
                for (int k = -1; k < 2; k++)
                {
                    va1 = k + w; va2 = v + j; va3 = u + i;
                    if ((k + w) < 0) { va1 = va1 + box_size / sub_bx_si; }
                    if ((k + w) >= box_size / sub_bx_si) { va1 = va1 - box_size / sub_bx_si; }
                    if ((v + j) < 0) { va2 = va2 + box_size / sub_bx_si; }
                    if ((v + j) >= box_size / sub_bx_si) { va2 = va2 - box_size / sub_bx_si; }
                    if ((u + i) < 0) { va3 = va3 + box_size / sub_bx_si; }
                    if ((u + i) >= box_size / sub_bx_si) { va3 = va3 - box_size / sub_bx_si; }
                    cell_num[o] = cell_number[va3][va2][va1];
                    o++;
                }
            }
        }
    }
}

```

More details on this code and the code with implemented Ewald summation are given in a Supercapacitor Sandbox toolkit (*SuSan*) manual, available by request from the author.





# Appendix B

## Empirical ion rearrangement algorithm

The following code lines are not complete. Only some representative code lines are shown.

- 1 Declaration of all variables and waves
- 2 Define a “probability function” `DOC_cat_no` & `DOC_an_no` that defines the probability of occupying a certain position within the pore structure, depending on the DoC.

```
for(i=0; i<100; i+=1)
  ions_DOC[i]=i*1/100
endfor

factor[0]=0.13; factor[1]=0.165; factor[2]=0.19; factor[3]=0.26; factor[4]=0.31; factor[5]=0.35; factor[6]=0.39;
factor[7]=0.44; factor[8]=0.53; factor[9]=3; factor[10]=2.3;

if(i==0)
  for(j=0; j<100; j+=1)
    ions_distr_funct_cat[j]=e^((-ions_DOC[j])/(factor[i])) //e^(-ions_DOC[i]/0.25)
  endfor
  for(j=0; j<100; j+=1)
    ions_distr_funct_an[j]=e^((ions_DOC[j]-1)/factor[10-i])/((-1)*e^((ions_DOC[i]-1)/10) //e^(-ions_DOC[i]/0.25)
  endfor
endif

if(i>0 && i<10)
  for(j=0; j<100; j+=1)
    ions_distr_funct_cat[j]=e^((-ions_DOC[j])/(factor[i])) //e^(-ions_DOC[i]/0.25)
  endfor
  for(j=0; j<100; j+=1)
    ions_distr_funct_an[j]=e^((-ions_DOC[j])/(factor[10-i])/((-1)*e^((ions_DOC[i]-1)/10) //e^(-ions_DOC[i]/0.25)
  endfor
endif

if(i>=10)
  for(j=0; j<100; j+=1)
    ions_distr_funct_cat[j]=e^((ions_DOC[j]-1)/(factor[i])) //e^(-ions_DOC[i]/0.25)
  endfor
  for(j=0; j<100; j+=1)
    ions_distr_funct_an[j]=e^((-ions_DOC[j])/factor[10-i])/((-1)*e^((ions_DOC[i]-1)/10) //e^(-ions_DOC[i]/0.25)
  endfor
endif
```

- 3 Arrange all ions (cations + anions) according to the probability functions defined above.

### 3.1 Loop over all ions; pick randomly a cation and anion:

```
for(u=0; u<(number_of_ions); u+=1)
  random_num=(enoise(0.05)+0.05)*10
  if(random_num<cat_fraction)
    cat_an=1; number_of_cations+=1
  else
    cat_an=0; number_of_anions+=1
  endif
  if(cat_an==1) // start with cations
    do (...) while()
```

#### 3.1.1 Choose randomly a new position in the box

```
x_pos_new=round(enoise(99.99)+99.5) ; y_pos_new=round(enoise(99.99)+99.5) ; z_pos_new=round(enoise(99.99)+99.5)
```

### 3.1.2 Check if new position lies in the pore

```
if (pore_structure_is[x_pos_new][y_pos_new][z_pos_new] == 0) count=0; count2=0; DOC_cat[v]=0 (...)
```

### 3.1.3 Check if ion isn't already occupied by another ion

### 3.1.4 If this is the case, calculate the DoC

### 3.1.5 Then perform a Monte Carlo like acceptance condition

```
(...)  
random_num_DOC=noise(DOC_cat_max/2)+(DOC_cat_max/2)  
error=abs(DOC_cat[v]-ions_DOC); FindValue /V=0 /T=.01 error  
else  
  continue  
endif
```

### 3.1.6 Exit condition: if ion position is accepted; Update new ion position;

```
while(count2 !=0 || random_num_DOC > ions_distr_funct_cat[v_value])  
  cat_x_pos[v]=x_pos_new; cat_y_pos[v]=y_pos_new; cat_z_pos[v]=z_pos_new; v+=1
```

## 3.2 Do the same with anions